NWX-2 up
-P-

NASA TECHNICAL MEMORANDUM

NASA TM X-2917

NASA TM X-2917

AN INVESTIGATION OF SEVERAL NACA 1-SERIES AXISYMMETRIC INLETS AT MACH NUMBERS FROM 0.4 TO 1.29

by Richard J. Re

Langley Research Center
Hampton, Va. 23665

NATIONAL AERONAUTICS AND SPACE ADMINISTRATION • WASHINGTON, D. C. • MARCH 1974

1. Report No.	2. Government Accession No.	3. Recipient's Catalog No.
NASA TM X-2917		

4. Title and Subtitle	5. Report Date
AN INVESTIGATION OF SEVERAL NACA 1-SERIES AXISYMMETRIC INLETS AT MACH NUMBERS FROM 0.4 TO 1.29	March 1974
	6. Performing Organization Code
7. Author(s) Richard J. Re	8. Performing Organization Report No. L-8588
	10. Work Unit No. 760-64-60-02
9. Performing Organization Name and Address NASA Langley Research Center Hampton, Va. 23665	11. Contract or Grant No.
	13. Type of Report and Period Covered Technical Memorandum
12. Sponsoring Agency Name and Address National Aeronautics and Space Administration Washington, D.C. 20546	14. Sponsoring Agency Code

15. Supplementary Notes

16. Abstract

An investigation was conducted in the Langley 16-foot transonic tunnel to determine the performance of seven inlets having NACA 1-series contours and one inlet having an elliptical contour over a range of mass-flow ratios and at angle of attack. The inlet diameter ratio varied from 0.81 to 0.89; inlet length ratio varied from 0.75 to 1.25; and internal contraction ratio varied from 1.009 to 1.093. Reynolds number based on inlet maximum diameter varied from 3.4×10^6 at a Mach number of 0.4 to 5.6×10^6 at a Mach number of 1.29.

17. Key Words (Suggested by Author(s))	18. Distribution Statement
Inlet NACA 1-series inlets Inlet performance	Unclassified – Unlimited STAR Category 01

19. Security Classif. (of this report)	20. Security Classif. (of this page)	21. No. of Pages	22. Price*
Unclassified	Unclassified	144	$4.75

*For sale by the National Technical Information Service, Springfield, Virginia 22151

AN INVESTIGATION OF SEVERAL NACA 1-SERIES AXISYMMETRIC INLETS AT MACH NUMBERS FROM 0.4 TO 1.29

By Richard J. Re
Langley Research Center

SUMMARY

An investigation was conducted in the Langley 16-foot transonic tunnel to determine the performance of seven inlets having NACA 1-series contours and one inlet having an elliptical contour over a range of mass-flow ratios and at angle of attack. The inlet diameter ratio varied from 0.81 to 0.89; inlet length ratio varied from 0.75 to 1.25; and internal contraction ratio varied from 1.009 to 1.093. Reynolds number based on inlet maximum diameter varied from 3.4×10^6 at a Mach number of 0.4 to 5.6×10^6 at a Mach number of 1.29.

INTRODUCTION

The development of airfoil sections which delay the formation of strong shocks until high supercritical local Mach numbers are reached has potentially opened the way for aircraft to operate efficiently at higher subsonic Mach numbers. The airfoil section characteristics demonstrated in wind-tunnel tests (refs. 1 to 5) have been confirmed in flight tests on a straight-wing airplane (ref. 6) and on a sweptback-wing airplane (refs. 7 to 9).

Evolution of complete transport aircraft configurations capable of cruising near a Mach number of 1.0 requires development of engine nacelles with performance compatible with airframe capability if the full potential of the supercritical airfoil is to be realized. Since the size and operating characteristics of an aircraft affect the number and location of engine macelles, various aircraft configurations will likely be considered. However, it is probable that most, if not all, configurations will have turbofan engines with axisymmetric or pitot-type inlets. Since the cruise speeds proposed for such transports are substantially above those of current subsonic transports, little of the inlet data in existence would aid in the design of a suitable inlet. The most comprehensive investigations of axisymmetric inlets (NACA 1-series) were conducted at low speeds and are reported in references 10 and 11. Investigations in the transonic speed range (refs. 12 to 17) were conducted on inlets having diameter ratios that are small compared with those required for high-bypass-ratio turbofan engines. The results of reference 18 indicate that inlet external pressures at high subsonic speeds are not significantly affected by the long cowl nacelle afterbody flow field. Therefore, valid evaluations of the external performance of axisymmetric inlets can be made experimentally without integrated development of nacelle afterbody shape.

The present investigation was conducted to obtain force and pressure data on seven NACA 1-series inlets and one elliptical profile inlet at mass-flow ratios typical of those of high-bypass-ratio turbofan engines. Five of the NACA 1-series inlets had different external shapes and two of them had greater amounts of internal area contraction. Inlet diameter and length ratios were in the ranges from 0.81 to 0.89 and 0.75 to 1.25, respectively. Internal area contraction ratio varied from 1.009 to 1.093.

The investigation was conducted in the Langley 16-foot transonic tunnel at Mach numbers from 0.4 to 1.29 and at angles of attack from 0° to about 6° at selected Mach numbers. Reynolds numbers based on model maximum diameter ranged from about 3.4×10^{6} at a Mach number of 0.4 to 5.6×10^{6} at a Mach number of 1.29.

SYMBOLS

A — area normal to inlet center line

C_A — axial-force coefficient, $\dfrac{\text{Axial force}}{q_\infty A_{max}}$

$C_{A,E}$ — external axial-force coefficient, $\dfrac{\text{External axial force}}{q_\infty A_{max}}$

$C_{A,F}$ — forebody pressure-force coefficient, $\dfrac{1}{A_{max}} \displaystyle\int_{A_{sp}}^{A_{max}} C_p \, dA$

$C_{A,w}$ — axial-force coefficient due to skin friction on rake support struts, and duct wall and centerbody surface between rake face and structural break

C_p — pressure coefficient, $\dfrac{p_l - p_\infty}{q_\infty}$

D — diameter

d — intake diameter of NACA 1-series inlet (difference between D_h and twice the inlet lip radius)

M — Mach number

$\dot{m}$ mass flow

$\dot{m}/\dot{m}_\infty$ inlet mass-flow ratio, $\frac{1}{\rho_\infty A_h V_\infty}\int \rho_r V_r \, dA$

p static pressure

p_t stagnation pressure

q dynamic pressure

R radius measured from model center line

R_∞ free-stream Reynolds number based on maximum diameter of model

r lip radius

T_t free-stream stagnation temperature

V velocity

X length of inlet from lip to start of cylindrical part of model

x distance from lip of inlet measured longitudinally

Y maximum ordinate measured perpendicular to reference line at maximum-diameter station for NACA 1-series inlets

y local ordinate measured perpendicular to reference line for NACA 1-series inlet

α angle of attack with respect to model center line, deg

ρ density

ϕ meridian angle, measured from top of model in clockwise direction when looking upstream, deg

Subscripts:

b	force balance
c	force balance cavity
cr	critical condition corresponding to local sonic flow
D	point at which $C_{A,E}$ reaches 1.1 times the level of $C_{A,E}$ at lower Mach numbers
h	most forward point on inlet lip
l	local
max	maximum
min	minimum
r	mass-flow rake station in duct
se	between seal and external surface of model
si	between duct wall and seal
sp	stagnation point on inlet lip
w	duct wall at mass-flow rake station
∞	free-stream condition

MODEL

The model had a maximum diameter of 45.72 cm and was mounted in the test section by a rear sting. The inlet part of the model was supported by a force balance and was structurally isolated from the afterbody which was attached directly to the sting. Photographs showing the model installed in the wind-tunnel test section are presented as figure 1 and a simplified cross-sectional sketch of the model assembly with the shortest inlet (NACA 1-85-75) is shown in figure 2.

Eight inlets were designed, seven of which had NACA 1-series outer profiles and the eighth inlet had an elliptical outer profile. Three of the NACA 1-series inlets had the same outer profile but different amounts of internal area contraction. The nondimensional NACA 1-series outer profile ordinates as presented for a given lip radius in reference 10 are reproduced in table I. A summary of the important geometric parameters for each inlet is contained in figure 3. The elliptical inlet is referred to herein by the designation "Elliptical-85-100" as a matter of convenience so that its geometric designation is analogous to the NACA 1-series inlets. Its external coordinates can be computed for an ellipse having a major axis of 91.440 cm and a minor axis of 3.348 cm. Nondimensional outer profile radii measured on a precision measuring machine are presented in table II and internal design ordinates for each inlet are presented in table III. The internal ordinates for the NACA 1-85-100 inlets with contraction ratios of 1.046 and 1.093 are elliptical between the lip leading edge and minimum duct area station (throat). From the throat to the 25 percent station, the internal contour of all the inlets consisted of a 1° semicone expansion. The remainder of the internal contour consisted of a faired curve with a maximum slope of 6.3° for the shortest inlet. The proportional rate of area growth as a function of distance in the faired section was identical for all inlets.

Static-pressure orifices were drilled into tubing placed in grooves in the model surface and covered with a filler material. The longitudinal locations of the orifices on each inlet outer profile forward of the structural break (station 69.85) are presented in table IV. The four struts which connected the inlets to the centerbody were used to route the inlet static-pressure tubes to differential pressure-scanning units mounted in the nose of the centerbody. Three of the struts were instrumented with the pressure probes necessary to measure the duct mass flow. (See fig. 4.) The model was constructed mainly of aluminum with some of the primary structure such as the sting made of steel. The structural break between the force-balance-mounted inlet and the sting-mounted afterbody housed a flexible seal strip to prevent airflow through the gap. (See detail sketch in fig. 2.)

For convenience, the model aft of the structural break is considered to be the afterbody $\left(1.36D_{max} \text{ in length}\right)$ although a part of the model $\left(0.53D_{max} \text{ in length}\right)$ mounted on the force balance is cylindrical. The ordinates and orifice locations for the afterbody presented in table V are based on the medium length inlet (X = 45.72 cm), where inlet length is only that part of the model defined by the inlet designation. The afterbody was attached directly to the sting by means of four struts as shown in figure 2. All pressure tubes associated with the afterbody were routed through the four supporting struts into the sting and out through the tunnel support system to individual differential pressure transducers or differential pressure scanning units.

The mass-flow throttle plug was driven by an internally housed remote-controlled motor and had a travel of about 25.4 cm aft of the position shown in figure 2. The open area at the exit of the model (normal to the free-stream flow direction) was varied from 678.55 cm^2 to 1229.59 cm^2 with the plug in its two extreme positions.

WIND TUNNEL

The investigation was conducted in the Langley 16-foot transonic tunnel which is a single-return atmospheric wind tunnel with continuous air exchange. The test section is octagonal in shape with 4.724 meters between opposite walls (equivalent to the area of a circle 4.85 meters in diameter) and has axial slots at the wall vertices. The total width of the eight slots in the vicinity of the model is approximately 3.7 percent of the test-section perimeter. At Mach numbers from 1.2 to 1.3, the divergence angle of the test-section walls is adjusted (based on calibration data) as a function of airstream dewpoint temperature to eliminate longitudinal static-pressure gradients that would occur on the center line because of condensation of atmospheric moisture. The solid blockage of the model in the test section is between 0.88 percent (no flow through model) and 0.33 percent (throttle plug area only).

The tunnel sting support system pivots in such a manner that the model remains on or near the test-section center line through the angle-of-attack range.

TESTS AND METHODS

Each inlet was tested at Mach numbers from 0.4 to 1.2 or 1.29 at an angle of attack of 0° and over a nominal angle-of-attack range from 0° to 6° at Mach numbers of 0.4, 0.8, 0.9, and 0.98 subject to force balance load limitations. At an angle of attack of 0°, data were taken at mass-flow ratio increments of 0.1 at all Mach numbers except 0.90, 0.96, and 0.98 where the increment was 0.05. At angle of attack, data were taken only at the maximum mass-flow ratio obtainable (throttle plug in its most aft position). Sketches showing the variations in inlet geometry included in this investigation are shown at the top of figure 3.

The variations of free-stream stagnation temperature and Reynolds number (based on maximum model diameter) with Mach number are shown in figure 5. For all the data presented herein, boundary-layer transition on the inlets was not artificially fixed since the Reynolds numbers at high subsonic speeds were approximately 50 percent of typical flight values at altitudes approaching the tropopause. A limited amount of data obtained with boundary-layer transition fixed on the external surface (0.125-cm-wide strip of number 100 silicon carbide particles, 2.54 cm aft of lip) showed no effect when compared with the free transition pressure data.

Angle of attack has been corrected for deflection of the sting and balance due to model aerodynamic forces and moments and for tunnel stream angularity. Duct mass flow was calculated by using the rake-area-weighted stagnation pressure measurements (fig. 4) and static pressures on the rake, centerbody, and duct walls. The axial-force data were adjusted to the condition of free-stream static pressure at the structural break station between the balance-supported inlet and the sting-supported afterbody parts of the model. That is, separate corrections were made in the area external to the seal in the break in the outer wall and in the area internal to the seal as well as in the cross-sectional area of the centerbody (balance cavity). In addition, the axial-force data were adjusted for the duct internal axial force based on the total-momentum loss from the free stream to the face of the mass-flow rake; and for the skin friction of the rake support struts, and the duct wall and centerbody surfaces from the face of the mass-flow rake to the structural break station. In equation form, the external axial-force coefficient is as follows:

$$C_{A,E} = C_{A,b} + C_{p,se}\left(\frac{A_{se}}{A_{max}}\right) + C_{p,si}\left(\frac{A_{si}}{A_{max}}\right) + C_{p,c}\left(\frac{A_c}{A_{max}}\right) - \frac{\dot{m}(V_\infty \cos\alpha - V_r)}{q_\infty A_{max}} + \frac{p_r - p_\infty}{q_\infty}\left(\frac{A_r}{A_{max}}\right) - C_{A,w}$$

The external axial force was not adjusted for the skin friction on the external cylindrical part of the model between the maximum diameter station of the cowl and the structural break station. The external axial force is presented only for $\alpha = 0^\circ$ and thus it is identically equal to the spillage drag coefficient.

No corrections were made to the force or pressure data for test-section wall interference effects or for local condensation effects that may have occurred in the model flow field. The presence of the mass-flow throttle plug at the base of the afterbody will have an effect on the afterbody pressure field. Therefore, the small amount of afterbody pressure data presented should be considered qualitative.

PRESENTATION OF RESULTS

The results of this investigation are presented in graphical form as axial-force or local external pressure coefficients. The external axial-force coefficient data (obtained from force balance measurements) are presented in figure 6 as a function of mass-flow ratio for each inlet at each Mach number. No axial-force data at angle of attack are presented because of intermittent structural contact between the balance-supported inlet and sting-supported afterbody at the outer periphery of the model at the break station. The pressure coefficient distributions on the inlet outer profiles are presented in figures 7 to 22 for each mass-flow ratio as a function of nondimensionalized inlet length. Some examples of the pressure coefficient distribution over the afterbody are contained in figures 23 to 25. The pressure coefficients were machine plotted and faired by connecting the readings of adjacent orifices with straight-line segments.

The basic data obtained for each inlet are presented in the figures as follows:

Inlet designation	Internal contraction ratio, A_h/A_{min}	Figure showing –		
		External axial-force coefficients, $\alpha \approx 0^o$	Pressure coefficients for –	
			$\alpha = 0^o$	α (range)
NACA 1-81-100	1.012	6(a)	7	15
NACA 1-85-100	1.009	6(b)	8	16
NACA 1-89-100	1.006	6(c)	9	17
NACA 1-85-75	1.009	6(d)	10	18
NACA 1-85-125	1.009	6(e)	11	19
Elliptical-85-100	1.009	6(f)	12	20
NACA 1-85-100	1.046	6(g)	13	21
NACA 1-85-100	1.093	6(h)	14	22

Summary plots showing the variation with Mach number of external axial-force coefficients for inlets of different diameter ratios, length ratios, nose shapes, and internal contraction ratios at constant values of mass-flow ratio are presented in figures 26 to 29. The variation of forebody axial-force coefficient (numerical integration in axial direction of pressure force coefficients from the stagnation point on the lip to the maximum diameter) with Mach number is presented in figure 30 for each inlet.

It should be noted that the mass-flow ratio ($\dot{m}/\dot{m}_\infty$) used herein is based on the area (A_h) at the lip station of each inlet. Therefore, diameter ratio must be taken into account if comparisons at constant mass flows are desired between inlets of differing diameter ratio. This has been done for the critical Mach number plot presented in figure 31. Critical Mach number was obtained from cross plots of peak negative pressure coefficient against mass-flow ratio and Mach number. The variation with mass-flow ratio of drag divergence Mach number which was determined from external axial-force data (fig. 6) is presented in figure 32 to show the effect of the various inlet parameters.

Some examples of the total-pressure distribution at the Mass-flow rake station are presented in figures 33 to 36 to show the effects of inlet diameter ratio, Mach number, internal contraction ratio, and mass-flow ratio.

RESULTS AND DISCUSSION

Pressure Coefficient Distributions at $\alpha = 0^{\circ}$

It was the conclusion of the study of reference 18 that development of inlets for nacelles designed for use at high subsonic Mach numbers need not be conducted on an integrated basis with the development of the afterbody (although the converse is not necessarily the case). The model of the present investigation has been designed to investigate inlets on a more or less isolated basis by inserting a cylindrical part 1.11 model diameters in length between the end of the inlet and the start of afterbody boattailing. (See fig. 2.) Pressure coefficient distributions over the length of the model (figs. 23 to 25) confirm that the afterbody boattail and mass-flow throttle plug had no significant effect on the inlet external pressure coefficients presented herein at Mach numbers below 0.98.

In general, the static-pressure distributions over the inlet external surfaces are comparable to those obtained in references 10 and 11. At low Mach numbers and low mass-flow ratios, high negative pressure peaks usually occurred on the inlet lips because of the large local angle of attack and flow separation was encountered in many cases. The inlets with the steeper local external slopes in the vicinity of the lip (NACA 1-81-100 (fig. 7), NACA 1-85-75 (fig. 10)), and (Elliptical-85-100 (fig. 12)) showed little evidence of flow separation at low Mach numbers and low mass-flow ratios. However, for the inlets with less steep local slopes near the lip (the three NACA 1-85-100 inlets), flow separation occurred at low Mach numbers and low mass-flow ratios and extended as far back on the inlet as $x/X = 0.05$ (figs. 8(a) and 8(b), 13(a) and 13(b), and 14(a) and 14(b)). The inlets with still lower slopes near the lip (NACA 1-89-100 and NACA 1-85-125) encountered more extensive separation. For example, flow separation on the inlet with the largest diameter ratio (NACA 1-89-100) extended as far back on the inlet as $x/X = 0.30$ at a Mach number of 0.80 (fig. 9(b)), and flow separation on the longest inlet (NACA 1-85-125) extended as far back on the inlet as $x/X = 0.10$ at a Mach number of 0.80 (fig. 11(b)). Flow separation in the vicinity of the lip on some of the inlets is further illustrated in figure 31 by the negative variation of critical Mach number with mass-flow ratio at the low mass-flow ratios; that is, pressure peaks were not attained (see fig. 11(b)).

As mass-flow ratio was increased, the negative pressure peaks decreased in severity, flow separation diminished, and at some large mass-flow ratio, a point was reached on most inlets where there was no pressure peak at the lip and the pressure distribution became nearly uniform over the inlet. Further increase in mass-flow ratio or Mach number rounded off the pressure distribution at the lip and resulted in positive pressure over part of the inlet. The peak value of negative pressure under these conditions occurred further back on the inlet in a region relatively insensitive to changes in mass-flow ratio.

At high subsonic Mach numbers and large mass-flow ratios, the pressure coefficients were nearly constant over the inlet length for many of the inlets. At the largest mass-flow ratios attainable at Mach numbers of 0.94 and 0.96 nearly uniform pressure distributions were obtained on the Elliptical-85-100 inlet (figs. 12(d) and 12(e)). However, it is likely that the NACA 1-89-100 (figs. 9(d) and 9(e)) and 1-85-125 (figs. 11(d) and 11(e)) inlets would have exhibited more uniform pressure distributions in this Mach number range if greater mass-flow ratios could have been obtained. The NACA 1-85-100 inlets (figs. 8(d) and 8(e), 13(d) and 13(e), and 14(d) and 14(e)) also had uniform pressure distributions over most of their length.

Pressure Coefficient Distributions at Angle of Attack

Angle of attack was varied in the range from 0° to 6° at Mach numbers of 0.40, 0.80, 0.90, and 0.98 at the maximum obtainable value of mass-flow ratio for each inlet. One angle-of-attack sweep at a low mass-flow ratio was made at a Mach number of 0.90 for the Elliptical-85-100 inlet (fig. 20(b)). The inlets had a row of pressure orifices on both the top ($\phi = 0^{\circ}$) and bottom ($\phi = 180^{\circ}$) external surfaces. Therefore, data presented for $\phi = 180^{\circ}$ in figures 15 to 22 can be considered to be for the inlet at negative angles of attack.

The effects of angle of attack were as would be expected, that is, the pressure peaks on the top of the inlet external surface became more severe and in some cases separated at the high angles of attack. On the bottom of the inlets, the extent of positive pressure coefficients over the inlet increased as angle of attack increased.

Pressure Coefficient Distributions Over Afterbody

In general, the changes made in inlet geometry had little effect on the pressure distribution over the model afterbody. The effect of the throttle plug at the base on the pressure coefficients on the boattailed part of the afterbody is much greater than inlet diameter ratio or length ratio, as can be seen by comparing figure 25 with figures 23 and 24.

To decrease the effect of throttle plug position on the pressure coefficient distributions, comparisons between inlets were made at the same mass flow for inlets of differing diameter ratio (fig. 23) or at the same mass-flow ratio for inlets of the same diameter ratio (fig. 24). Under these conditions the data of figures 23 and 24 show that inlet geometry had little effect on the boattailed afterbody pressure distributions at Mach numbers of 0.80 or 0.90 except at low mass flows where separation occurred at the inlet lip. At a Mach number of 0.98, however, inlet length had a large effect on the boattail pressure distributions especially at low mass-flow ratios (fig. 24(b)). This effect of inlet length is even greater on the constant-diameter center section of the model. Inlet diameter ratio affected the pressure distribution over the center section of the model at low Mach numbers only when lip separation occurred (fig. 23(a)), and at a Mach number of 0.98 only at large mass flows (fig. 23(b)).

External Axial-Force Coefficient

The amount of flow separation on the external surface of the inlets varied with mass-flow ratio as indicated by the pressure distributions. This condition is further illustrated by the axial-force coefficients of figure 6, where inlets whose pressure distributions indicated little or no separation (NACA 1-81-100, NACA 1-85-75, and Elliptical-85-100) show little variation of axial-force coefficient with mass-flow ratio at low Mach numbers. The other inlets whose pressure distributions indicated more extensive lip separation show large decreases in axial-force coefficient with increasing mass-flow ratio as the amount of separation decreased. At high supercritical Mach numbers, the inlets encountered wave drag which increased the drag over the mass-flow range especially at low mass-flow ratios. The magnitude of axial-force coefficient decreases with increasing mass-flow ratio, and approaches the minimum at high mass-flow ratio where the inlet would choke at the higher subsonic Mach numbers. This condition was not reached during this investigation except for the NACA 1-81-100 inlet (fig. 6(a)) although several other inlets attained a nearly flat variation of axial-force coefficient with mass-flow ratio at the maximum mass-flow ratio.

Effect of inlet diameter ratio, d/D_{max}.- Comparison of the axial-force data of figures 6(a), 6(b), and 6(c) indicates that the inlet with the smallest diameter ratio 0.81 was least affected by varying mass flow at a given Mach number whereas the inlet with the largest diameter ratio 0.89 was affected the most. At high subsonic Mach numbers, the inlet with the smallest diameter ratio reached its minimum value of axial-force coefficient within the test mass-flow range; whereas the inlet with the middle diameter ratio 0.85 appears to have just attained the minimum value of axial-force coefficient near the maximum mass flow. However, the inlet with the largest diameter ratio did not reach a minimum value of axial-force coefficient at the maximum mass flow for any of the high subsonic Mach numbers.

Comparisons of the variation of axial-force coefficient with Mach number for three values of mass-flow ratio for the three inlet diameter ratios are shown in figure 26, although it is likely that the high mass-flow ratio would be the only region such inlets would normally operate in. The inlet with the smallest diameter ratio had the lowest axial-force coefficient at each of the mass-flow ratios. However, no appreciable advantage of one diameter ratio inlet over the others is discernible on the basis of drag divergence Mach number over the range of the mass-flow ratios. (See fig. 32.)

Effect of inlet length ratio, X/D_{max}.- Comparison of the axial-force data of figures 6(b), 6(d), and 6(e) indicates that the inlet with the smallest length ratio 0.75 was least affected by varying mass flow at a given Mach number, whereas the inlet with the largest length ratio 1.25 was affected the most. This condition occurred because of two predominant effects: (1) the longest inlet encountered severe flow separation at low mass-flow ratios for low Mach numbers and the shortest inlet did not; and (2) at higher Mach numbers where separation was not a factor, the longest inlet had lower wave drag for high mass-flow ratios because of its greater fineness ratio.

These effects are illustrated in figure 27 where the variation of axial-force coefficient with Mach number for four values of mass-flow ratio is shown for the three inlet length ratios. At the lowest mass-flow ratio, the shortest inlet has the lowest axial-force coefficient up to a Mach number of 0.95 and has the same axial-force coefficient as the two longer inlets at Mach numbers from 0.95 to 1.01. At the highest mass-flow ratio, all three inlets have comparable values of axial-force coefficient up to 0.92 in Mach number after which the longest inlet is clearly better. The superiority of the longest inlet when the three inlets are compared on a drag divergence Mach number basis is shown in figure 32 where the drag divergence Mach number for the longest inlet is 0.04 to 0.05 higher than that for the shortest inlet.

Effect of external inlet contour for a given diameter ratio.- Comparison of the axial-force data of figures 6(b) and 6(f) shows only small differences between the NACA 1-85-100 inlet and the elliptical inlet except at combined low Mach numbers and low mass-flow ratios where the elliptical nose inlet encountered less flow separation and therefore had lower axial force.

The variation of axial-force coefficient with Mach number for four values of mass-flow ratio for the two inlet nose shapes is shown in figure 28. At high mass-flow ratios, the axial-force coefficients were nearly the same until the drag break occurred. Comparison of the drag divergence Mach number variation with mass-flow ratio presented in figure 32 shows that the NACA 1-series had a higher drag divergence Mach number in general.

Effect of internal contraction ratio.- Comparison of the axial-force data for figures 6(b), 6(g), and 6(h) shows that internal contraction had no significant effect over the range of mass flow of the investigation. The variation of axial-force coefficient with Mach number at constant values of mass-flow ratio presented in figure 29 further illustrates the small effect. The drag divergence data of figure 32 tend to indicate that the inlet with a contraction ratio of 1.046 had a lower value of drag divergence Mach number than the other two inlets. However, this condition may be due to the rather erratic variation of axial-force coefficient with Mach number indicated in figure 29.

Internal Total-Pressure Measurements

Total-pressure distributions measured at the mass-flow rake station are presented in figures 33 to 36 to illustrate internal performance for several inlet and flow parameters. The model internal geometry and instrumentation were not intended to be definitive for an internal performance analysis of the quality of flow being supplied to an engine compressor. However, the necessity of making total-pressure measurements for mass-flow (internal momentum) computations in the constant-diameter section of the duct did result in the rakes being located rearward of – but reasonably close to – what would be typical of an engine compressor face station.

In general, the total-pressure distributions indicate that up to a Mach number of 0.98 the total pressure was uniform across the duct at an angle of attack of 0^{o} with only small losses in total pressure recovery close to the wall and centerbody. The inlet with the smallest diameter ratio (NACA 1-81-100, fig. 33) had the most rapidly diverging diffuser lines of the three diameter ratios and at high mass flow, shows signs of separation on the outer duct wall at a Mach number of 0.90. At a Mach number of 1.20 (fig. 33(c)), the combination of choked flow and separation on the duct wall produced poor pressure recovery for this inlet at high mass-flow ratios. Similar characteristics were exhibited by the NACA 1-85-100 with a contraction ratio of 1.093 (fig. 34). The effect of mass-flow ratio on the total pressure distribution in the duct for the NACA 1-85-100 inlet with two contraction ratios is shown in figure 35. At a Mach number of 1.20 the inlet with a 1.093 contraction ratio (fig. 35(b)) encountered considerable separation on the duct wall at a mass-flow ratio of 0.89 that was causing – or was caused by – choking in the inlet.

At angle of attack (and high mass-flow ratios) the total-pressure distributions over the top and bottom arms of the rake indicate considerable flow asymmetry even at the lower Mach numbers (compare figs. 36(a) and 36(b)) for the NACA 1-85-100 inlet with a contraction ratio of 1.093.

CONCLUDING REMARKS

An investigation has been conducted to determine the external performance of seven NACA 1-series contours and one inlet having an elliptical contour over a range of mass-flow ratios and at angle of attack. For a constant length ratio (1.00), the inlet with the smallest diameter ratio (0.81) had the lowest axial-force coefficient over the range of mass-flow ratios and Mach numbers. Of the eight inlets tested, the NACA 1-81-100 inlet, the NACA 1-85-75 inlet, and the elliptical contour inlet encountered the least flow separation at the lip at low mass-flow ratios and low Mach numbers because of their blunt external lip shapes. Internal area contraction up to 9 percent had no appreciable effect on the external axial-force coefficient of an NACA 1-85-100 inlet at Mach numbers up to 1.01. Inlet pressure distributions showed no significant effect of afterbody boattailing (which started 1.11 model diameters downstream of the end of the inlet) at Mach numbers below 0.98.

Langley Research Center,
National Aeronautics and Space Administration,
Hampton, Va., October 25, 1973.

REFERENCES

1. Whitcomb, Richard T.; and Clark, Larry R.: An Airfoil Shape for Efficient Flight at Supercritical Mach Numbers. NASA TM X-1109, 1965.

2. Blackwell, James A., Jr.: Aerodynamic Characteristics of an 11-Percent-Thick Symmetrical Supercritical Airfoil at Mach Numbers Between 0.30 and 0.85. NASA TM X-1831, 1969.

3. Harris, Charles D.: Wind-Tunnel Investigation of Effects of Trailing-Edge Geometry on a NASA Supercritical Airfoil Section. NASA TM X-2336, 1971.

4. Harris, Charles D.; and Blackwell, James A., Jr.: Wind-Tunnel Investigation of Effects of Rear Upper Surface Modification on an NASA Supercritical Airfoil. NASA TM X-2454, 1972.

5. Whitcomb, Richard T.; and Blackwell, James A., Jr.: Status of Research on a Supercritical Wing. Conference on Aircraft Aerodynamics, NASA SP-124, 1966, pp. 367-381.

6. Palmer, William E.; and Elliott, Donald W.: Summary of T-2C Supercritical Wing Program. Supercritical Wing Technology – A Progress Report on Flight Evaluations. NASA SP-301, 1972, pp. 13-34.

7. Harris, Charles D.: Wind-Tunnel Measurements of Aerodynamic Load Distribution on an NASA Supercritical-Wing Research Airplane Configuration. NASA TM X-2469, 1972.

8. Bartlett, Dennis W.; and Re, Richard J.: Wind-Tunnel Investigation of the Basic Aerodynamic Characteristics of a Supercritical-Wing Research Airplane Configuration. NASA TM X-2470, 1972.

9. Anon.: Supercritical Wing Technology – A Progress Report on Flight Evaluations. NASA SP-301, 1972.

10. Baals, Donald D.; Smith, Norman F.; and Wright, John B.: The Development and Application of High-Critical-Speed Nose Inlets. NACA Rep. 920, 1948. (Supersedes NACA ACR L5F30a.)

11. Nichols, Mark R.; and Keith, Arvid L., Jr.: Investigation of a Systematic Group of NACA 1-Series Cowlings With and Without Spinners. NACA Rep. 950, 1949. (Supersedes NACA RM L8A15.)

12. Pendley, Robert E.; and Robinson, Harold L.: An Investigation of Several NACA 1-Series Nose Inlets With and Without Protruding Central Bodies at High-Subsonic Mach Numbers and at a Mach Number of 1.2. NACA TN 3436, 1955.

13. Pendley, Robert E.; Robinson, Harold L.; and Williams, Claude V.: An Investigation of Three Transonic Fuselage Air Inlets At Mach Numbers From 0.4 to 0.94 and at a Mach Number of 1.19. NACA RM L50H24, 1950.

14. Nichols, Mark R.; and Pendley, Robert E.: Performance of Air Inlets at Transonic and Low Supersonic Speeds. NACA RM L52A07, 1952.

15. Pendley, Robert E.; Milillo, Joseph R.; and Fleming, Frank F.: An Investigation of Three NACA 1-Series Nose Inlets at Subsonic and Transonic Speeds. NACA RM L52J23, 1953.

16. Pendley, Robert E.; and Smith, Norman F.: An Investigation of the Characteristics of Three NACA 1-Series Nose Inlets At Subcritical and Supercritical Mach Numbers. NACA RM L8L06, 1949.

17. Pendley, Robert E.; Milillo, Joseph R.; Fleming, Frank F.; and Bryan, Carroll R.: An Experimental Study of Five Annular-Air-Inlet Configurations at Subsonic and Transonic Speeds. NACA RM L53F18a, 1953.

18. Leynaert, J.: Transonic Testing of the Engine Nacelle Air Intake and Afterbody. NASA TT F-14,154, 1972.

TABLE I.- NACA 1-SERIES ORDINATES

[Ordinates in percent]

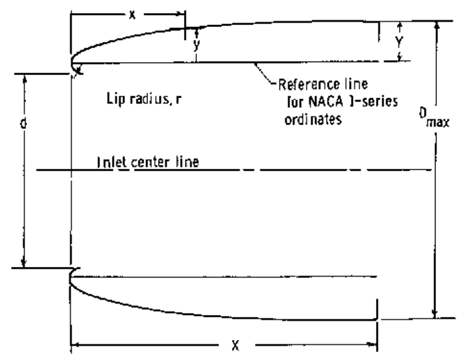

$$X = \left(\frac{X}{D_{max}}\right) D_{max} \qquad Y = \frac{D_{max} - d}{2} - r$$

Sample NACA 1-series designation: NACA $\underbrace{1}_{\text{Series}} - \underbrace{81}_{\frac{d}{D_{max}}\text{ (in percent)}} - \underbrace{100}_{\frac{X}{D_{max}}\text{ (in percent)}}$

x/X	y/Y	x/X	y/Y	x/X	y/Y
0	0	20.0	52.70	48.0	81.25
.2	4.80	21.0	54.05	49.0	81.99
.4	6.63	22.0	55.37	50.0	82.69
.6	8.12	23.0	56.66	52.0	84.10
.8	9.33	24.0	57.92	54.0	85.45
1.0	10.38	25.0	59.15	56.0	86.73
1.5	12.72	26.0	60.35	58.0	87.95
2.0	14.72	27.0	61.52	60.0	89.11
2.5	16.57	28.0	62.67	62.0	90.20
3.0	18.31	29.0	63.79	64.0	91.23
3.5	19.94	30.0	64.89	66.0	92.20
4.0	21.48	31.0	65.97	68.0	93.11
4.5	22.96	32.0	67.03	70.0	93.95
5.0	24.36	33.0	68.07	72.0	94.75
6.0	27.01	34.0	69.08	74.0	95.48
7.0	29.47	35.0	70.08	76.0	96.16
8.0	31.81	36.0	71.05	78.0	96.79
9.0	34.03	37.0	72.00	80.0	97.35
10.0	36.13	38.0	72.94	82.0	97.87
11.0	38.15	39.0	73.85	84.0	98.33
12.0	40.09	40.0	74.75	86.0	98.74
13.0	41.94	41.0	75.63	88.0	99.09
14.0	43.66	42.0	76.48	90.0	99.40
15.0	45.30	43.0	77.32	92.0	99.65
16.0	46.88	44.0	78.15	94.0	99.85
17.0	48.40	45.0	78.95	96.0	99.93
18.0	49.88	46.0	79.74	98.0	99.98
19.0	51.31	47.0	80.50	100.0	100.00
Lip radius: 0.025Y					

TABLE II.- NONDIMENSIONALIZED EXTERNAL ORDINATES MEASURED ON INLETS

NACA 1-81-100;
Contraction ratio, 1.012

x/X	R/R_{max} for -	
	$\phi = 0^o$	$\phi = 180^o$
0.0000	0.8160	0.8148
.0020	.8232	.8233
.0040	.8266	.8268
.0060	.8295	.8296
.0100	.8339	.8337
.0150	.8383	.8381
.0200	.8421	.8420
.0250	.8455	.8454
.0300	.8487	.8486
.0400	.8545	.8546
.0500	.8600	.8599
.0700	.8694	.8693
.1000	.8818	.8817
.1500	.8987	.8986
.2000	.9121	.9120
.2500	.9244	.9242
.3000	.9352	.9351
.3500	.9450	.9449
.4000	.9535	.9534
.4500	.9614	.9614
.5000	.9687	.9687
.6000	.9809	9809
.7000	.9903	.9903
.8000	.9966	.9967
.9000	1.0003	1.0005

NACA 1-85-100;
Contraction ratio, 1.009

x/X	R/R_{max} for -	
	$\phi = 0^o$	$\phi = 180^o$
0.0000	0.8543	0.8547
.0020	.8625	.8619
.0040		.8646
.0060	.8672	.8667
.0150	.8738	.8733
.0200	.8767	.8763
.0250	.8793	.8790
.0300	.8818	.8814
.0400	.8864	.8859
.0500	.8907	.8902
.0700	.8982	.8977
.1000	.9076	.9072
.1500	.9205	.9202
.2000	.9317	.9312
.2500	.9411	.9405
.3000	.9495	.9489
.3500	.9572	.9565
.4000	.9637	.9632
.4500	.9699	.9693
.5000	.9754	.9747
.6000	.9846	.9841
.7000	.9918	.9912
.8000	.9969	.9962
.9000	.9998	.9991

NACA 1-89-100;
Contraction ratio, 1.006

x/X	R/R_{max} for -	
	$\phi = 0^o$	$\phi = 180^o$
0.0000	0.8947	0.8945
.0020	.8993	.8993
.0040	.9015	.9015
.0060	.9032	.9031
.0150	.9080	.9080
.0200	.9100	.9100
.0250	.9119	.9119
.0300	.9138	.9137
.0400	.9172	.9171
.0500	.9202	.9202
.0700	.9255	.9255
.1000	.9326	.9326
.1500	.9424	.9424
.2000	.9504	.9504
.2500	.9572	.9572
.3000	.9632	.9631
.3500	.9689	.9689
.4000	.9738	.9737
.4500	.9780	.9779
.5000	.9821	.9820
.6000	.9889	.9887
.7000	.9941	.9939
.8000	.9975	.9973
.9000	.9996	.9994

NACA 1-85-75;
Contraction ratio, 1.009

x/X	R/R_{max} for -	
	$\phi = 0^o$	$\phi = 180^o$
0.0000	0.8537	0.8538
.0021	.8601	.8610
.0040	.8629	.8637
.0061	.8651	.8660
.0099	.8687	.8693
.0150	.8722	.8728
.0200	.8753	.8757
.0250	.8781	.8785
.0301	.8807	.8810
.0400	.8853	.8857
.0499	.8895	.8898
.0701	.8970	.8973
.1000	.9067	.9070
.1501	.9211	.9213
.2000	.9315	.9316
.2501	.9406	.9410
.3000	.9492	.9494
.3499	.9567	.9569
.4000	.9635	.9637
.4501	.9695	.9698
.5000	.9752	.9753
.6000	.9846	.9847
.7000	.9919	.9920
.8000	.9963	.9963
.9000	1.0005	1.0004

NACA 1-85-125;
Contraction ratio, 1.009

x/X	R/R_{max} for -	
	$\phi = 0^o$	$\phi = 180^o$
0.0000	0.8552	0.8543
.0020	.8628	.8616
.0040	.8654	.8642
.0059	.8672	.8662
.0100	.8704	.8695
.0150	.8738	.8728
.0200	.8767	.8757
.0250	.8793	.8783
.0400	.8865	.8856
.0500	.8906	.8897
.0700	.8980	.8971
.1000	.9071	.9061
.1500	.9210	.9200
.2000	.9316	.9306
.2500	.9410	.9400
.3000	.9494	.9485
.3500	.9570	.9560
.4000	.9638	.9628
.4500	.9697	.9687
.5000	.9751	.9741
.6000	.9842	.9832
.7000	.9915	.9905
.8000	.9966	.9956
.9000	.9996	.9987

Elliptical-85-100;
Contraction ratio, 1.009

x/X	R/R_{max} for -	
	$\phi = 0^o$	$\phi = 180^o$
0.0000	0.8548	0.8550
.0021	.8636	.8642
.0030	.8656	.8662
.0046	.8685	.8691
.0064	.8713	.8718
.0110	.8765	.8771
.0213	.8852	.8857
.0297	.8906	.8912
.0426	.8974	.8980
.0664	.9071	.9076
.0937	.9164	.9170
.1254	.9256	.9262
.1613	.9341	.9346
.2013	.9425	.9430
.2453	.9501	.9507
.2984	.9578	.9583
.3439	.9643	.9648
.3982	.9708	.9713
.4553	.9767	.9772
.5152	.9817	.9823
.5774	.9863	.9869
.6416	.9901	.9907
.7076	.9933	.9938
.7751	.9958	.9964
.8349	.9974	.9980
.9042	.9987	.9993

NACA 1-85-100;
Contraction ratio, 1.046

x/X	R/R_{max} for -	
	$\phi = 0^o$	$\phi = 180^o$
0.0000	0.8557	0.8558
.0020	.8634	.8639
.0040	.8660	.8666
.0060	.8682	.8685
.0150	.8747	.8750
.0200	.8776	.8779
.0250	.8802	.8805
.0300	.8826	.8829
.0400	.8872	.8874
.0500	.8914	.8916
.0700	.8988	.8991
.1000	.9083	.9085
.1500	.9212	.9213
.2000	.9321	.9322
.2500	.9415	.9416
.3000	.9500	.9501
.3500	.9576	.9577
.4000	.9642	.9643
.4500	.9703	.9704
.5000	.9758	.9759
.6000	.9850	.9850
.7000	.9920	.9920
.8000	.9969	.9970
.9000	.9997	.9997

NACA 1-85-100;
Contraction ratio, 1.093

x/X	R/R_{max} for -	
	$\phi = 0^o$	$\phi = 180^o$
0.0000	0.8547	
.0020	.8624	0.8628
.0040	.8648	.8650
.0060	.8667	.8669
.0150	.8733	.8735
.0200	.8763	.8764
.0250	.8788	.8791
.0300	.8813	.8814
.0400	.8858	.8860
.0500	.8901	.8902
.0700	.8976	.8978
.1000	.9071	.9072
.1500	.9201	.9204
.2000	.9312	.9313
.2500	.9406	.9407
.3000	.9490	.9492
.3500	.9566	.9568
.4000	.9633	.9634
.4500	.9694	.9696
.5000	.9750	.9752
.6000	.9844	.9846
.7000	.9915	.9915
.8000	.9965	.9967
.9000	.9995	.9995

TABLE III.- INTERNAL ORDINATES OF INLETS

[Ordinates in percent]

NACA 1-81-100;
Contraction ratio, 1.012;
Diffuser area ratio, 1.270

x/X	y/Y
0	0
.2	-2.6
12.5	-.3
25.0	2.1
35.0	5.0
45.0	9.3
60.0	19.9
80.0	44.0
90.0	56.2
100.0	64.0

NACA 1-85-100;
Contraction ratio, 1.009;
Diffuser area ratio, 1.154

x/X	y/Y
0	0
.2	-2.4
12.5	.5
25.0	3.5
35.0	5.9
45.0	9.3
60.0	17.9
80.0	37.8
90.0	48.0
100.0	54.5

NACA 1-89-100;
Contraction ratio, 1.006;
Diffuser area ratio, 1.052

x/X	y/Y
0	0
.1	-2.5
12.5	1.4
25.0	5.6
35.0	7.0
45.0	9.1
60.0	14.5
80.0	27.1
90.0	33.7
100.0	37.9

NACA 1-85-75;
Contraction ratio, 1.009;
Diffuser area ratio, 1.154

x/X	y/Y
0	0
.2	-2.4
12.5	-.3
25.0	2.0
35.0	4.4
45.0	8.0
60.0	16.8
80.0	37.2
90.0	47.8
100.0	54.5

NACA 1-85-125;
Contraction ratio, 1.009
Diffuser area ratio, 1.154

x/X	y/Y
0	0
.1	-2.4
12.5	1.2
25.0	5.0
35.4	7.3
45.0	10.6
60.0	19.1
80.0	38.2
100.0	54.5

Elliptical-85-100;
Contraction ratio, 1.009
Diffuser area ratio, 1.154

x/X	y/Y
0	0
.2	-2.4
12.5	.5
25.0	3.5
35.0	5.9
45.0	9.3
60.0	17.9
80.0	37.8
90.0	48.0
100.0	54.5

NACA 1-85-100;
Contraction ratio, 1.046;
Diffuser area ratio, 1.197

x/X	y/Y
0	0
.1	-2.8
.2	-4.2
.3	-4.9
.5	-6.1
.6	-7.1
1.1	-9.0
2.1	-11.5
3.0	-12.6
4.1	-13.1
4.4	-13.1
13.9	-10.8
25.0	-8.1
35.0	-5.2
45.0	-1.0
60.0	9.7
80.0	34.1
90.0	46.5
100.0	54.5

NACA 1-85-100;
Contraction ratio, 1.093;
Diffuser area ratio, 1.250

x/X	y/Y
0	0
.1	-5.5
.2	-8.0
.3	-9.6
.5	-11.8
.6	-13.7
1.1	-17.3
2.1	-22.3
3.0	-24.4
4.1	-25.3
4.4	-25.3
13.9	-23.1
25.0	-20.4
35.0	-16.9
45.0	-11.8
60.0	1.1
80.0	30.2
90.0	45.0
100.0	54.5

TABLE IV.- PRESSURE ORIFICE LOCATIONS ON INLET EXTERNAL SURFACES

NACA 1-81-100,
NACA 1-85-100,
NACA 1-89-100,
Elliptical-85-100;
Contraction ratio, ≈1.0

Orifice locations for –

x/X	ϕ, deg	
	0	180
0	×	×
.0031	×	
.0062	×	×
.0125	×	×
.0188	×	×
.025	×	×
.0312	×	×
.0375	×	×
.0438	×	×
.05	×	×
.075	×	×
.10	×	×
.125	×	
.15	×	×
.175	×	
.20	×	×
.30	×	×
.40	×	×
.50	×	×
.60	×	×
.70	×	×
.80	×	×
.90	×	×
1.2222	×	×
1.3889	×	×

NACA 1-85-75;
Contraction ratio, 1.009

Orifice locations for –

x/X	ϕ, deg	
	0	180
0	×	×
.0031	×	
.0062	×	×
.0125	×	×
.0188	×	×
.025	×	×
.0312	×	×
.0375	×	×
.0438	×	×
.05	×	×
.075	×	×
.10	×	×
.125	×	
.15	×	×
.175	×	
.20	×	×
.30	×	×
.40	×	×
.50	×	×
.60	×	×
.70	×	×
.80	×	×
.90	×	×
1.2963	×	×
1.5185	×	×

NACA 1-85-125;
Contraction ratio, 1.009

Orifice locations for –

x/X	ϕ, deg	
	0	180
0	×	×
.0031	×	
.0062	×	×
.0125	×	×
.0188	×	×
.025	×	×
.0312	×	×
.0375	×	×
.0438	×	×
.05	×	×
.075	×	×
.10	×	×
.125	×	
.15	×	×
.175	×	
.20	×	×
.30	×	×
.40	×	×
.50	×	×
.60	×	×
.70	×	×
.80	×	×
.90	×	×
1.1778	×	×
1.3111	×	×

NACA 1-85-100;
Contraction ratios,
1.046 and 1.093

Orifice locations for –

x/X	ϕ, deg	
	0	180
0	×	×
.0031	×	
.0062	×	×
.0125	×	×
.0188	×	×
.025	×	×
.0312	×	×
.0375	×	×
.0438	×	
.05	×	×
.075	×	×
.10	×	×
.125	×	
.15	×	×
.175	×	
.20	×	×
.30	×	×
.40	×	×
.50	×	×
.60	×	×
.70	×	×
.80	×	×
.90	×	×
1.2222	×	×
1.3889	×	×

TABLE V.- NONDIMENSIONALIZED EXTERNAL DESIGN ORDINATES AND ORIFICE LOCATIONS FOR AFTERBODY

External ordinates	
x/X (for X = 45.72 cm)	R/R_{max}
1.533	1.000
2.111	1.000
2.222	.998
2.333	.992
2.444	.984
2.556	.968
2.611	.959
2.667	.949
2.722	.937
2.778	.923
2.806	.915
2.833	.907
2.861	.898
2.889	.889

Orifice locations
x/X (for X = 45.72 cm)
1.667
1.833
2.000
2.167
3.889
2.556
2.667
2.722
2.778
2.833

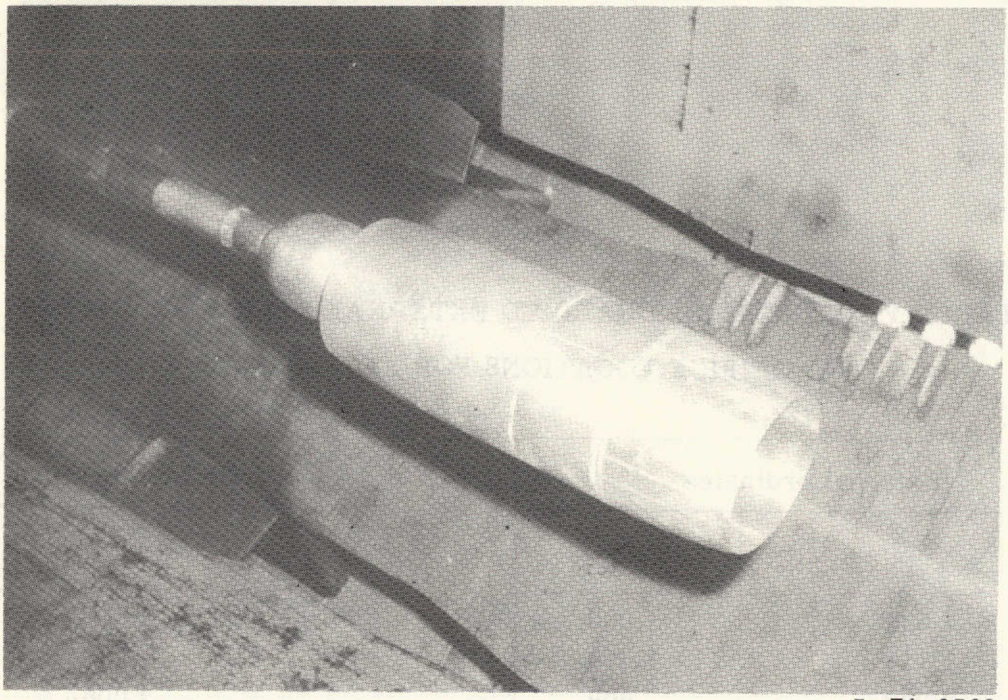

L-71-6562

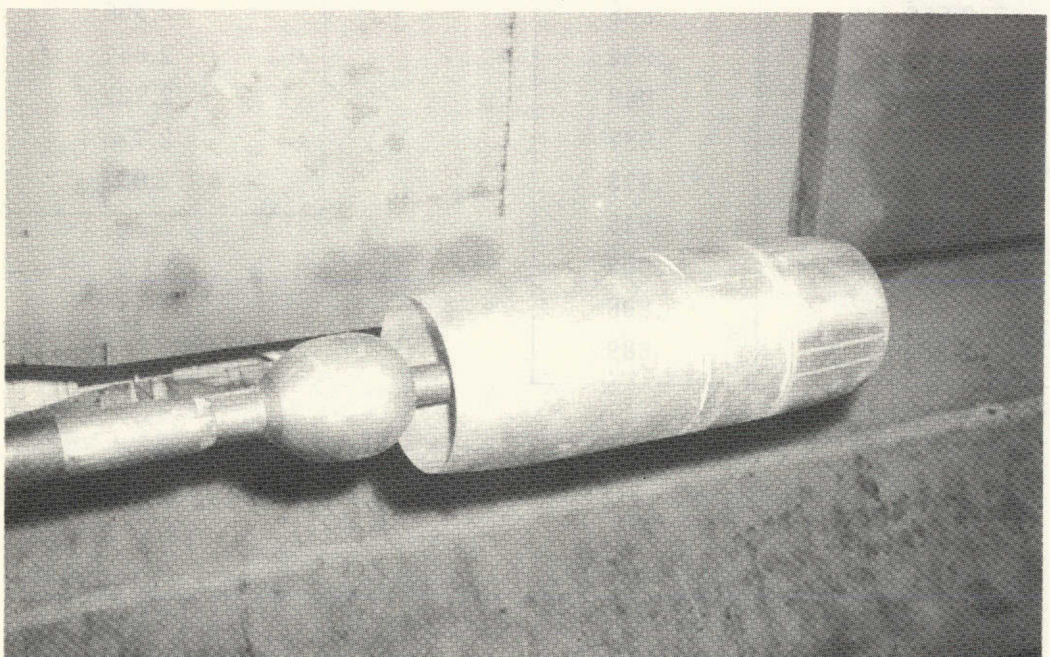

L-71-6561

Figure 1.- Photograph of model with NACA 1-85-75 inlet installed.

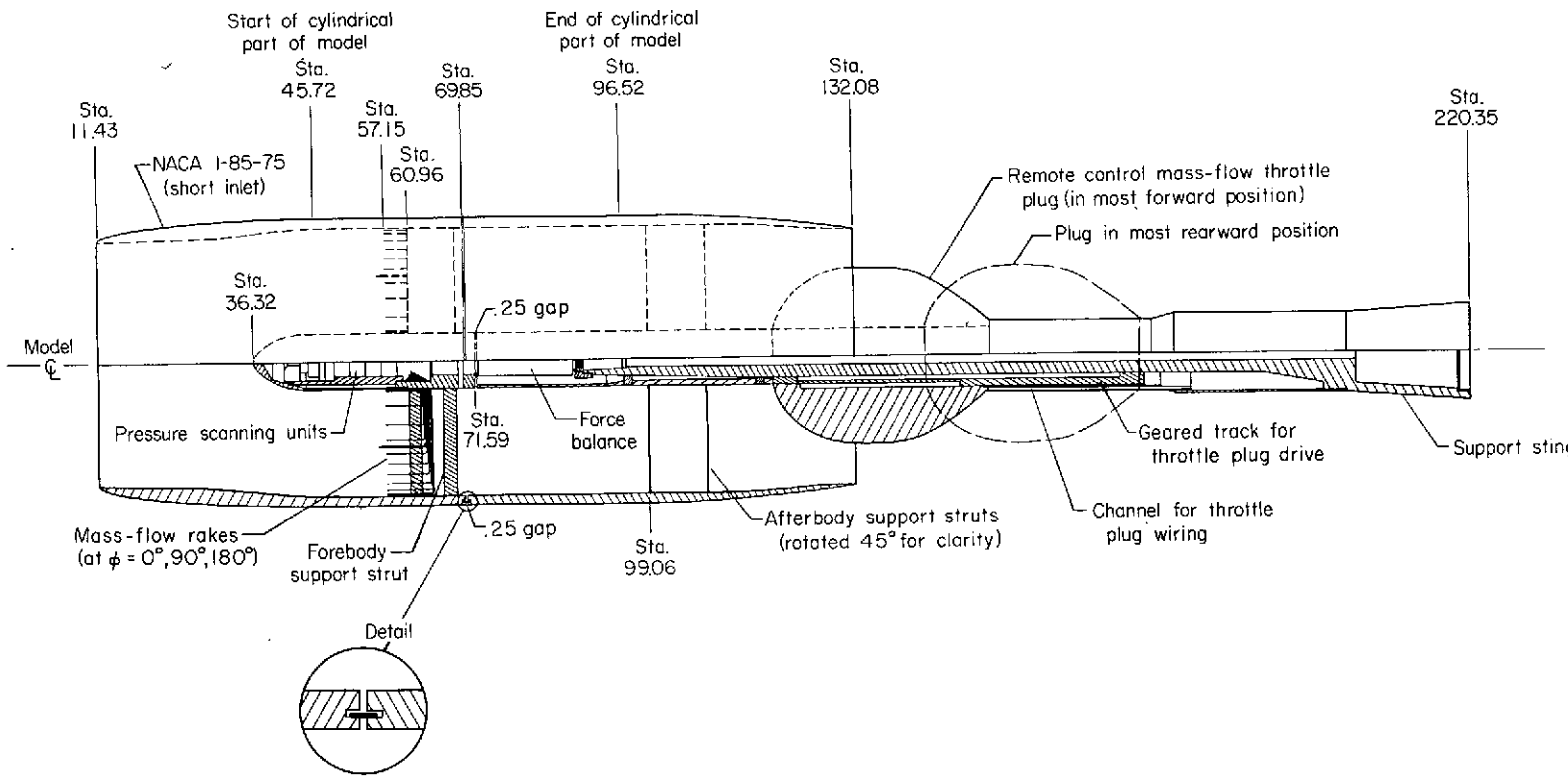

Figure 2.- Simplified cross-sectional sketch of complete model with NACA 1-85-75 inlet. All dimensions in centimeters unless otherwise noted.

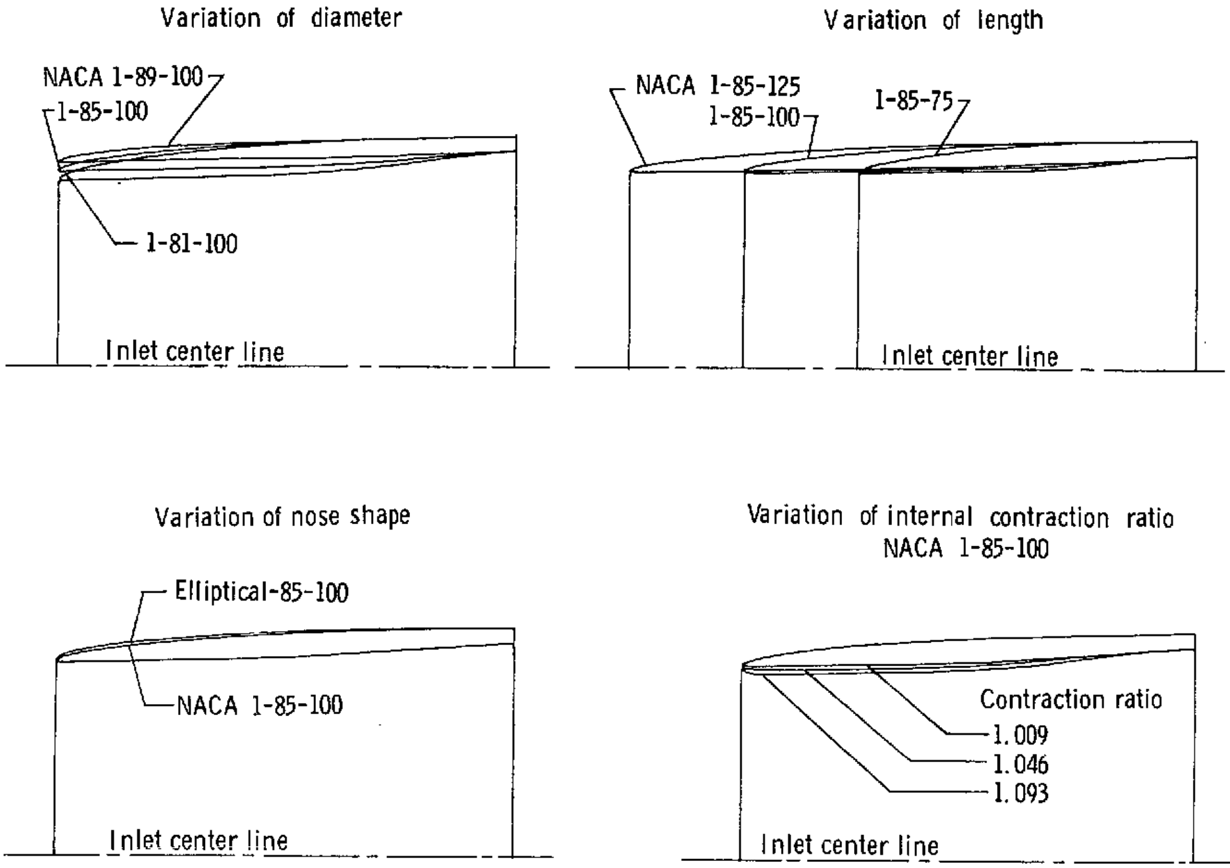

Inlet designation	Lip radius, cm	Internal contraction ratio, A_h/A_{min}	A_h/A_{max}
NACA 1-81-100	0.107	1.012	0.6638
1-85-100	.084	1.009	.7286
1-89-100	.061	1.006	.7968
1-85-75	.084	1.009	.7286
1-85-125			
Elliptical-85-100			
NACA 1-85-100		1.046	
1-85-100		1.093	

Figure 3.- Sketch showing the variations in inlet geometry provided in investigation.

Pressure probe radial location, R/R_w
0.2131
.2268
.3305
.4720
.5851
.6373 *
.6893
.7622
.8373
.9058
.9549
.9808
.9952
* Static pressure probe

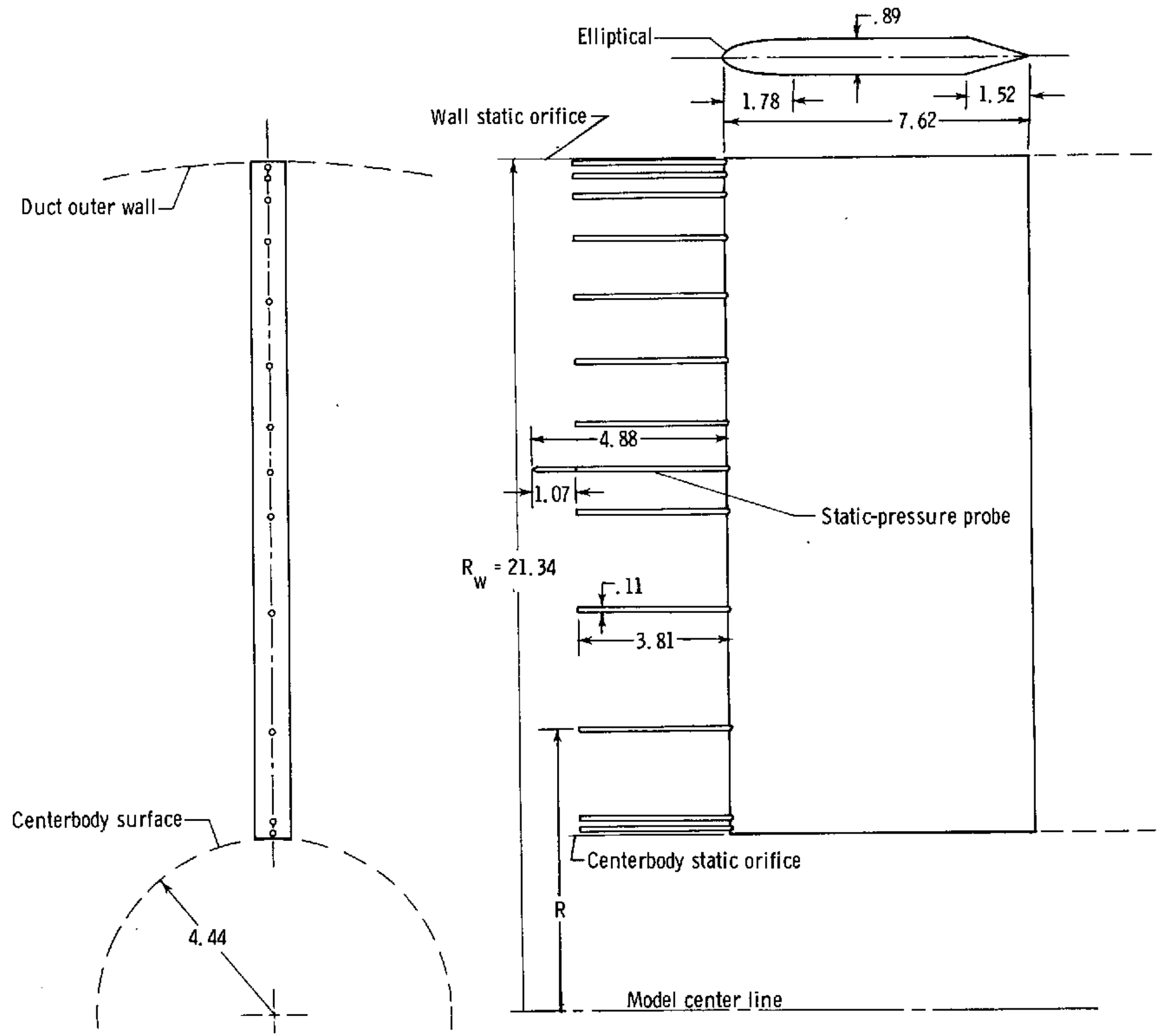

Figure 4.- Pressure instrumentation (on struts at $\phi = 0^{\circ}$, 90°, and 180°) used to obtain data for mass-flow computations. All dimensions in centimeters unless otherwise noted.

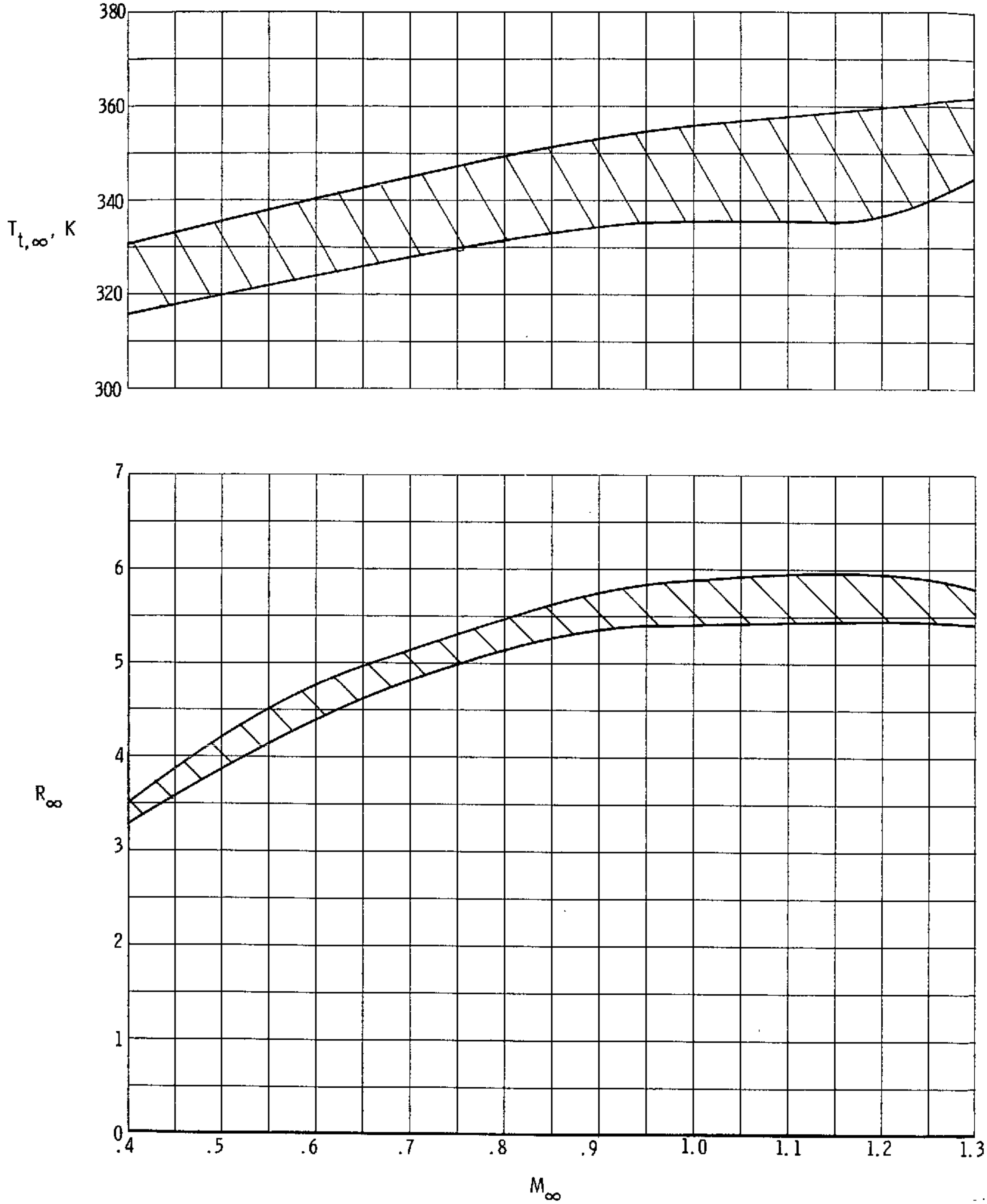

Figure 5.- Variation of Reynolds number (based on maximum model diameter) and free-stream stagnation temperature with free-stream Mach number.

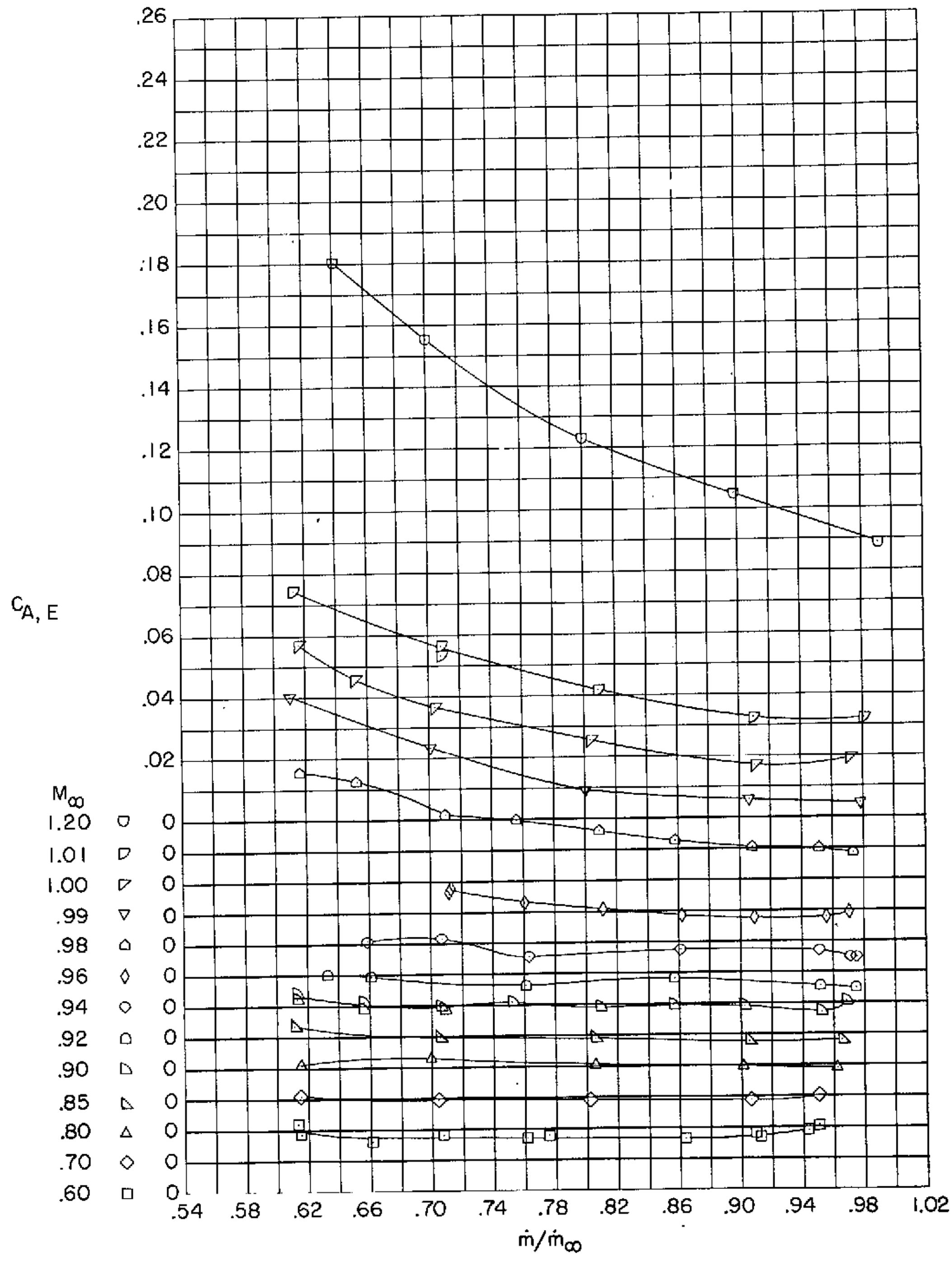

(a) NACA 1-81-100; contraction ratio 1.012.

Figure 6.- Variation of inlet external axial-force coefficient with mass-flow ratio for a range of free-stream Mach numbers.

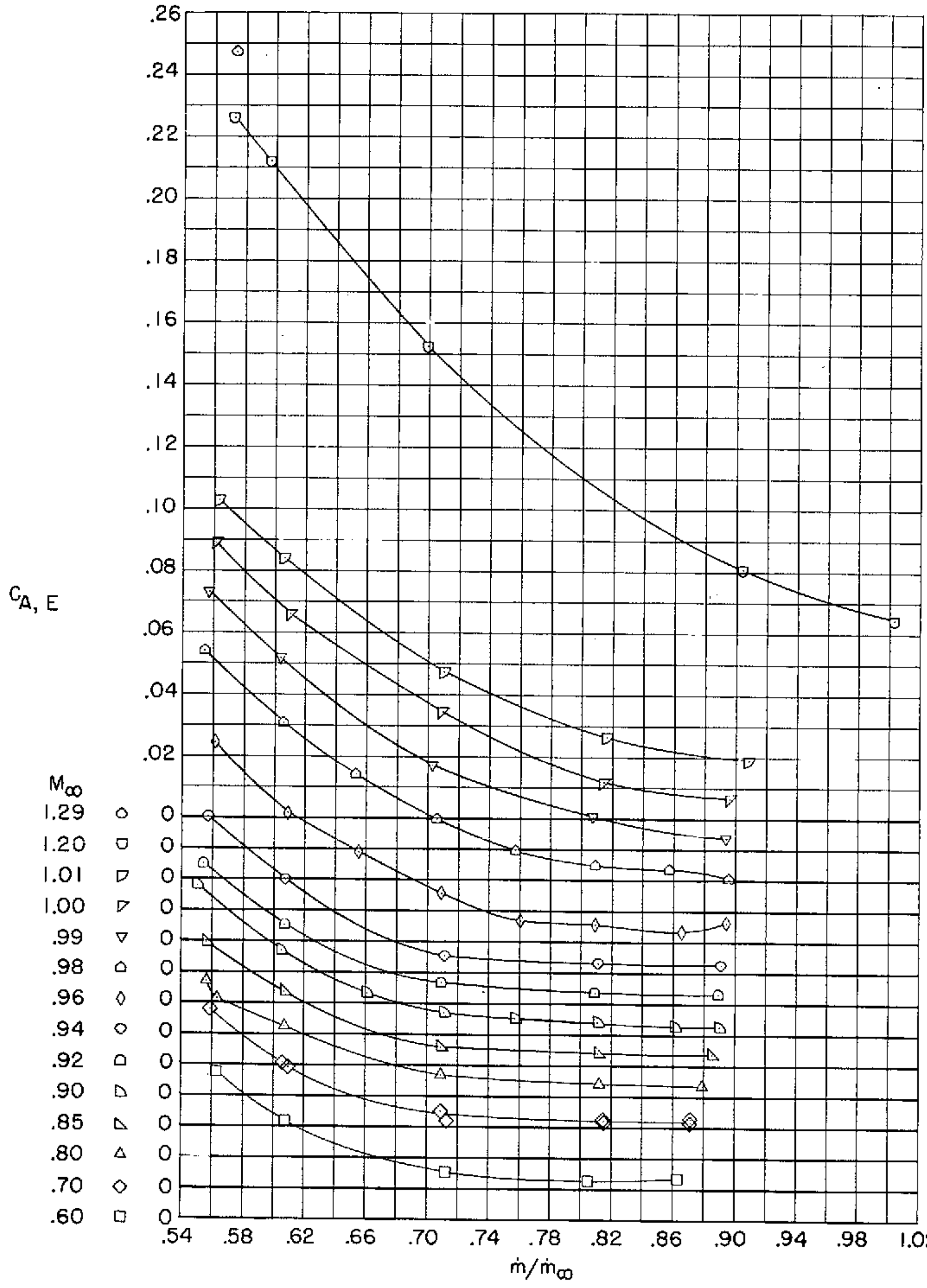

(b) NACA 1-85-100; contraction ratio 1.009.

Figure 6.- Continued.

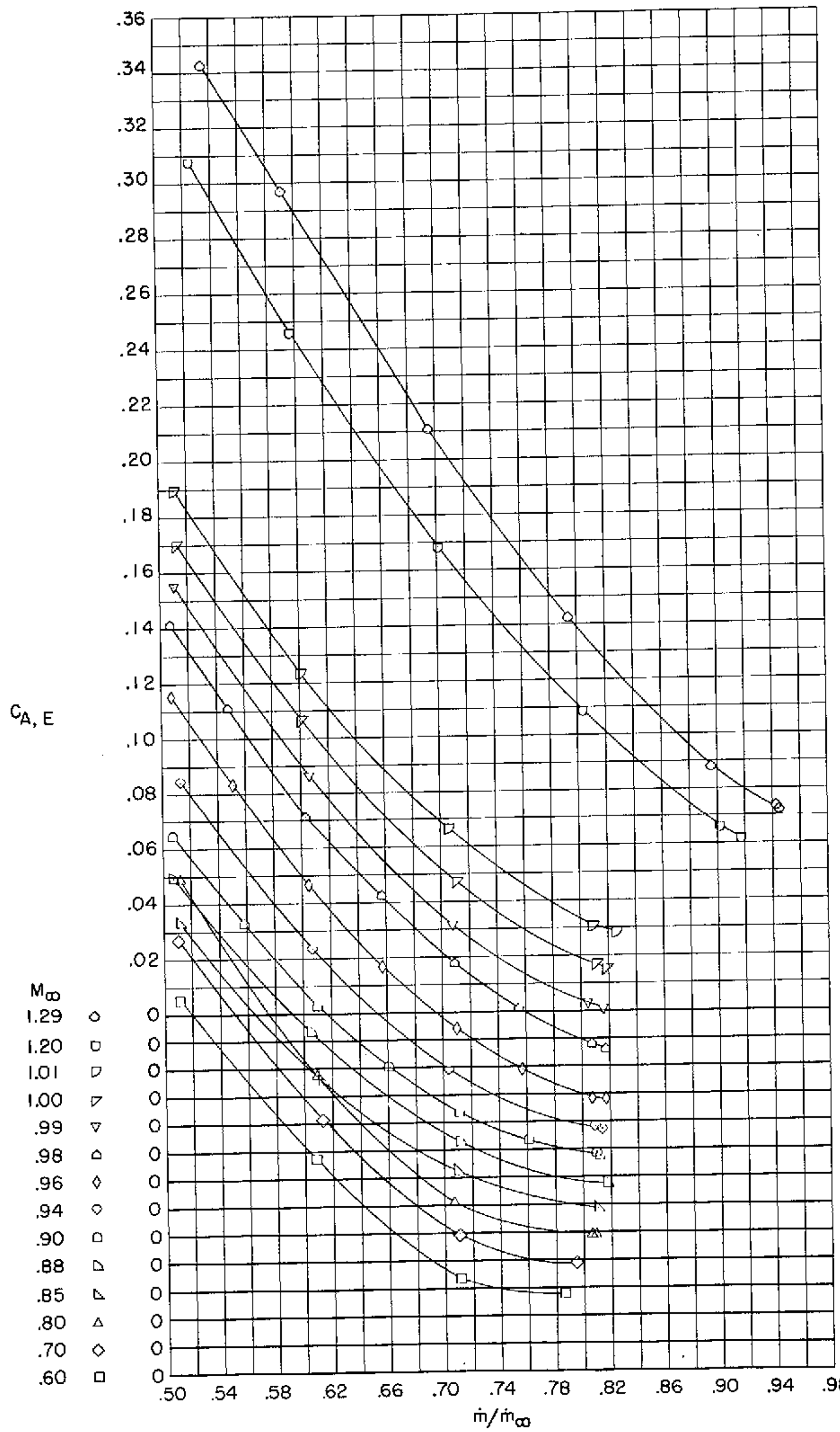

(c) NACA 1-89-100; contraction ratio 1.006.

Figure 6.- Continued.

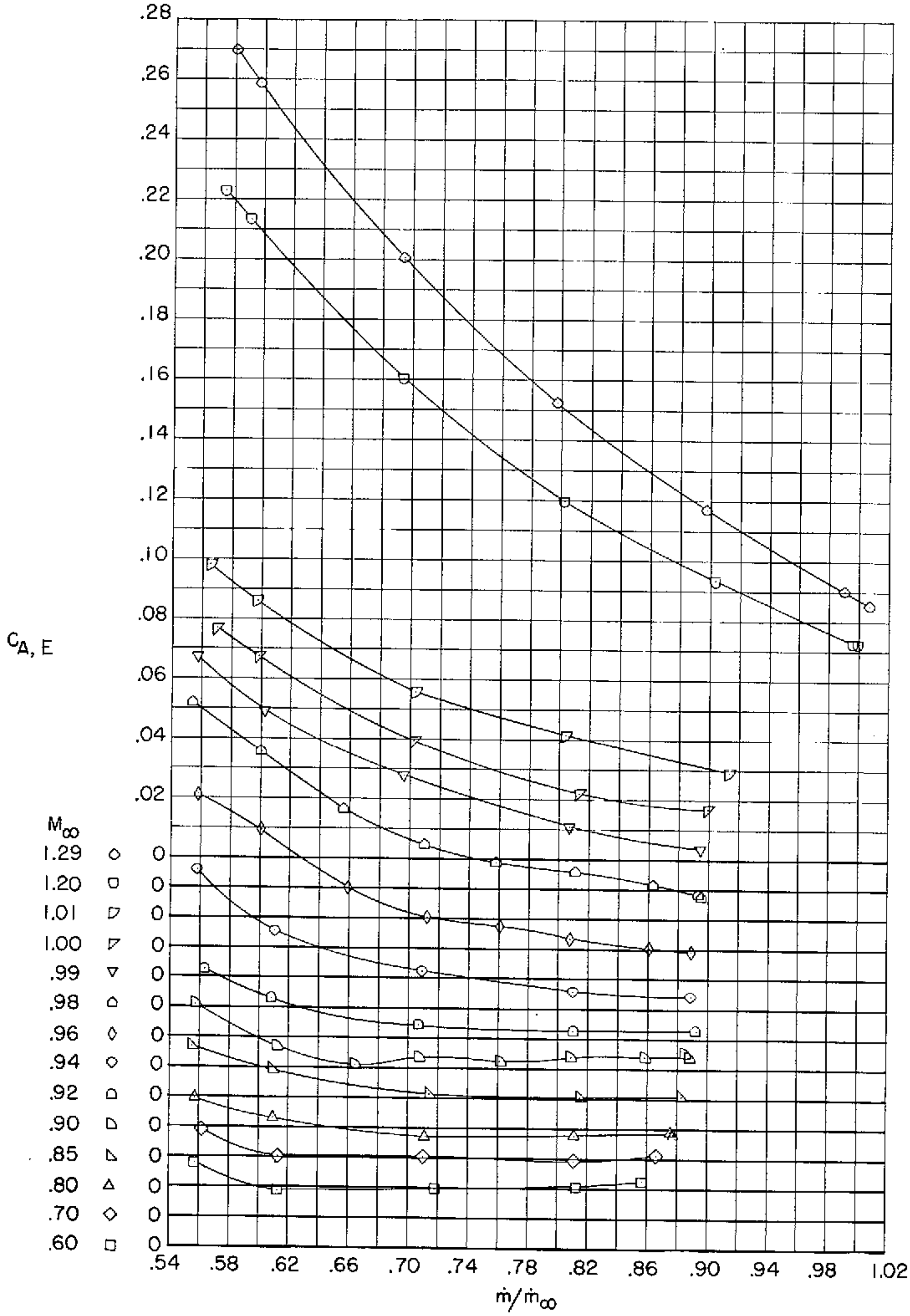

(d) NACA 1-85-75; contraction ratio 1.009.

Figure 6.- Continued.

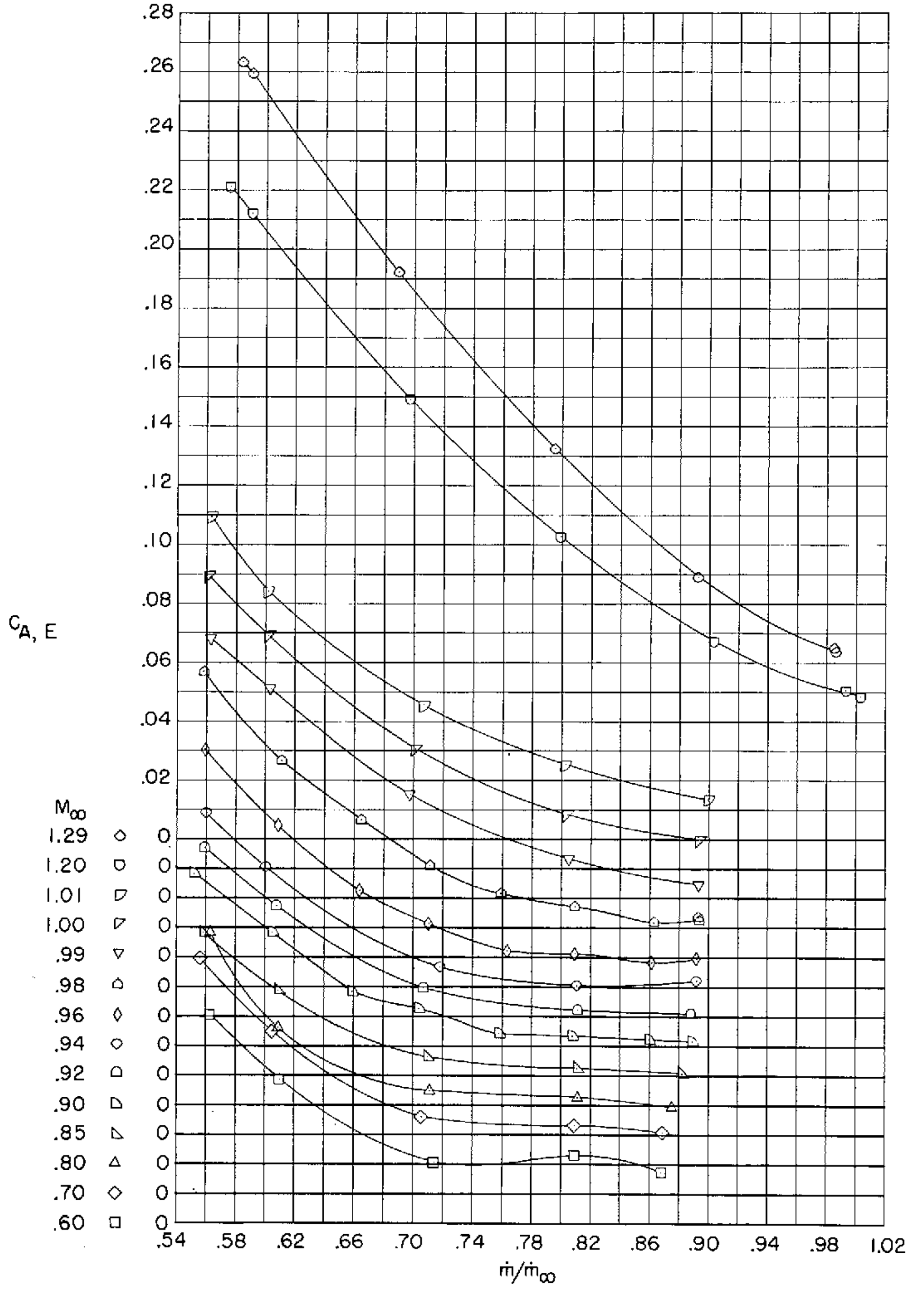

(e) NACA 1-85-125; contraction ratio 1.009.

Figure 6.- Continued.

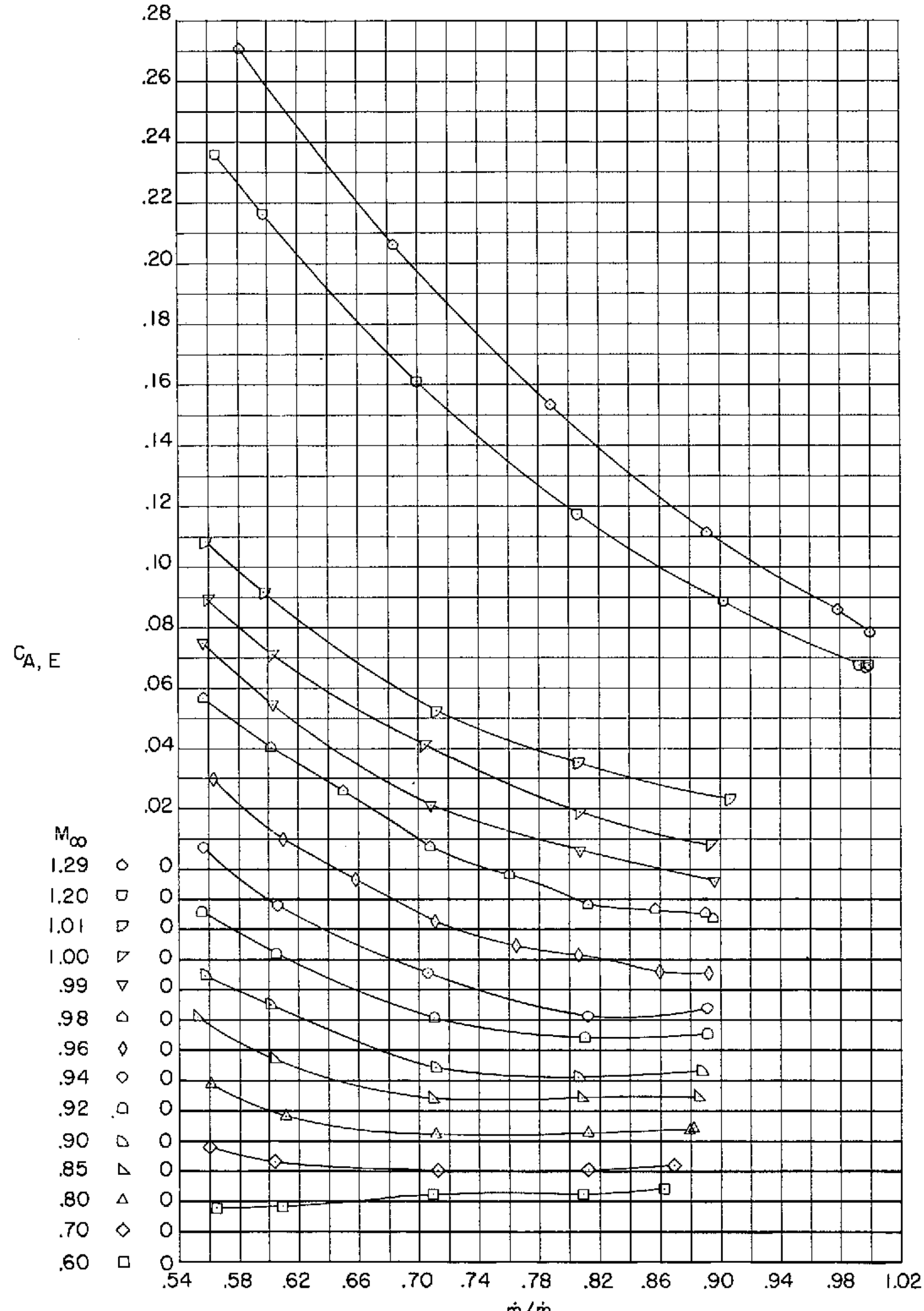

(f) Elliptical 1-85-100; contraction ratio 1.009.

Figure 6.- Continued.

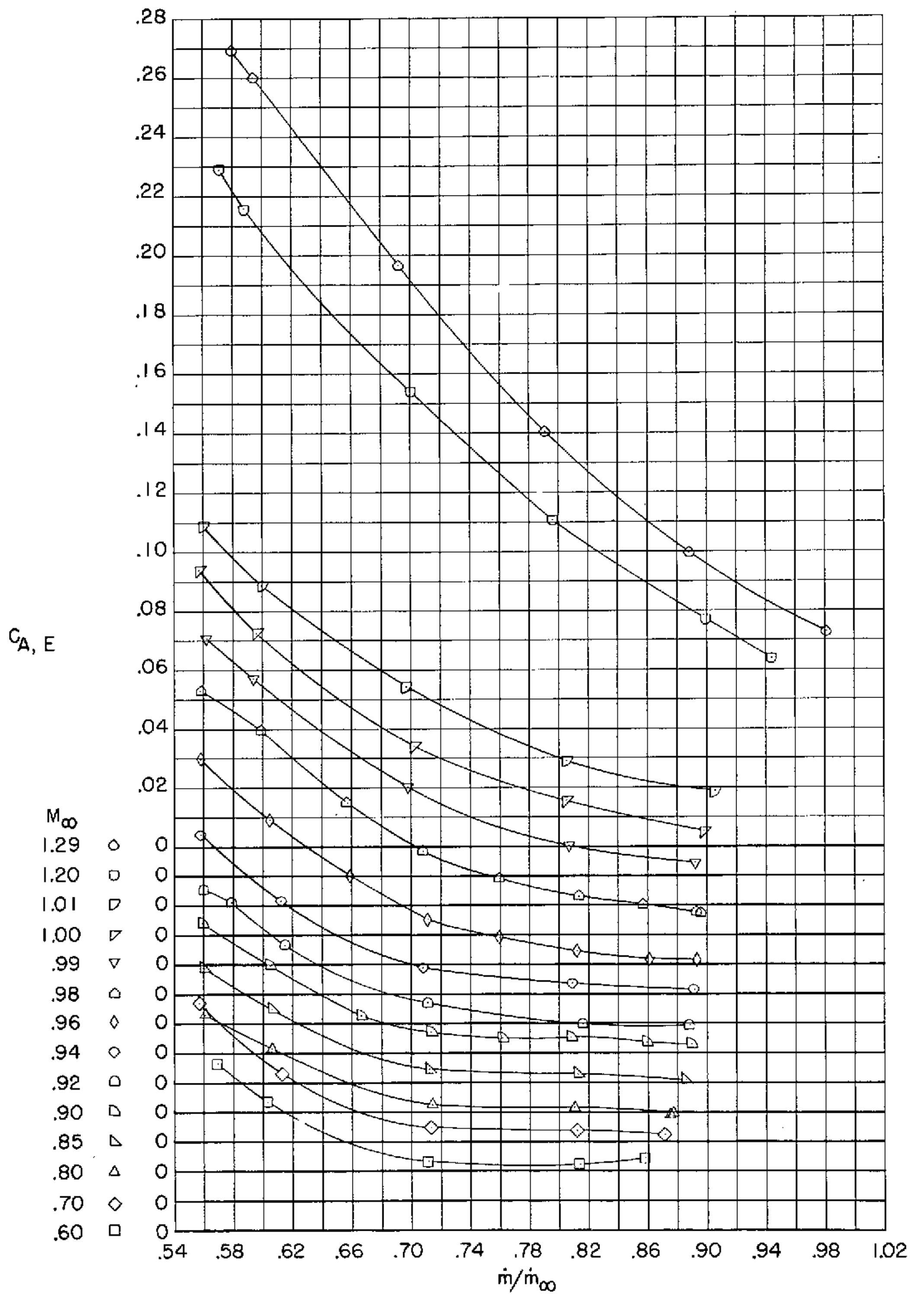

(g) NACA 1-85-100; contraction ratio 1.046.

Figure 6.- Continued.

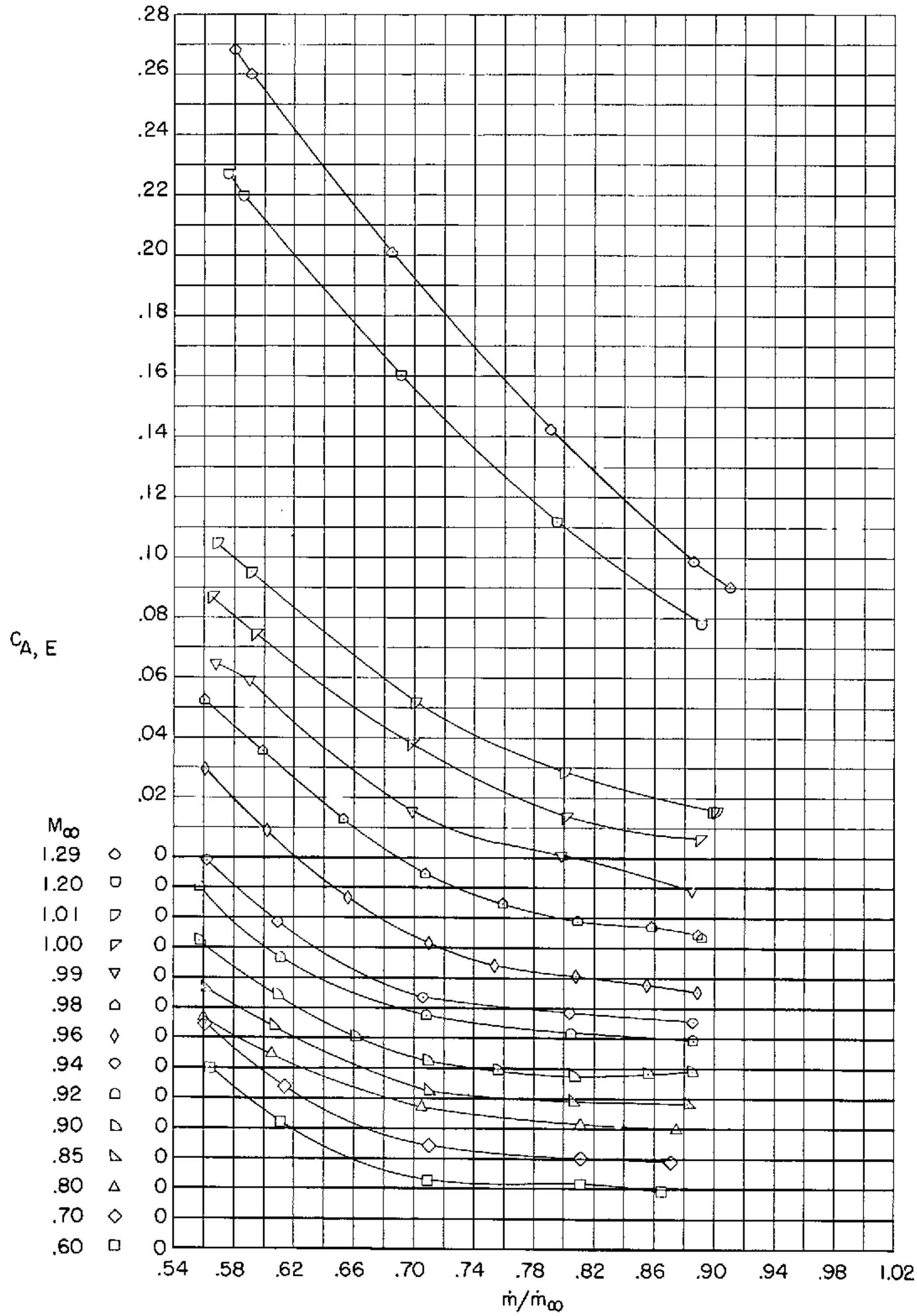

(h) NACA 1-85-100; contraction ratio 1.093.

Figure 6.- Concluded.

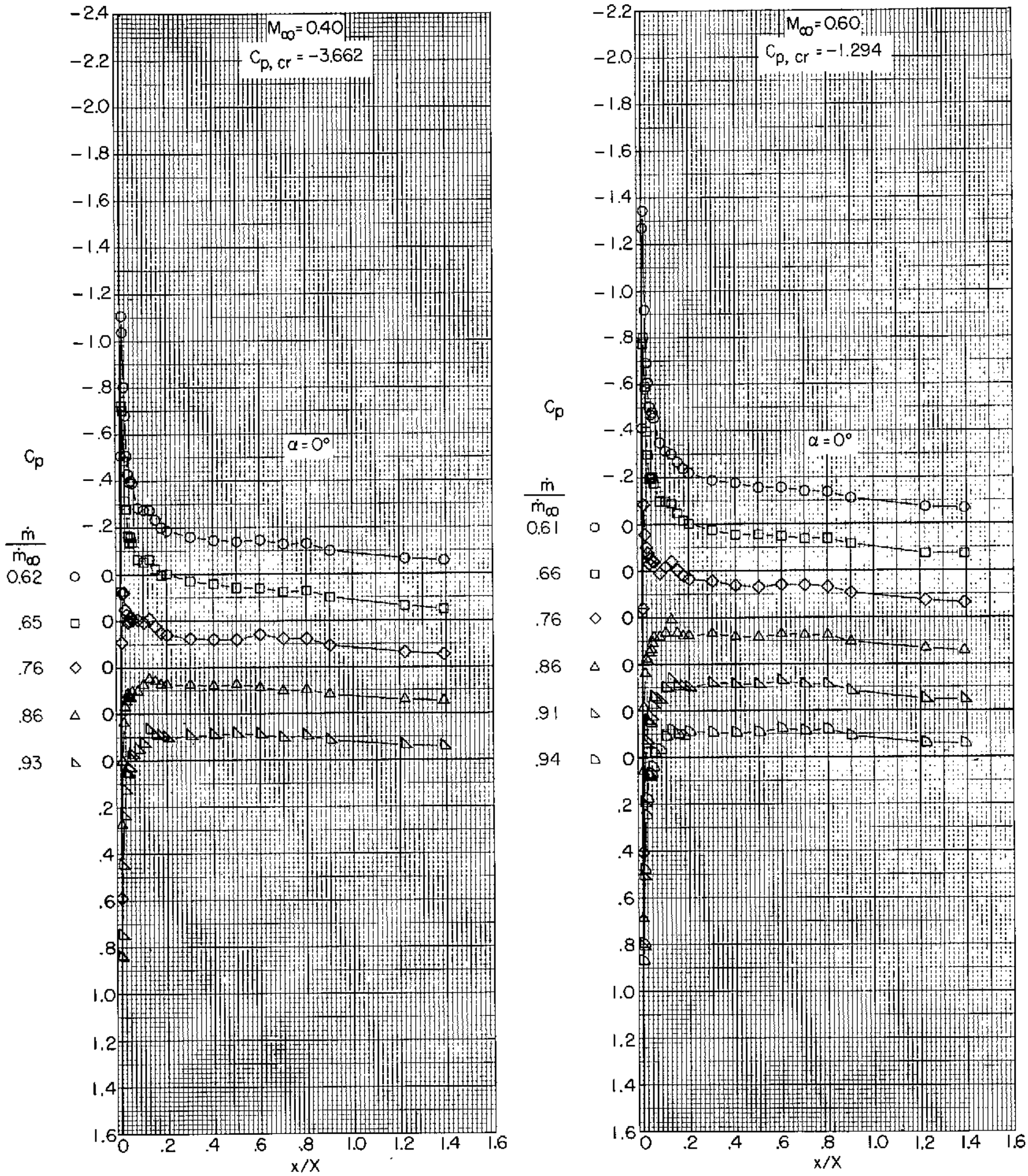

(a) M_∞ = 0.40 and 0.60.

Figure 7.- Variation with length of pressure coefficient over the outer profile of an NACA 1-81-100 (contraction ratio 1.012) inlet.

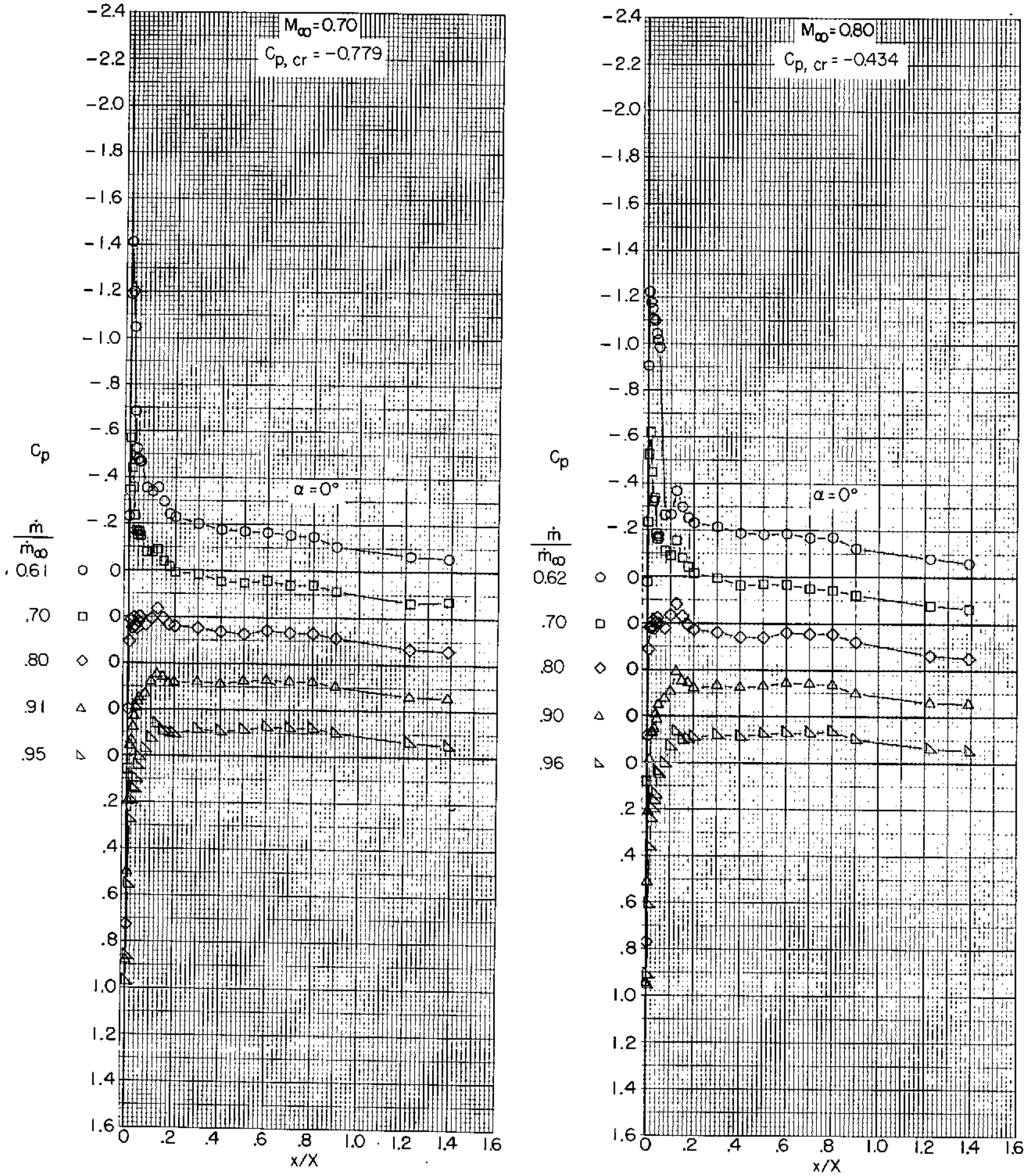

(b) M_∞ = 0.70 and 0.80.

Figure 7.- Continued.

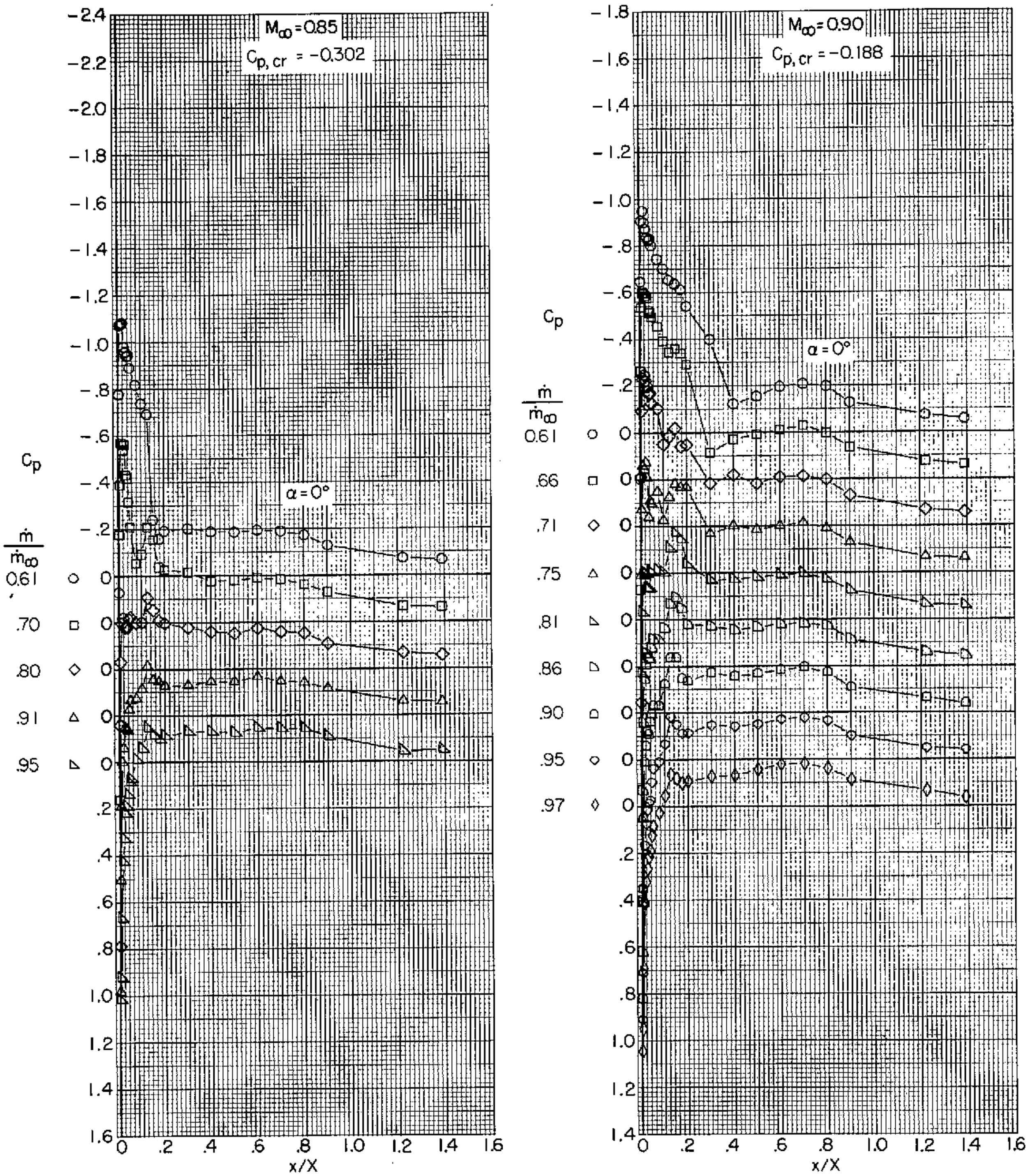

(c) M_∞ = 0.85 and 0.90.

Figure 7.- Continued.

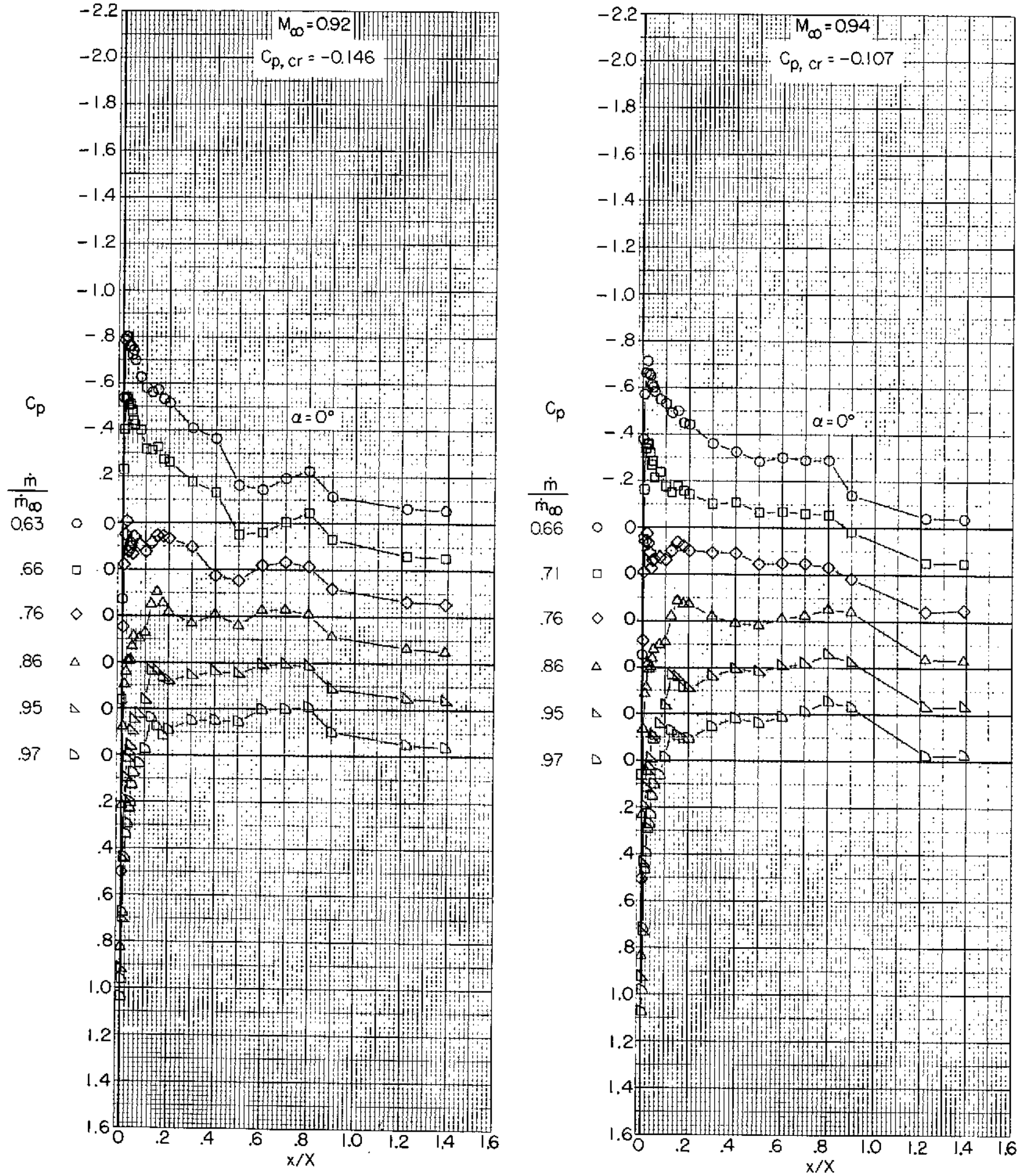

(d) M_∞ = 0.92 and 0.94.

Figure 7.- Continued.

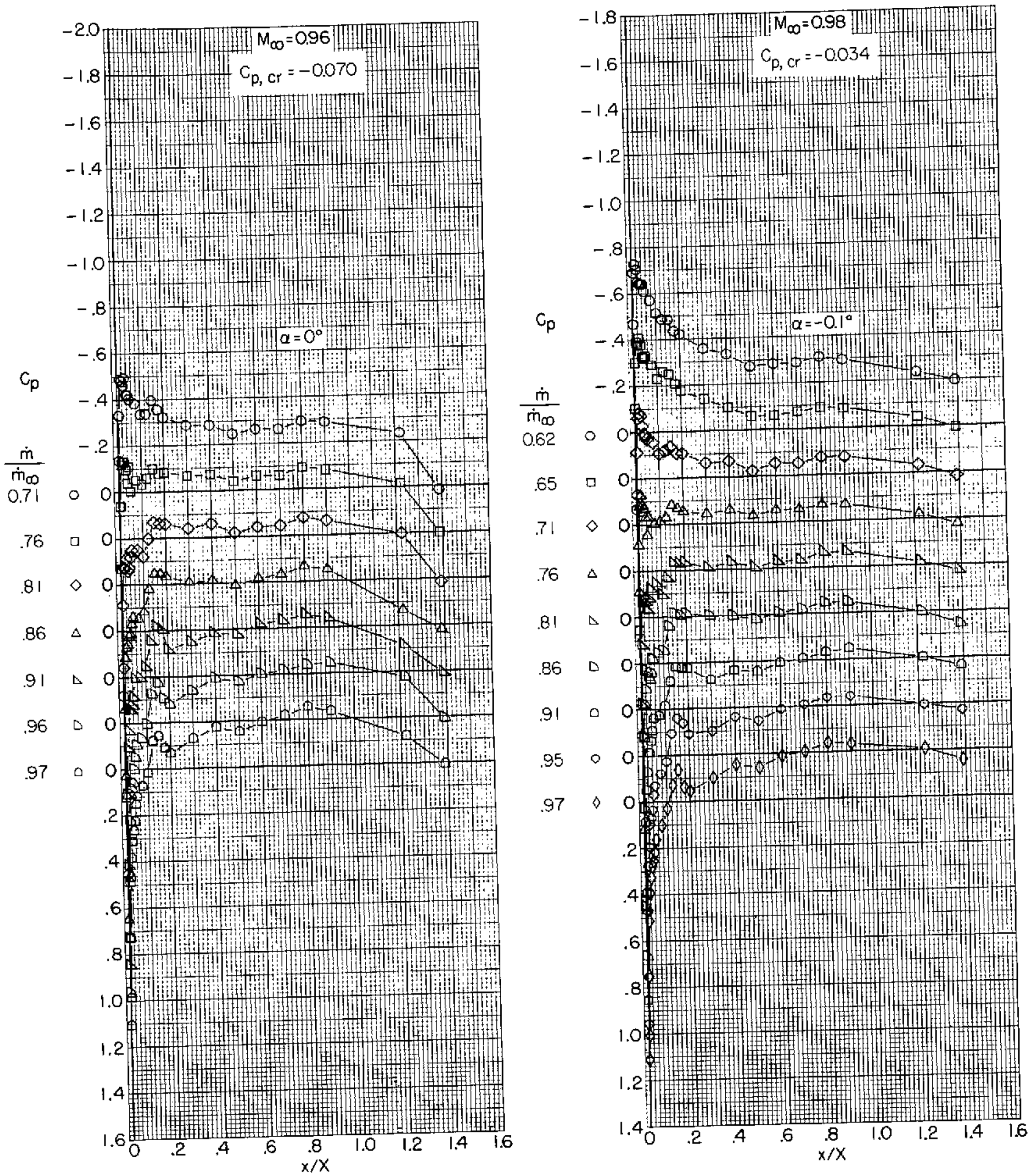

(e) M_∞ = 0.96 and 0.98.

Figure 7.- Continued.

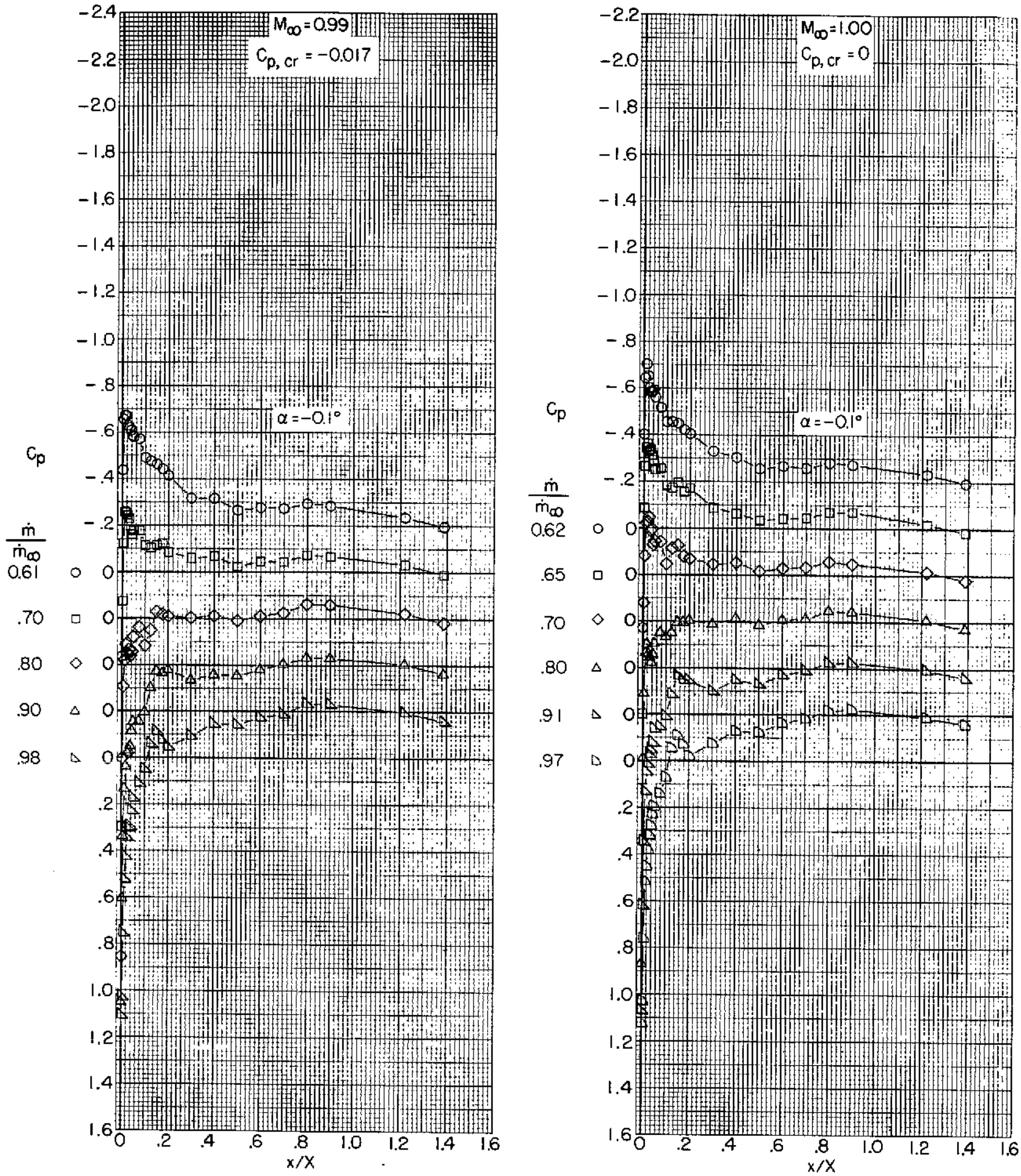

(f) M_∞ = 0.99 and 1.00.

Figure 7.- Continued.

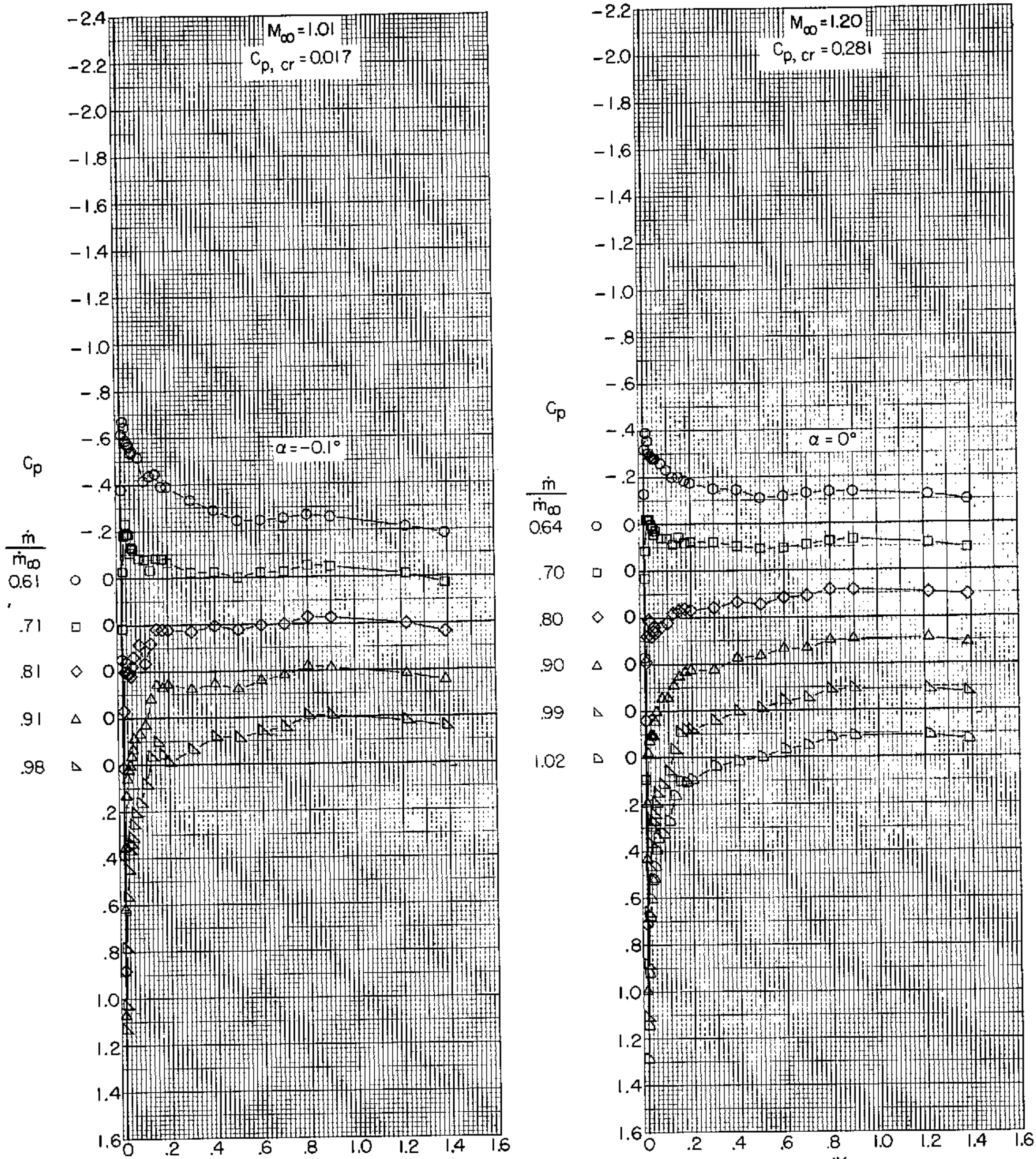

(g) M_∞ = 1.01 and 1.20.

Figure 7.- Concluded.

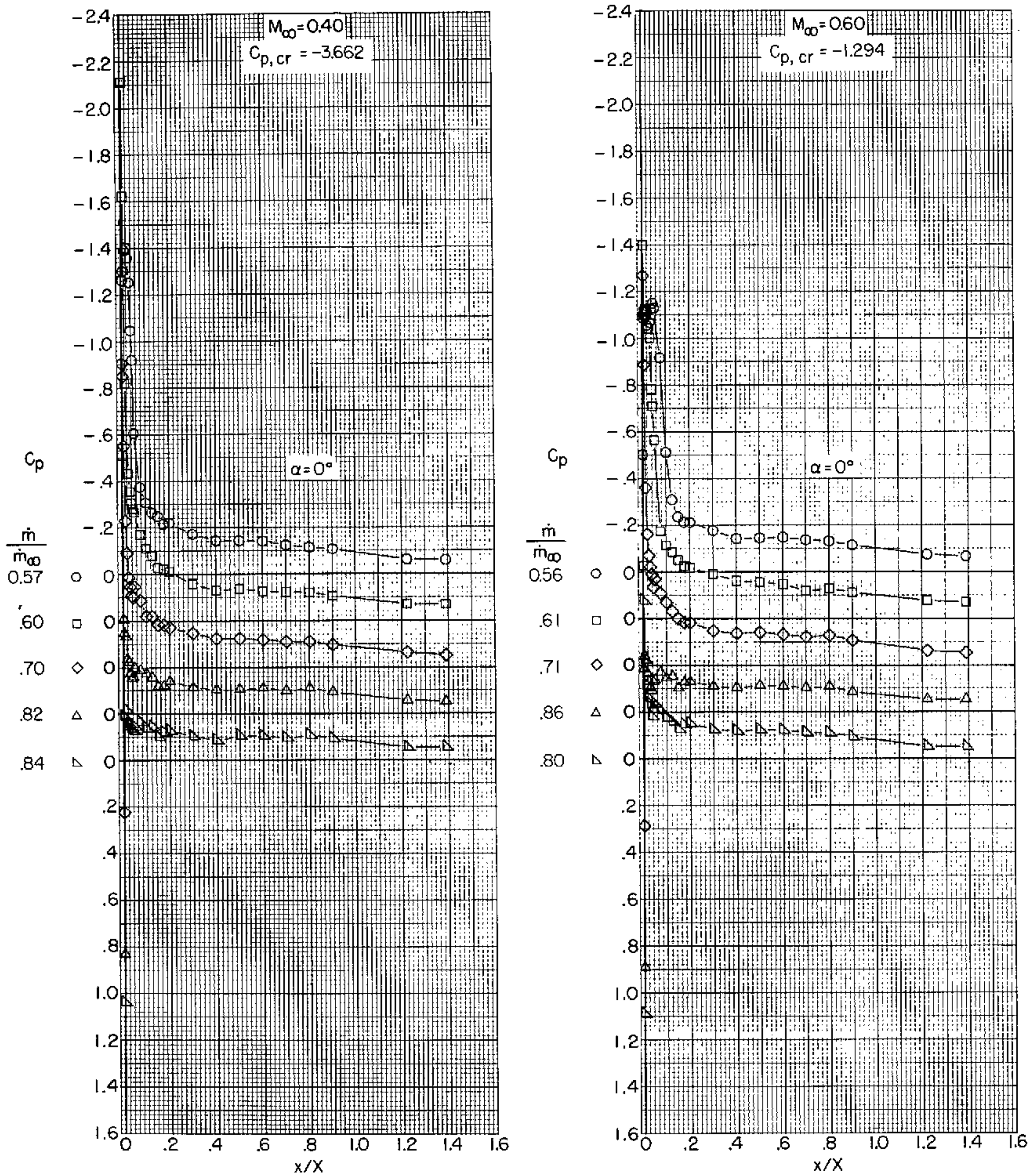

(a) M_∞ = 0.40 and 0.60.

Figure 8.- Variation with length of pressure coefficient over the outer profile of an NACA 1-85-100 (contraction ratio 1.009) inlet.

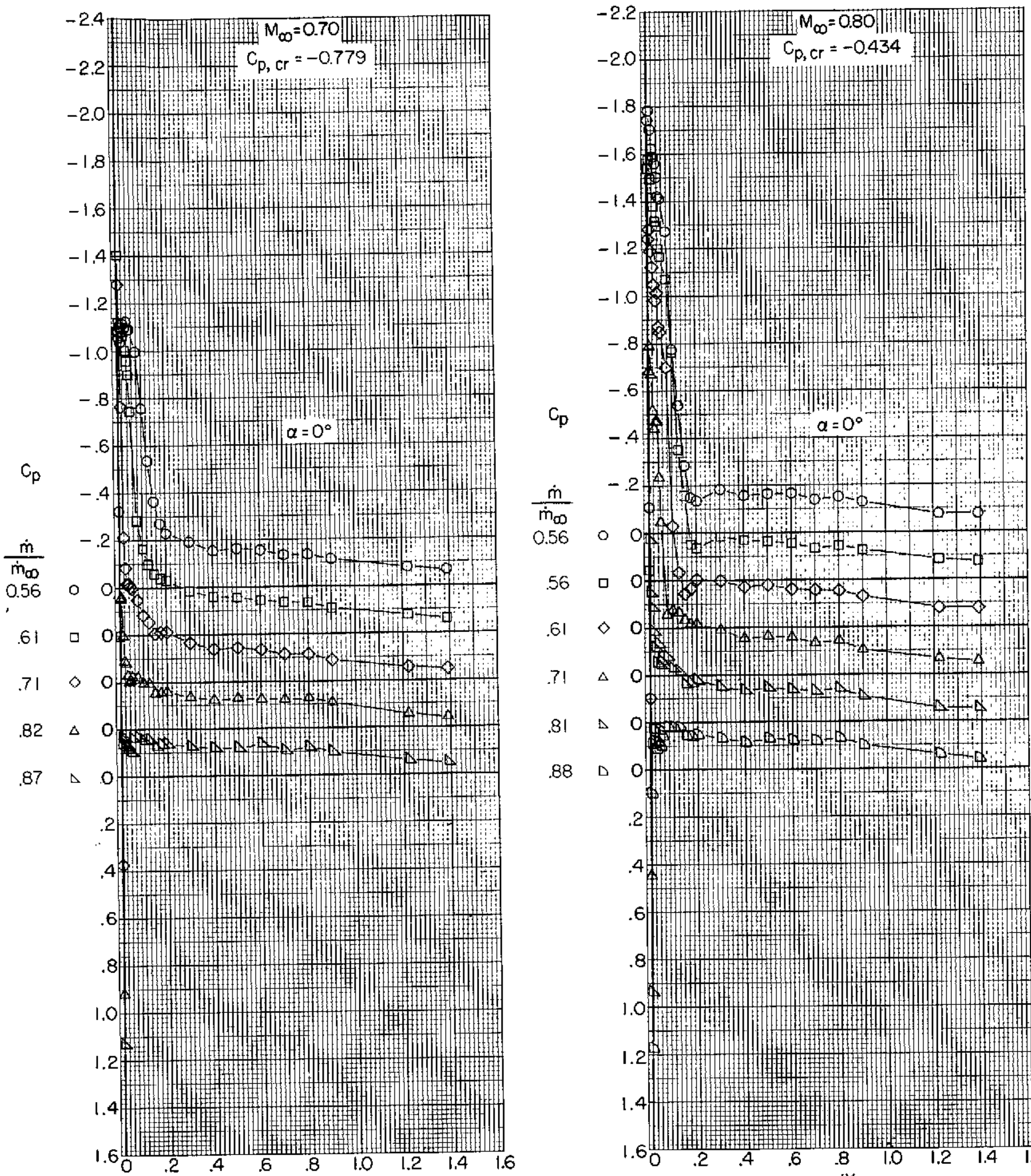

(b) M_∞ = 0.70 and 0.80.

Figure 8.- Continued.

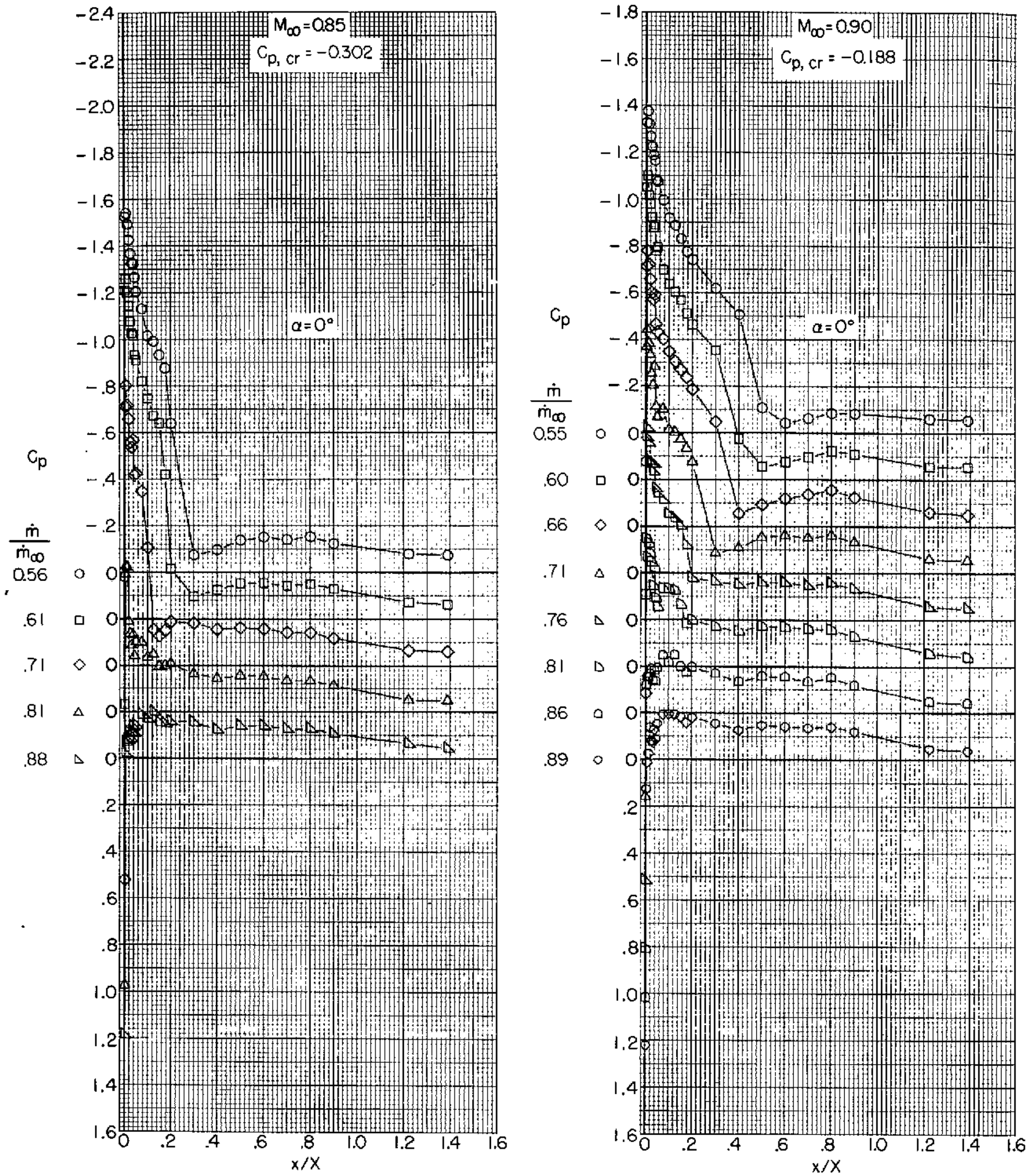

(c) M_∞ = 0.85 and 0.90.

Figure 8.- Continued.

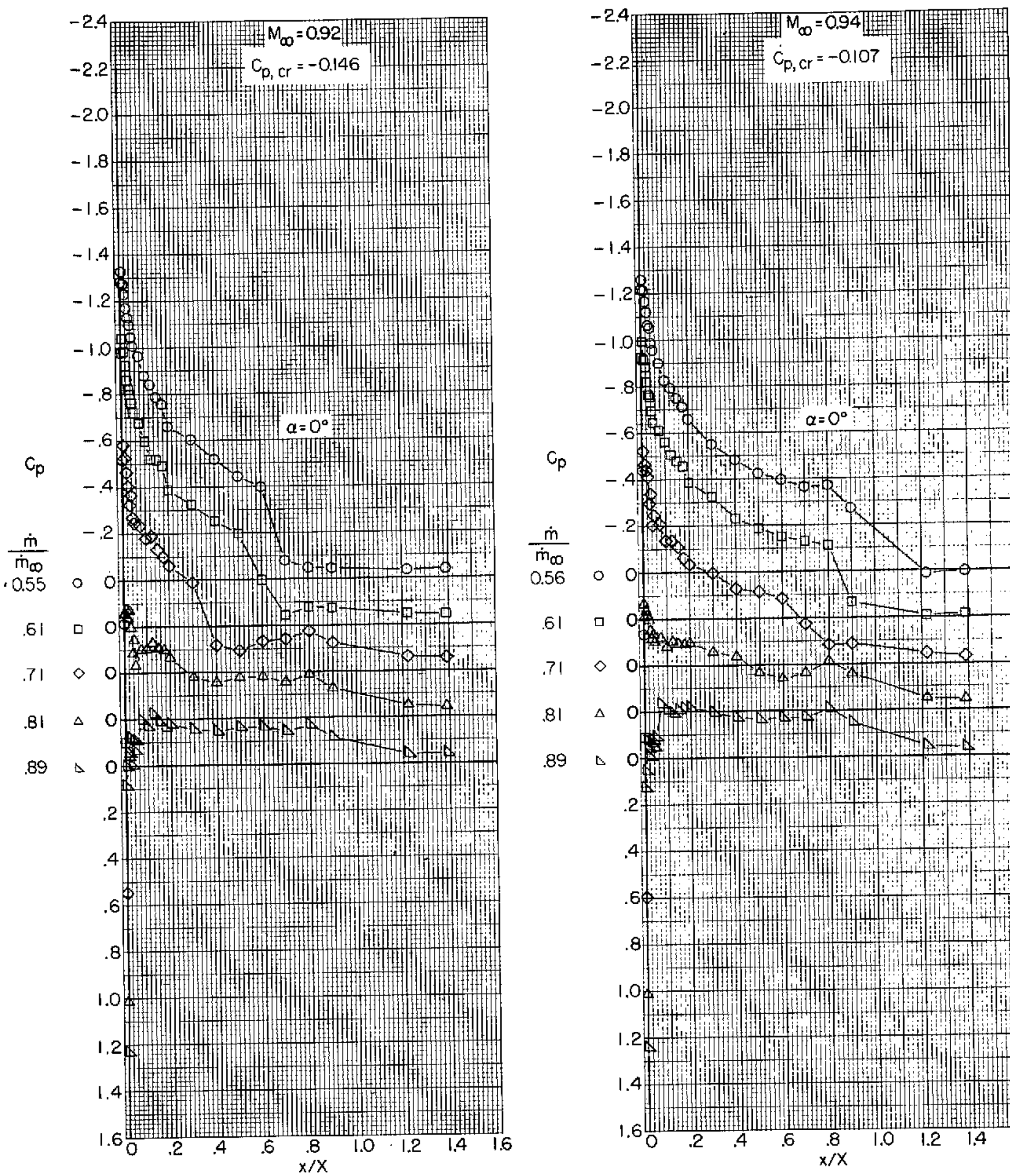

(d) M_∞ = 0.92 and 0.94.

Figure 8.- Continued.

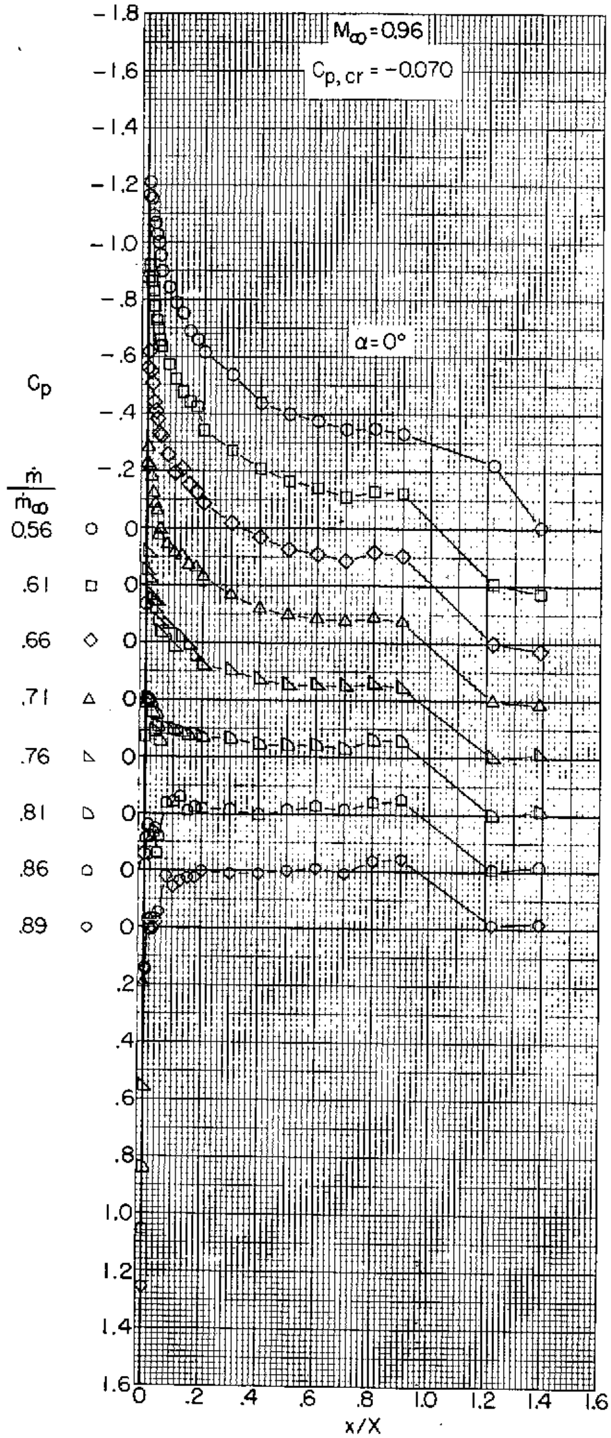

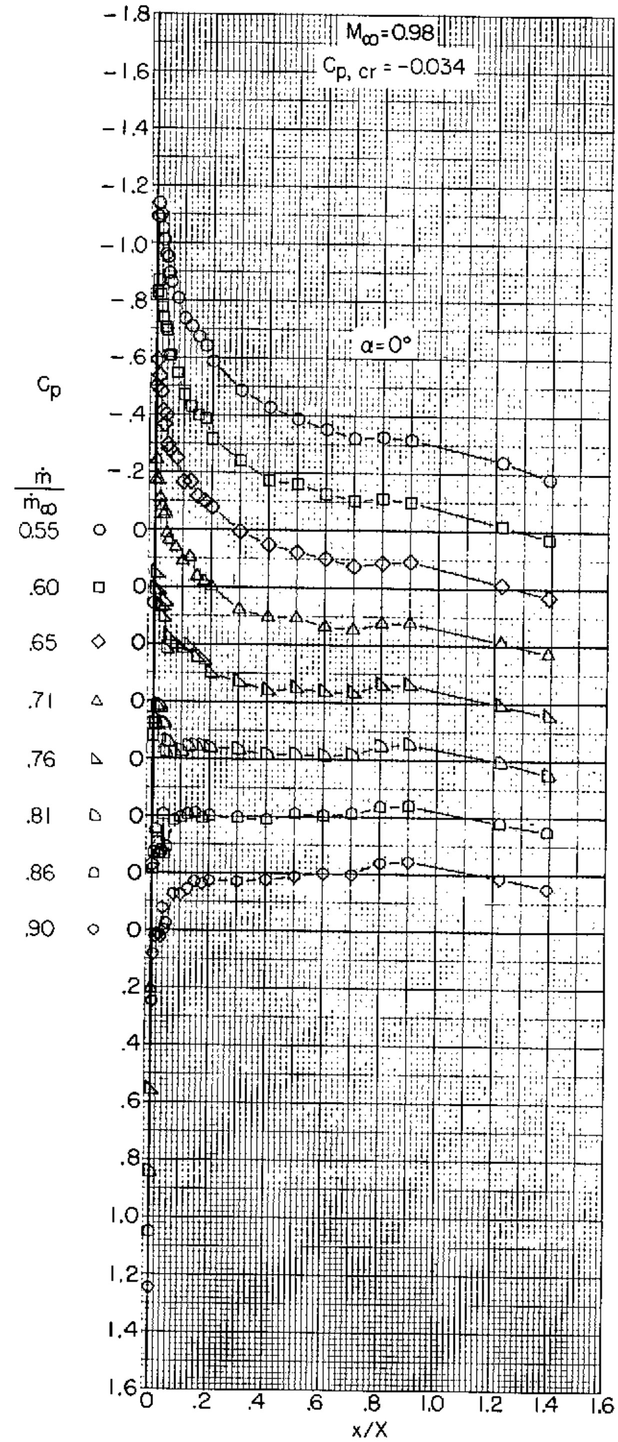

(e) $M_\infty = 0.96$ and 0.98.

Figure 8.- Continued.

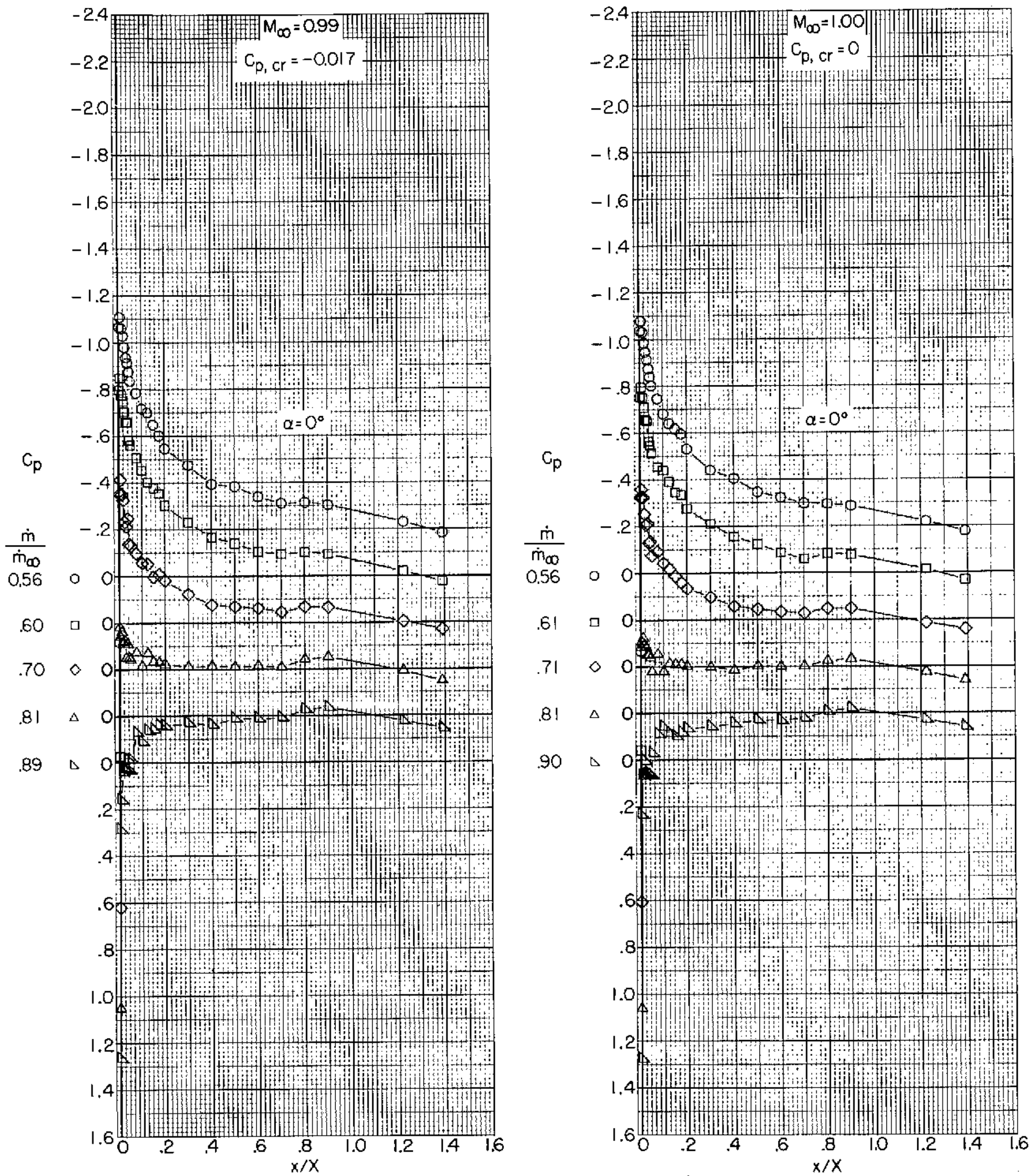

(f) $M_\infty = 0.99$ and 1.00.

Figure 8.- Continued.

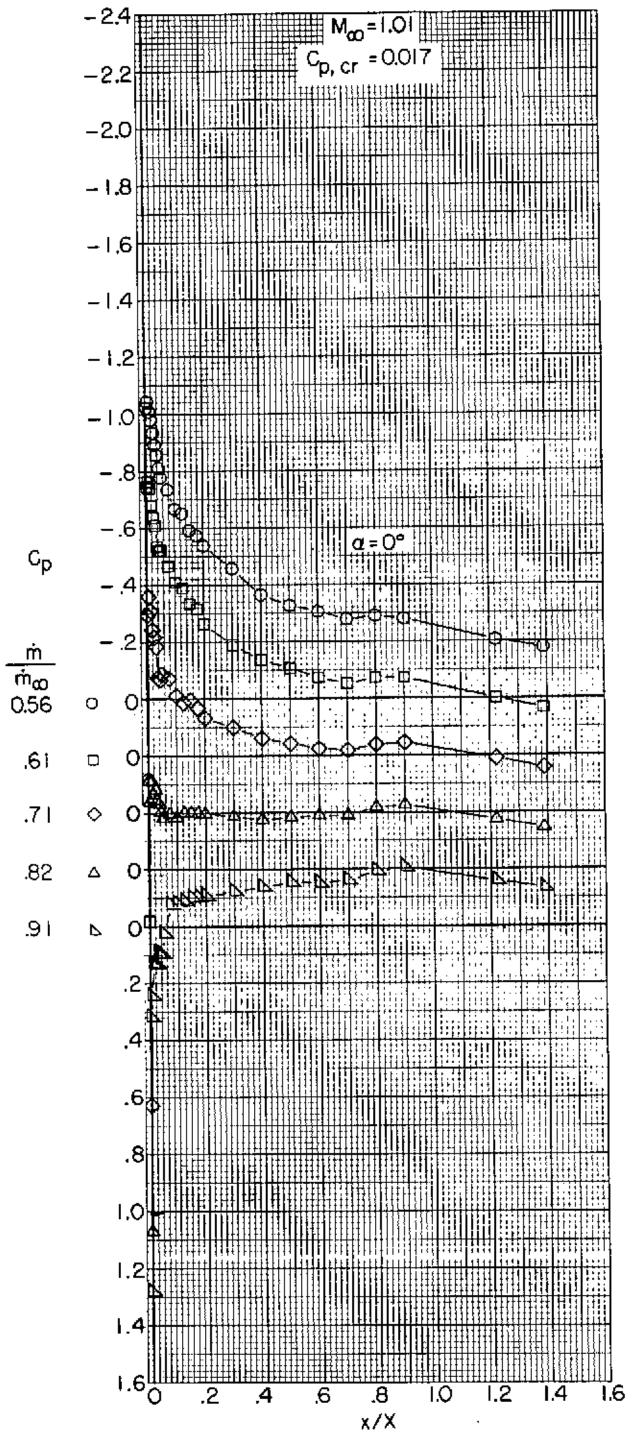

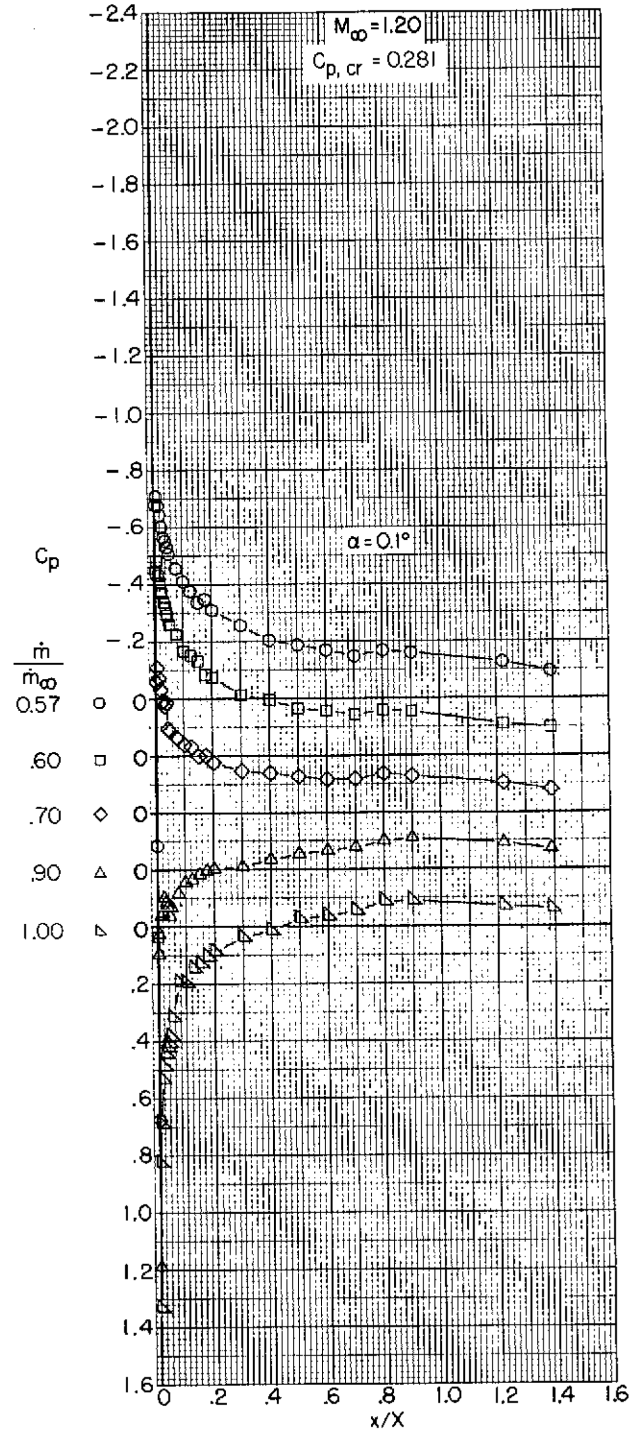

(g) M_∞ = 1.01 and 1.20.

Figure 8.- Continued.

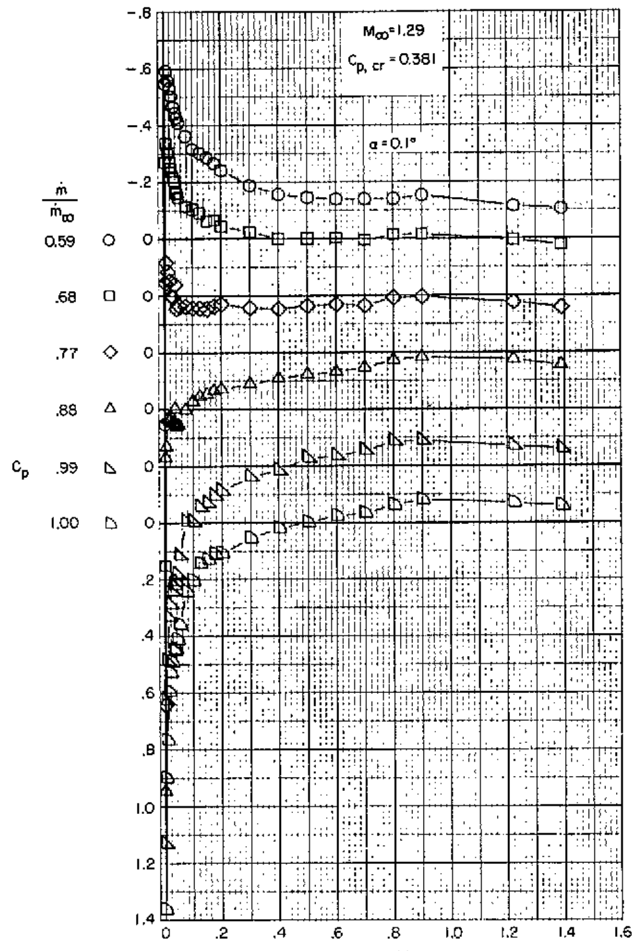

(h) $M_\infty = 1.29$.

Figure 8.- Concluded.

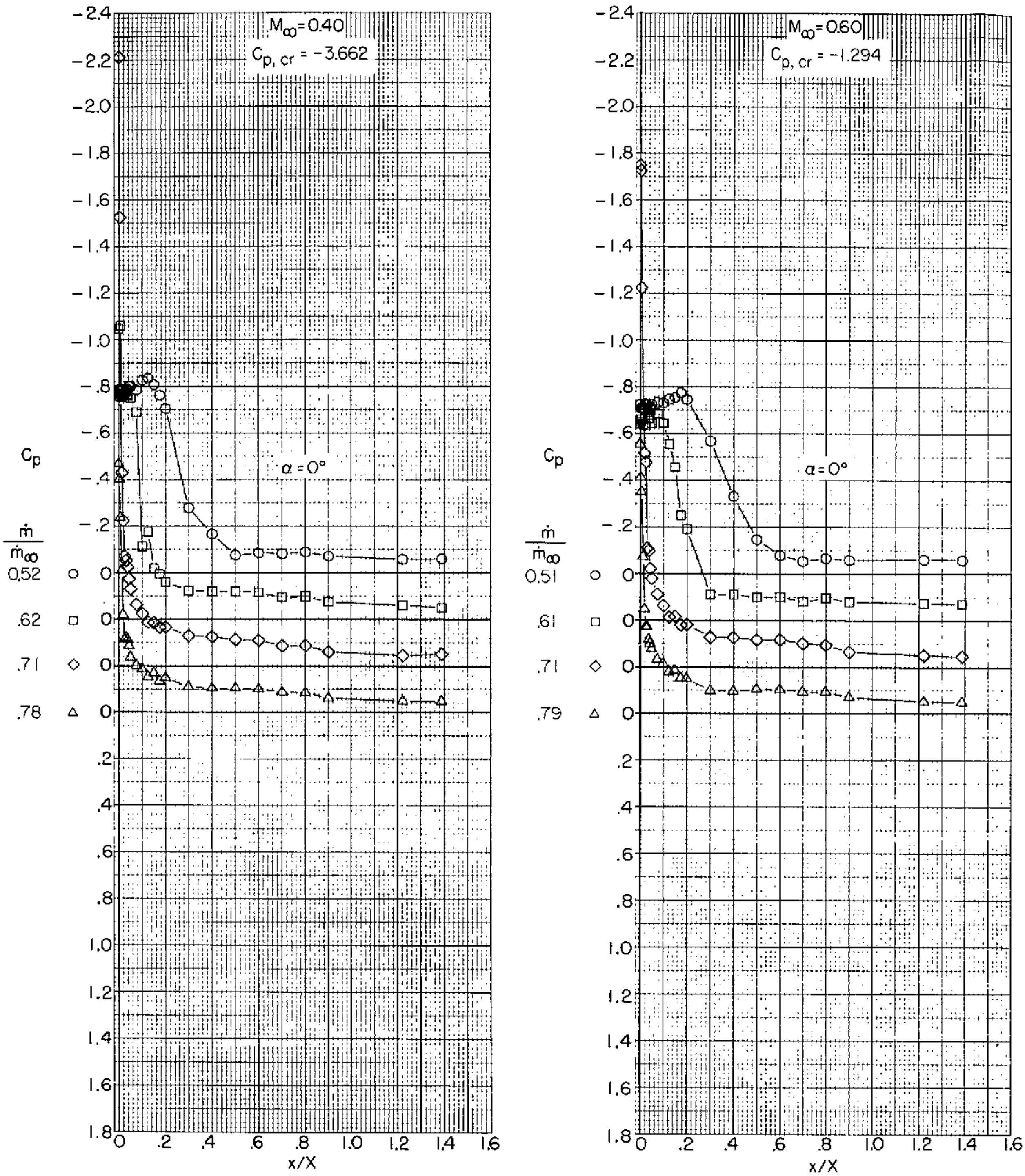

(a) M_∞ = 0.40 and 0.60.

Figure 9.- Variation with length of pressure coefficient over the outer profile of an NACA 1-89-100 (contraction ratio 1.006) inlet.

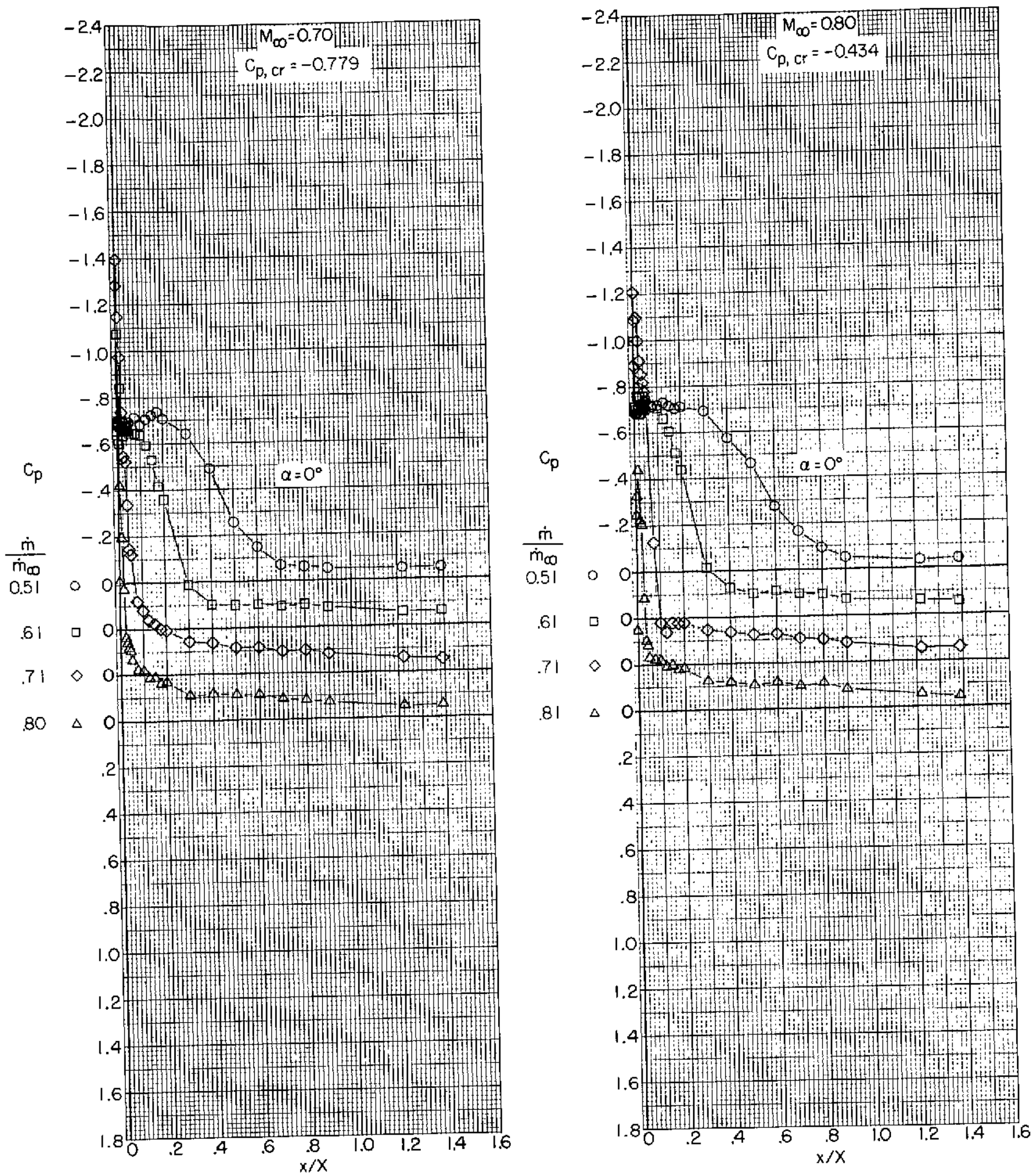

(b) M_∞ = 0.70 and 0.80.

Figure 9.- Continued.

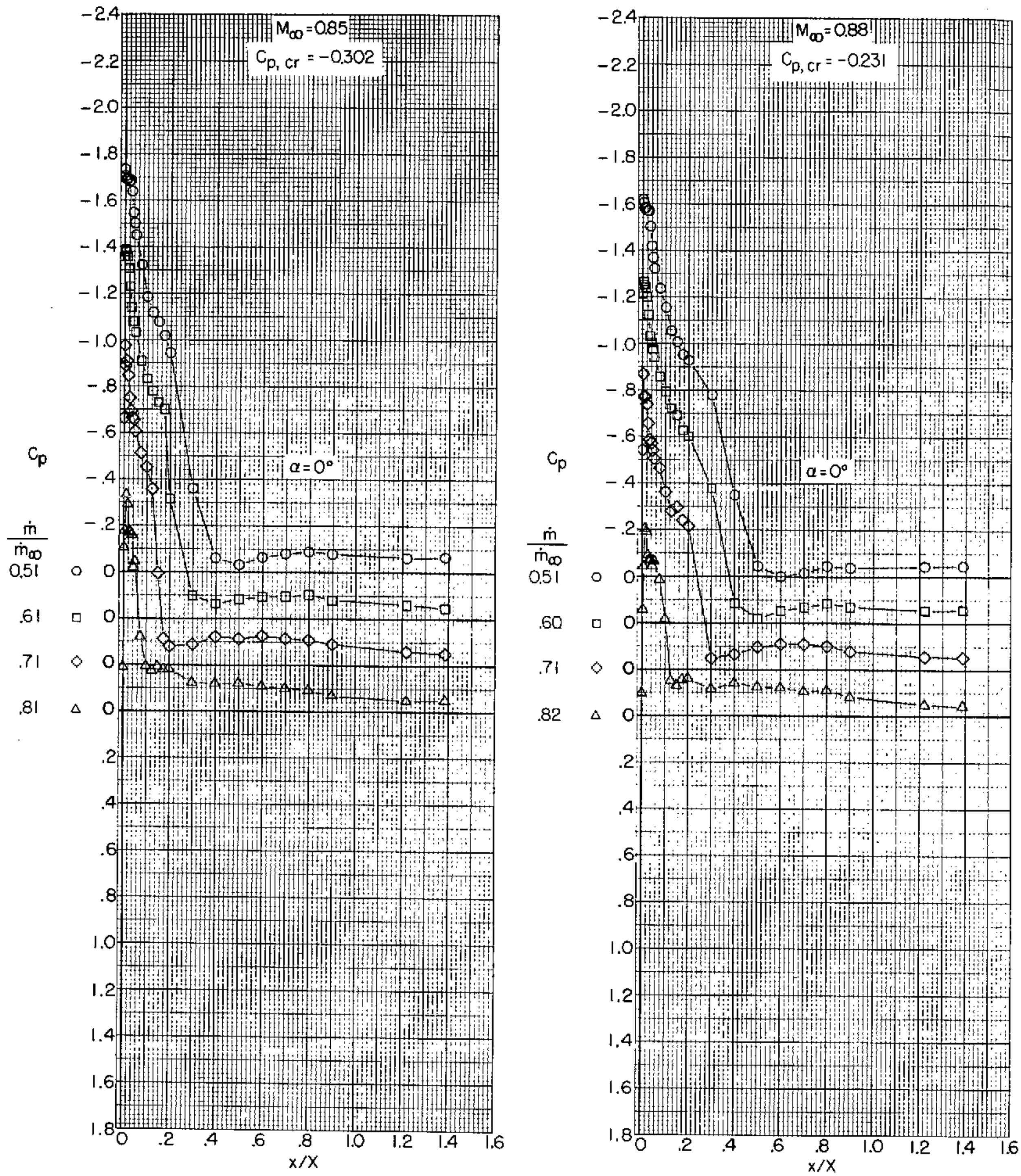

(c) M_∞ = 0.85 and 0.88.

Figure 9.- Continued.

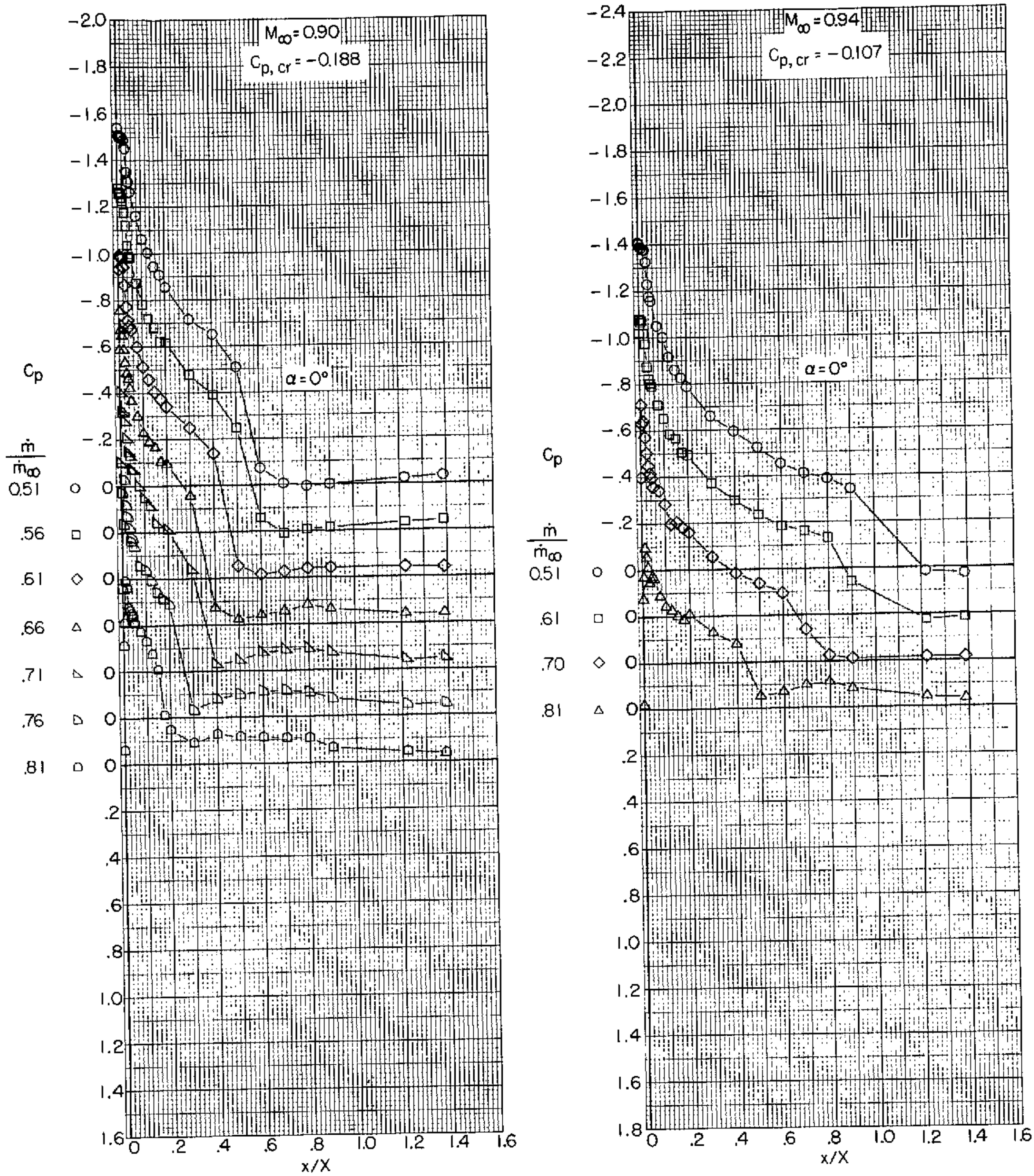

(d) $M_\infty = 0.90$ and 0.94.

Figure 9.- Continued.

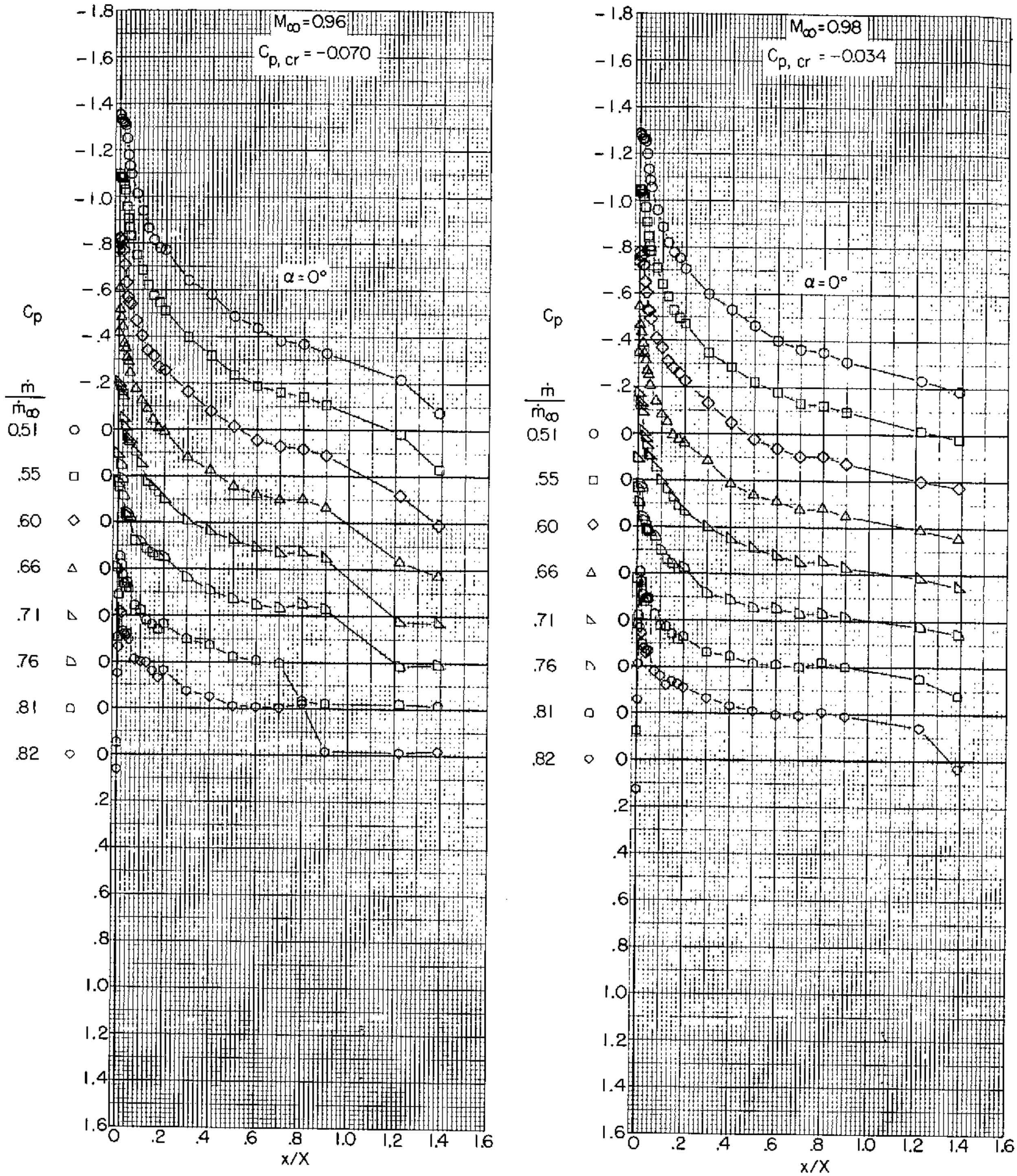

(e) M_∞ = 0.96 and 0.98.

Figure 9.- Continued.

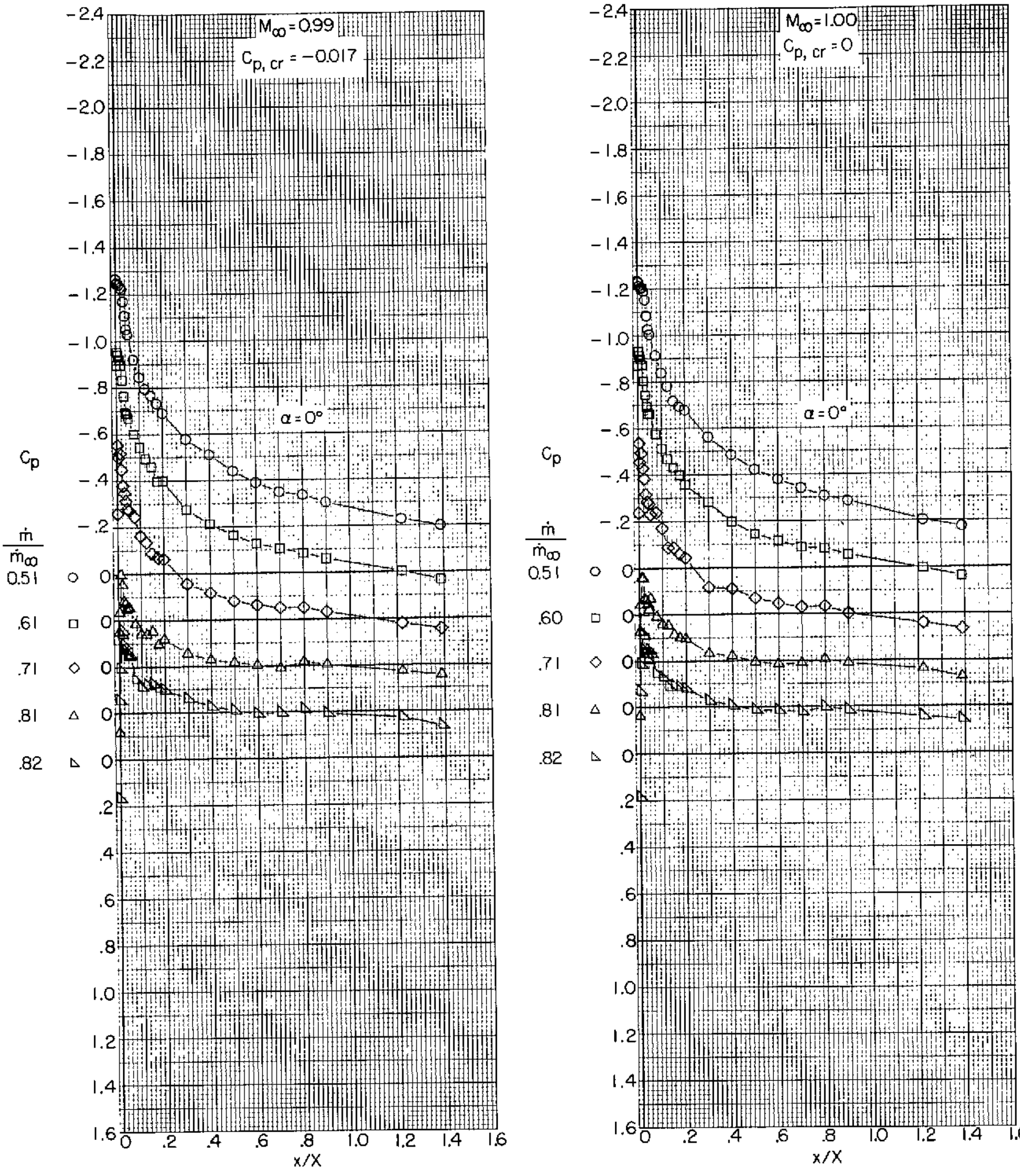

(f) $M_\infty = 0.99$ and 1.00.

Figure 9.- Continued.

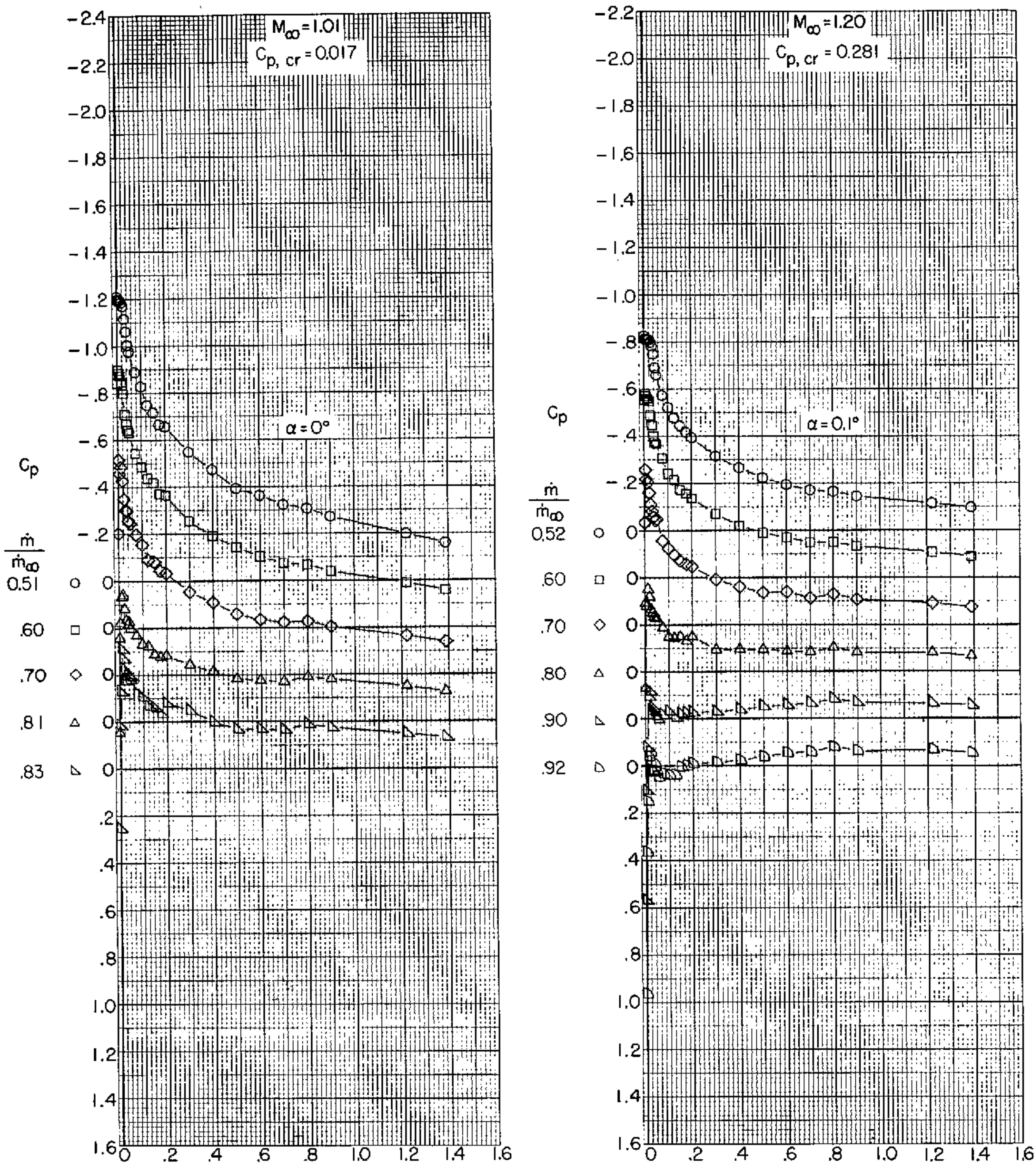

(g) M_∞ = 1.01 and 1.20.

Figure 9.- Continued.

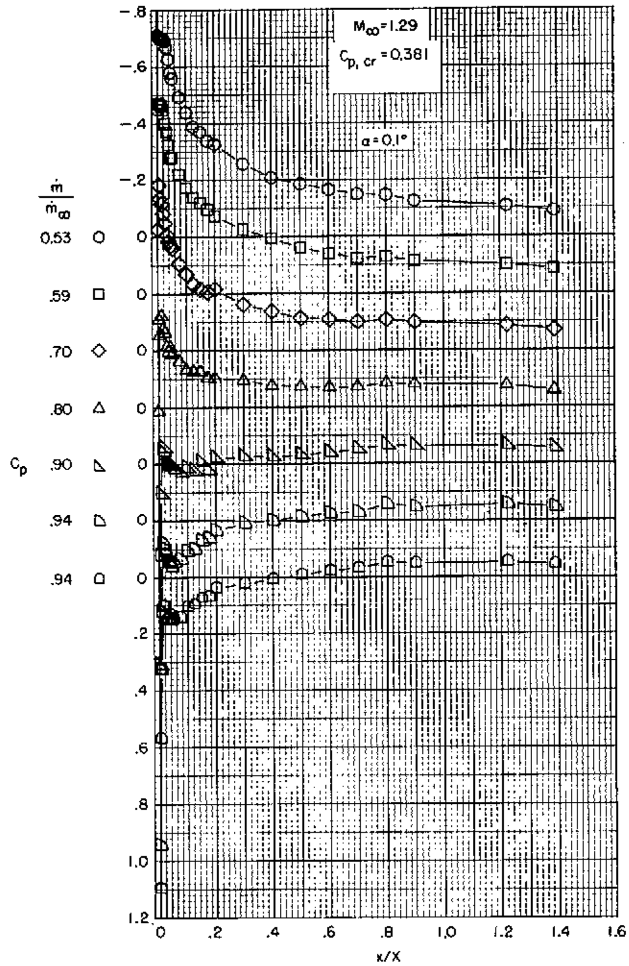

(h) $M_\infty = 1.29$.

Figure 9.- Concluded.

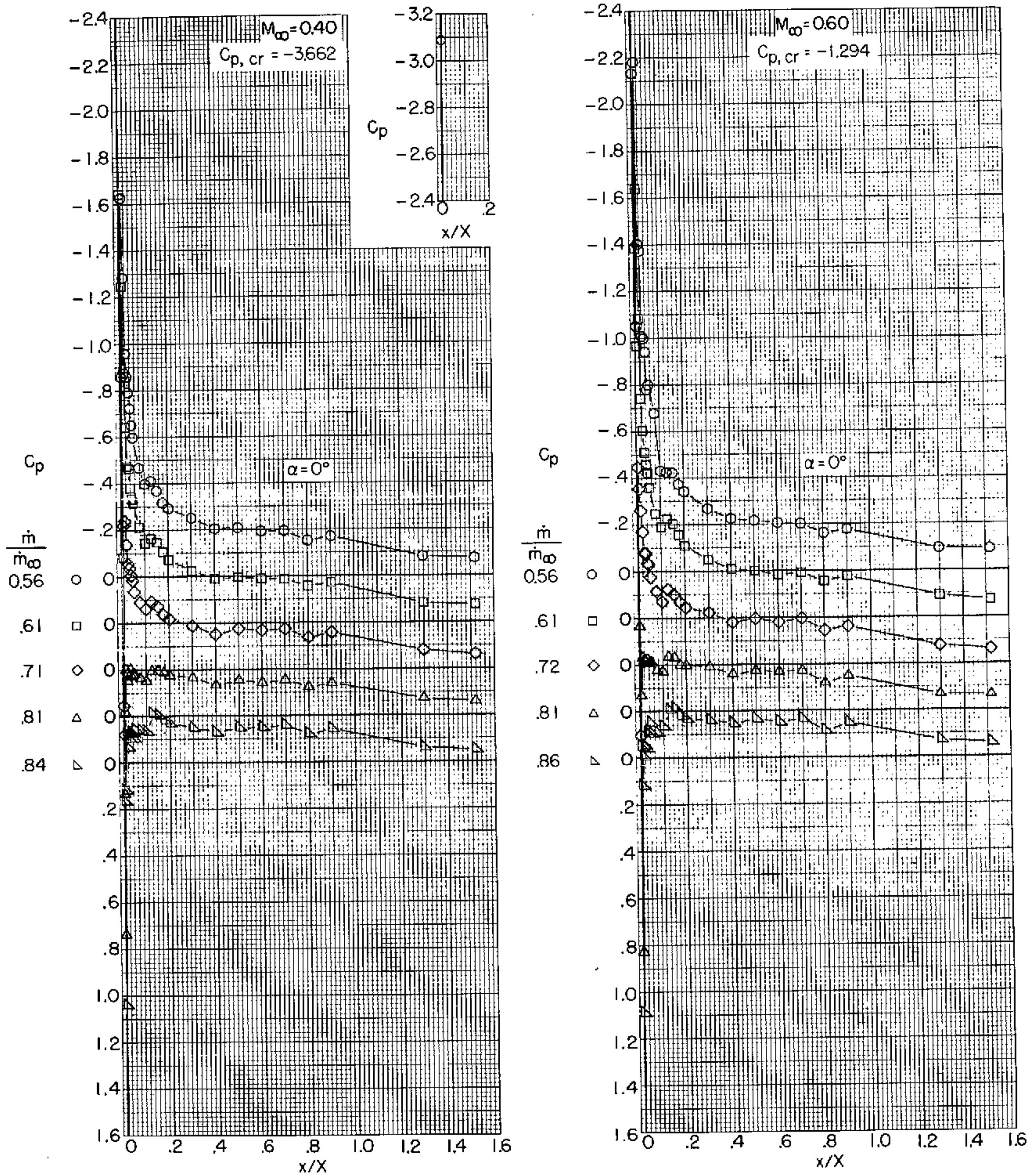

(a) M_∞ = 0.40 and 0.60.

Figure 10.- Variation with length of pressure coefficient over the outer profile of an NACA 1-85-75 (contraction ratio 1.009) inlet.

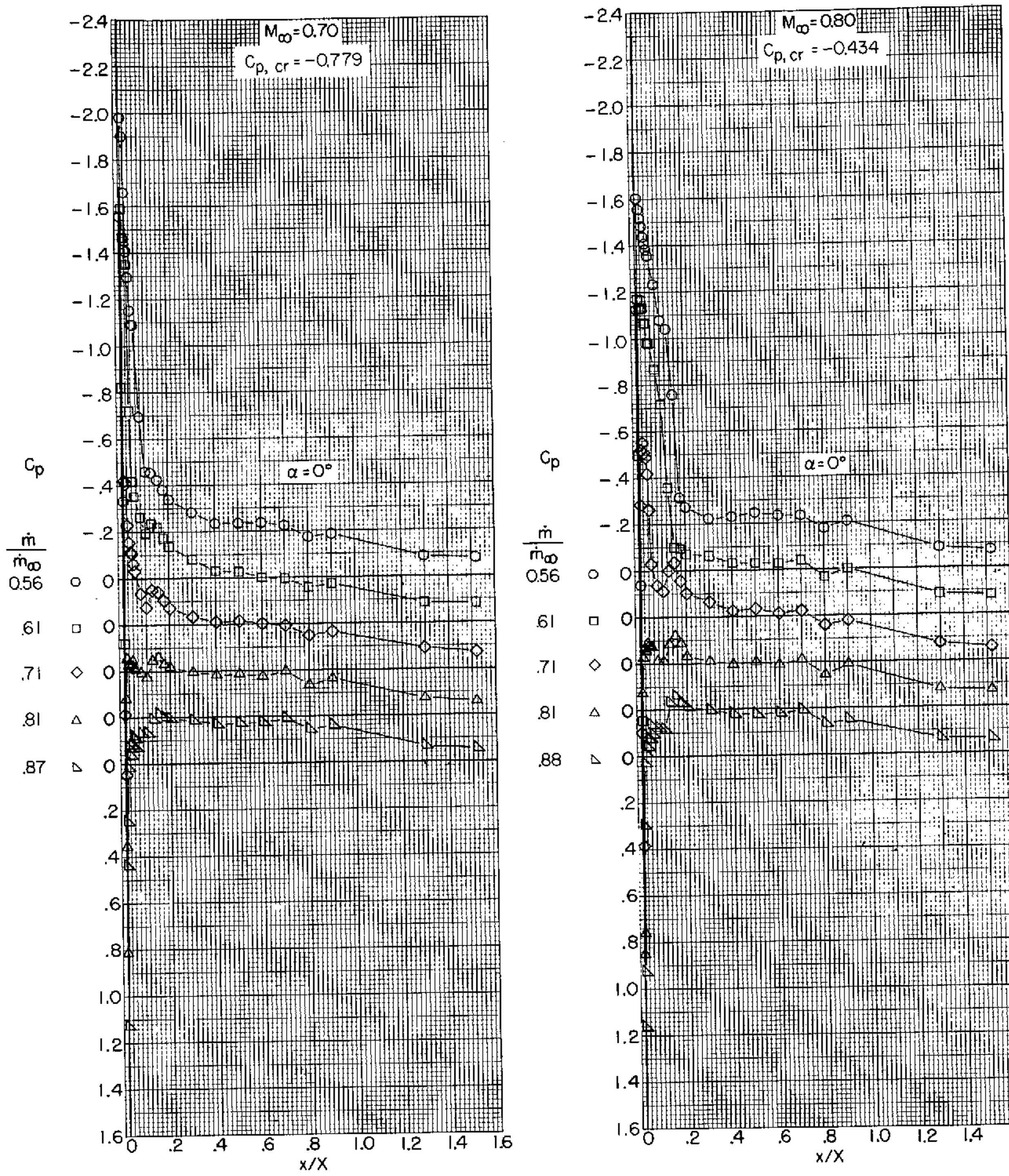

(b) M_∞ = 0.70 and 0.80.

Figure 10.- Continued.

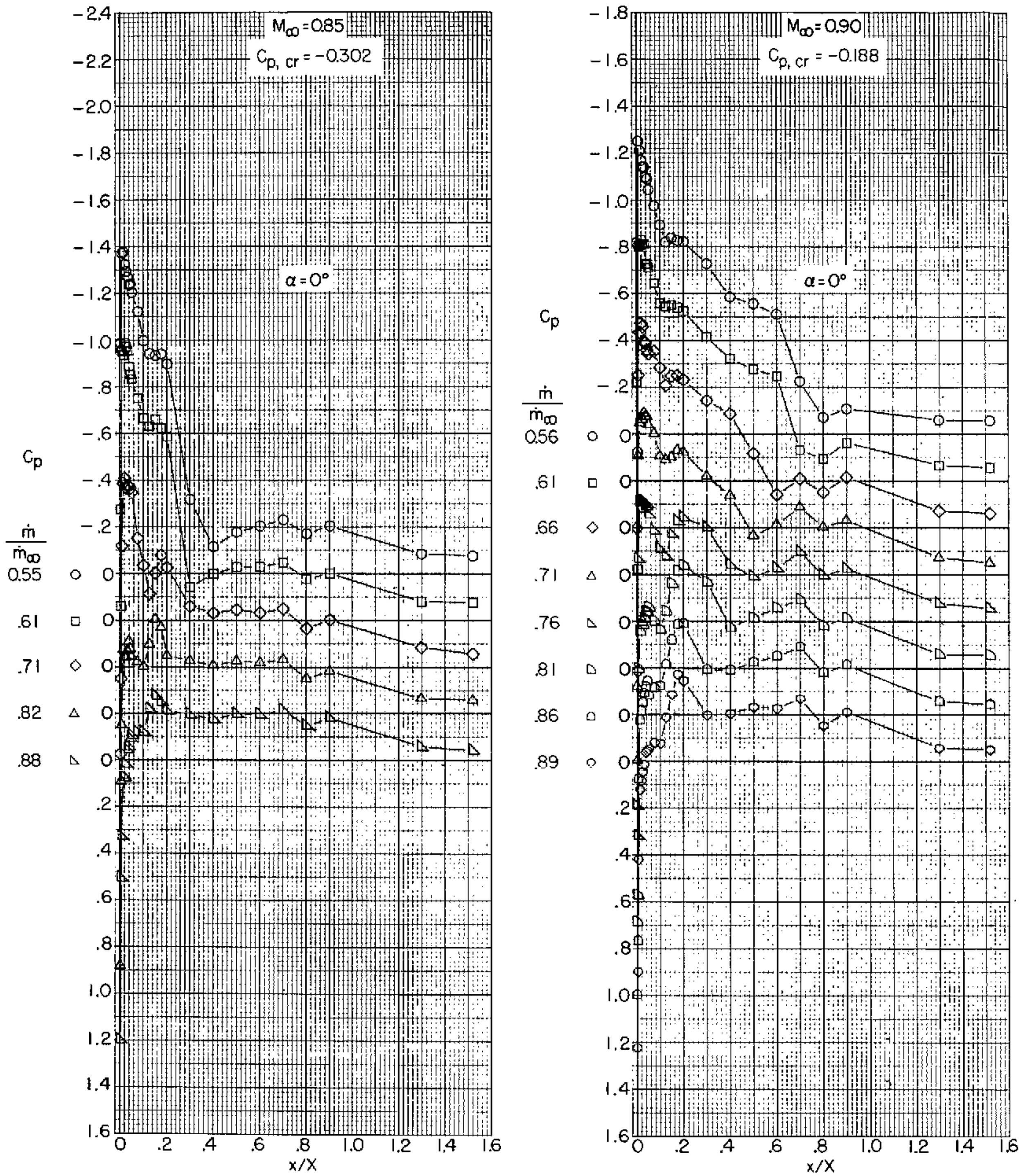

(c) M_∞ = 0.85 and 0.90.

Figure 10.- Continued.

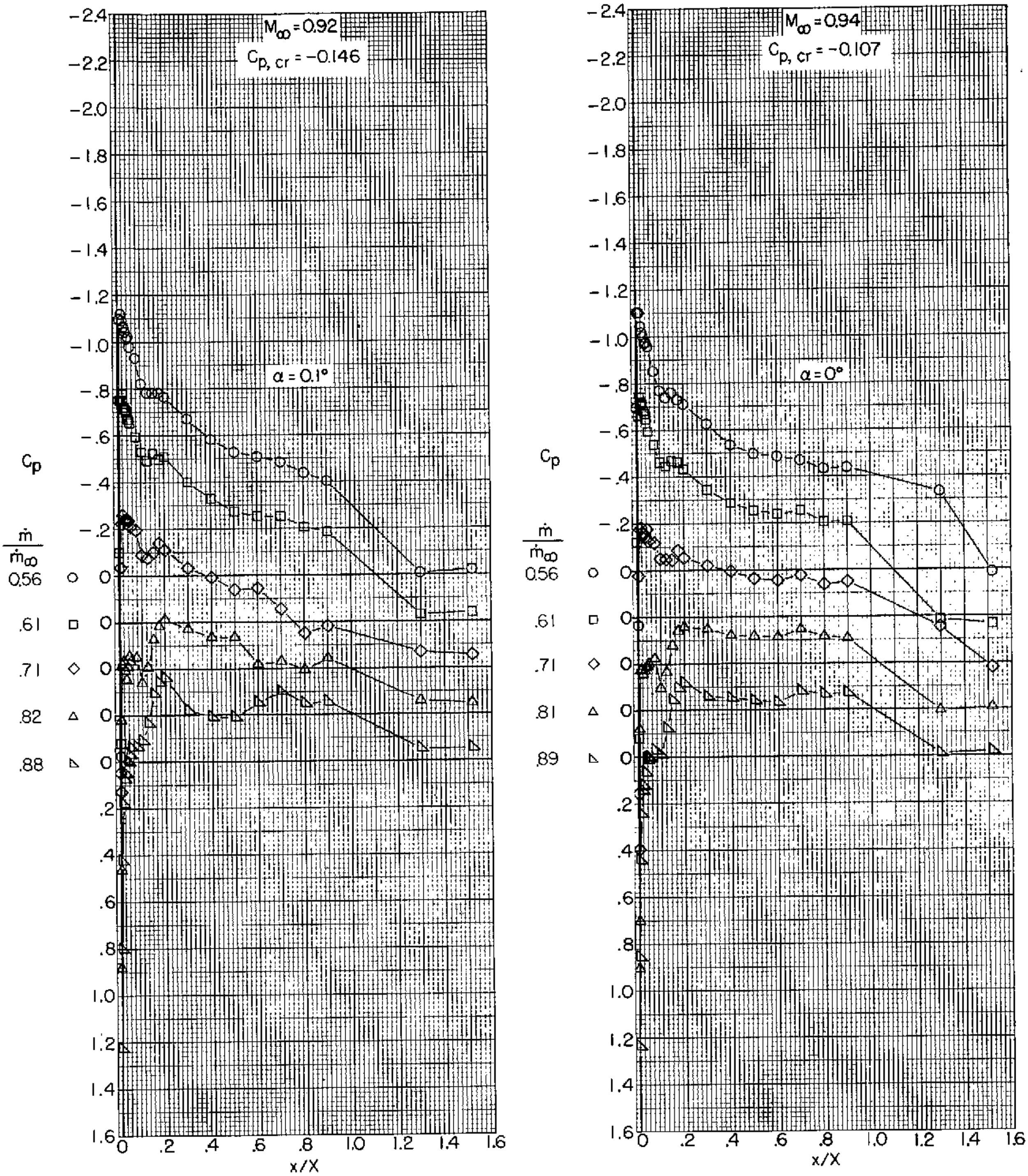

(d) M_∞ = 0.92 and 0.94.

Figure 10.- Continued.

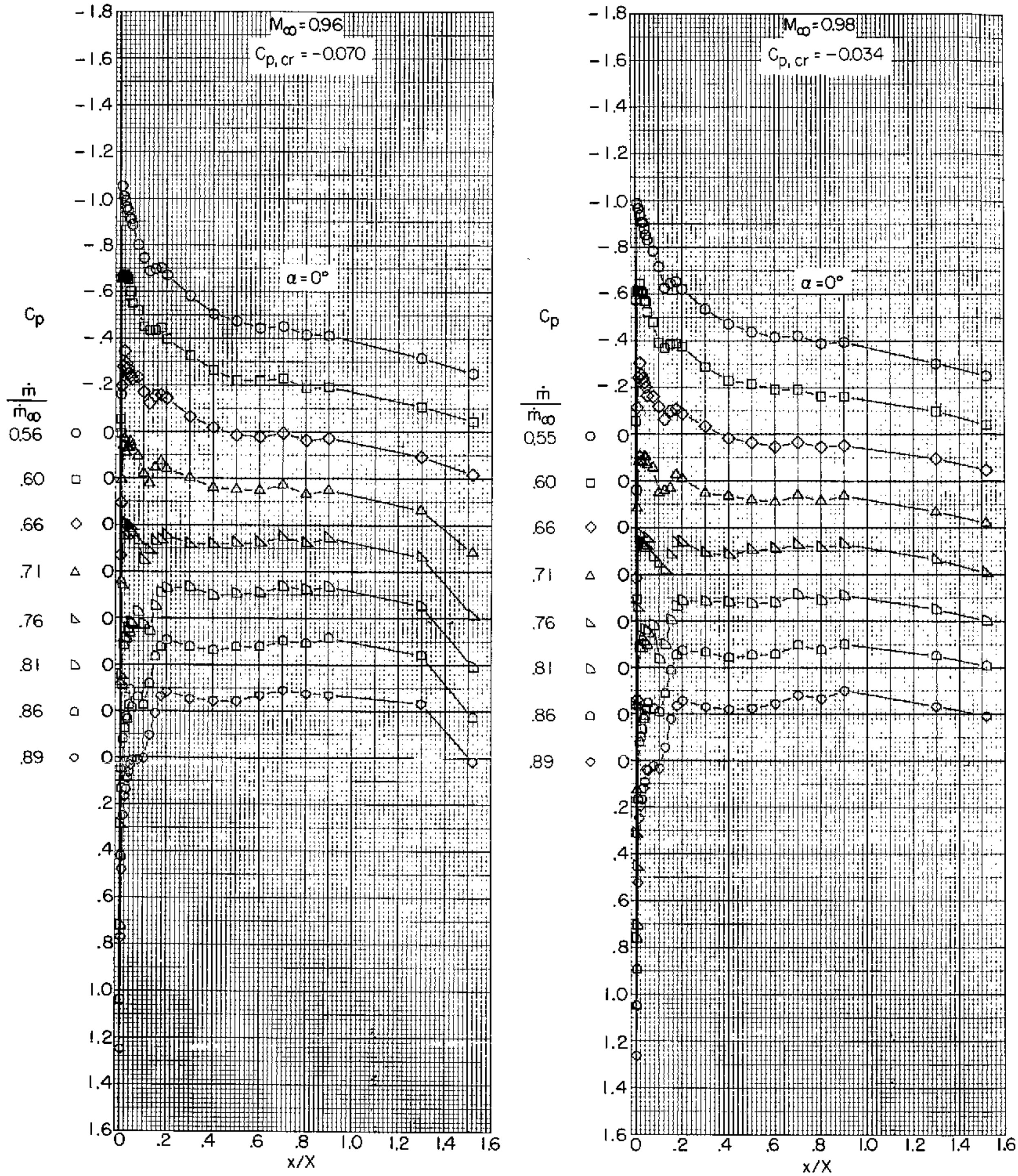

(e) M_∞ = 0.96 and 0.98.

Figure 10.- Continued.

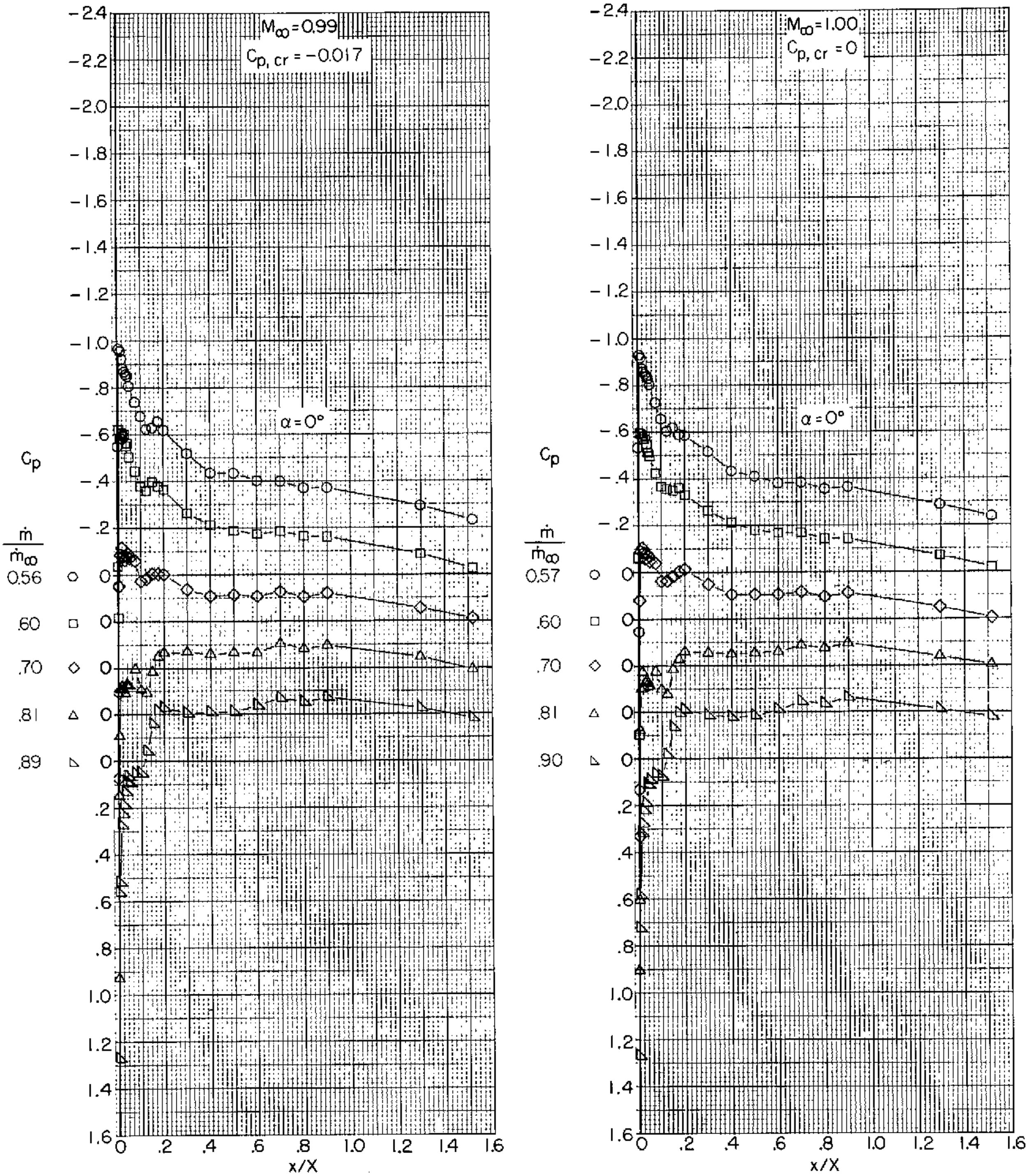

(f) M_∞ = 0.99 and 1.00.

Figure 10.- Continued.

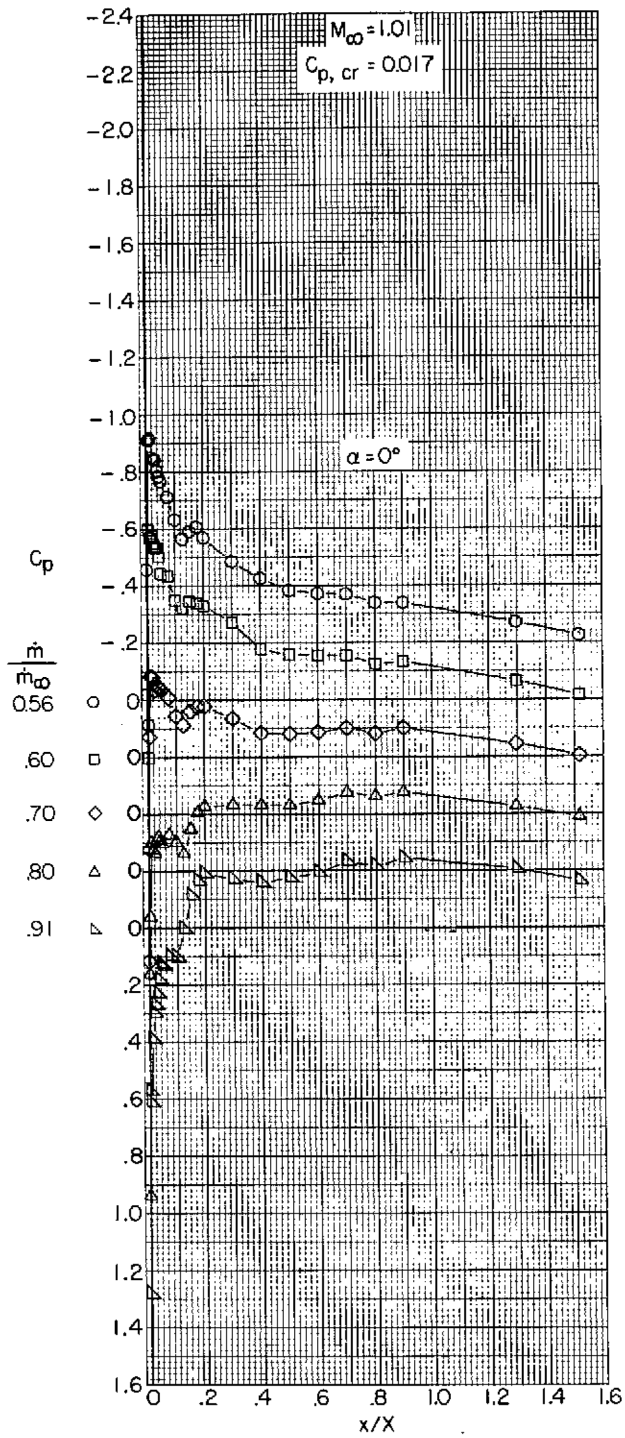

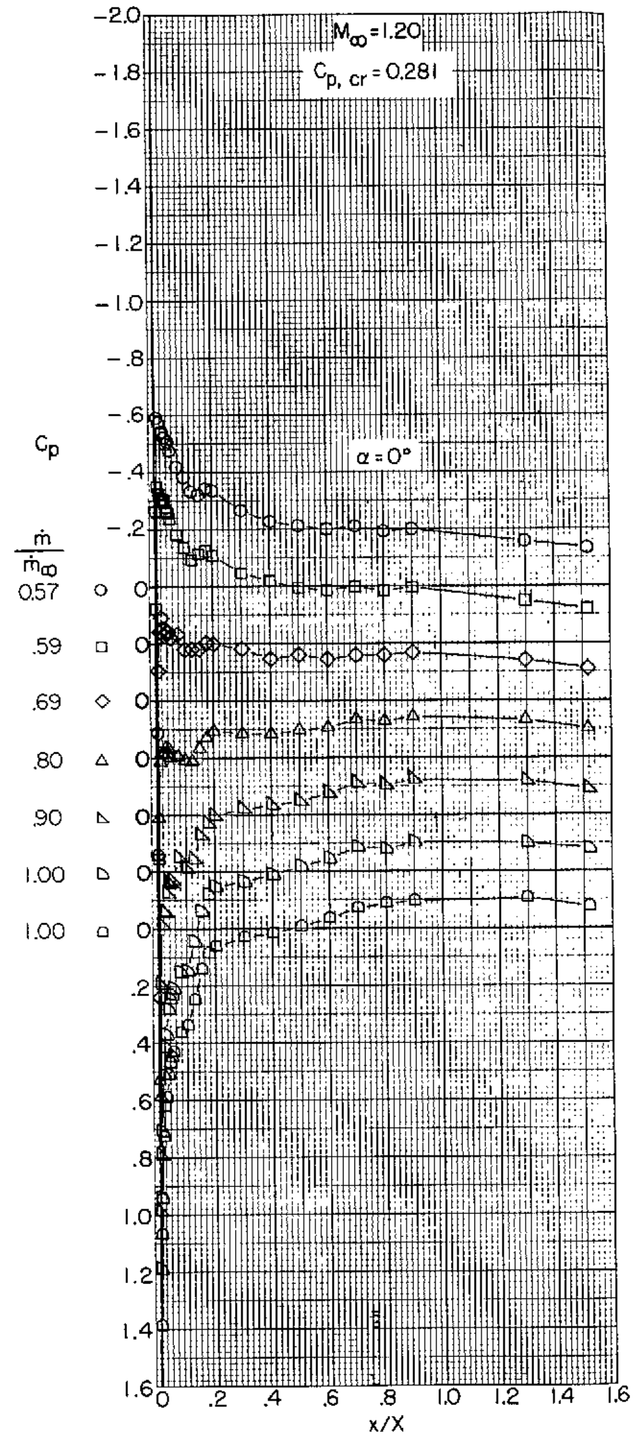

(g) M_∞ = 1.01 and 1.20.

Figure 10.- Continued.

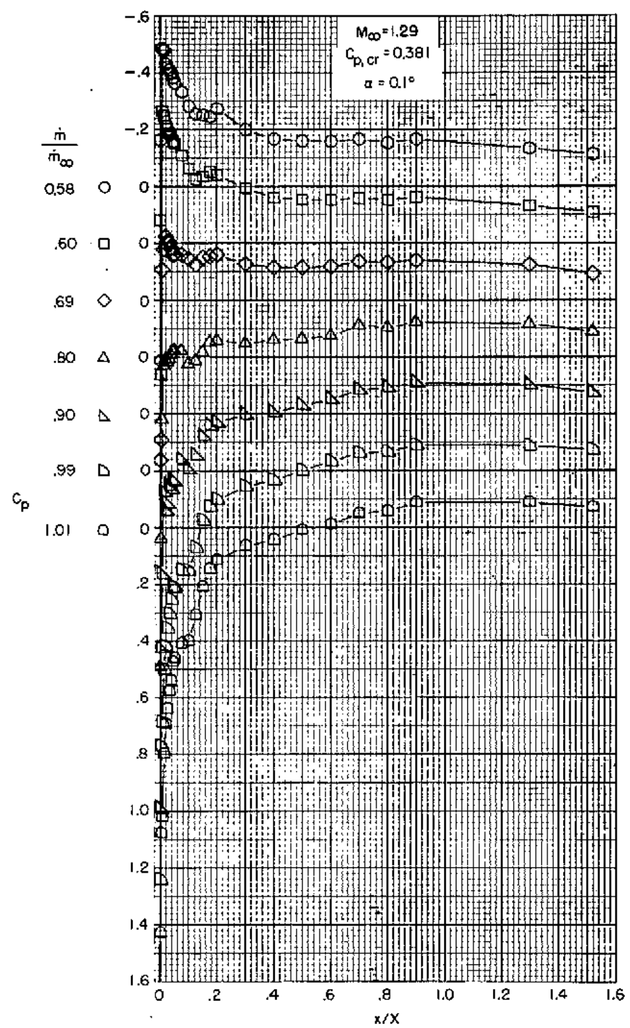

(h) $M_\infty = 1.29$.

Figure 10.- Concluded.

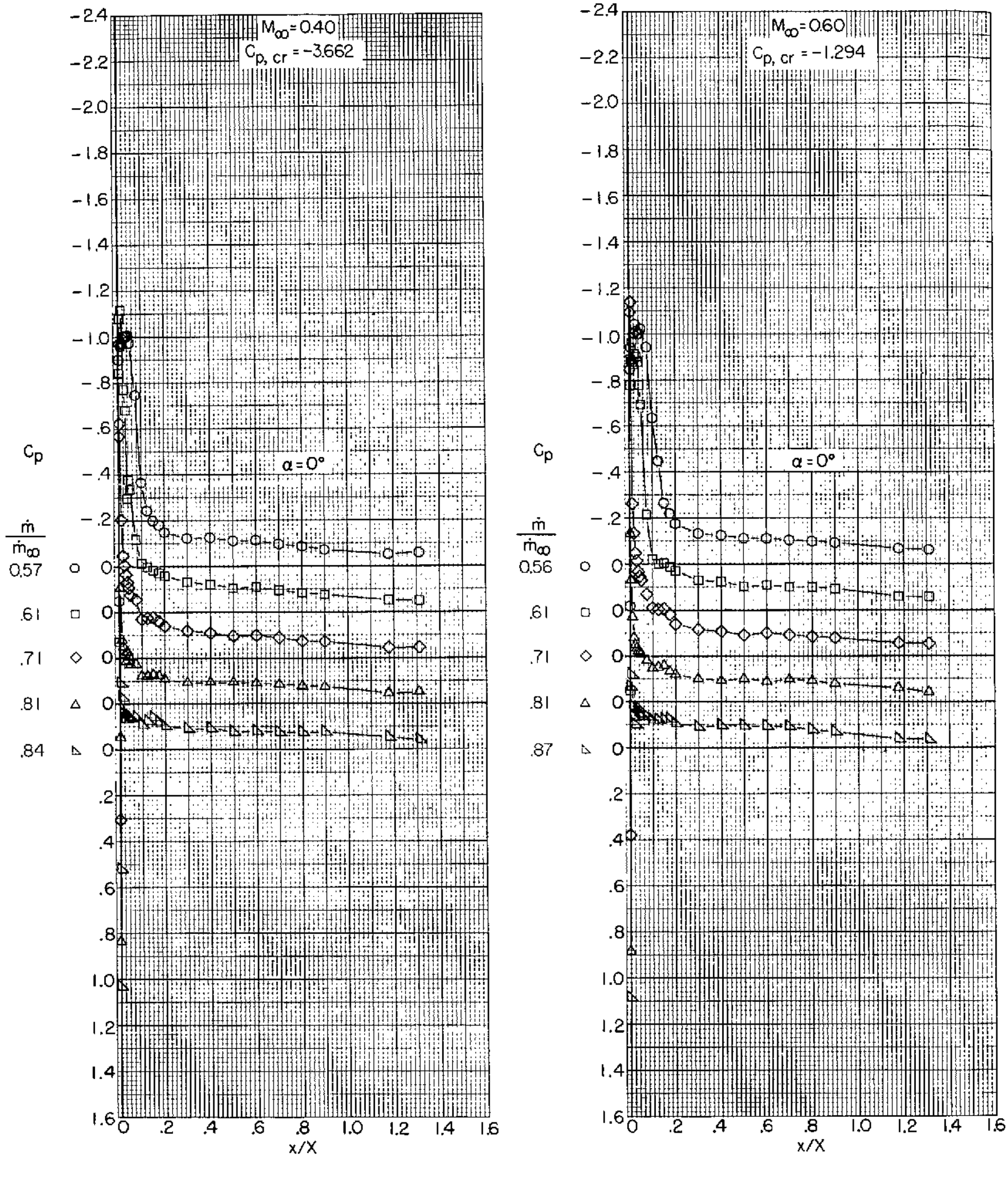

(a) $M_\infty = 0.40$ and 0.60.

Figure 11.- Variation with length of pressure coefficient over the outer profile of an NACA 1-85-125 (contraction ratio 1.009) inlet.

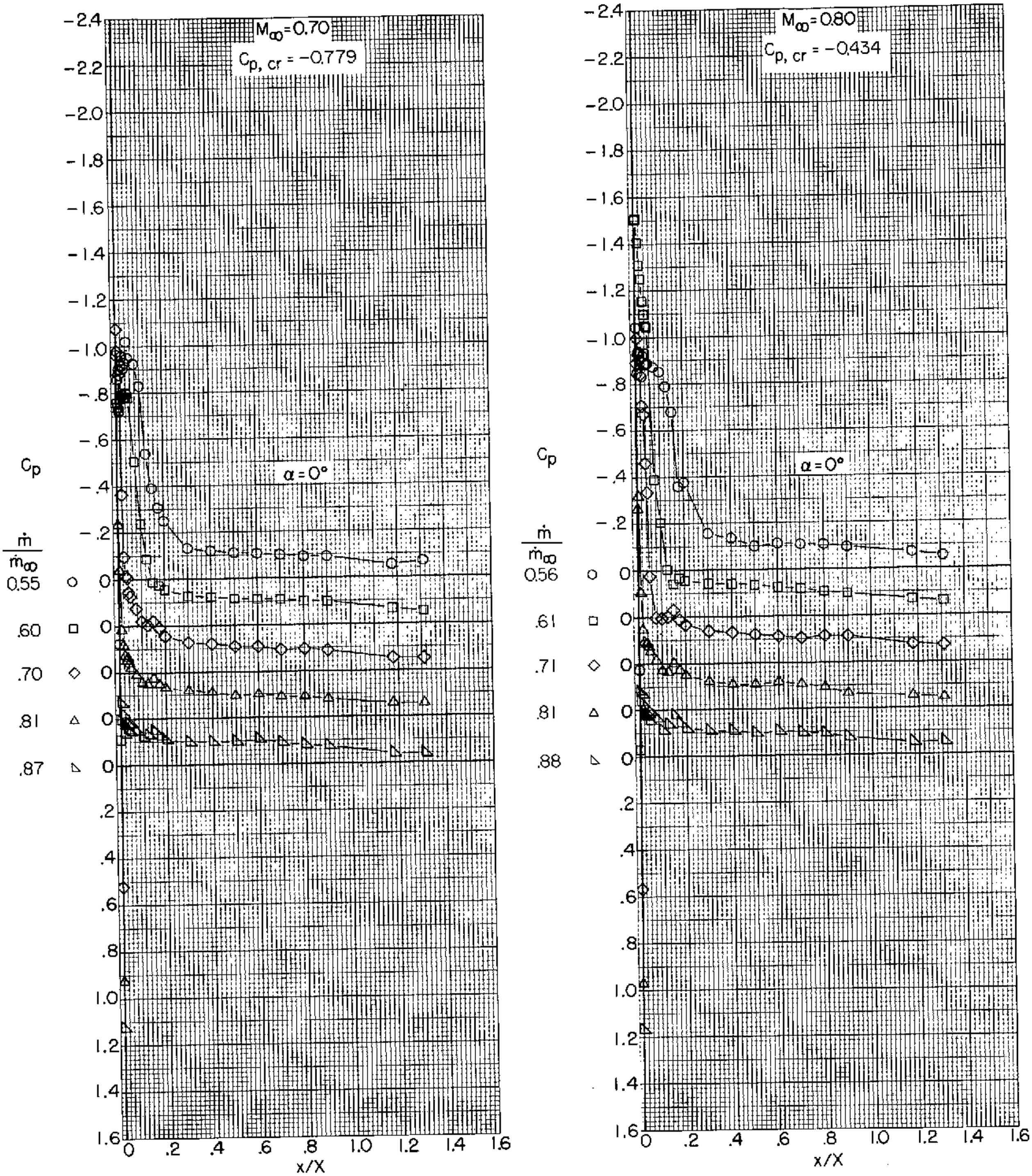

(b) M_∞ = 0.70 and 0.80.

Figure 11.- Continued.

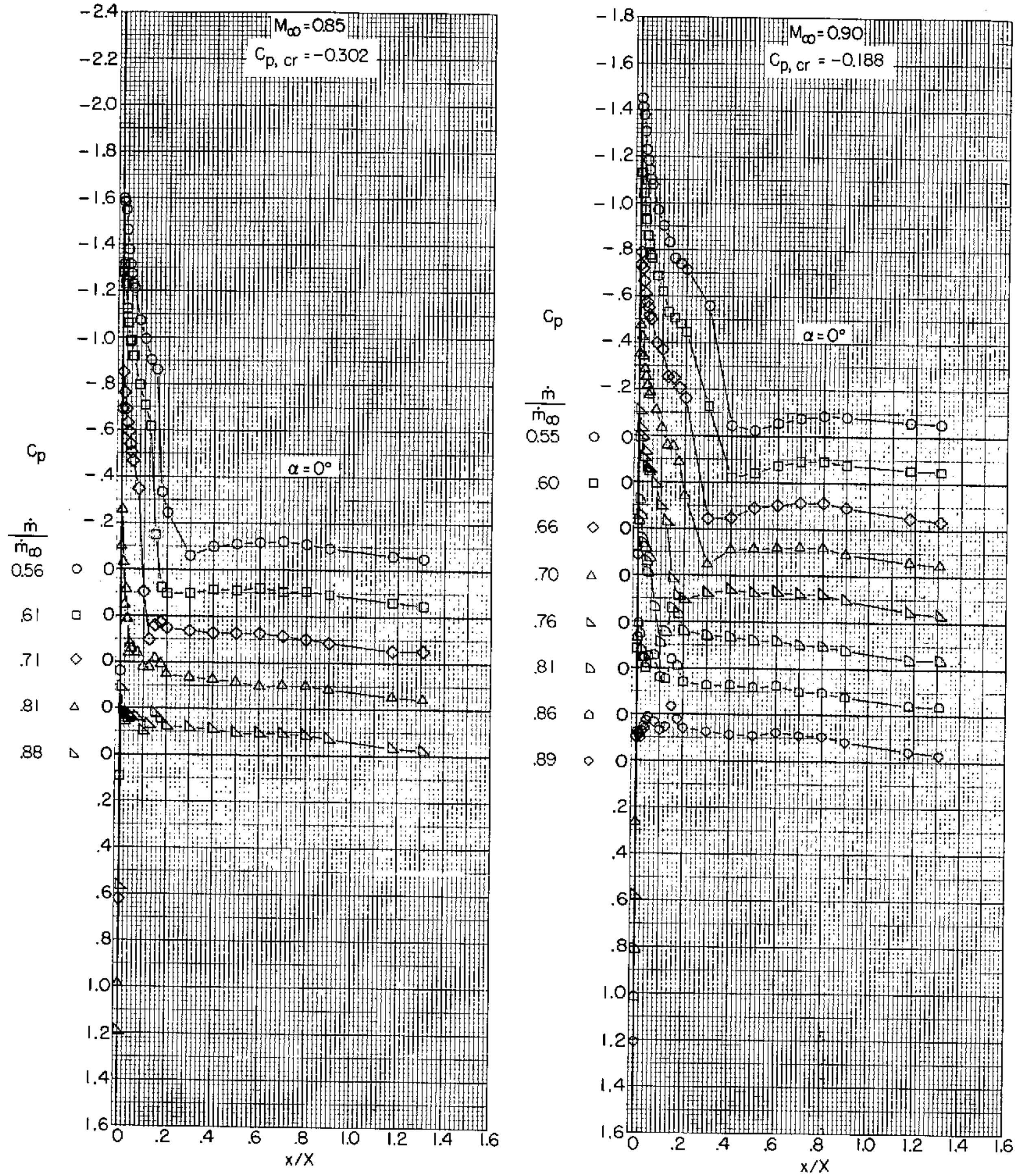

(c) M_∞ = 0.85 and 0.90.

Figure 11.- Continued.

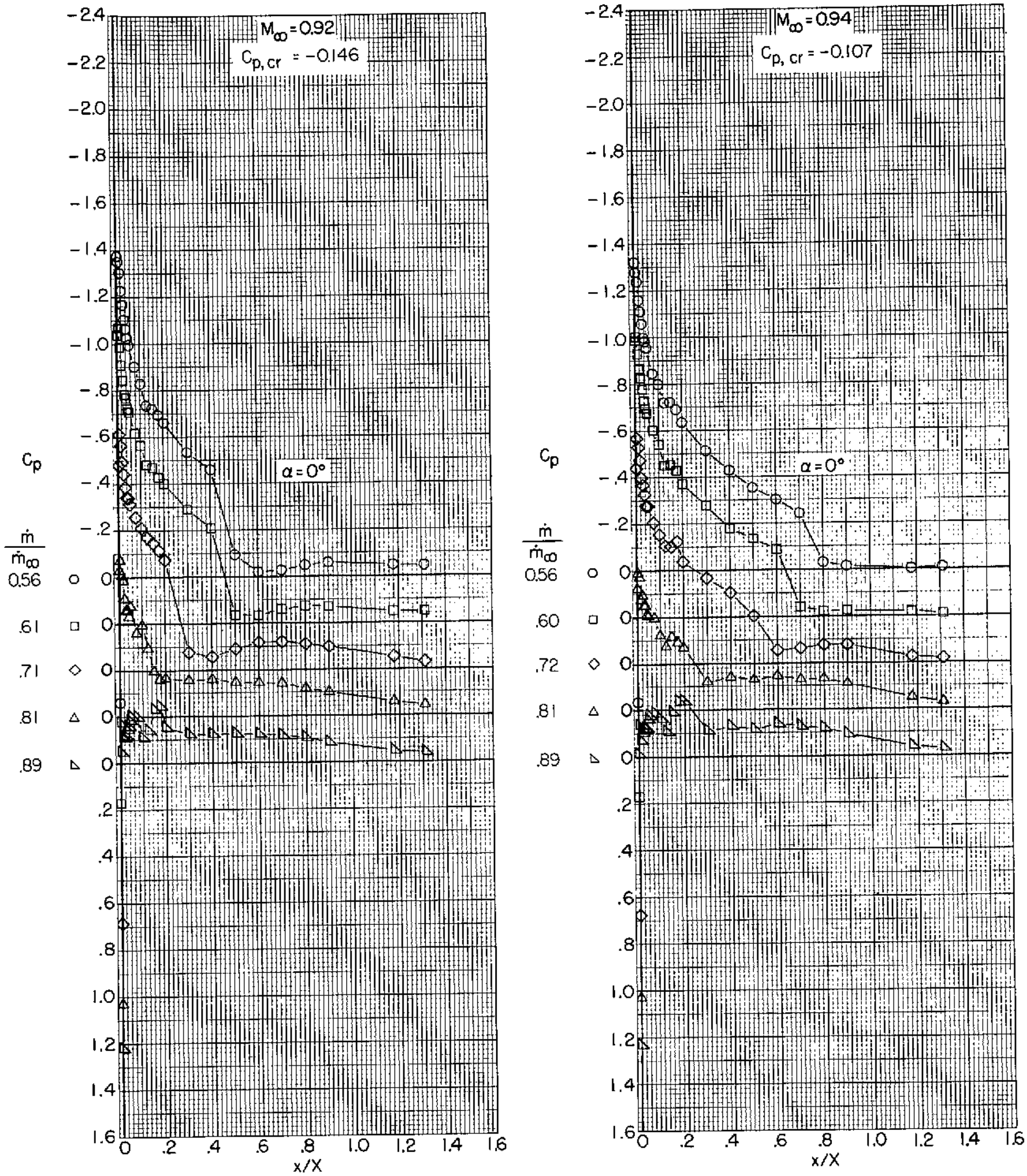

(d) M_∞ = 0.92 and 0.94.

Figure 11.- Continued.

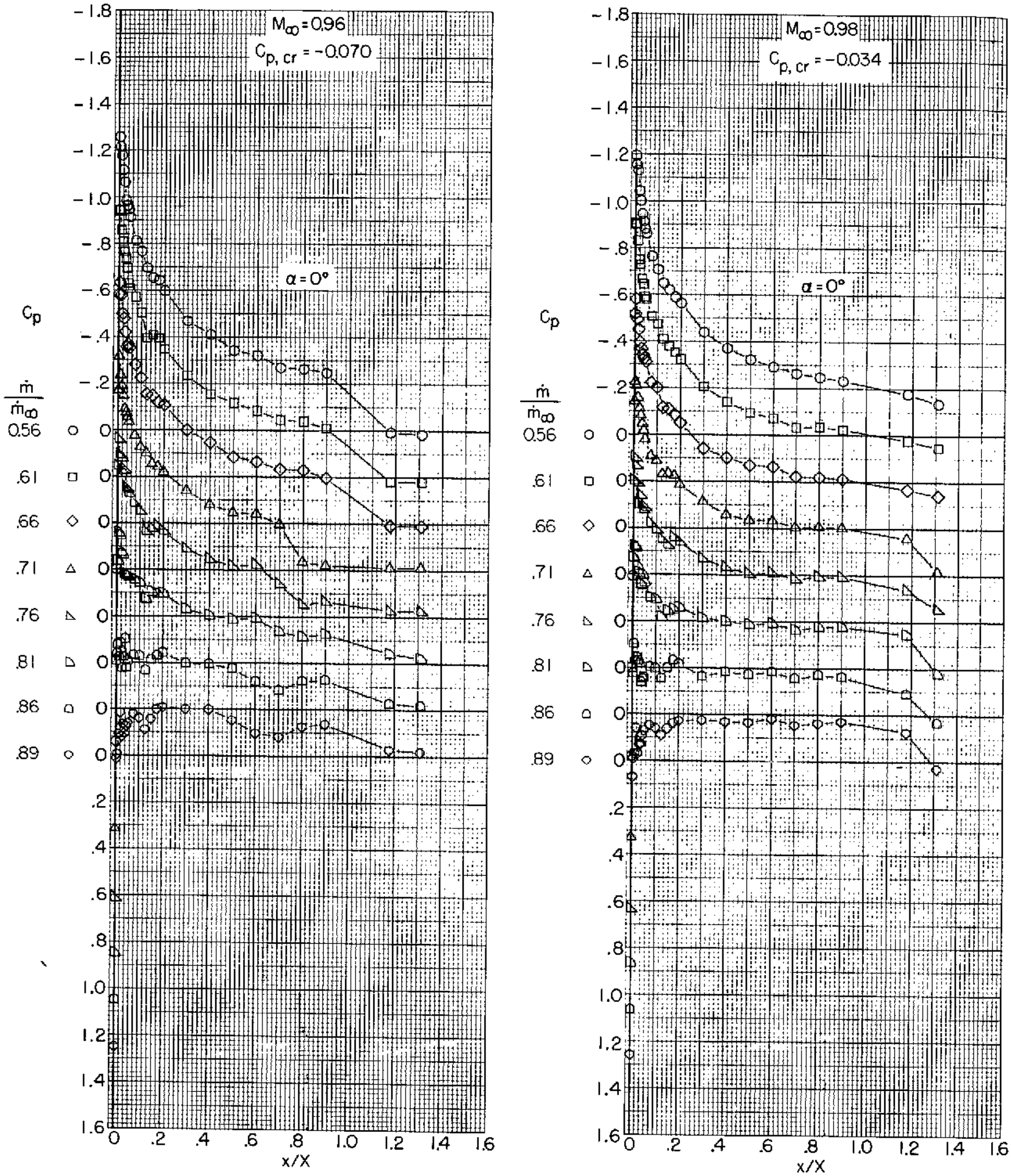

(e) M_∞ = 0.96 and 0.98.

Figure 11.- Continued.

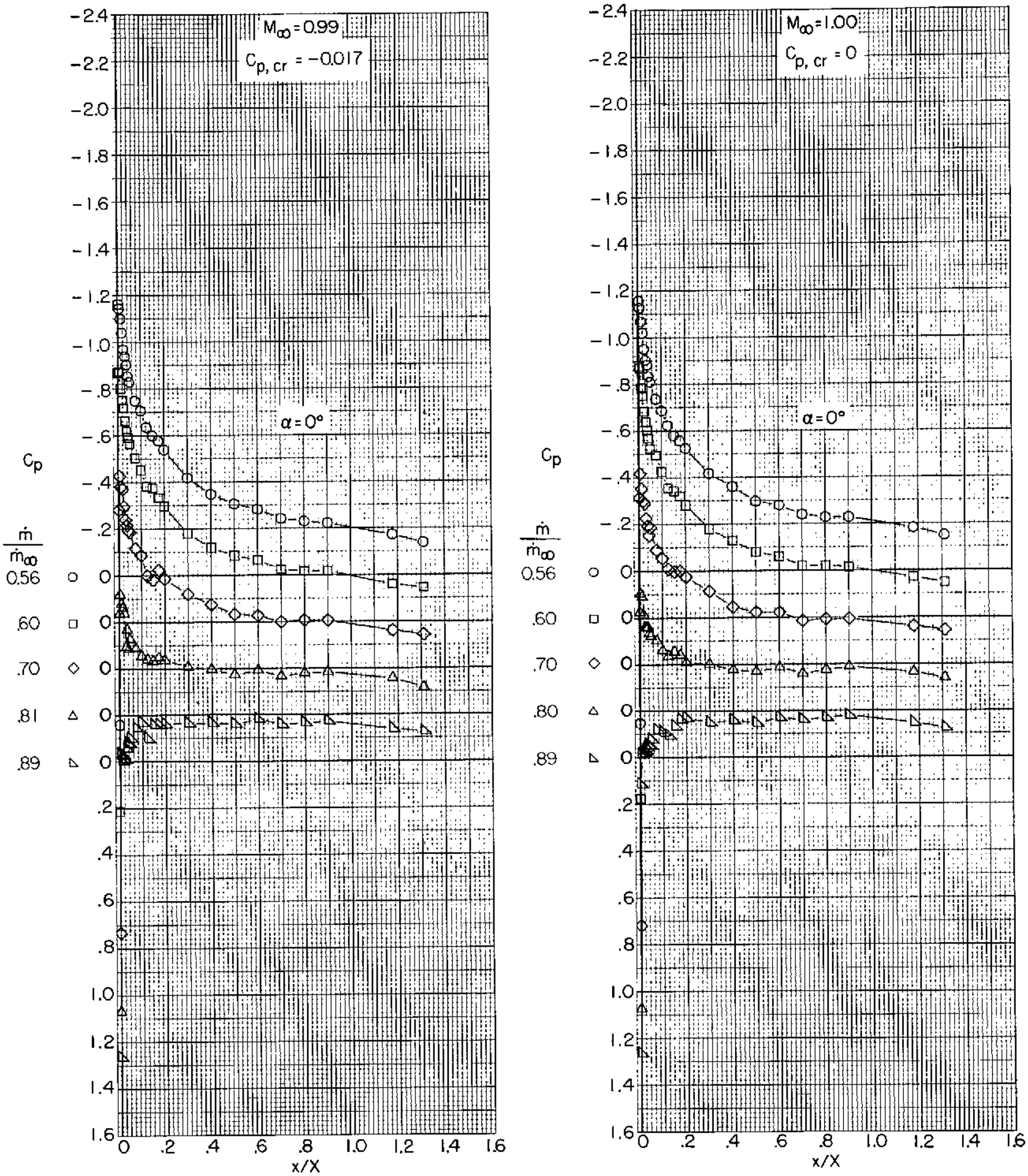

(f) $M_\infty = 0.99$ and 1.00.

Figure 11.- Continued.

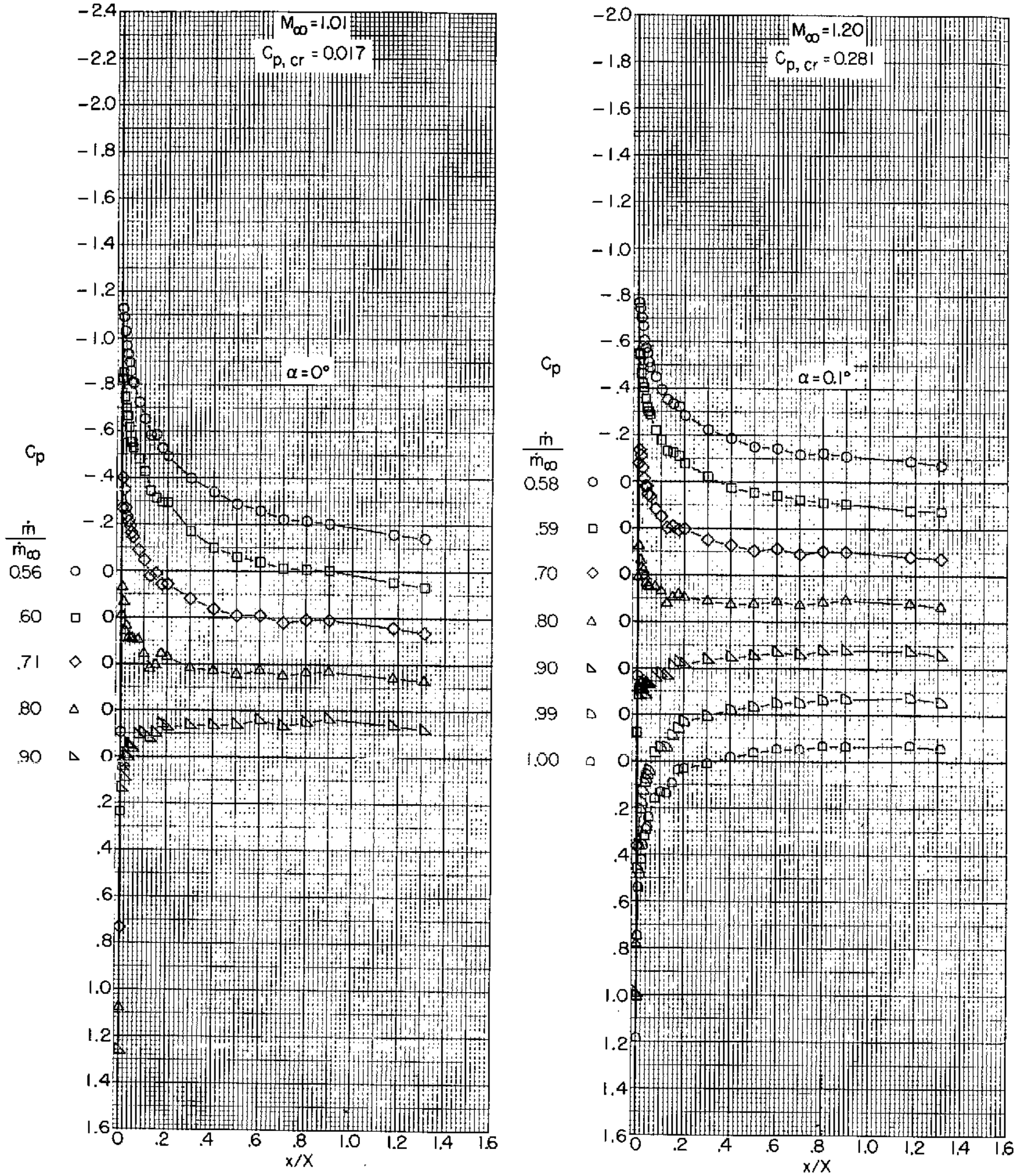

(g) M_∞ = 1.01 and 1.20.

Figure 11.- Continued.

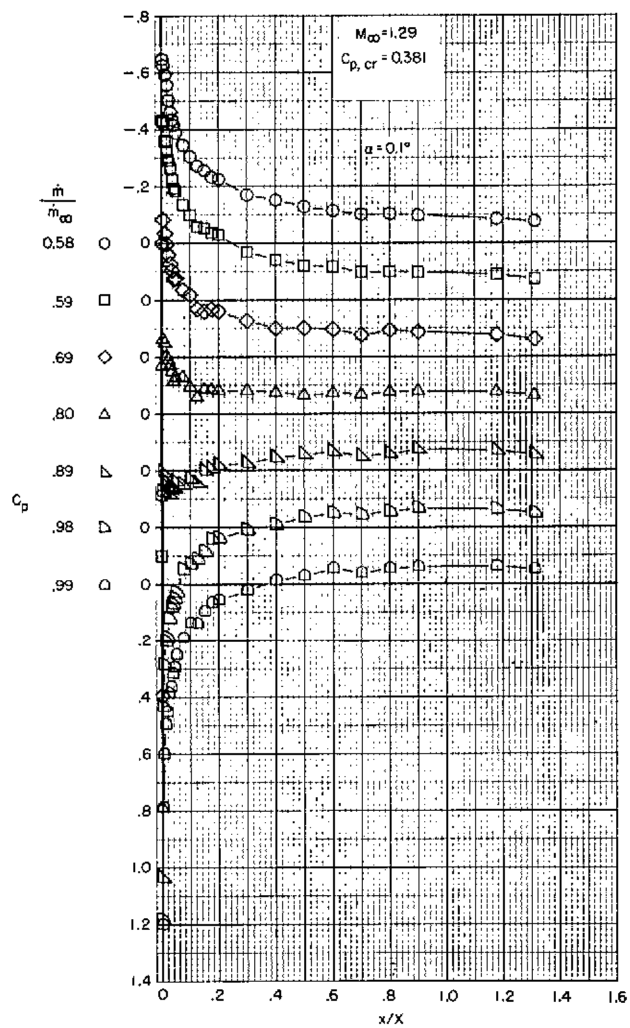

(h) $M_\infty = 1.29$.

Figure 11.- Concluded.

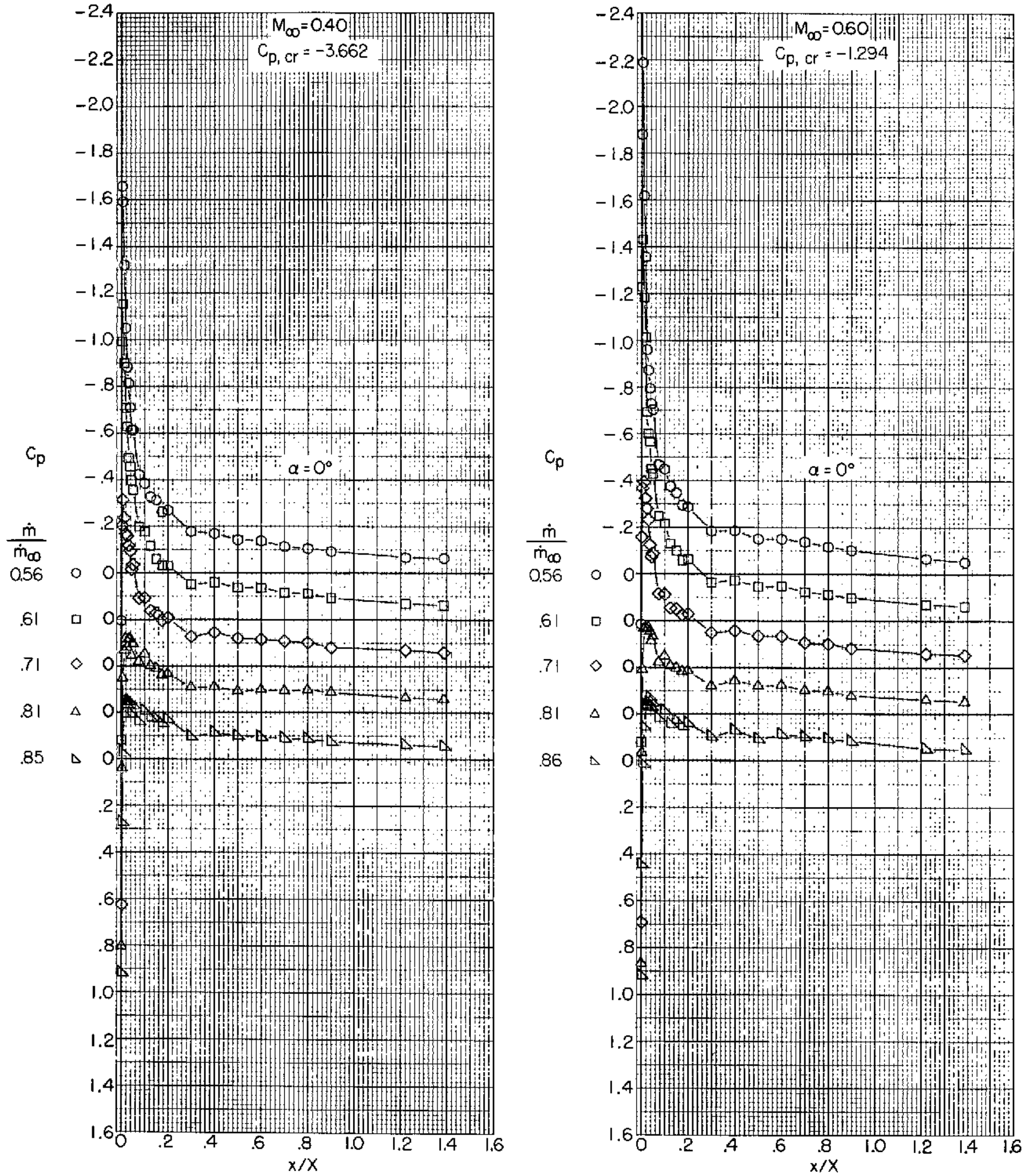

(a) $M_\infty = 0.40$ and 0.60.

Figure 12.- Variation with length of pressure coefficient over the outer profile of an Elliptical-85-100 (contraction ratio 1.009) inlet.

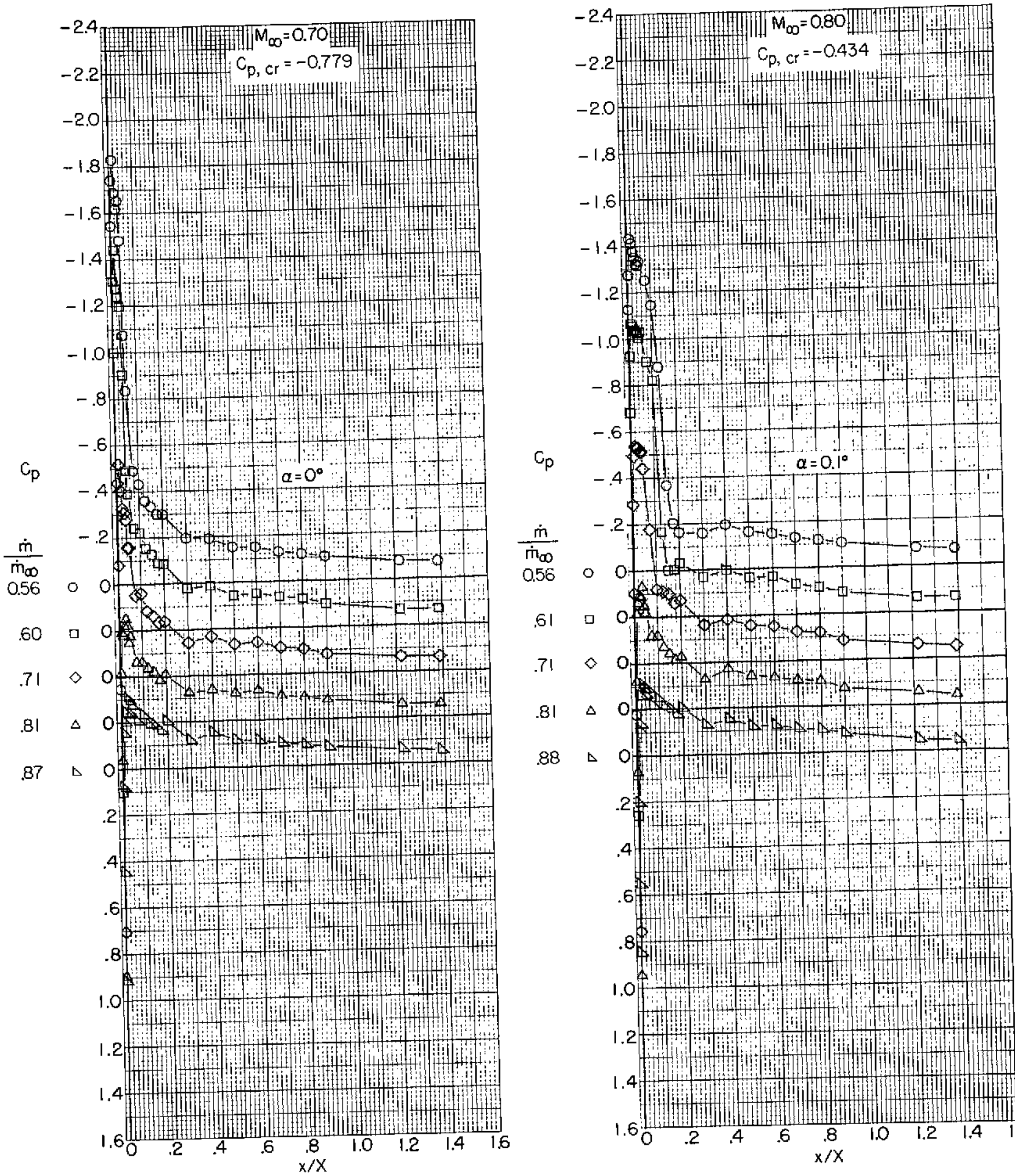

(b) M_∞ = 0.70 and 0.80.

Figure 12.- Continued.

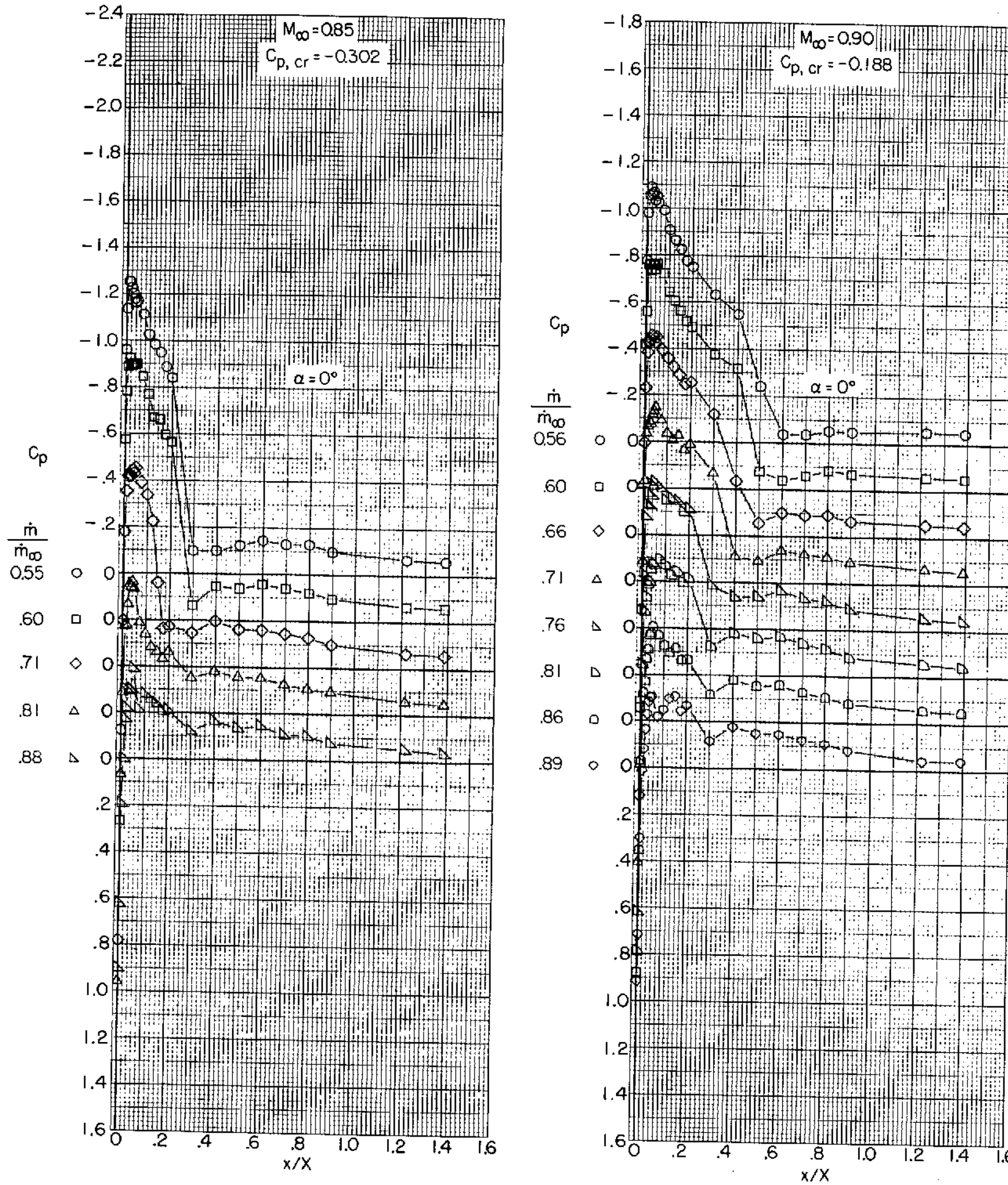

(c) M_∞ = 0.85 and 0.90.

Figure 12.- Continued.

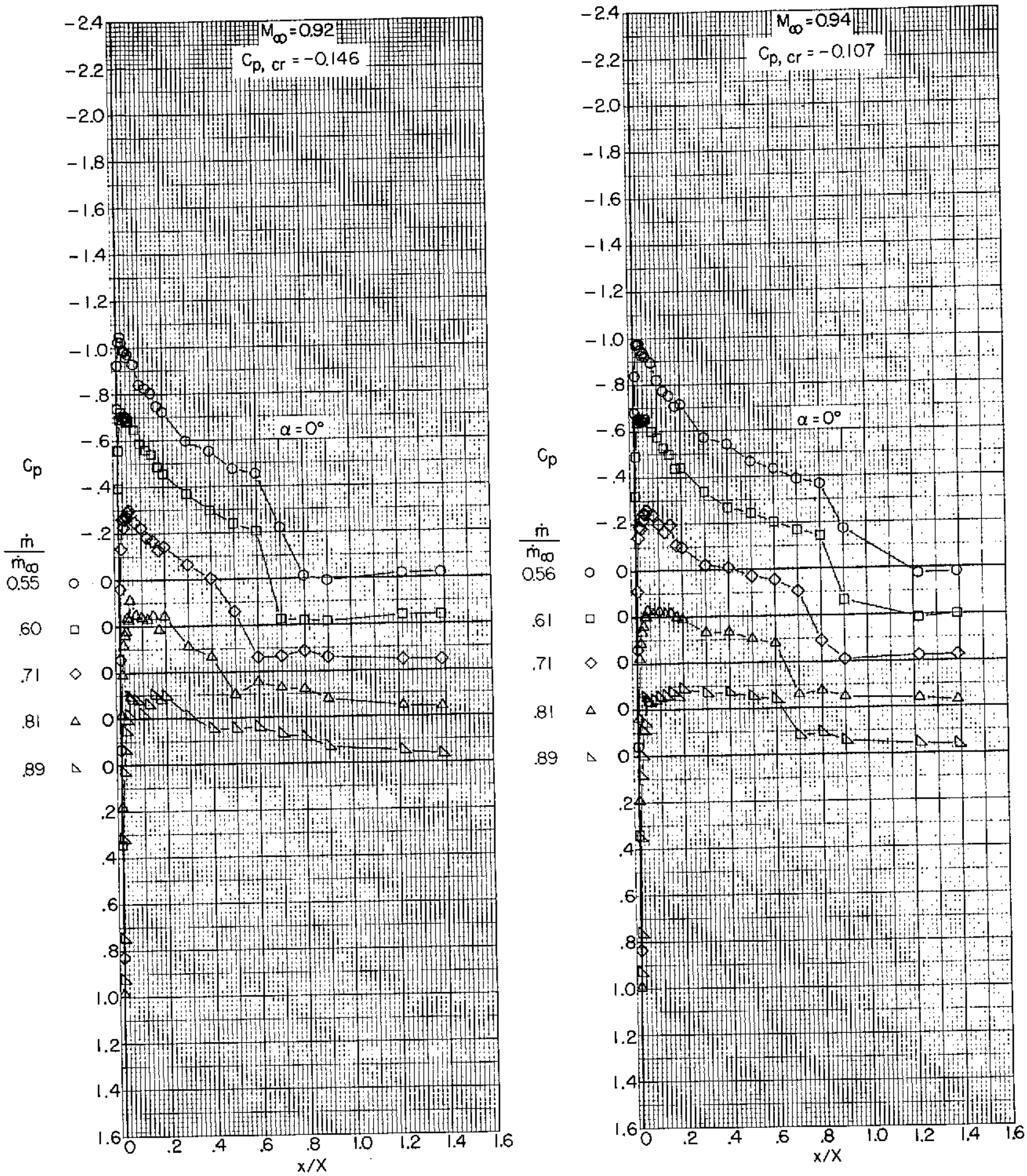

(d) M_∞ = 0.92 and 0.94.

Figure 12.- Continued.

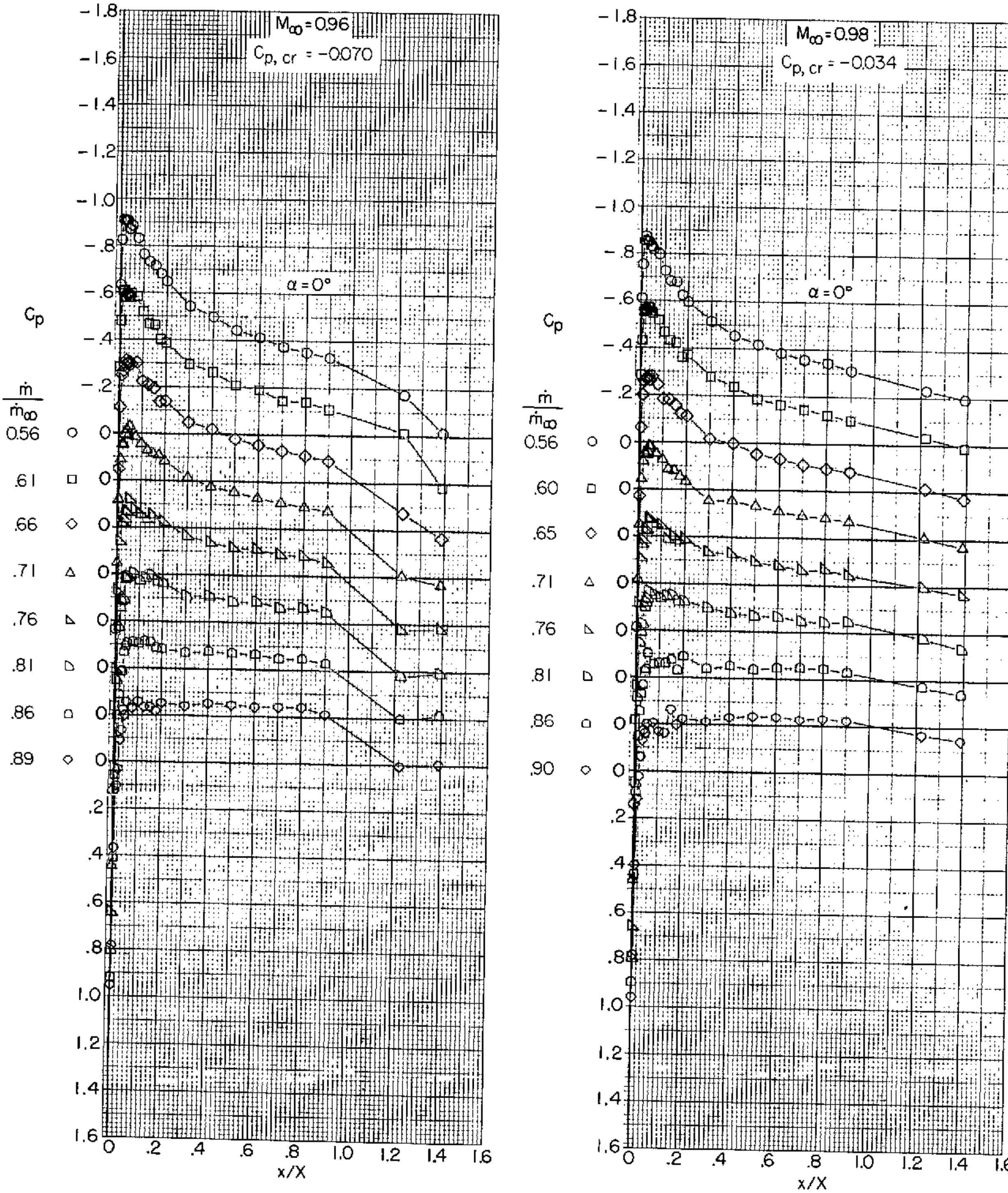

(e) M_∞ = 0.96 and 0.98.

Figure 12.- Continued.

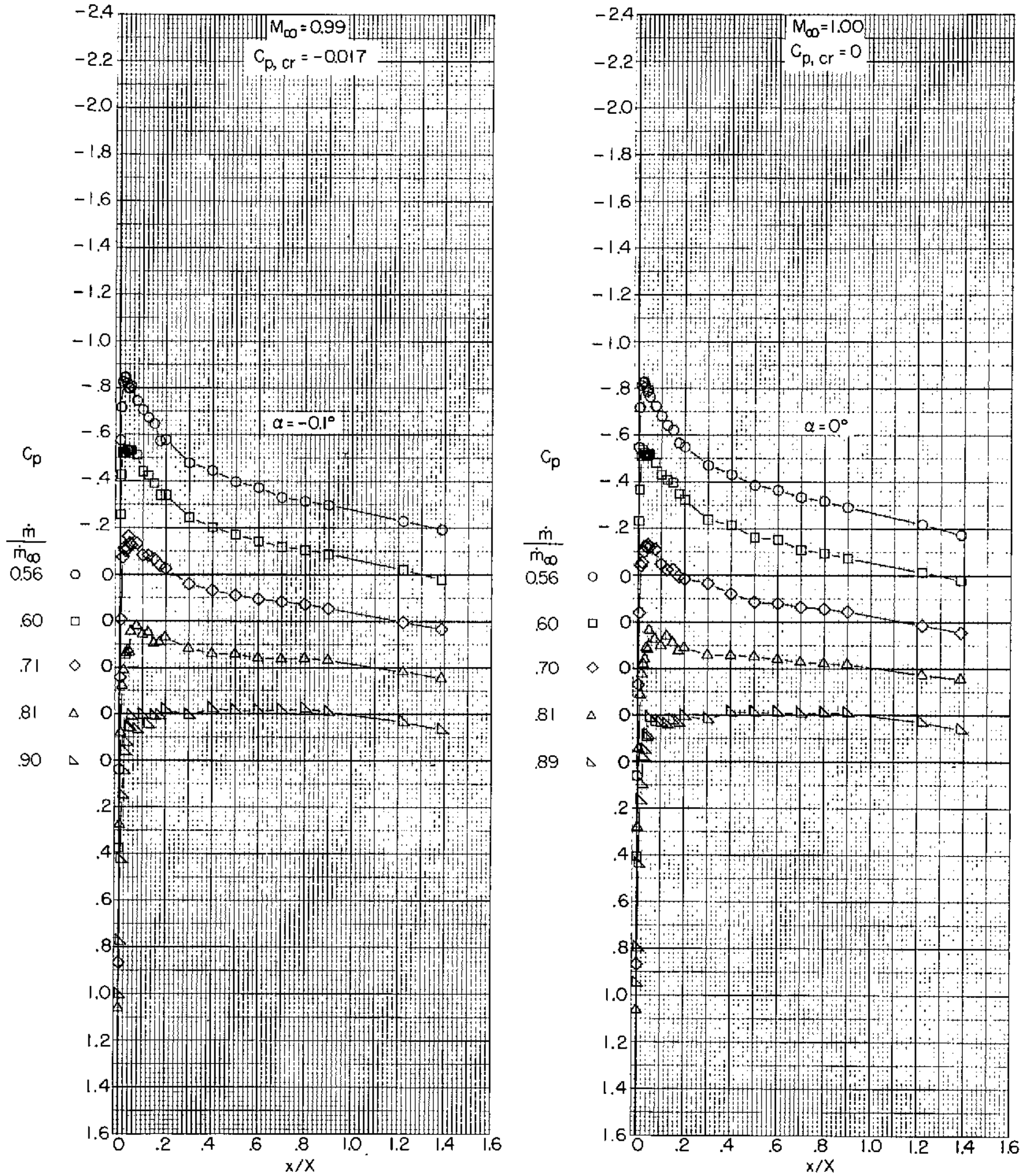

(f) M_∞ = 0.99 and 1.00.

Figure 12.- Continued.

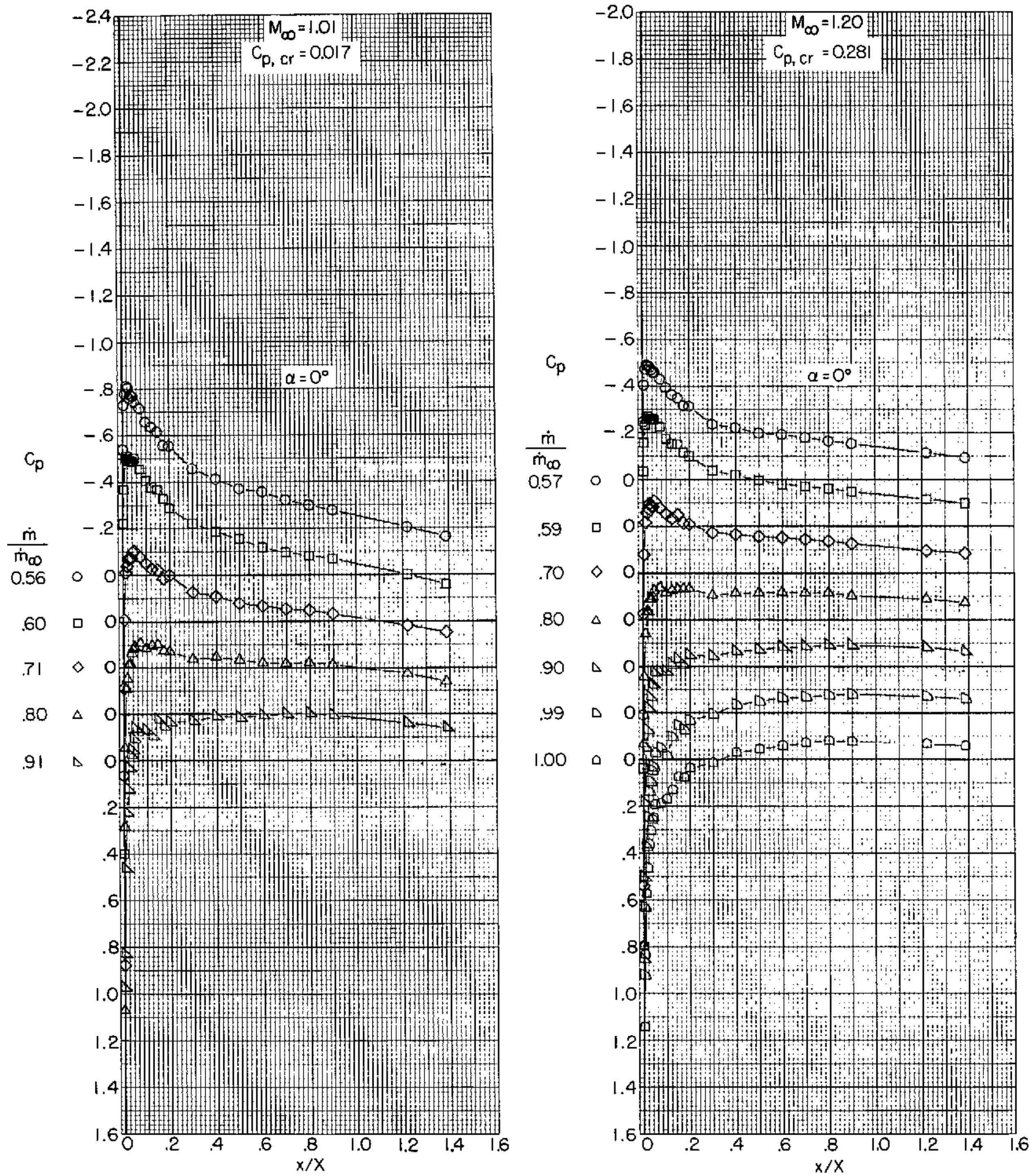

(g) M_∞ = 1.01 and 1.20.

Figure 12.- Continued.

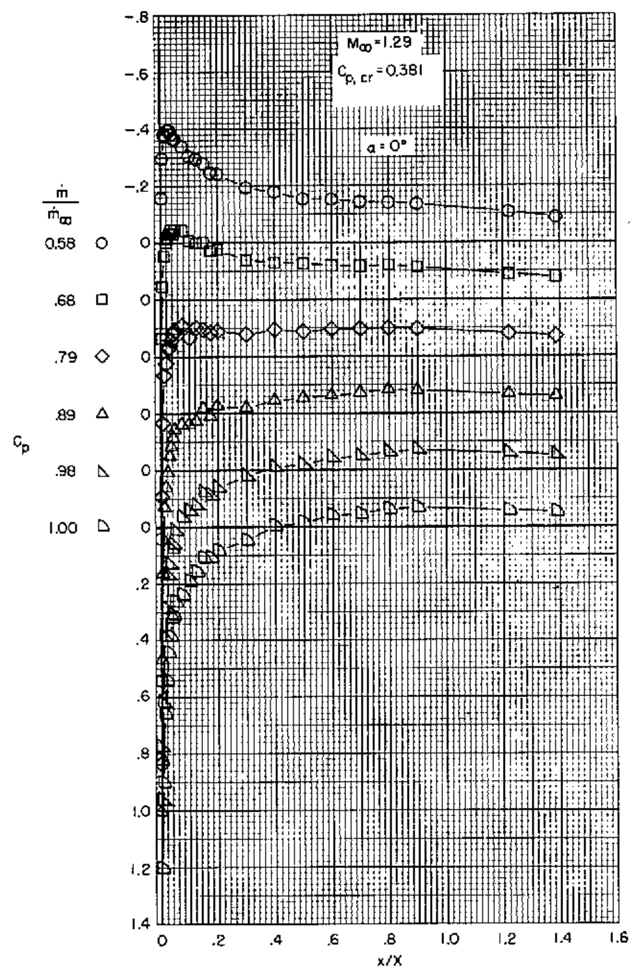

(h) $M_\infty = 1.29$.

Figure 12.- Concluded.

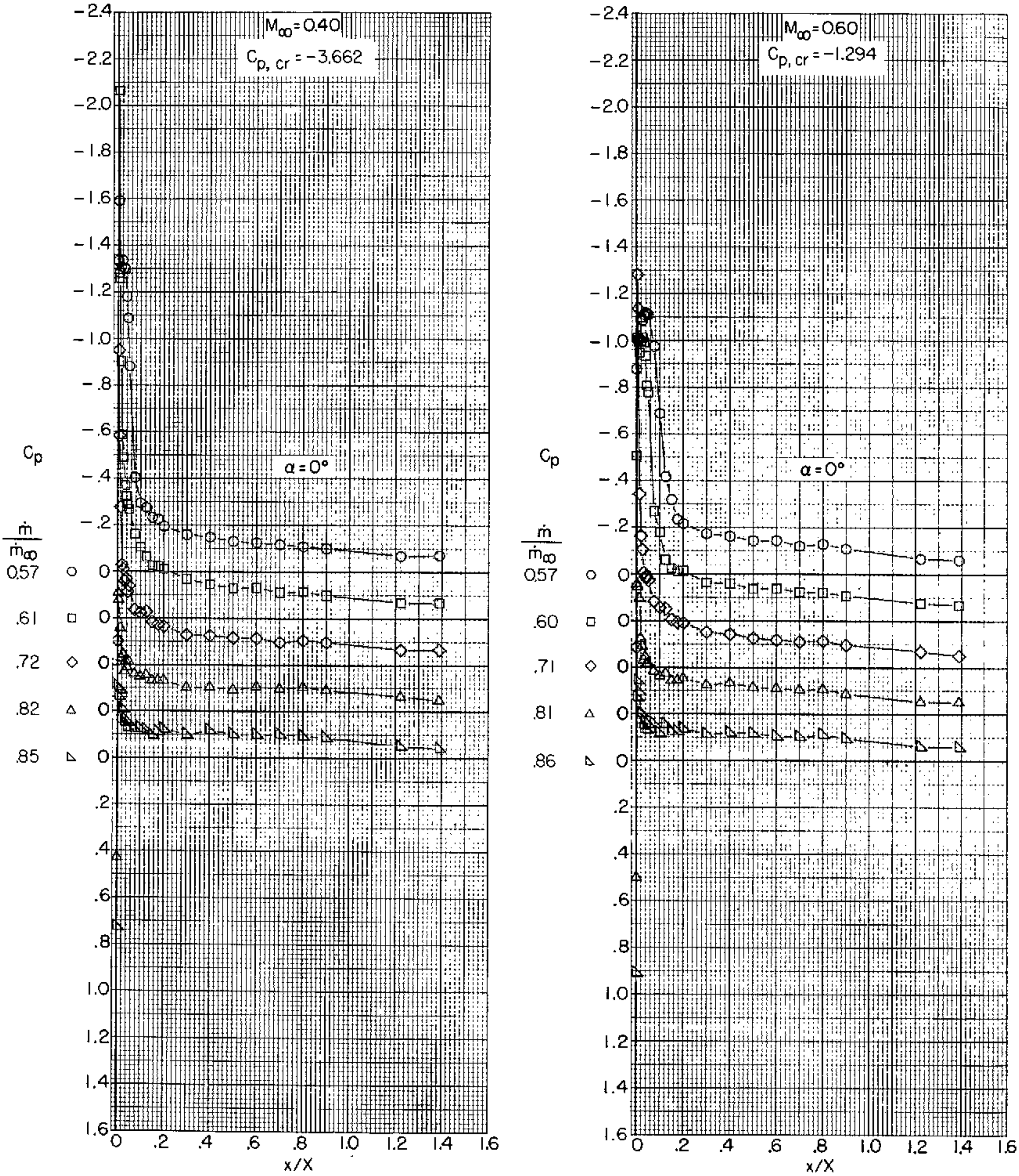

(a) $M_\infty = 0.40$ and 0.60.

Figure 13.- Variation with length of pressure coefficient over the outer profile of an NACA 1-85-100 (contraction ratio 1.046) inlet.

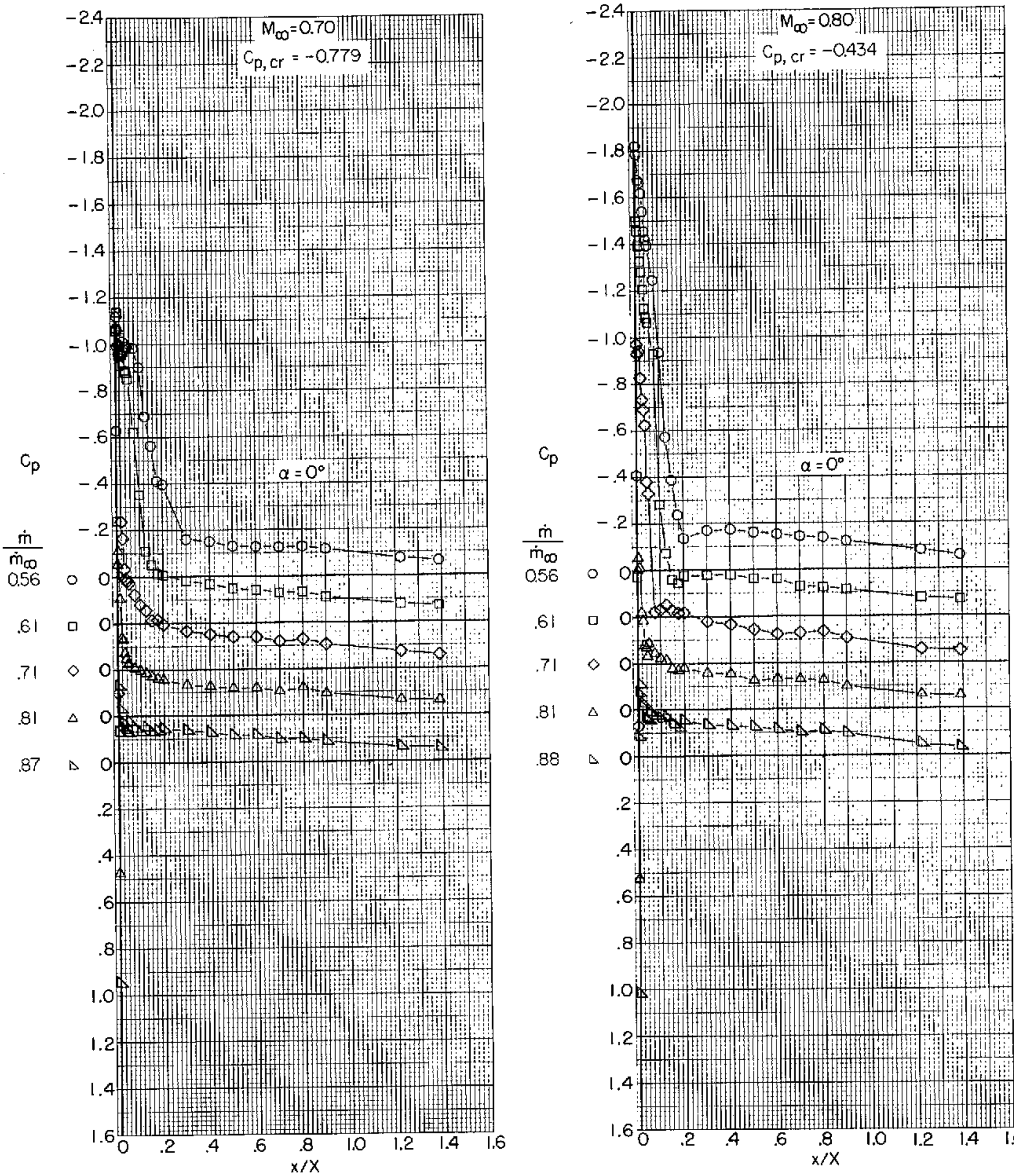

(b) M_∞ = 0.70 and 0.80.

Figure 13.- Continued.

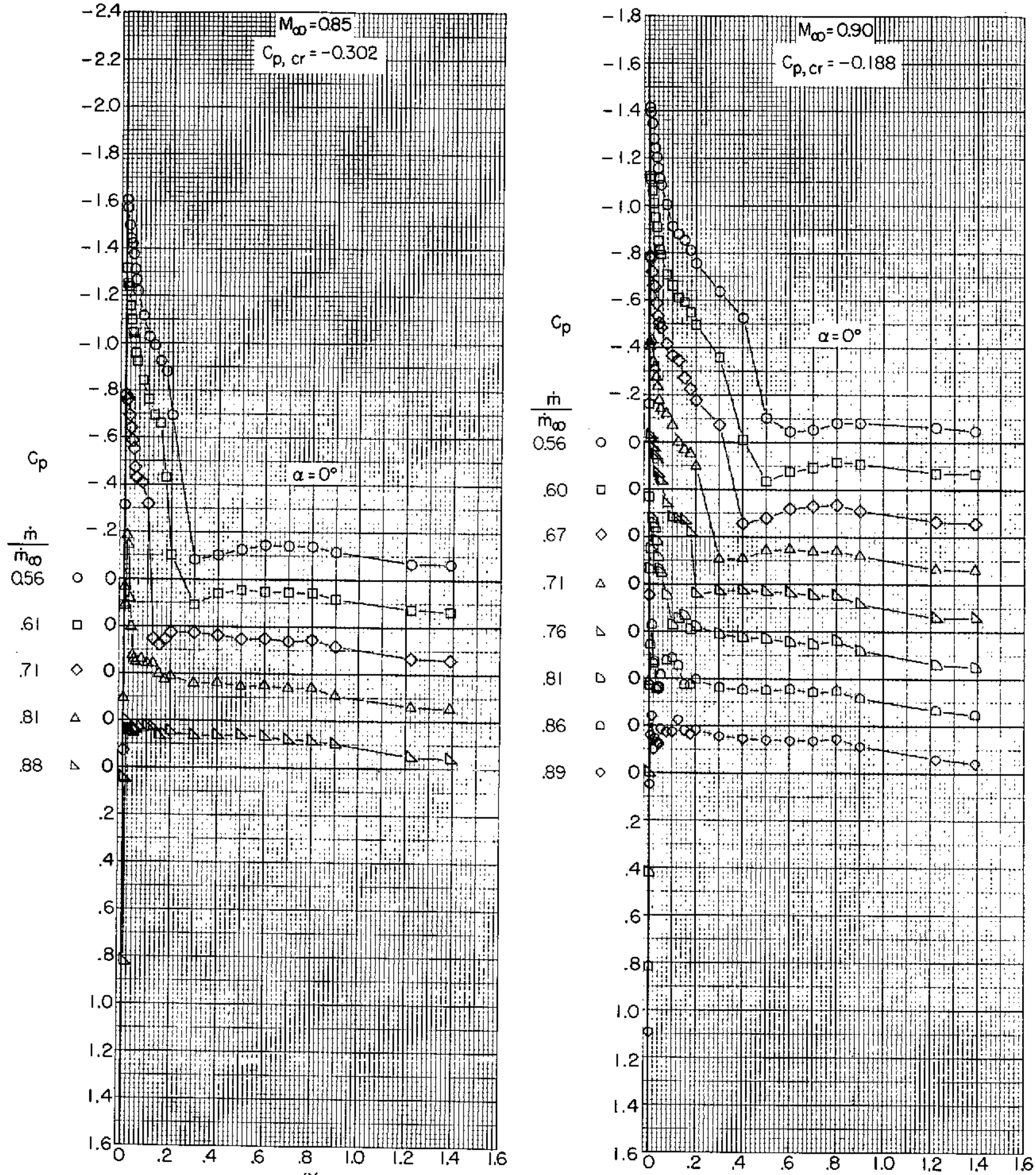

(c) M_∞ = 0.85 and 0.90.

Figure 13.- Continued.

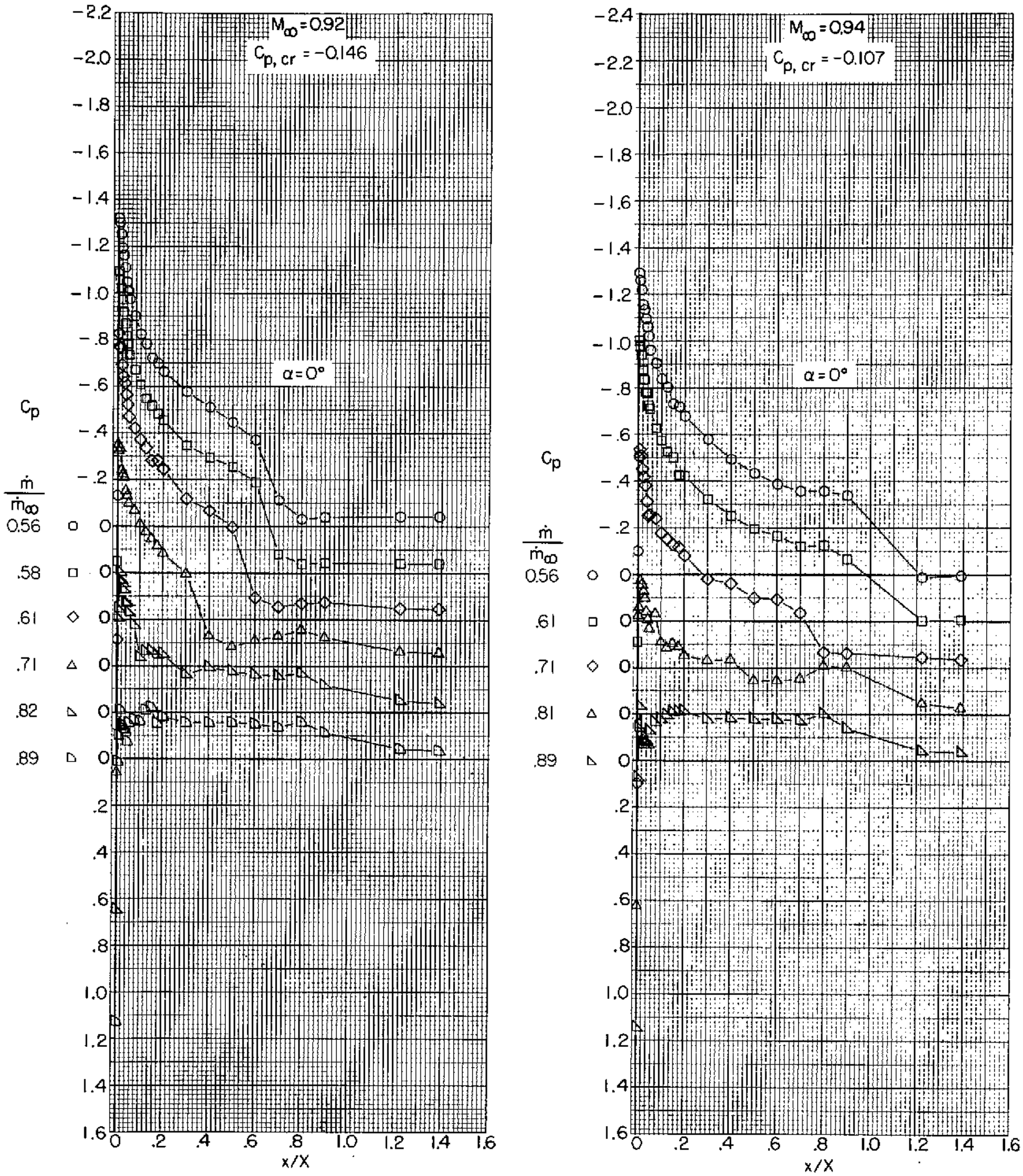

(d) M_∞ = 0.92 and 0.94.

Figure 13.- Continued.

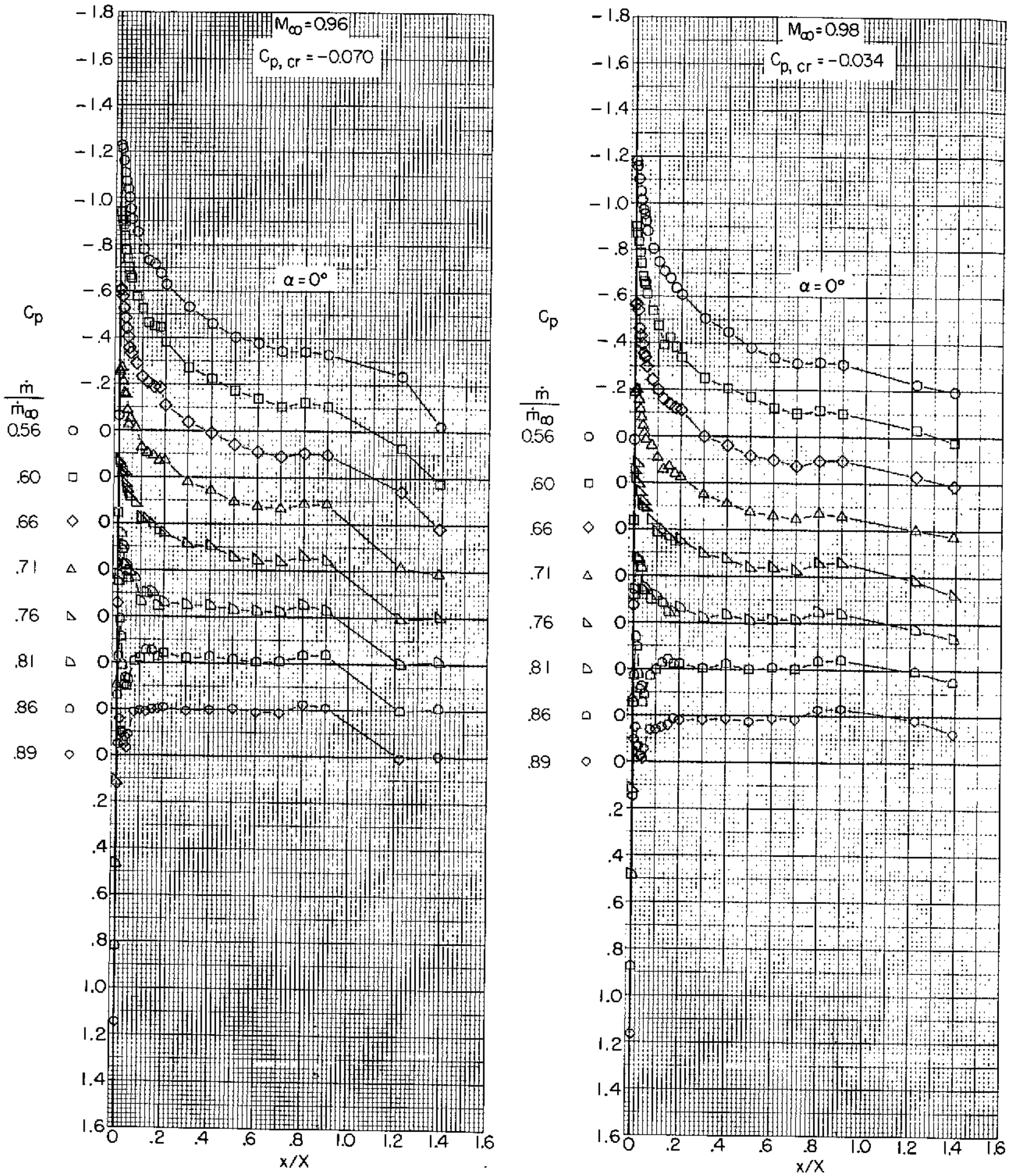

(e) M_∞ = 0.96 and 0.98.

Figure 13.- Continued.

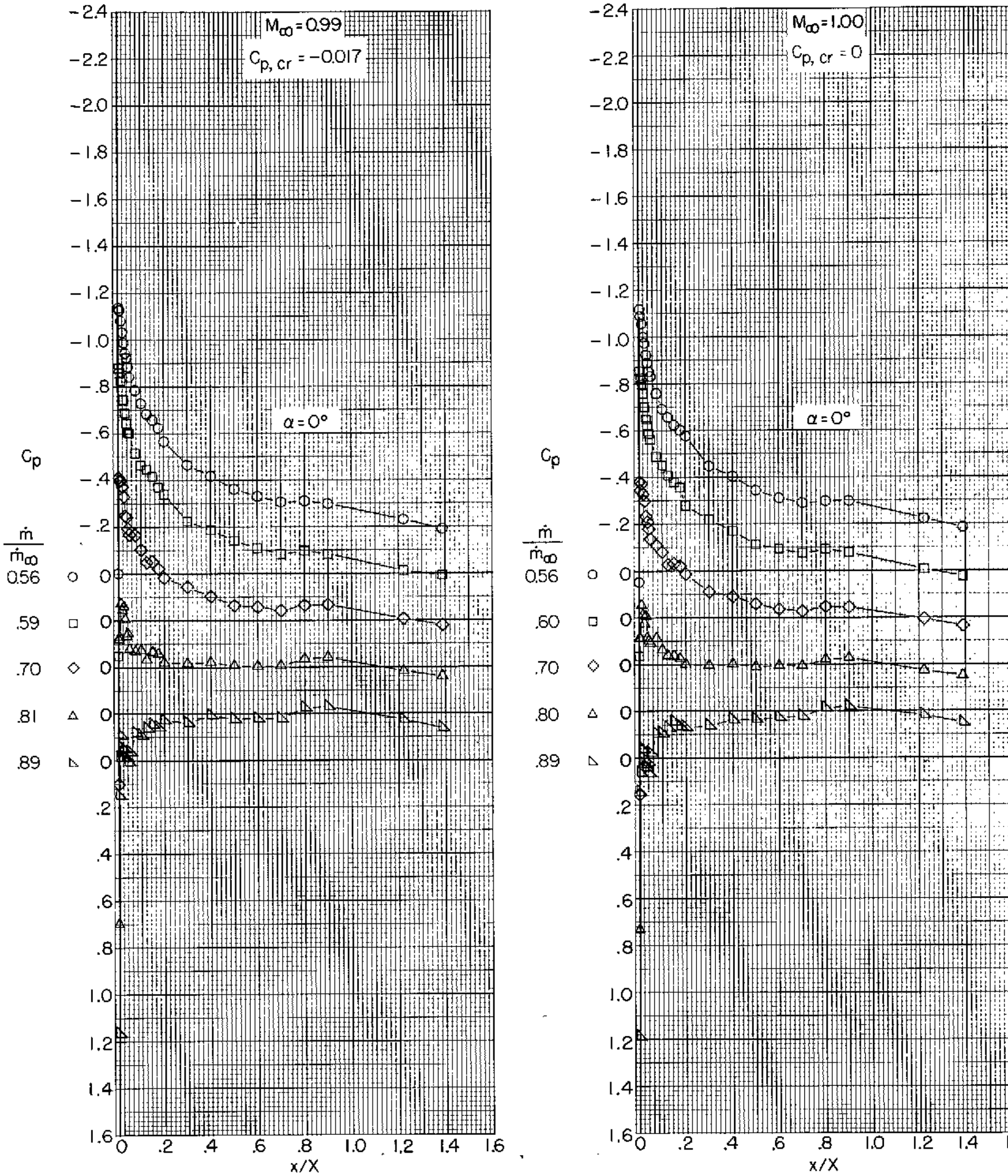

(f) M_∞ = 0.99 and 1.00.

Figure 13.- Continued.

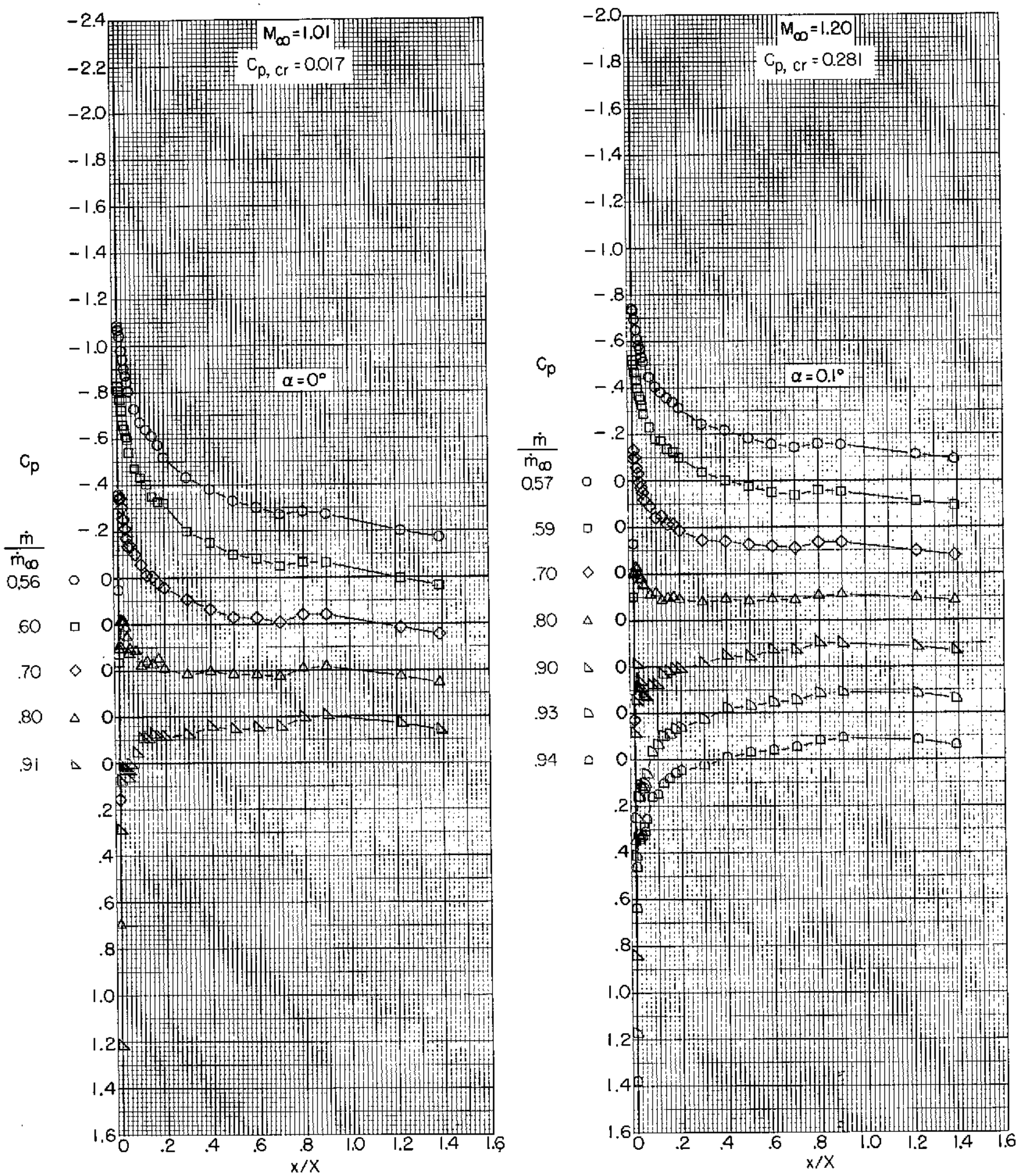

(g) M_∞ = 1.01 and 1.20.

Figure 13.- Continued.

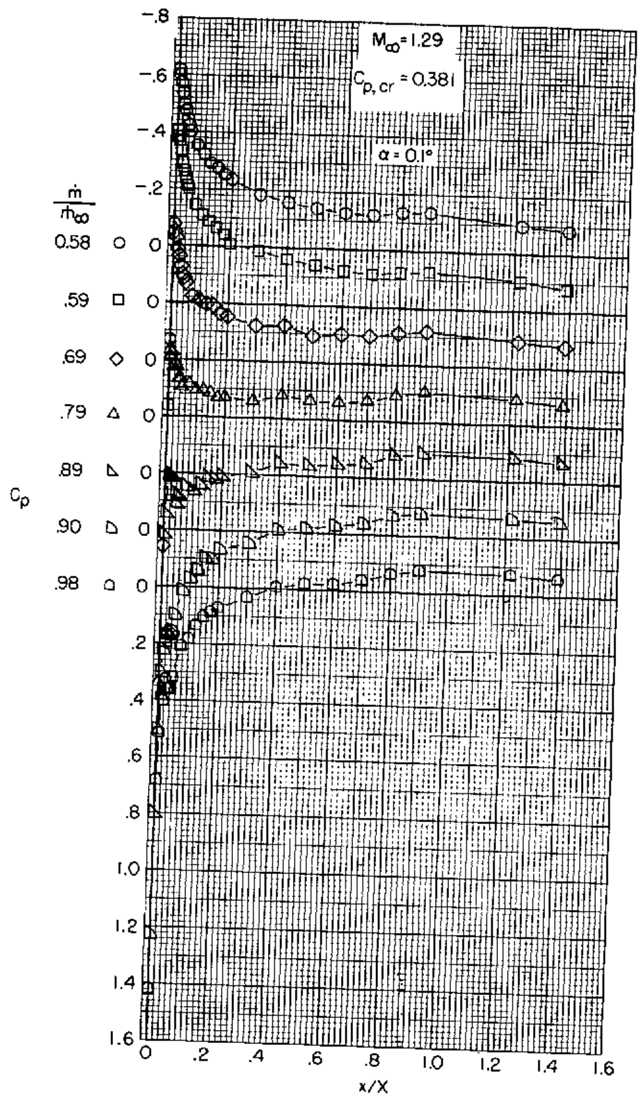

(h) $M_\infty = 1.29$.

Figure 13.- Concluded.

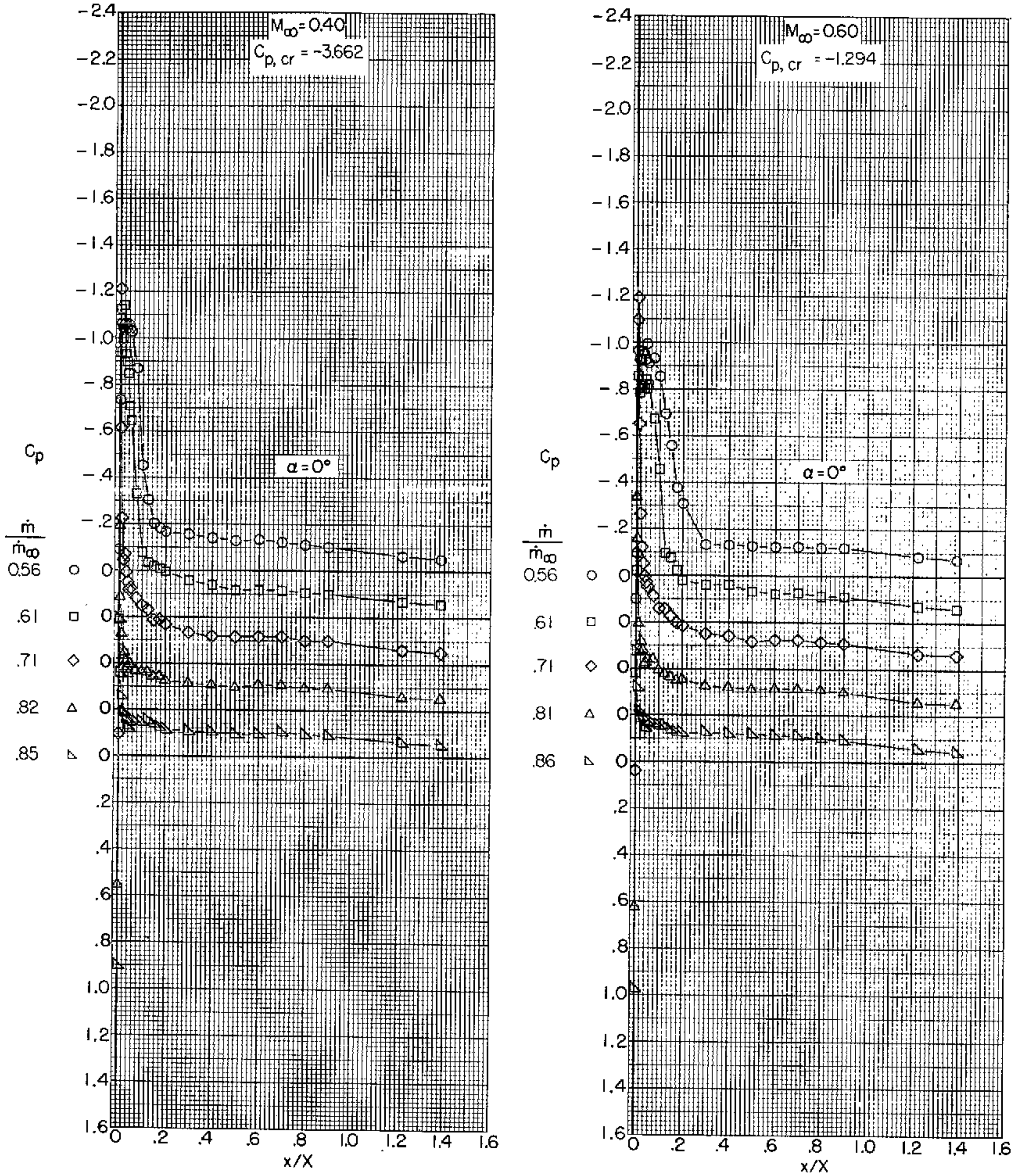

(a) $M_\infty = 0.40$ and 0.60.

Figure 14.- Variation with length of pressure coefficient over the outer profile of an NACA 1-85-100 (contraction ratio 1.093) inlet.

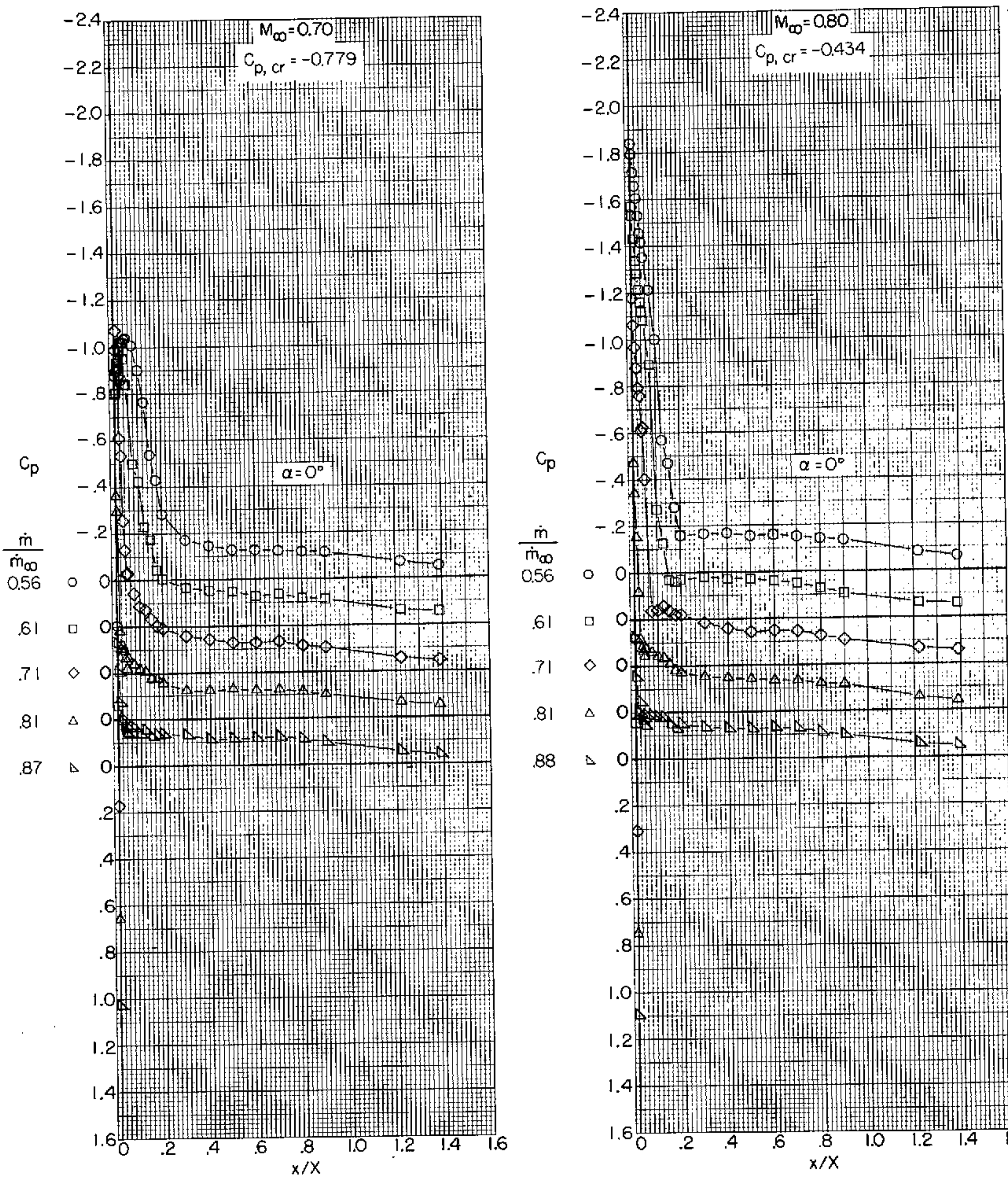

(b) M_∞ = 0.70 and 0.80.

Figure 14.- Continued.

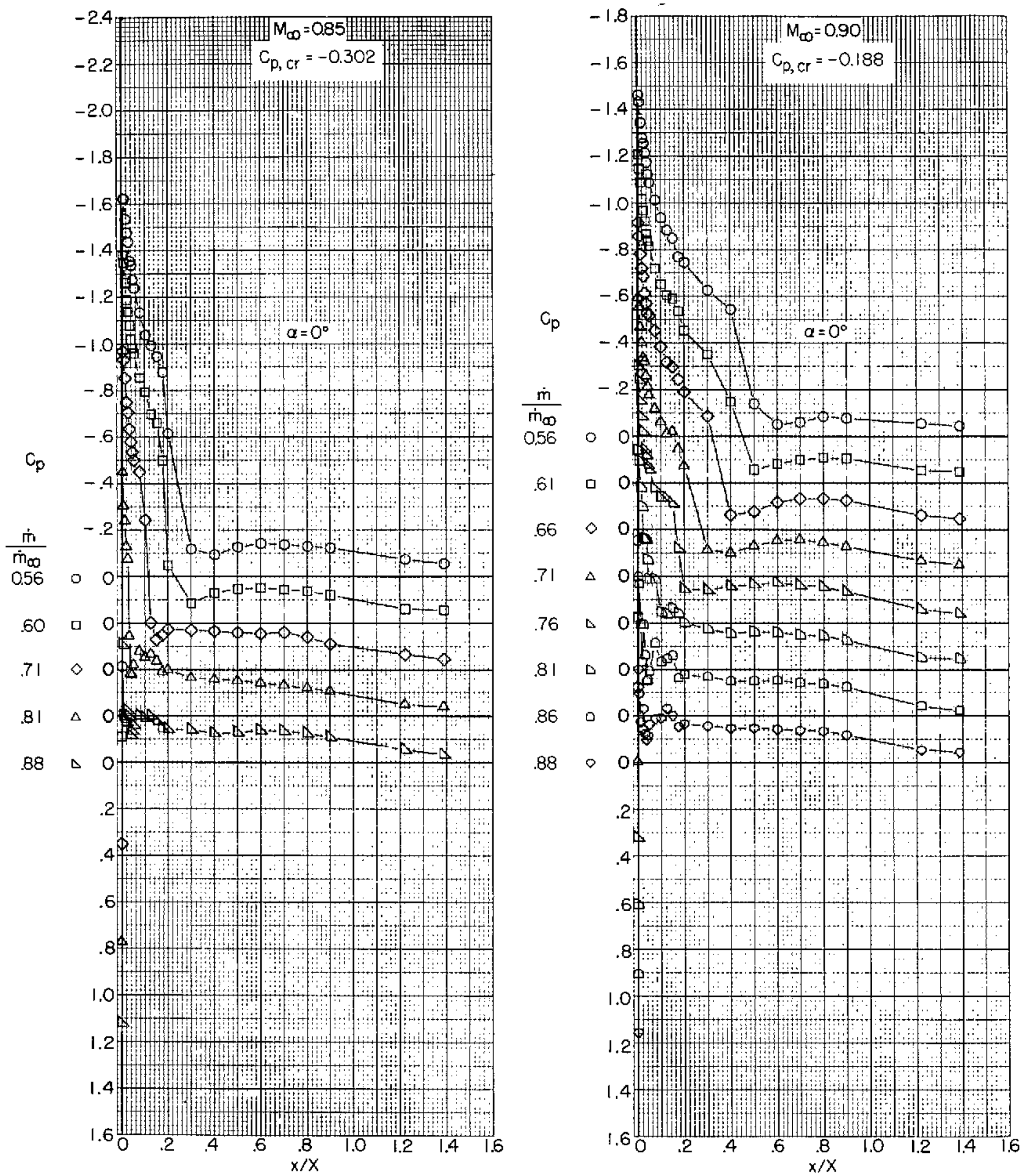

(c) M_∞ = 0.85 and 0.90.

Figure 14.- Continued.

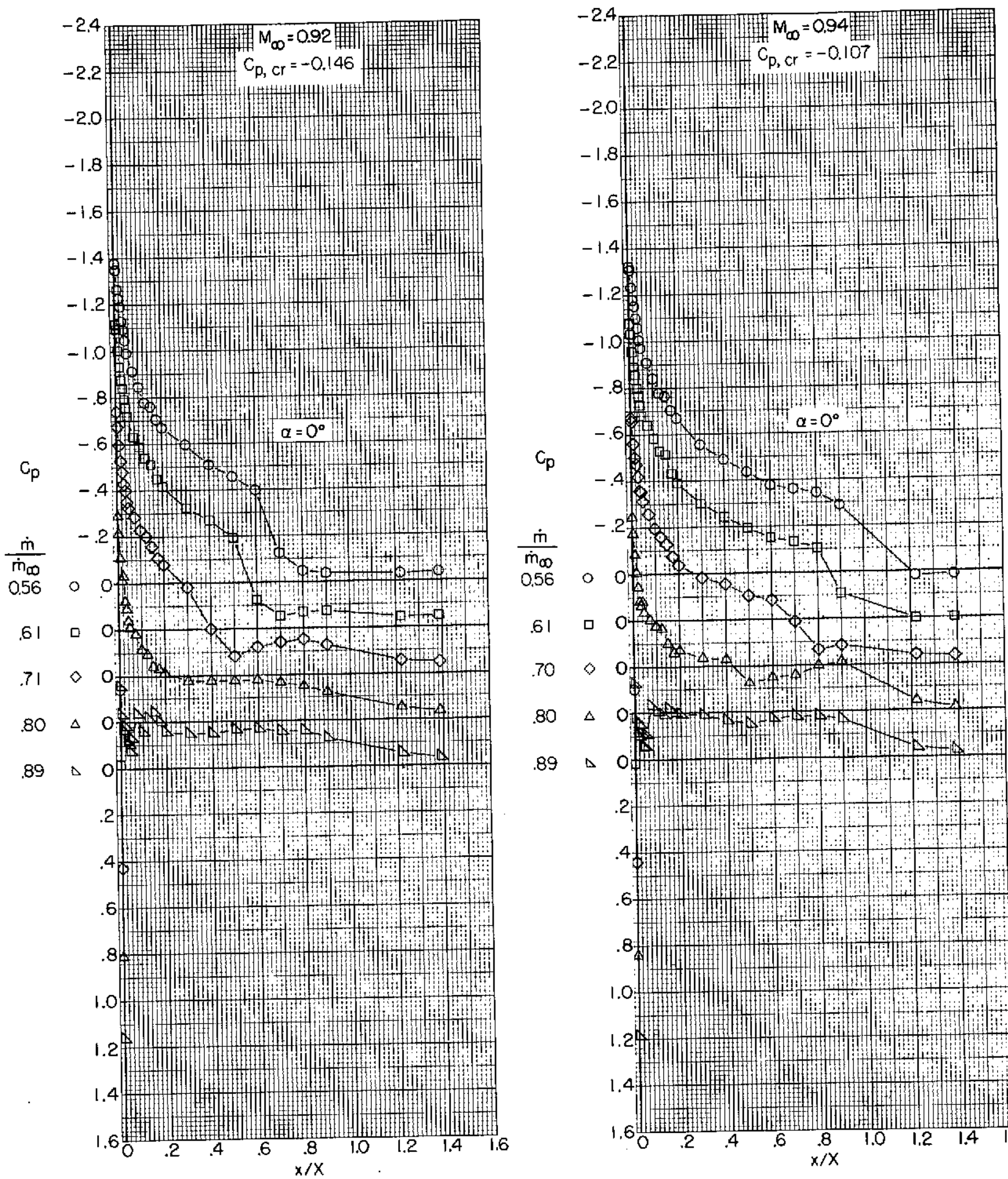

(d) $M_\infty = 0.92$ and 0.94.

Figure 14.- Continued.

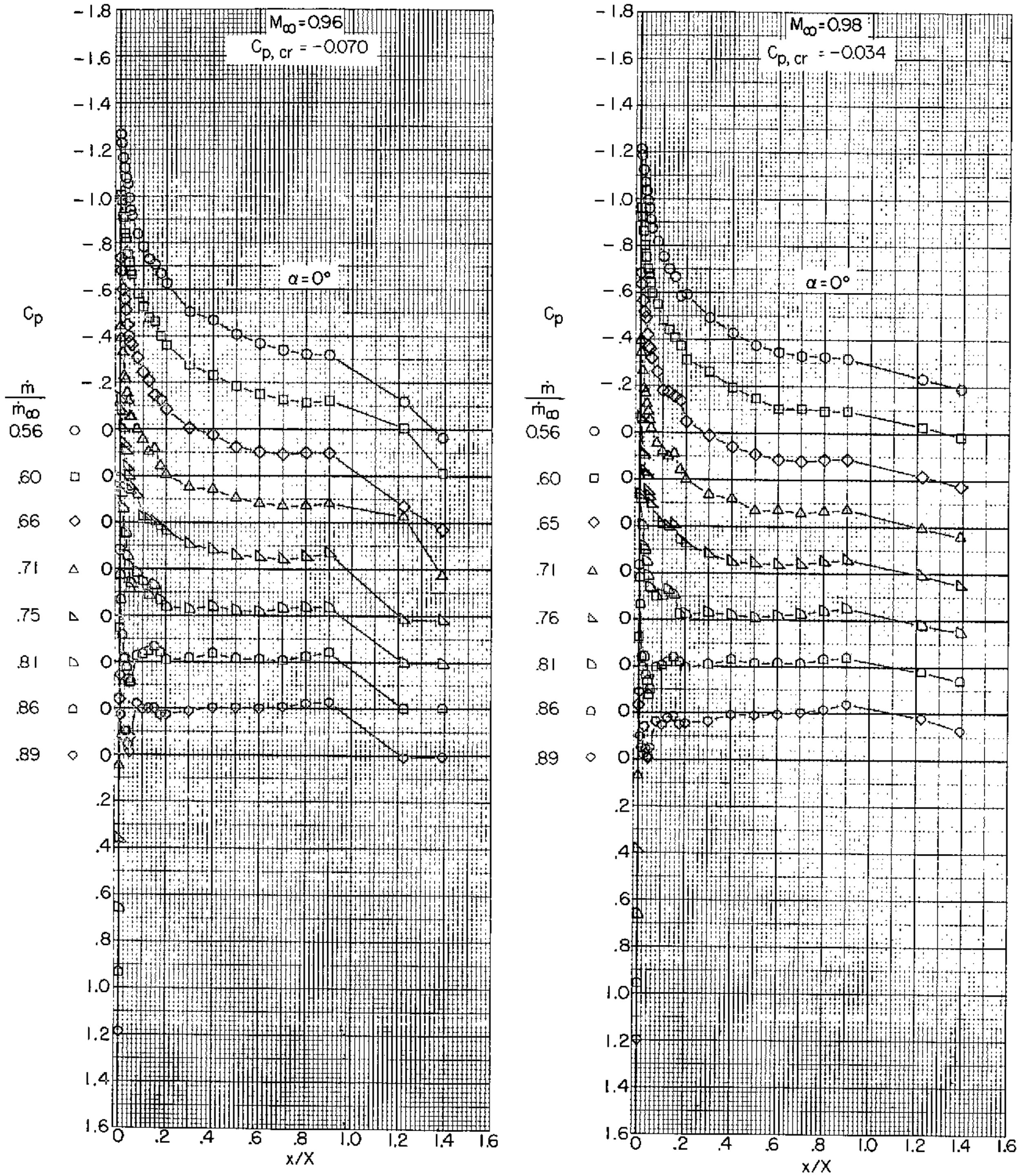

(e) $M_\infty = 0.96$ and 0.98.

Figure 14.- Continued.

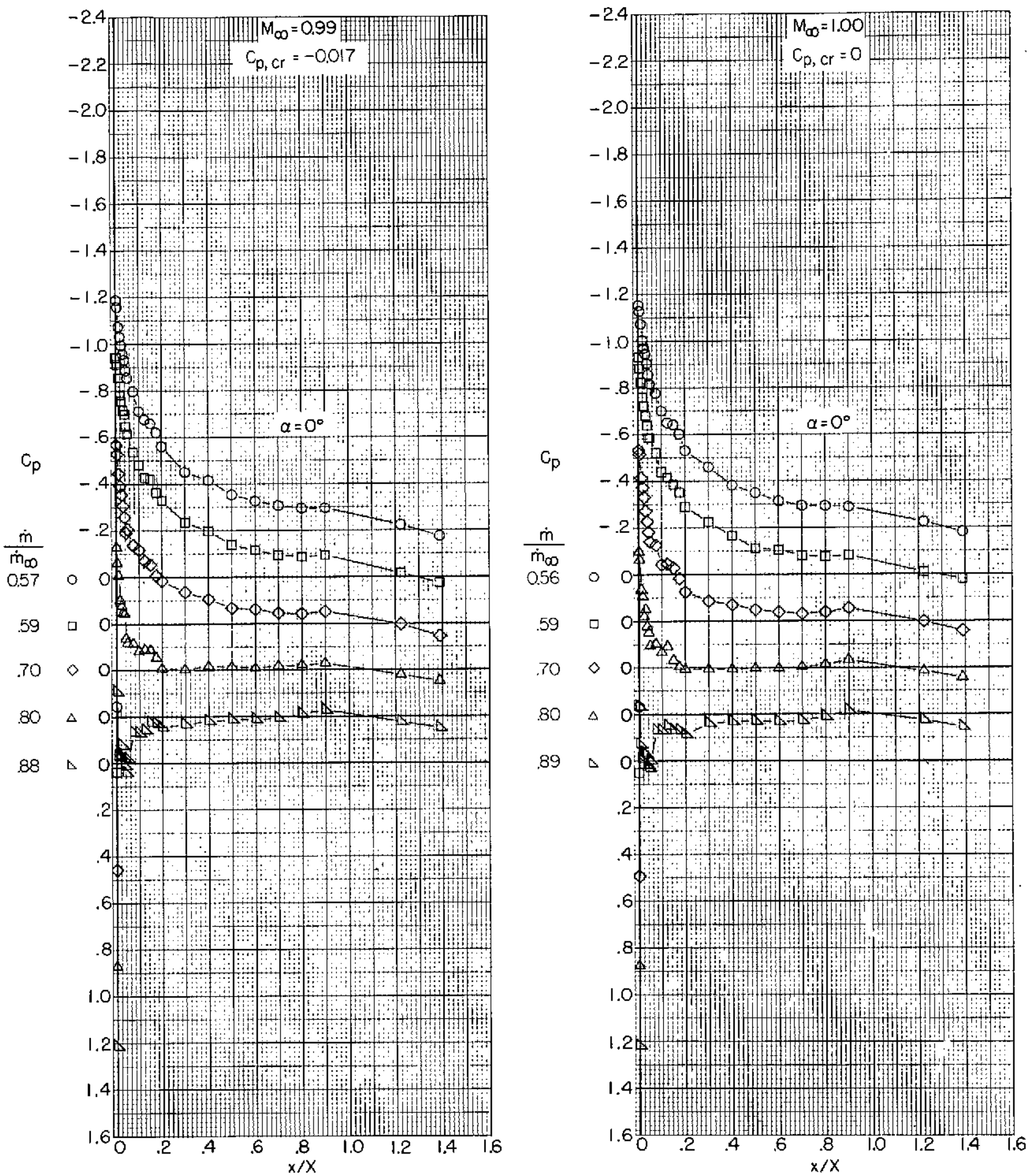

(f) M_∞ = 0.99 and 1.00.

Figure 14.- Continued.

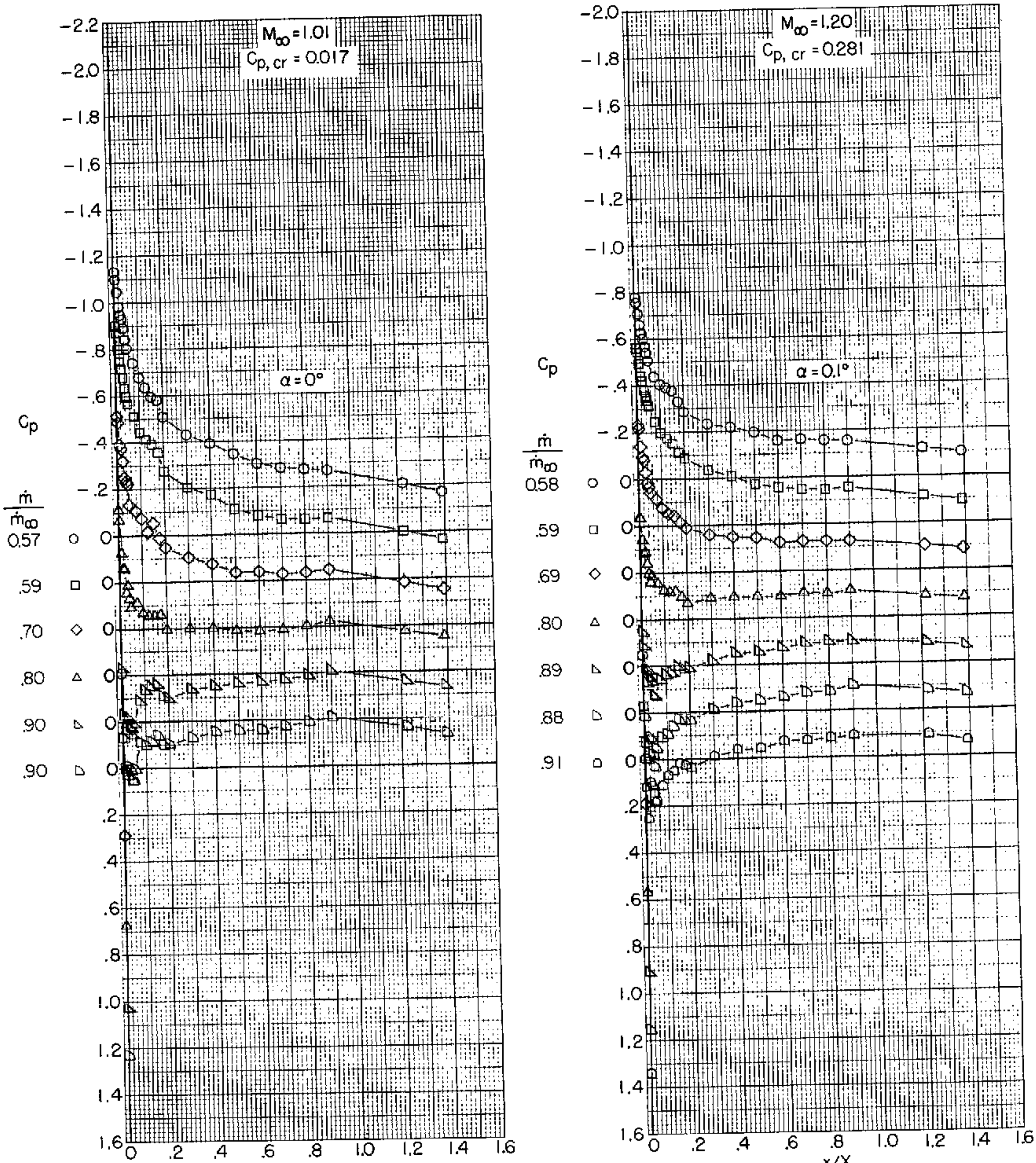

(g) M_∞ = 1.01 and 1.20.

Figure 14.- Continued.

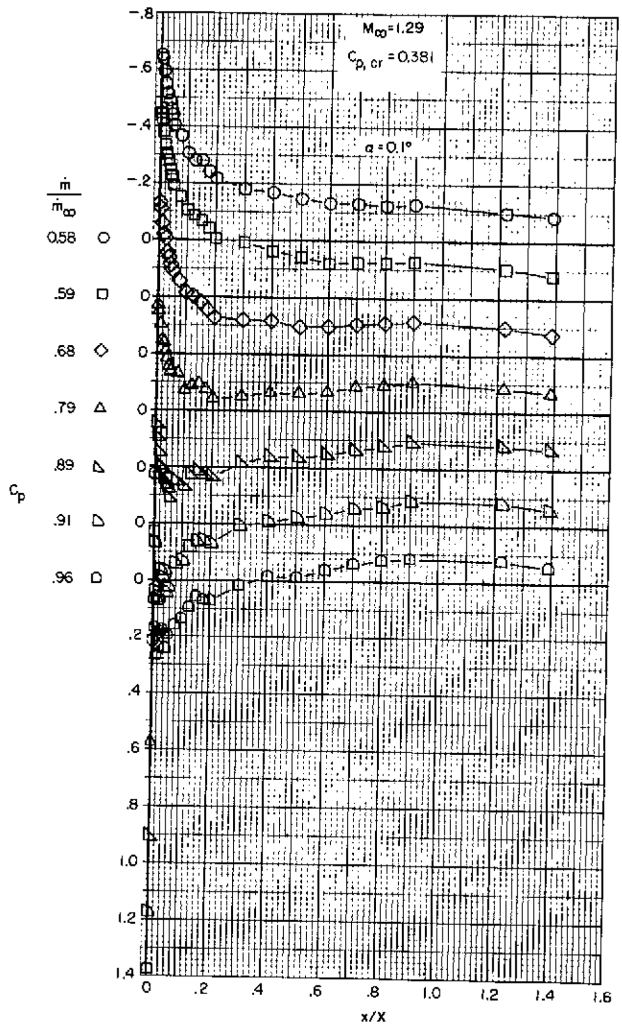

(h) $M_\infty = 1.29$.

Figure 14.- Concluded.

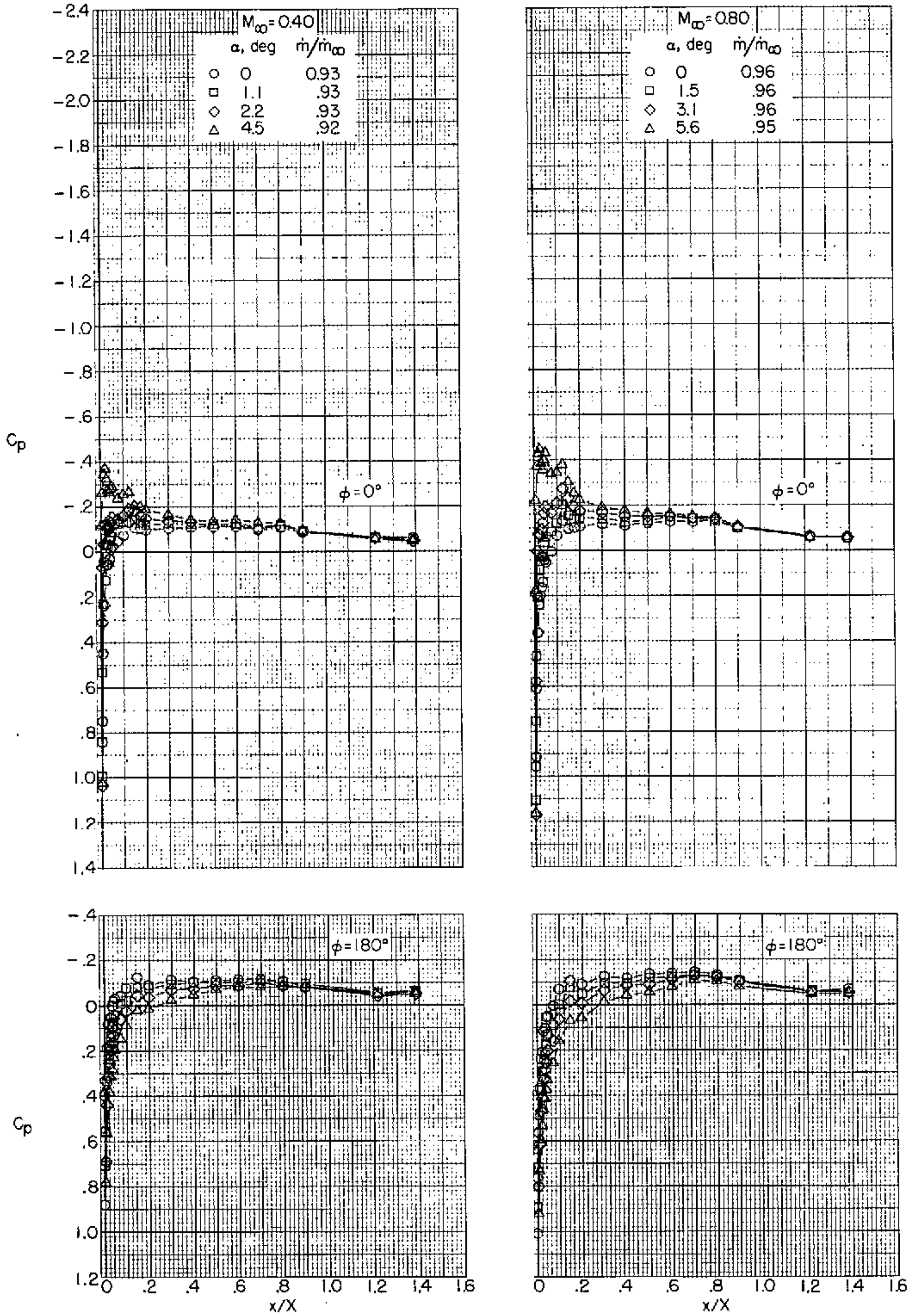

(a) M_∞ = 0.40 and 0.80.

Figure 15.- Variation with length of pressure coefficient on top and bottom of an NACA 1-81-100 (contraction ratio 1.012) inlet at several angles of attack.

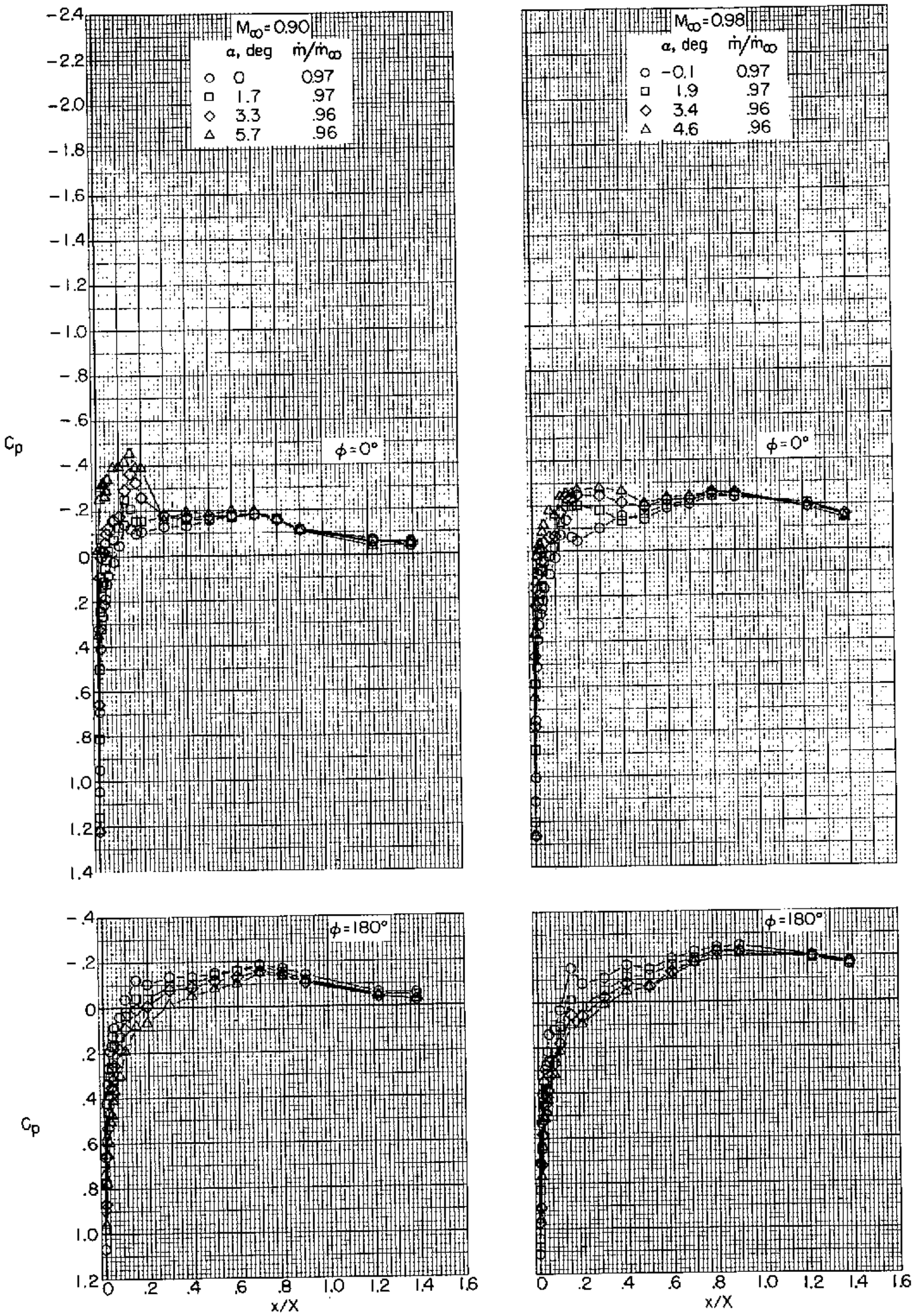

(b) M_∞ = 0.90 and 0.98.

Figure 15.- Concluded.

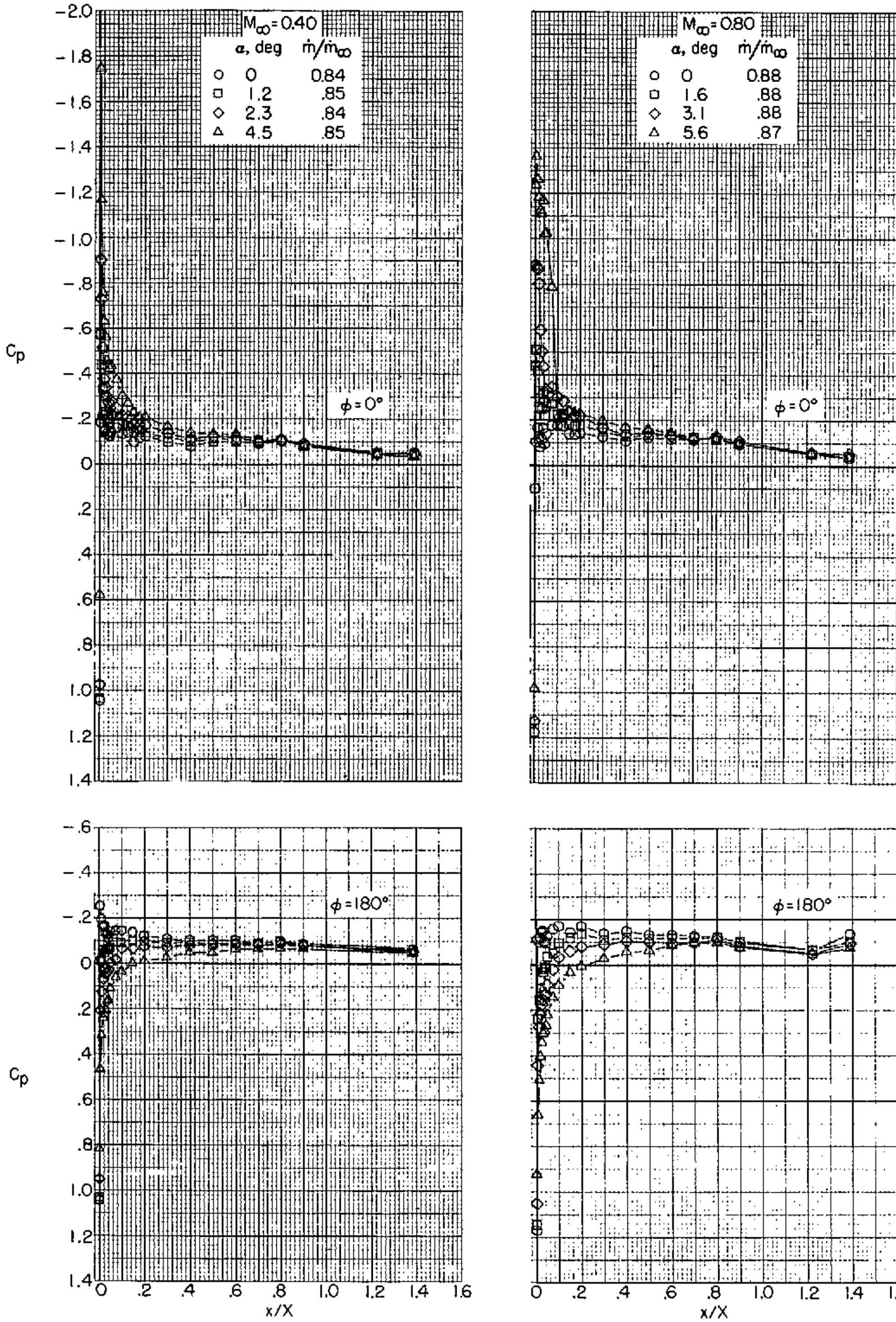

(a) M_∞ = 0.40 and 0.80.

Figure 16.- Variation with length of pressure coefficient on top and bottom of an NACA 1-85-100 (contraction ratio 1.009) inlet at several angles of attack.

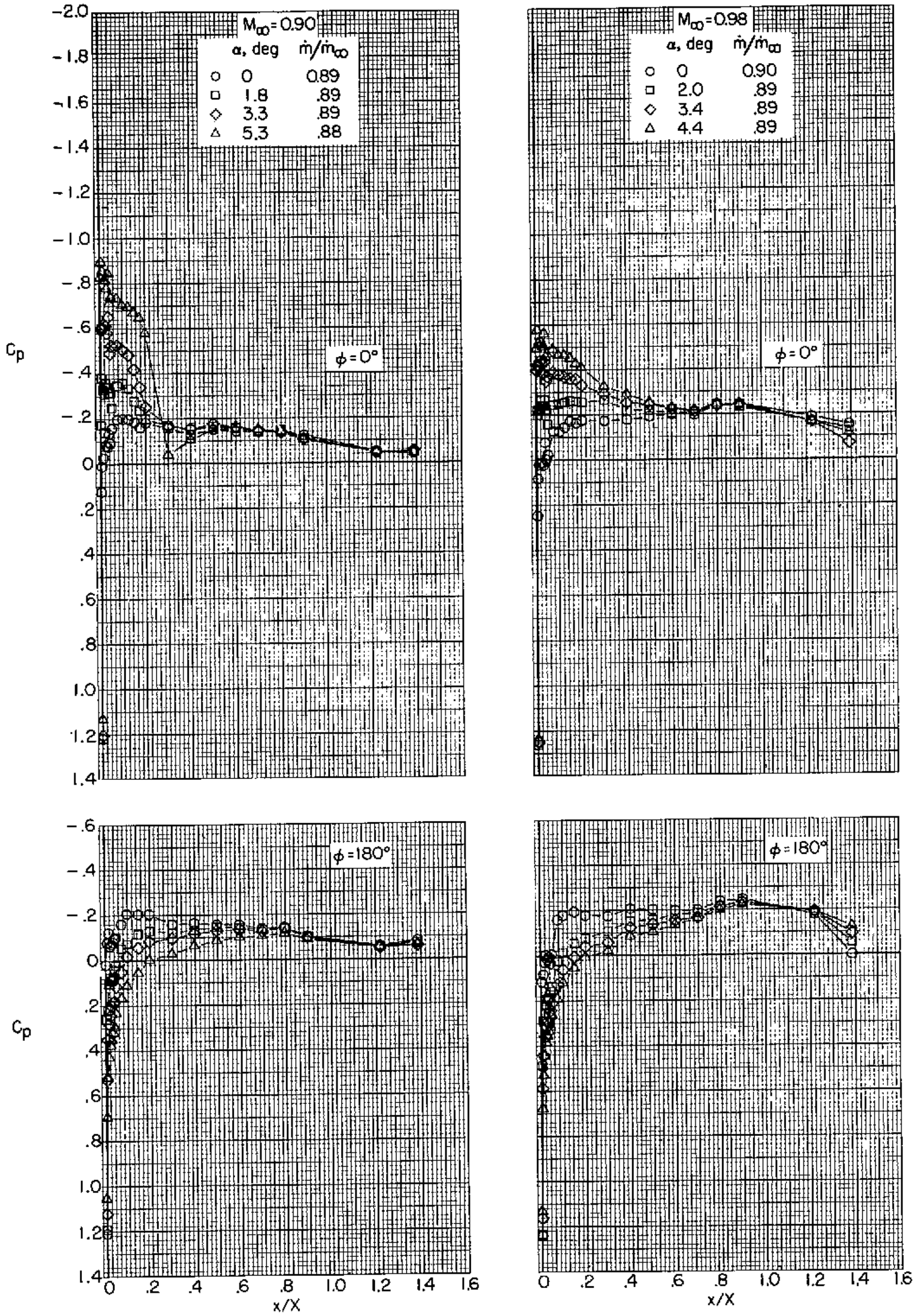

(b) M_∞ = 0.90 and 0.98.

Figure 16.- Concluded.

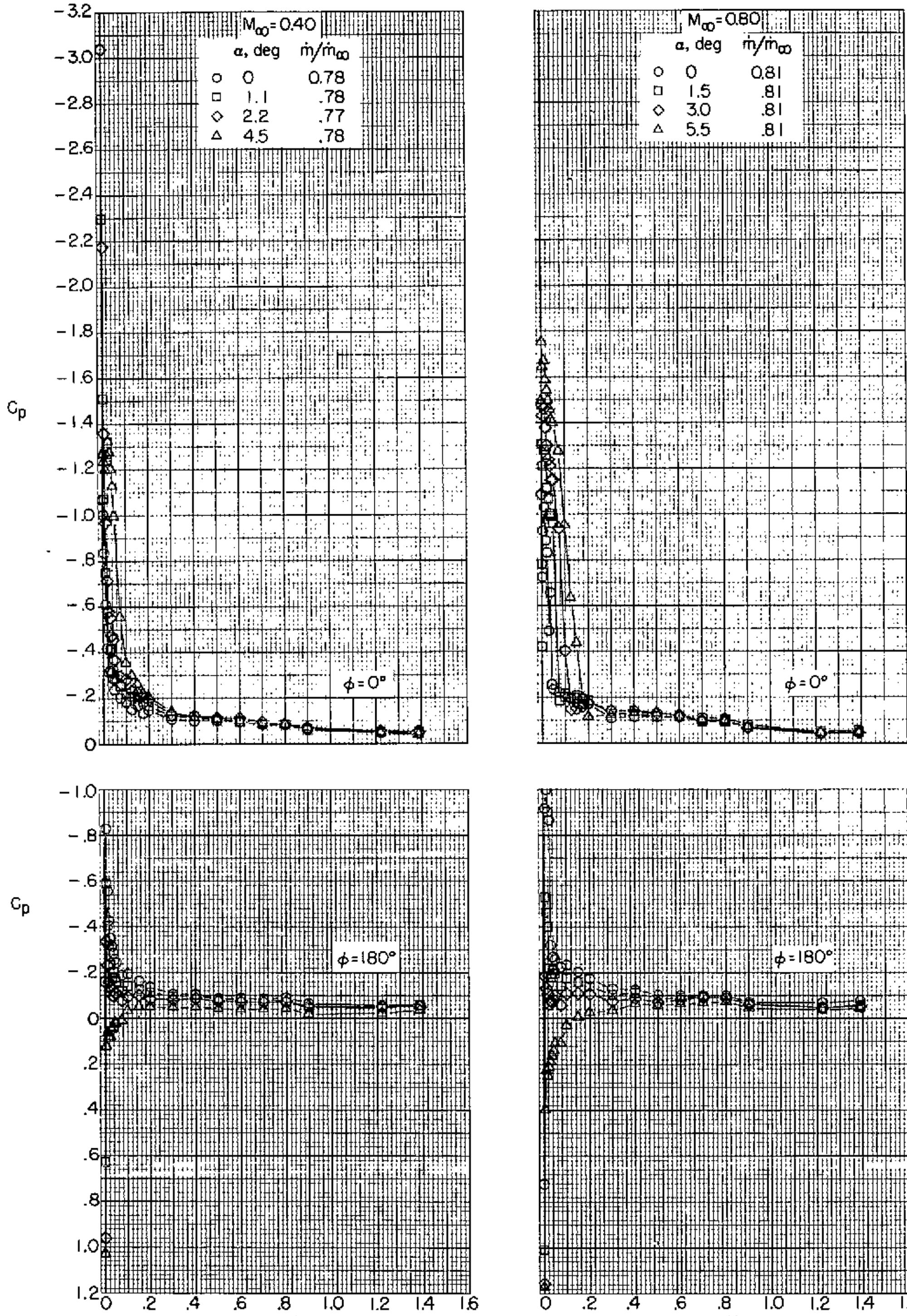

(a) M_∞ = 0.40 and 0.80.

Figure 17.- Variation with length of pressure coefficient on top and bottom of an NACA 1-89-100 (contraction ratio 1.006) inlet at several angles of attack.

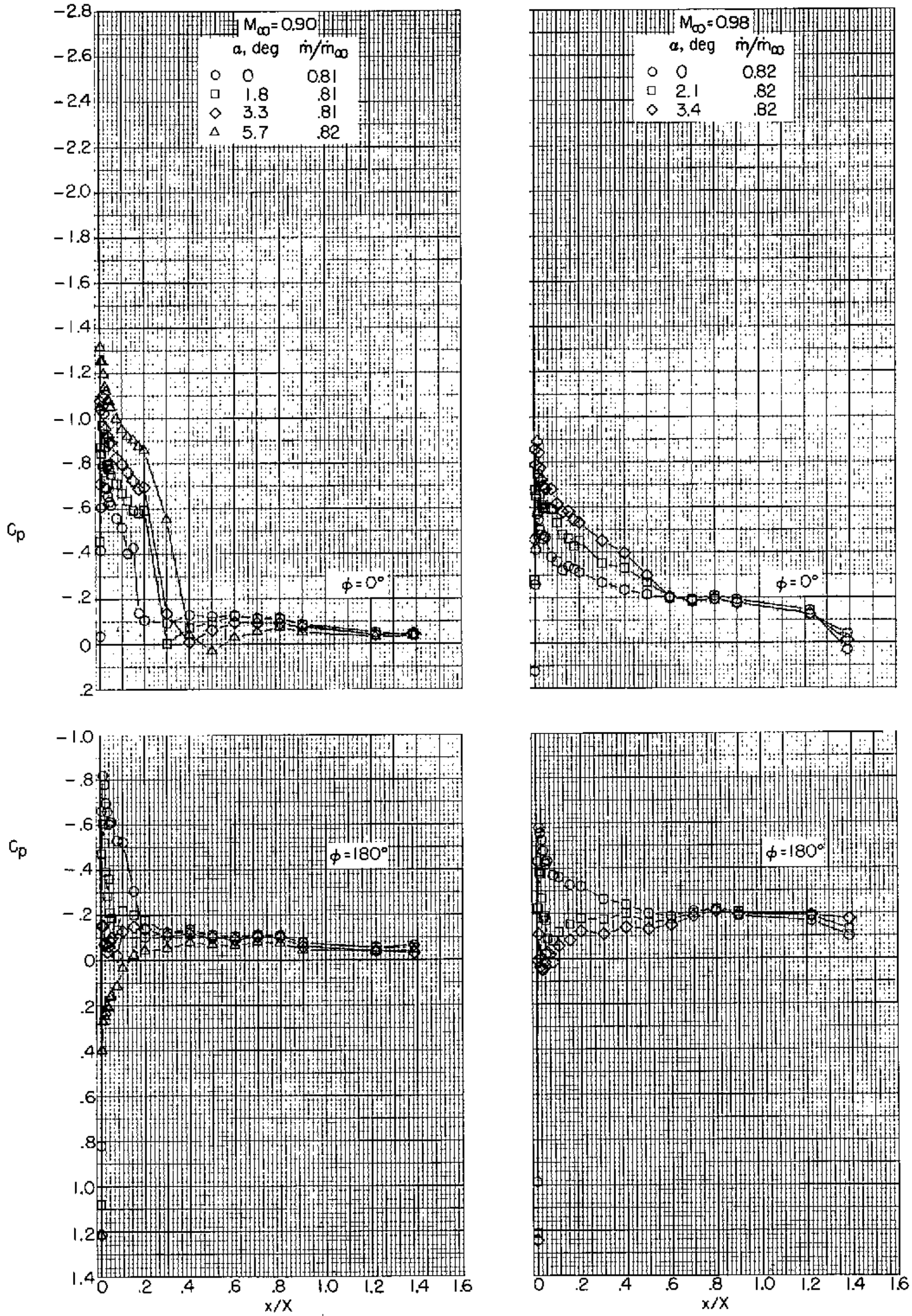

(b) M_∞ = 0.90 and 0.98.

Figure 17.- Concluded.

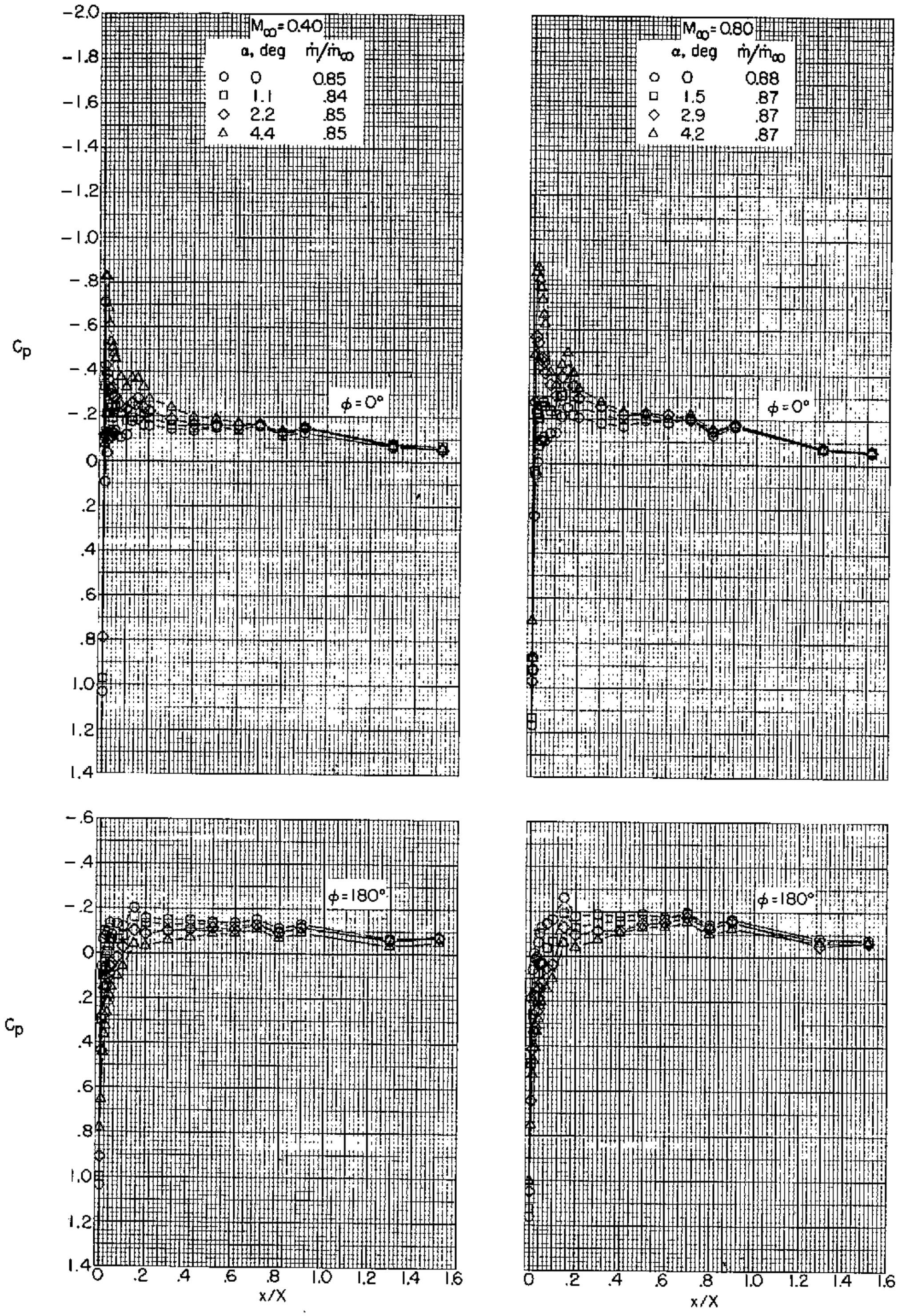

(a) M_∞ = 0.40 and 0.80.

Figure 18.- Variation with length of pressure coefficient on top and bottom of an NACA 1-85-75 (contraction ratio 1.009) inlet at several angles of attack.

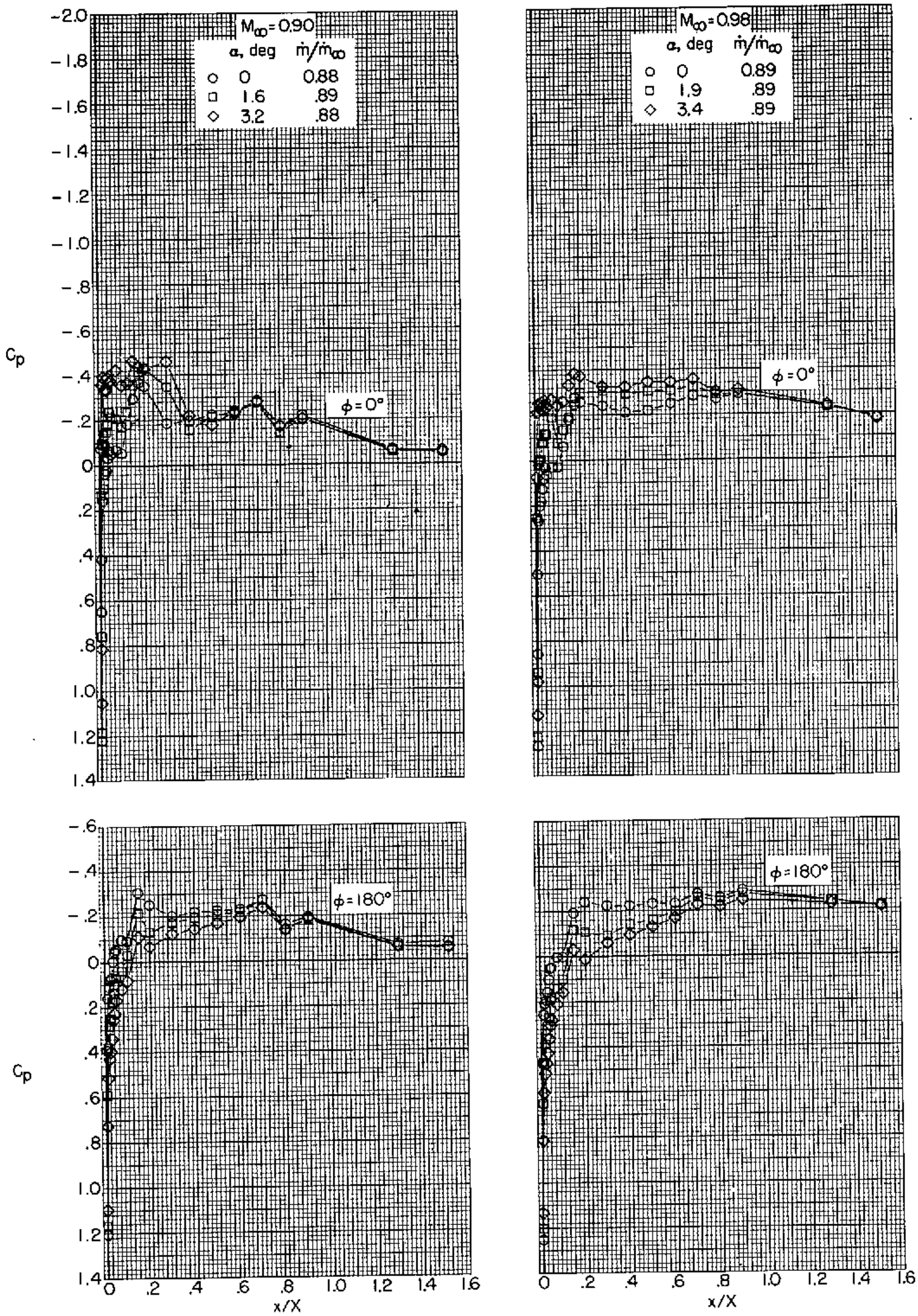

(b) M_∞ = 0.90 and 0.98.

Figure 18.- Concluded.

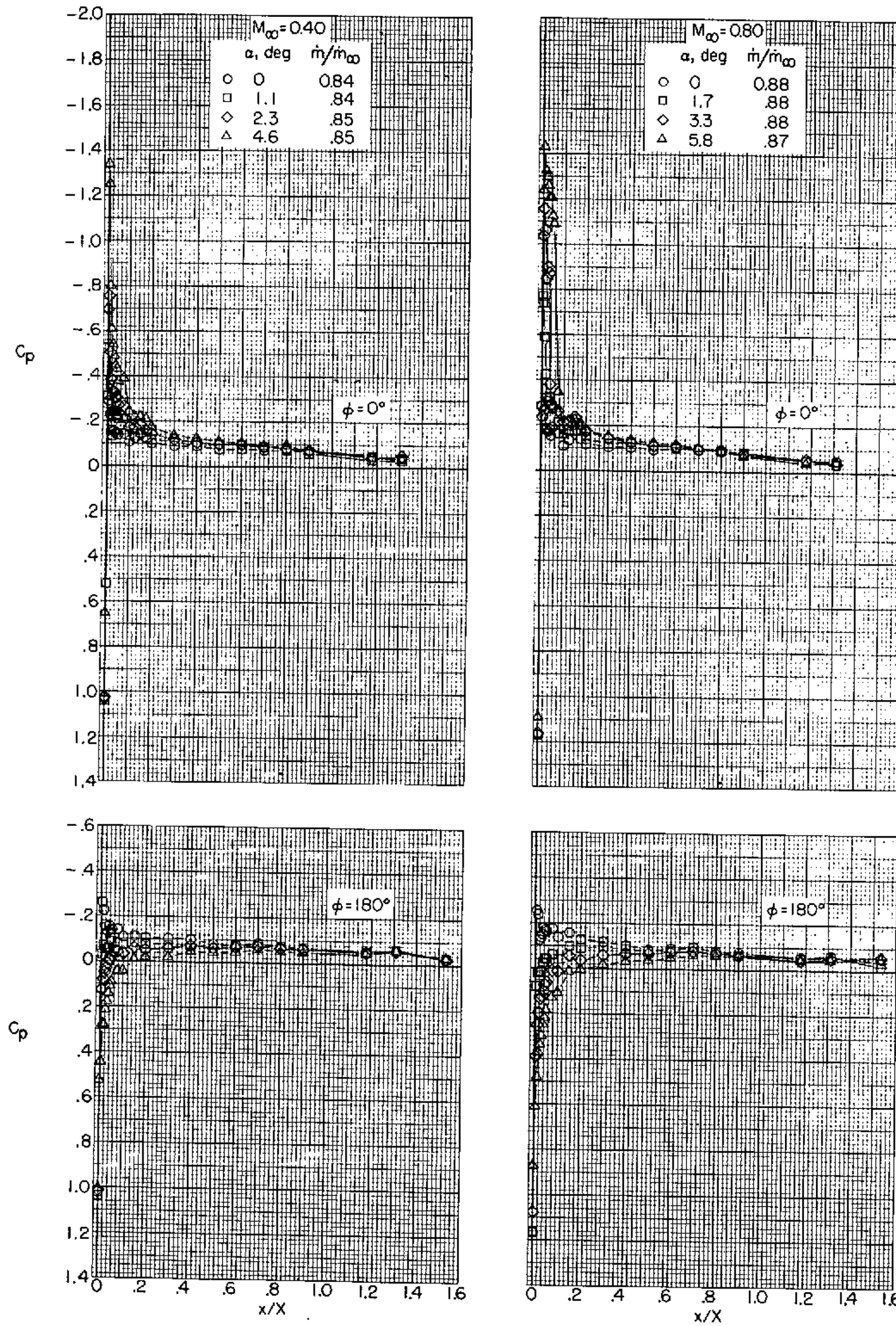

(a) $M_\infty = 0.40$ and 0.80.

Figure 19.- Variation with length of pressure coefficient on top and bottom of an NACA 1-85-125 (contraction ratio 1.009) inlet at several angles of attack.

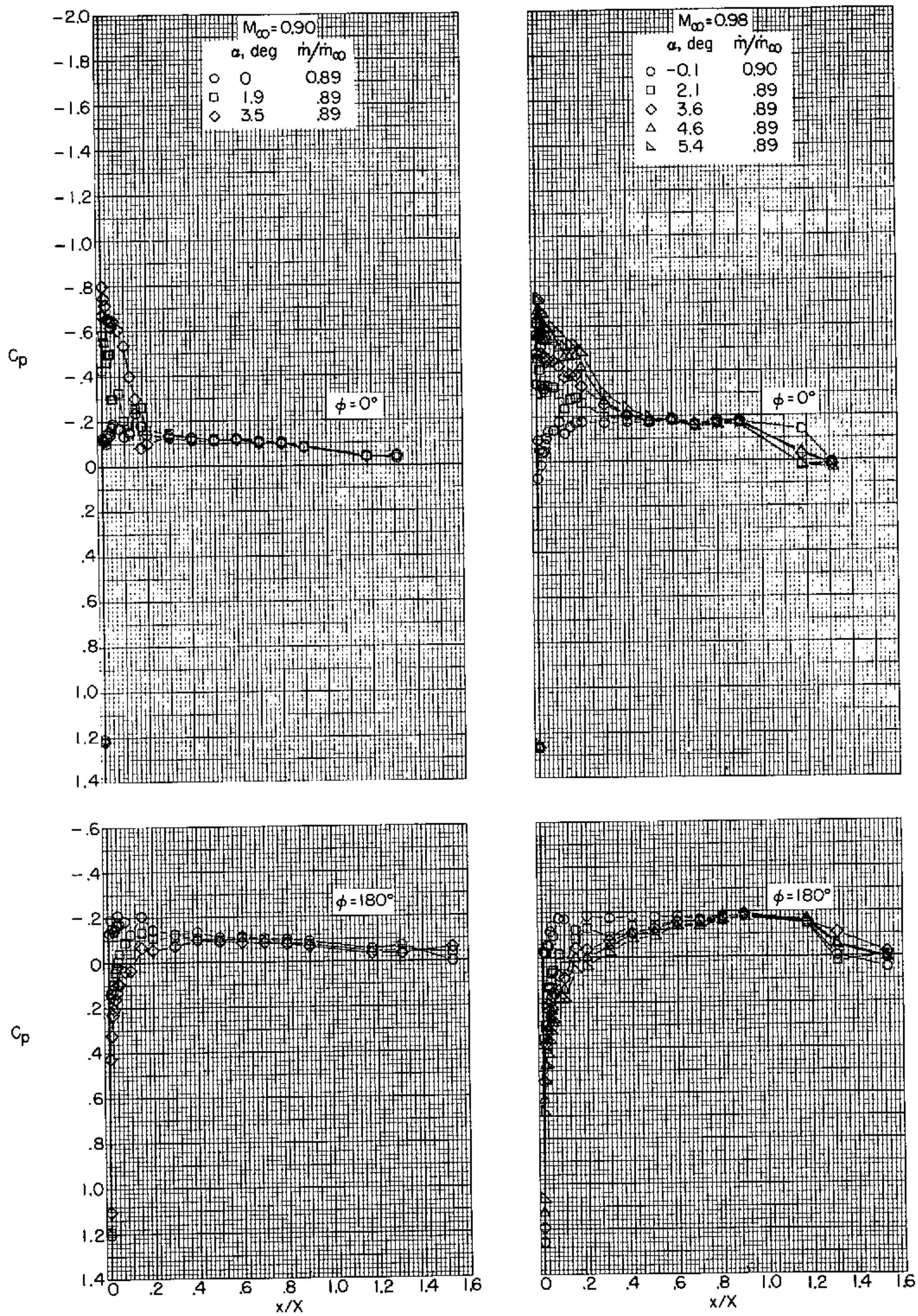

(b) M_∞ = 0.90 and 0.98.

Figure 19.- Concluded.

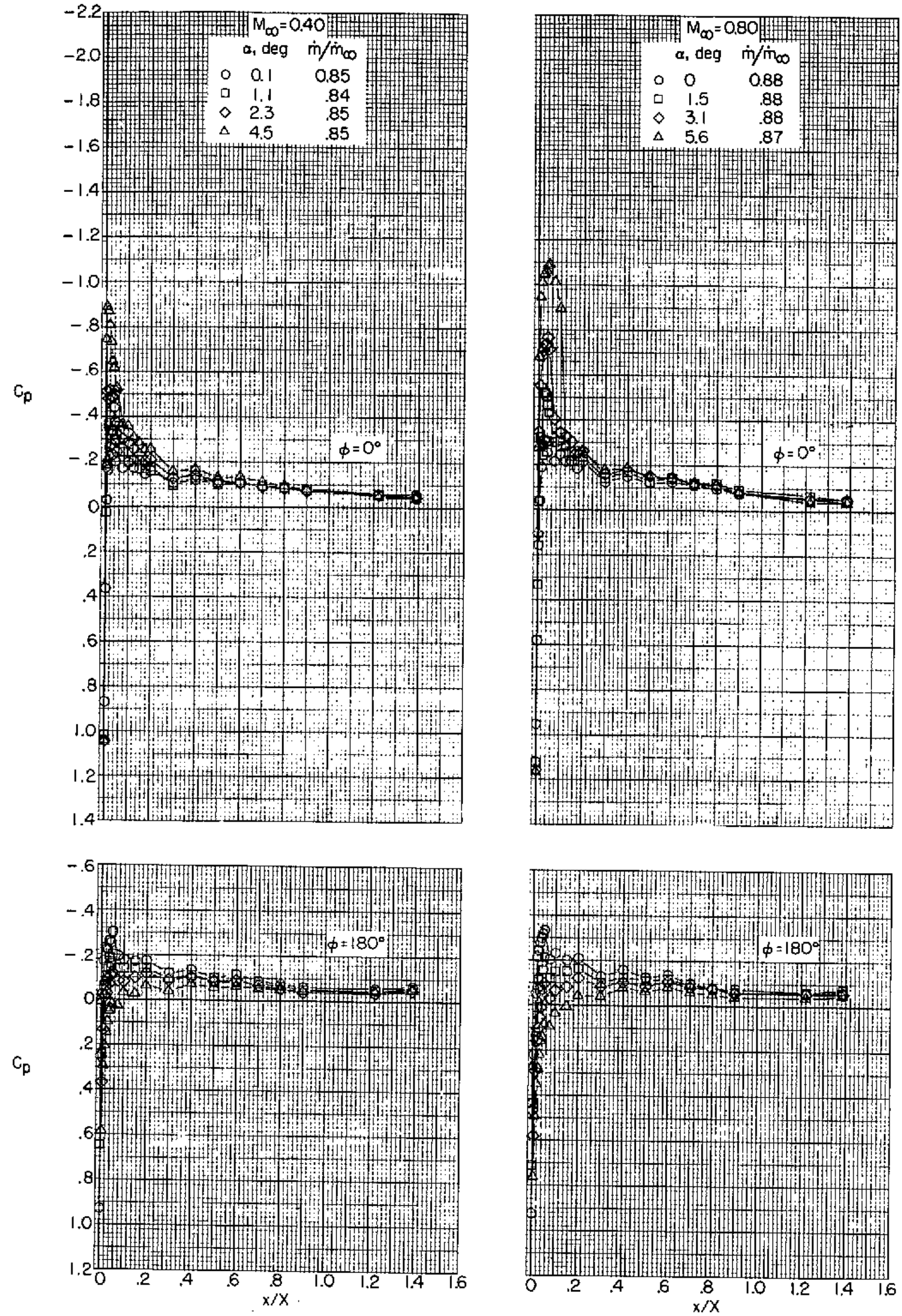

(a) M_∞ = 0.40 and 0.80.

Figure 20.- Variation with length of pressure coefficient on top and bottom of an Elliptical-85-100 (contraction ratio 1.009) inlet at several angles of attack.

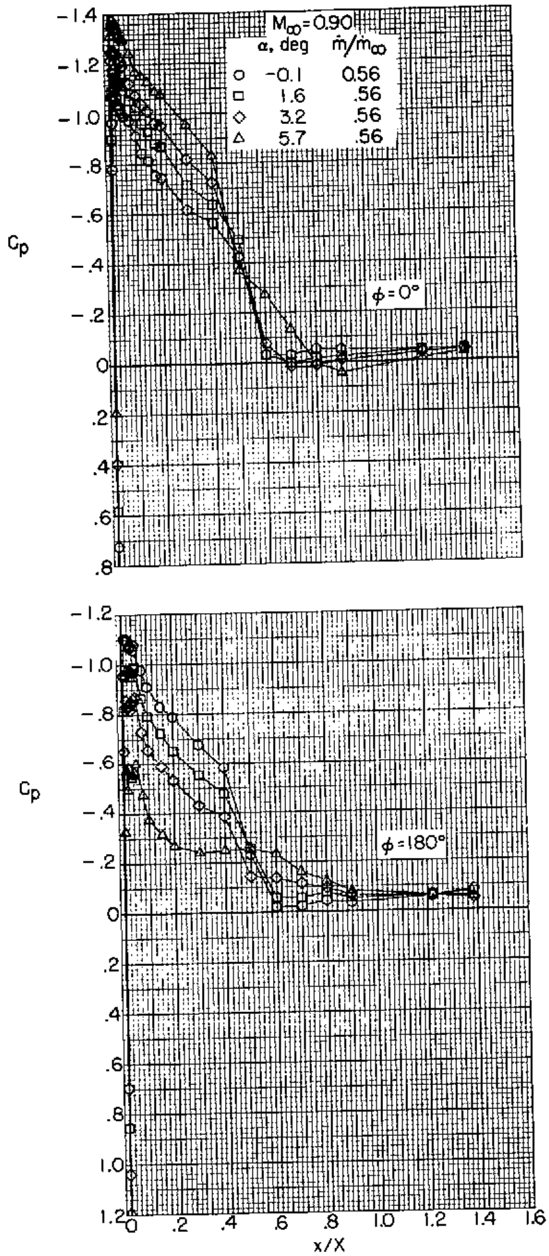

(b) $M_\infty = 0.90$ (low mass-flow ratio).

Figure 20.- Continued.

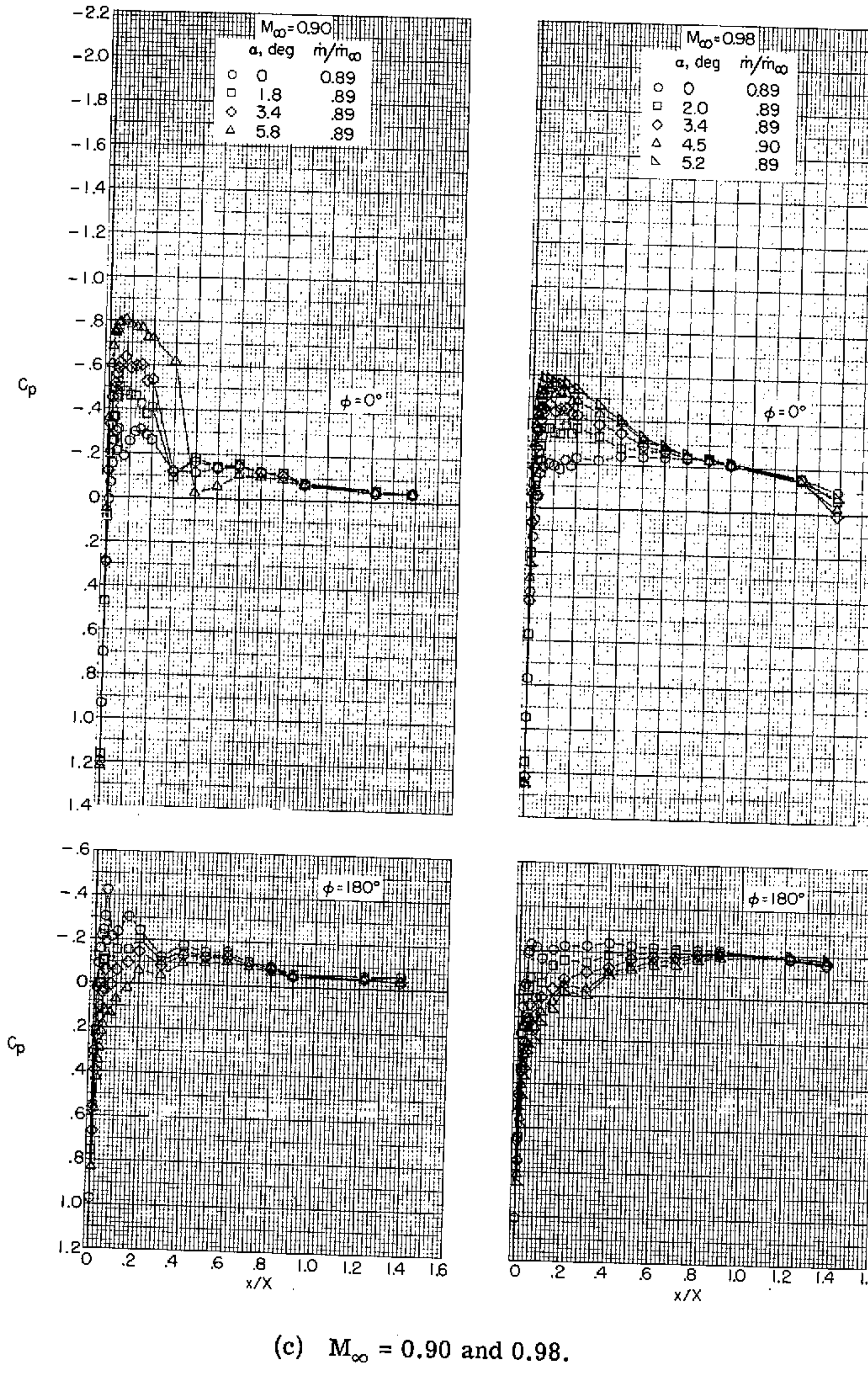

(c) M_∞ = 0.90 and 0.98.

Figure 20.- Concluded.

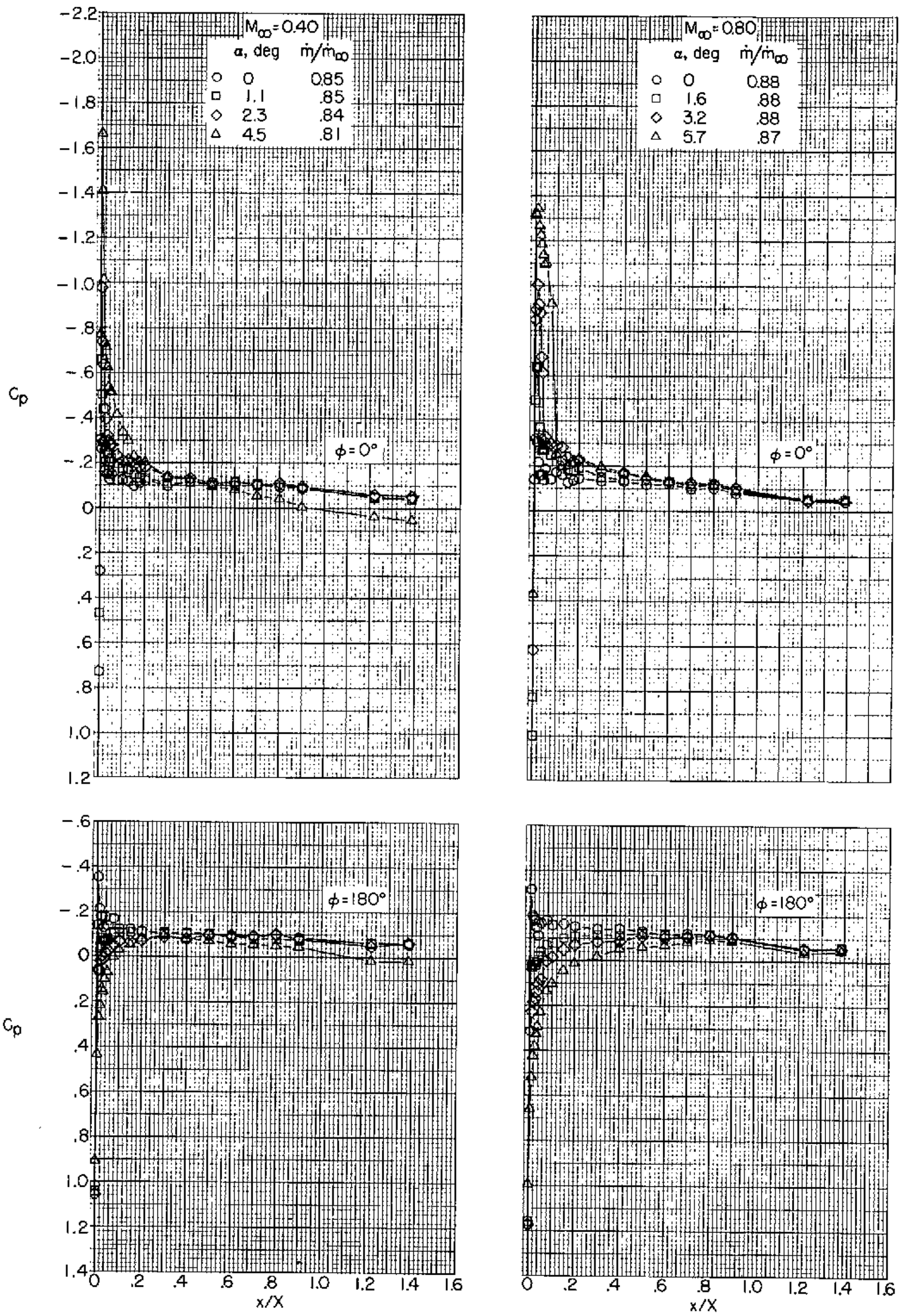

(a) $M_\infty = 0.40$ and 0.80.

Figure 21.- Variation with length of pressure coefficient on top and bottom of an NACA 1-85-100 (contraction ratio 1.046) inlet of several angles of attack.

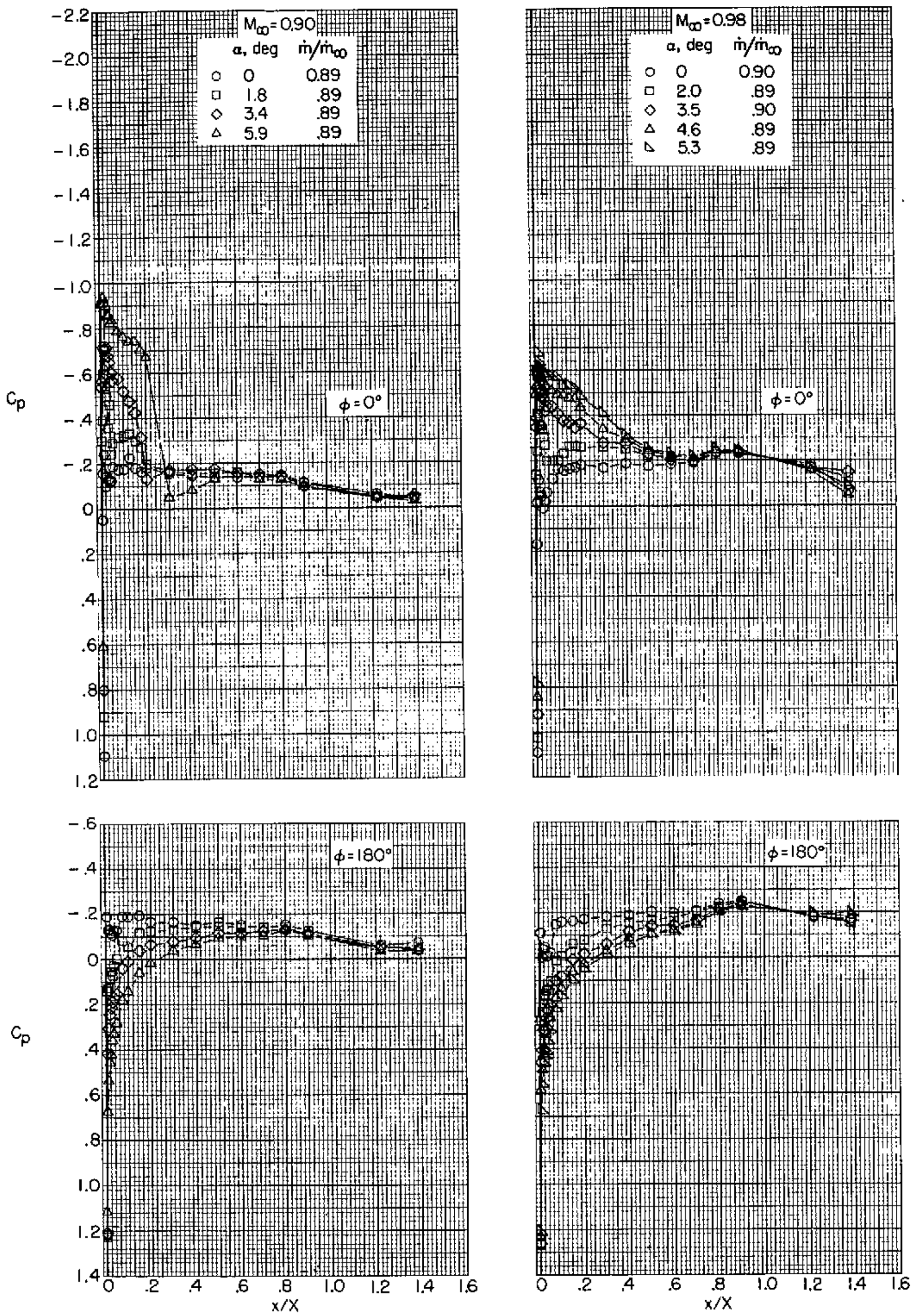

(b) M_∞ = 0.90 and 0.98.

Figure 21.- Concluded.

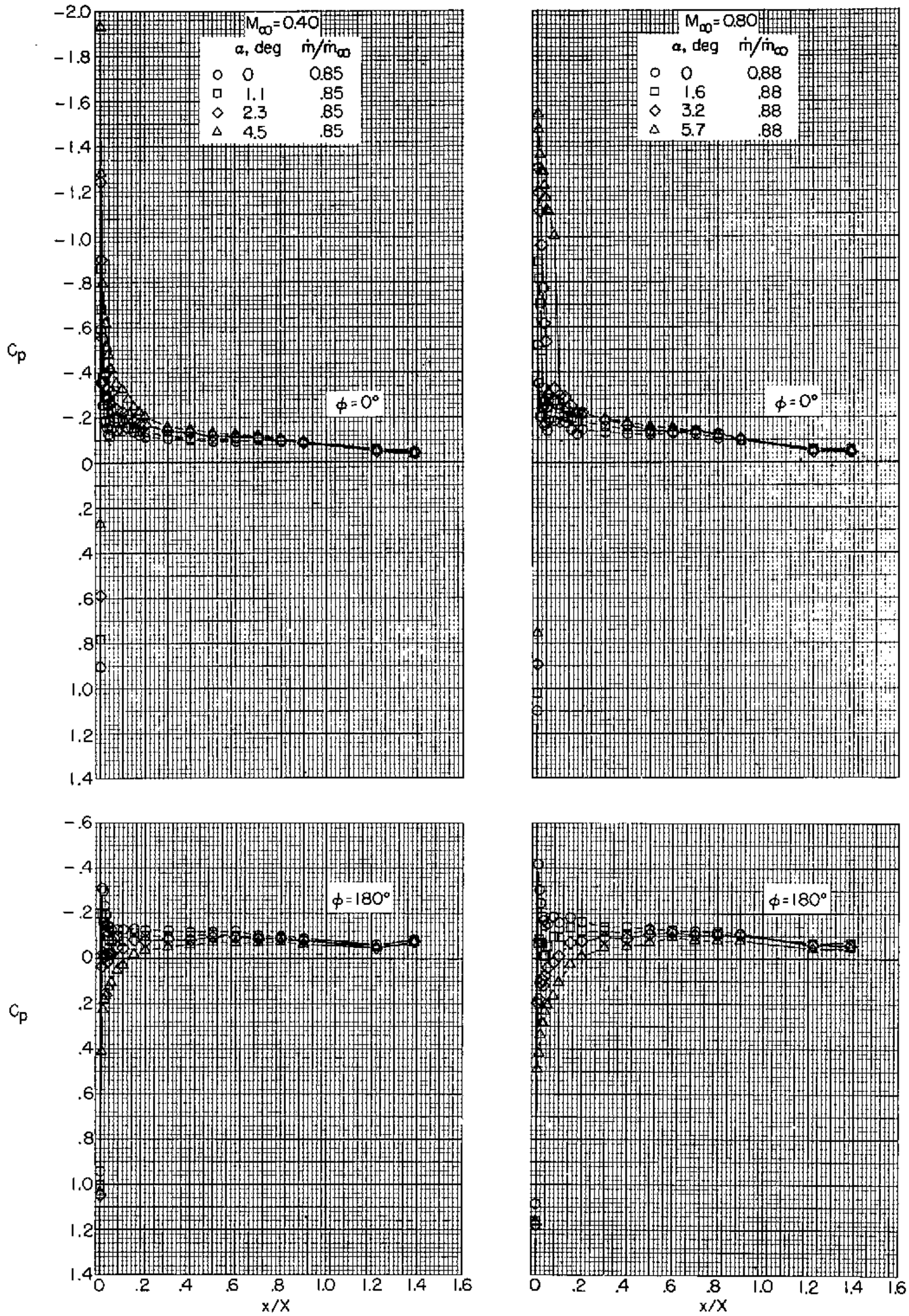

(a) M_∞ = 0.40 and 0.80.

Figure 22.- Variation with length of pressure coefficient on top and bottom of an NACA 1-85-100 (contraction ratio 1.093) inlet at several angles of attack.

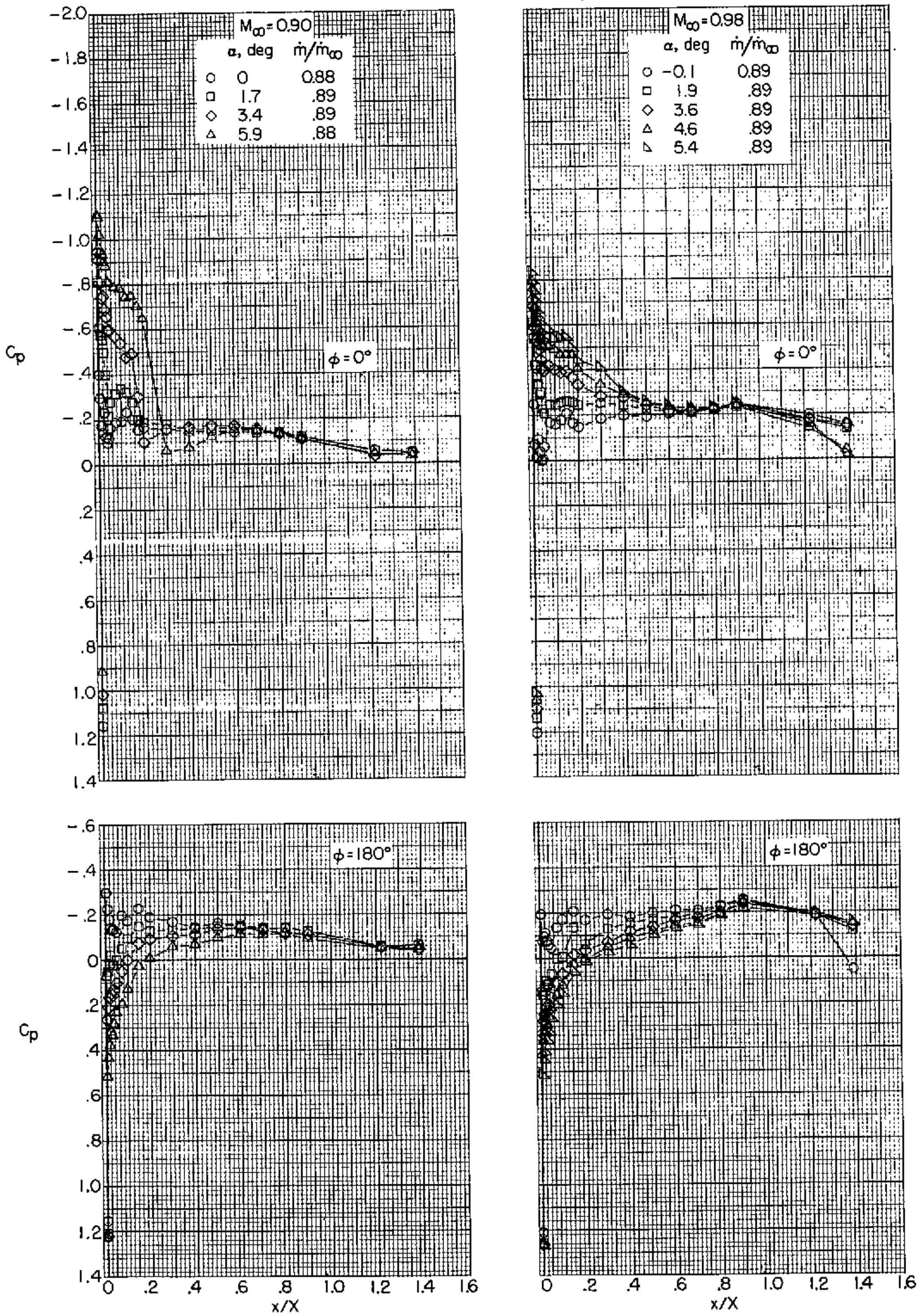

(b) M_∞ = 0.90 and 0.98.

Figure 22.- Concluded.

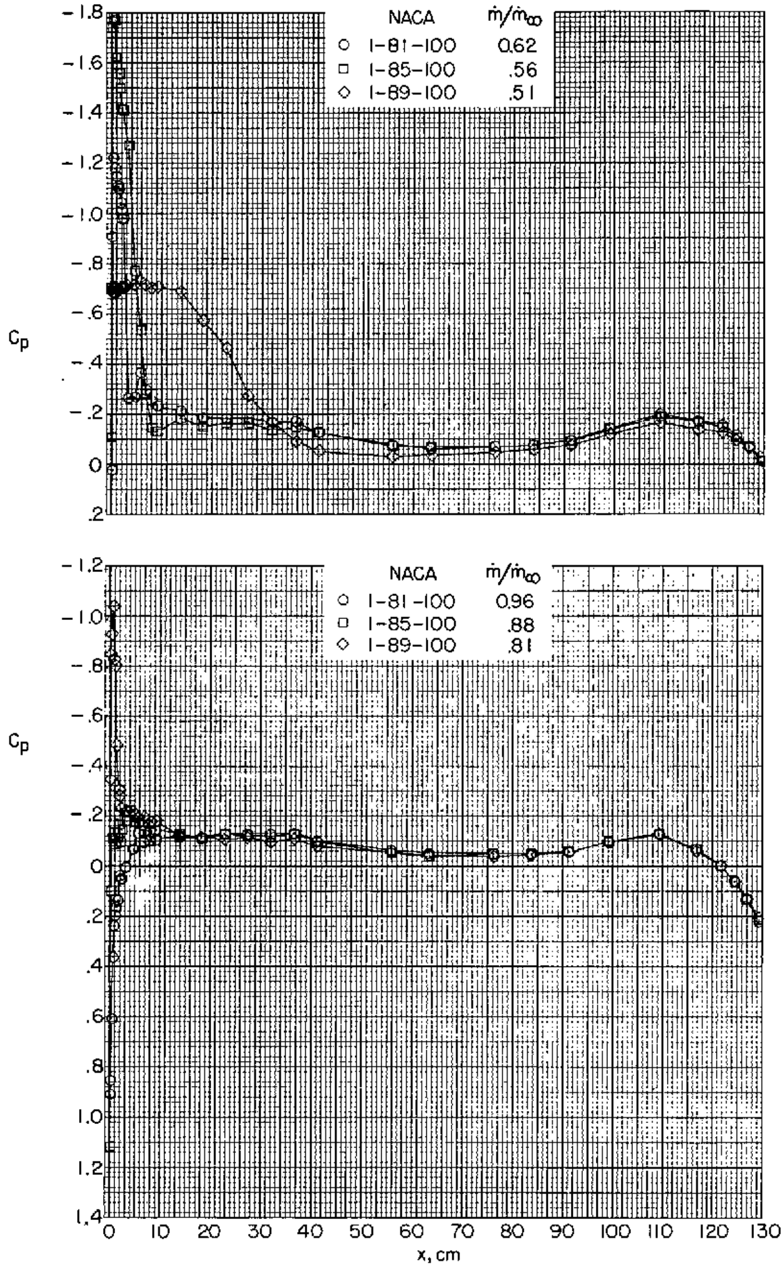

(a) M = 0.80.

Figure 23.- Effect of inlet diameter ratio on the afterbody pressure distribution for approximately the same amount of internal mass flow for each inlet ($\alpha = 0^{\circ}$). All dimensions are in centimeters unless otherwise noted.

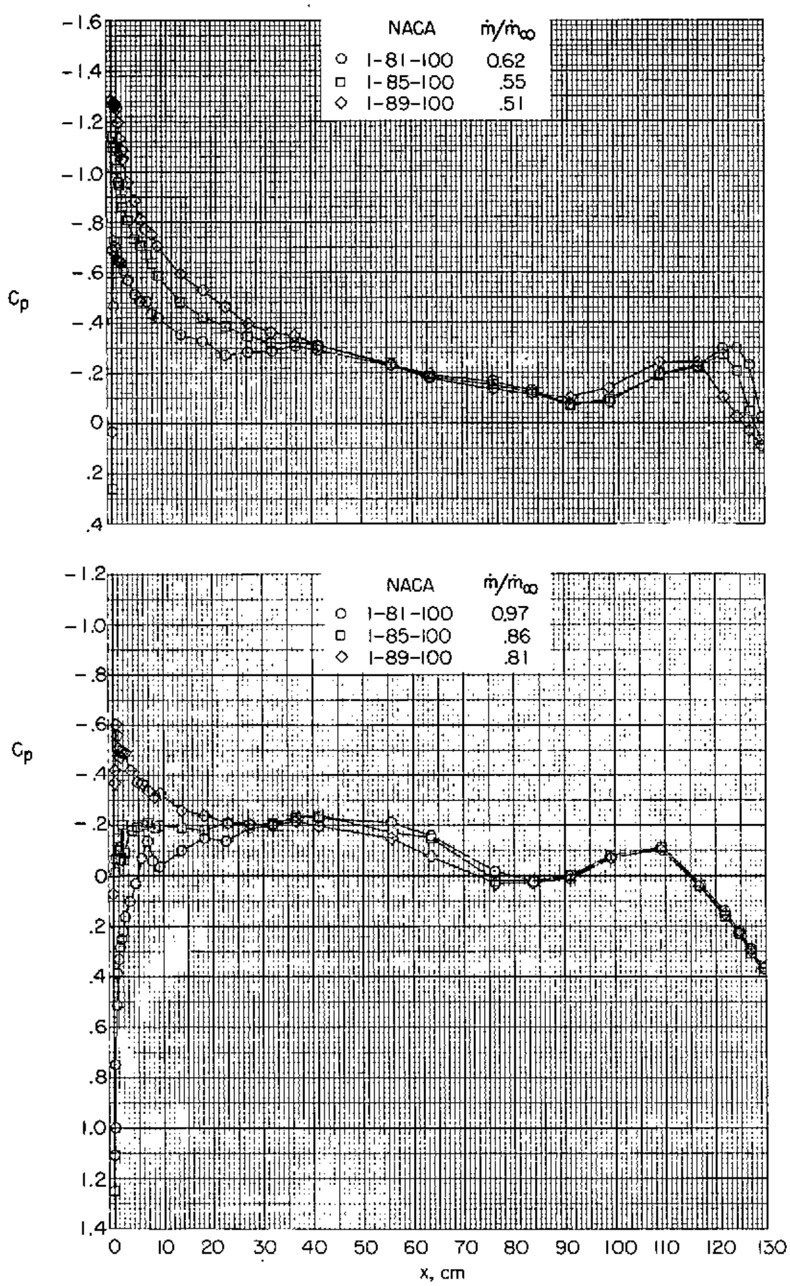

(b) M = 0.98.

Figure 23.- Concluded.

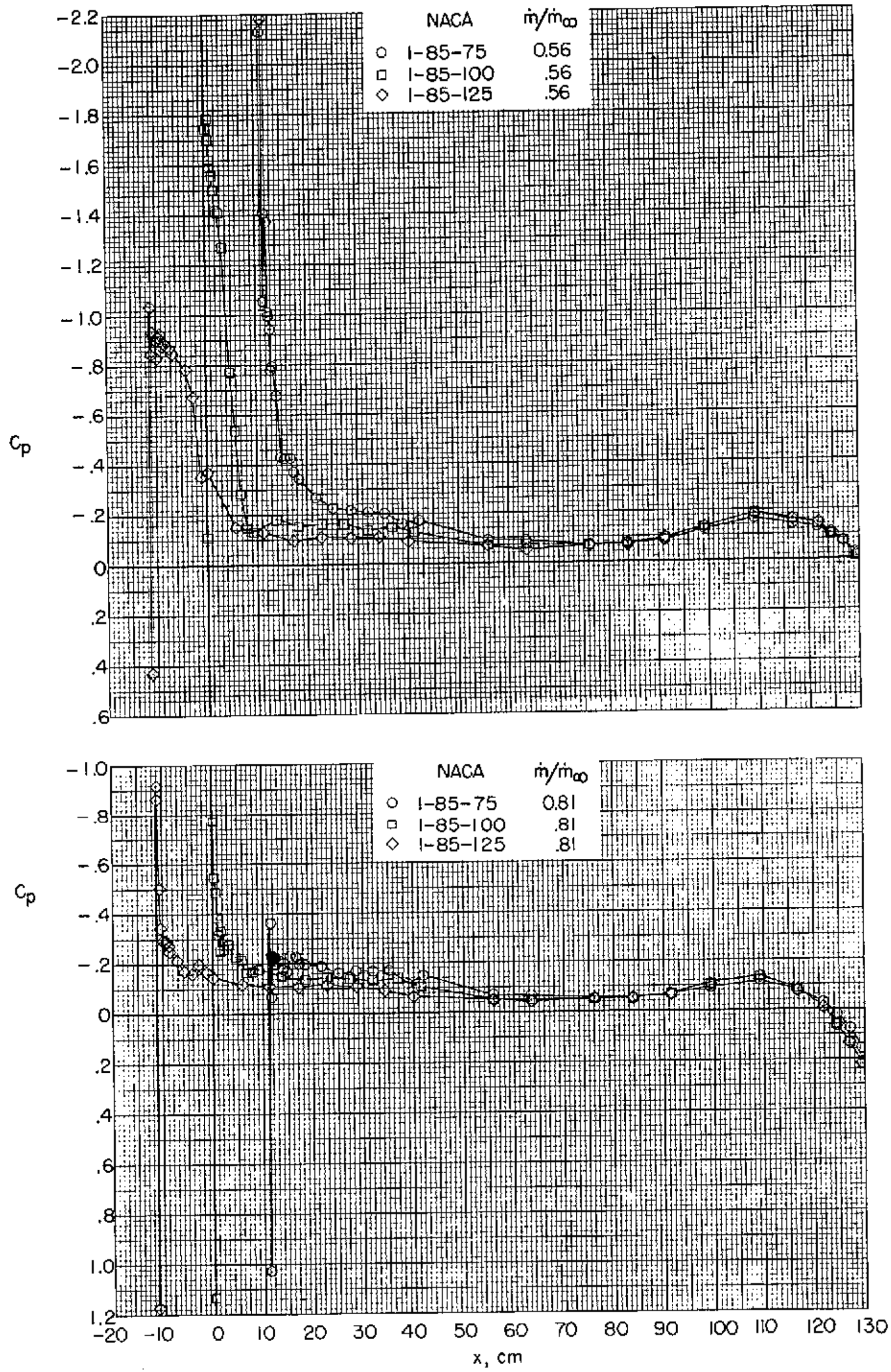

(a) M = 0.80.

Figure 24.- Effect of inlet length ratio on the afterbody pressure distribution for the same mass-flow ratio for each inlet ($\alpha = 0^0$). Origin for axis at nose of NACA 1-85-100 inlet for data presented in this figure. All dimensions are in centimeters unless otherwise noted.

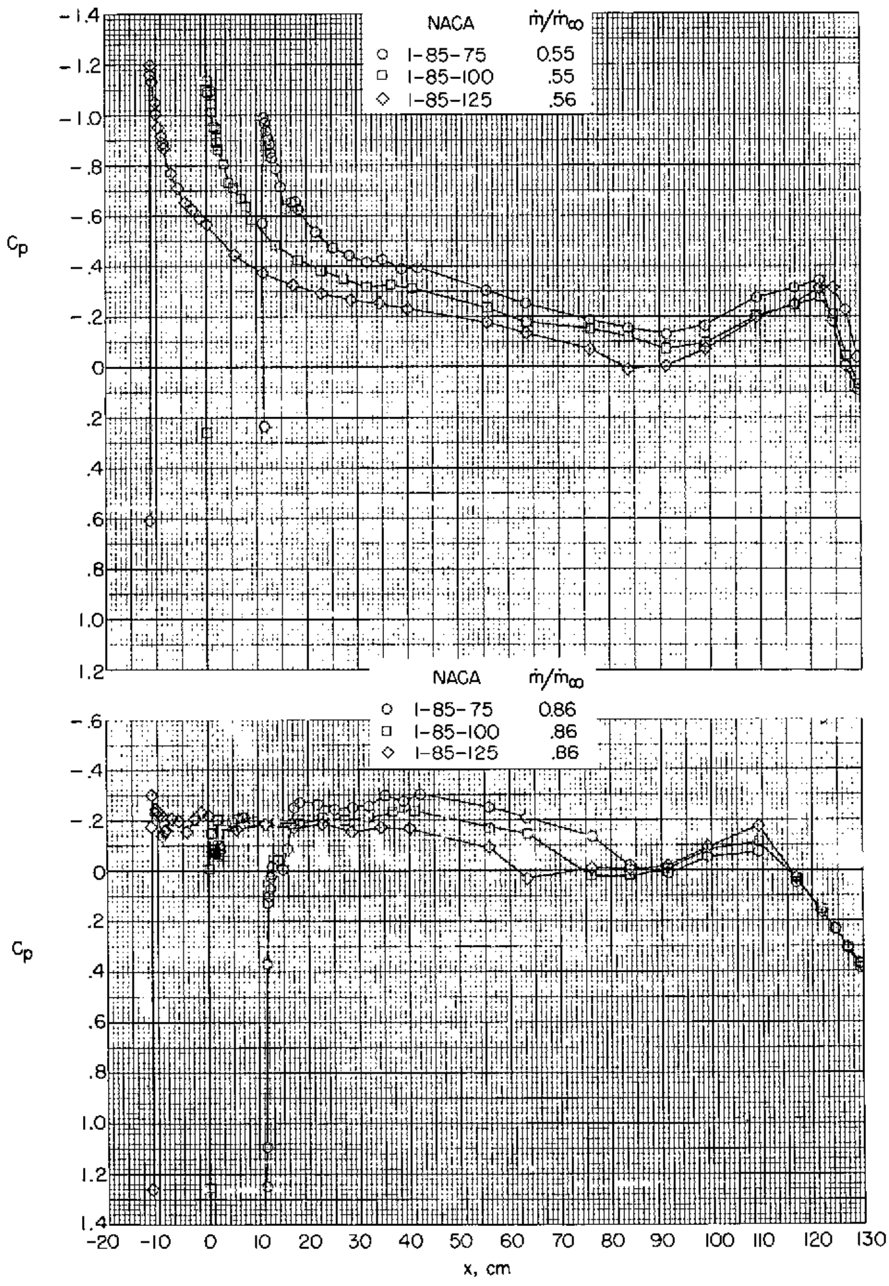

(b) M = 0.98.

Figure 24.- Concluded.

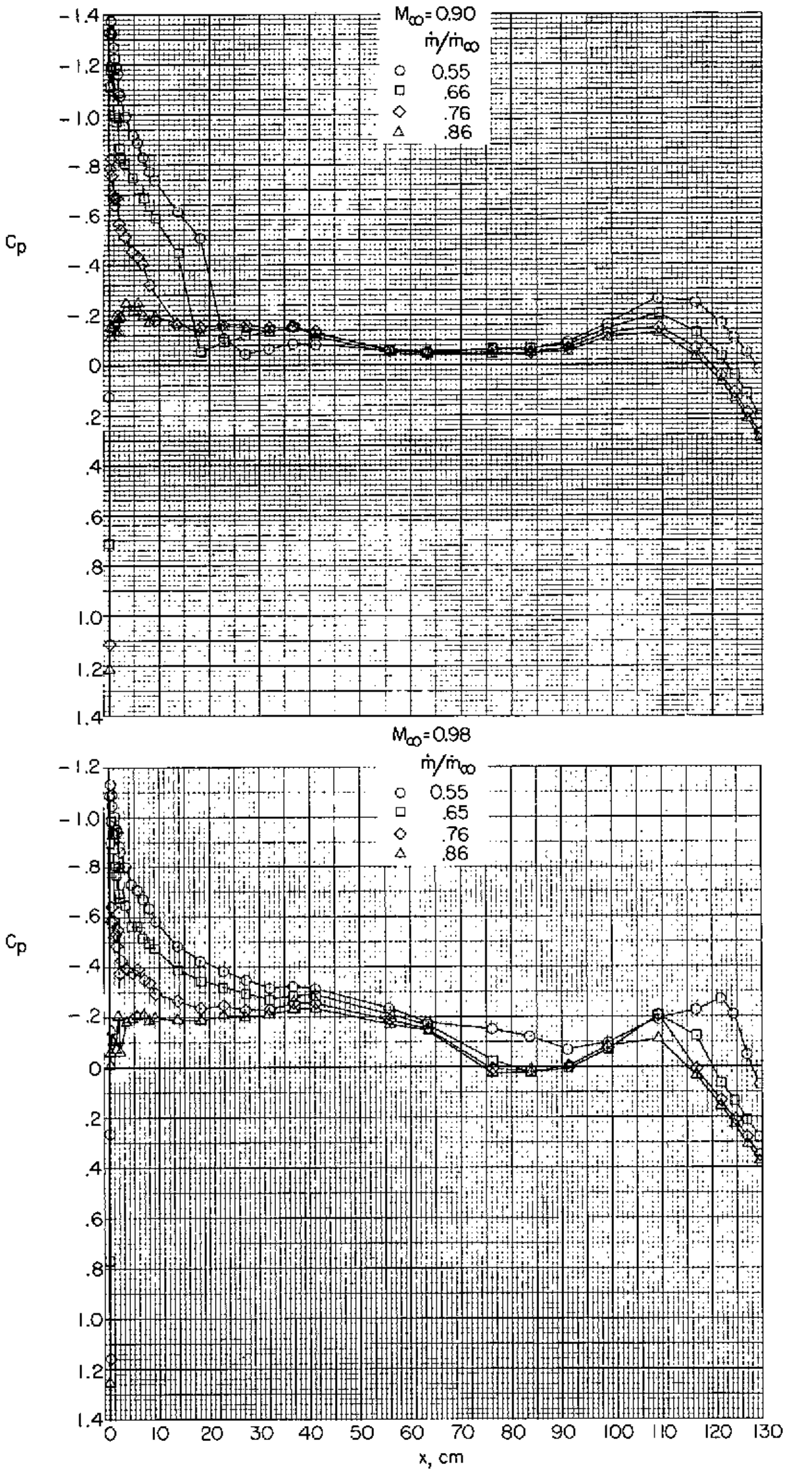

Figure 25.- Effect of inlet mass-flow ratio on the afterbody pressure distribution for the NACA 1-85-100 (contraction ratio 1.009) inlet at Mach numbers of 0.90 and 0.98 ($\alpha = 0^\circ$). All dimensions are in centimeters unless otherwise noted.

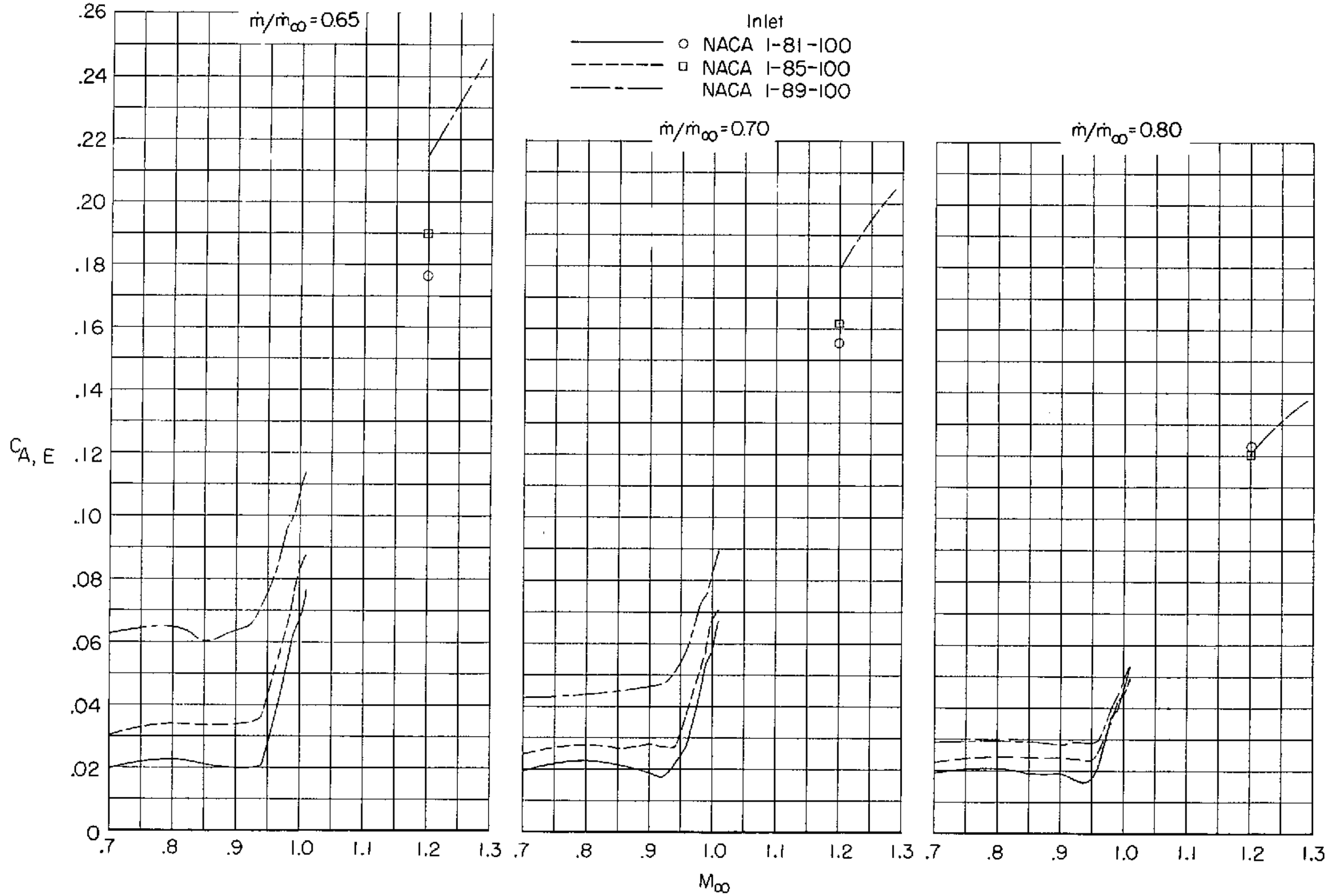

Figure 26.- Variation of inlet axial-force coefficient with Mach number for three inlet diameter ratios at mass-flow ratios of 0.65, 0.70, and 0.80 ($\alpha = 0^{\circ}$).

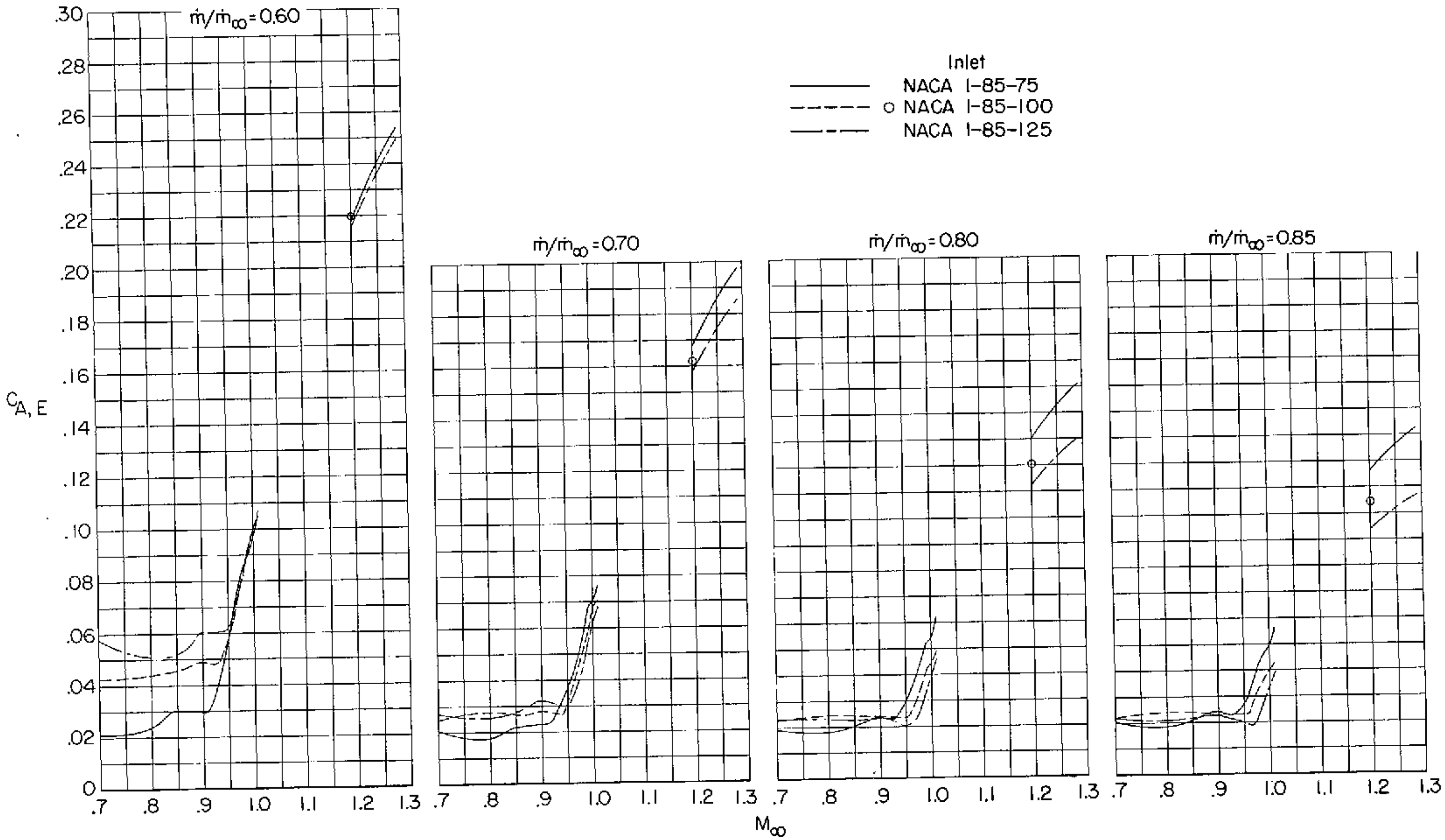

Figure 27.- Variation of inlet axial-force coefficient with Mach number for three inlet length ratios at mass-flow ratios of 0.60, 0.70, 0.80, and 0.85 ($\alpha = 0^{\circ}$).

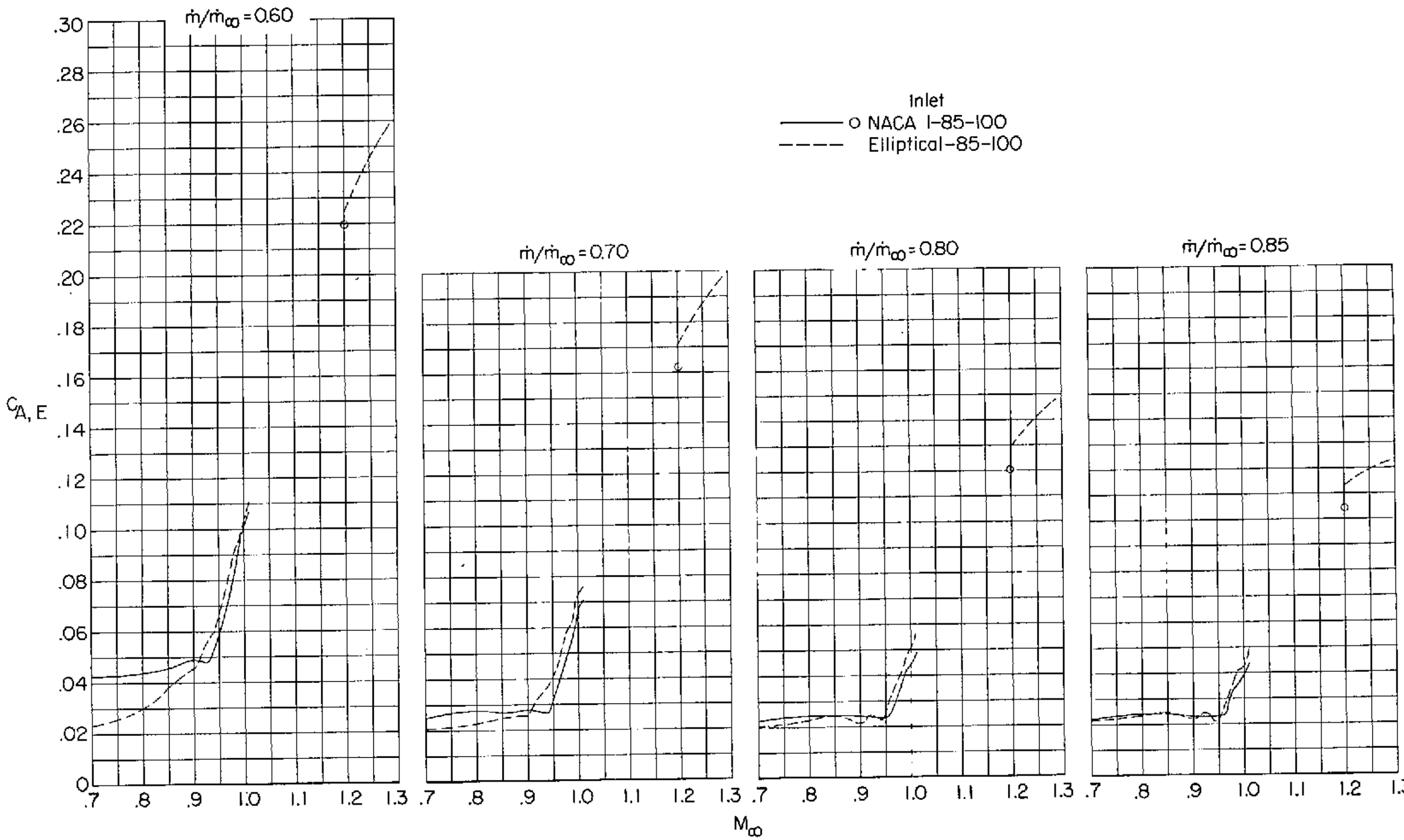

Figure 28.- Variation of inlet axial-force coefficient with Mach number for the NACA 1-85-100 (contraction ratio 1.009) and elliptical nose inlets at mass-flow ratios of 0.60, 0.70, 0.80, and 0.85 ($\alpha = 0^{\circ}$).

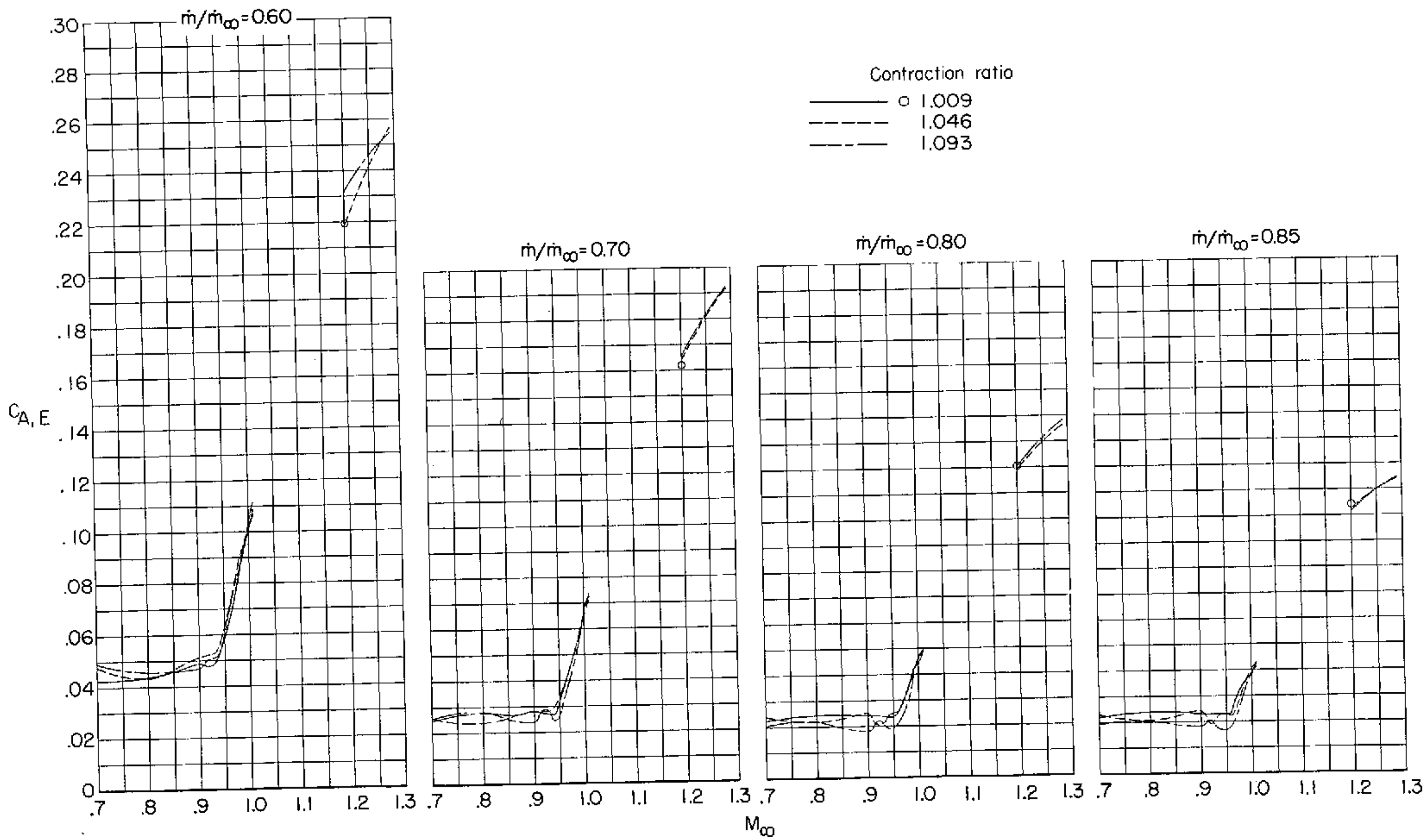

Figure 29.- Variation of inlet axial-force coefficient with Mach number for the NACA 1-85-100 inlet with internal contraction ratios of 1.009, 1.046, and 1.093 at mass-flow ratios of 0.60, 0.70, 0.80, and 0.85 ($\alpha = 0^{\circ}$).

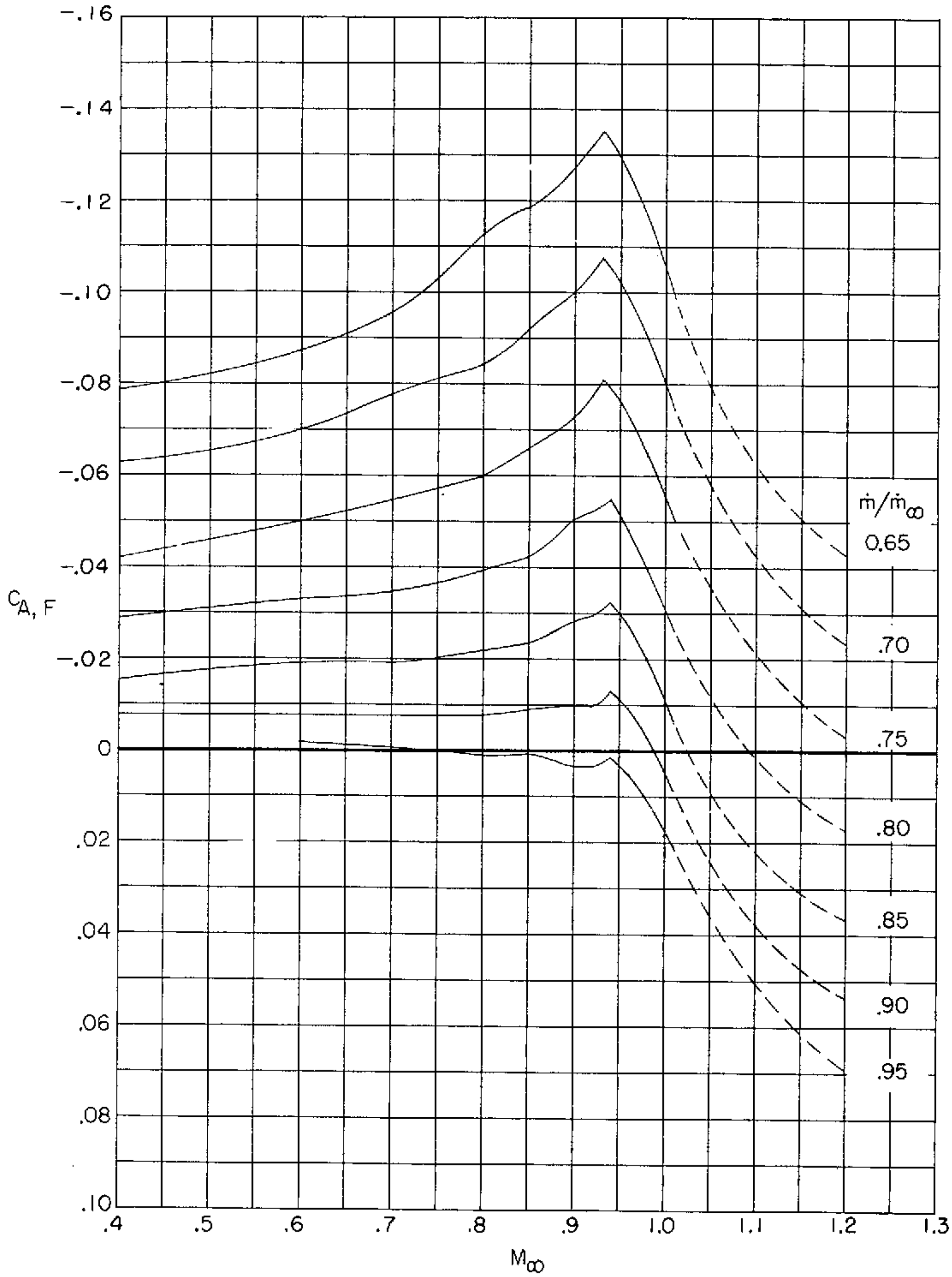

(a) NACA 1-81-100.

Figure 30.- Variation with Mach number of forebody axial-force coefficient obtained by integration of inlet pressures in the axial direction.

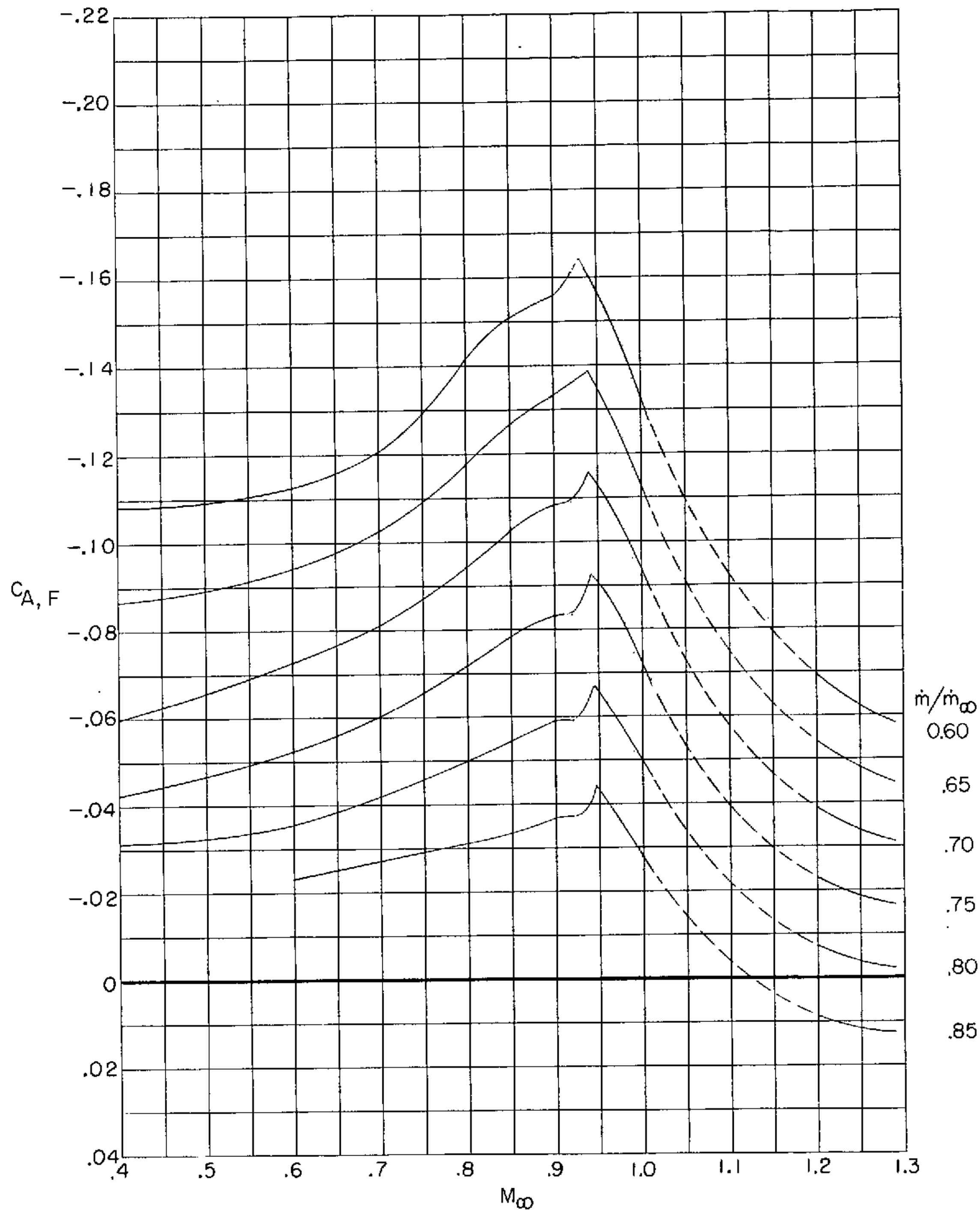

(b) NACA 1-85-100, contraction ratio 1.009.

Figure 30.- Continued.

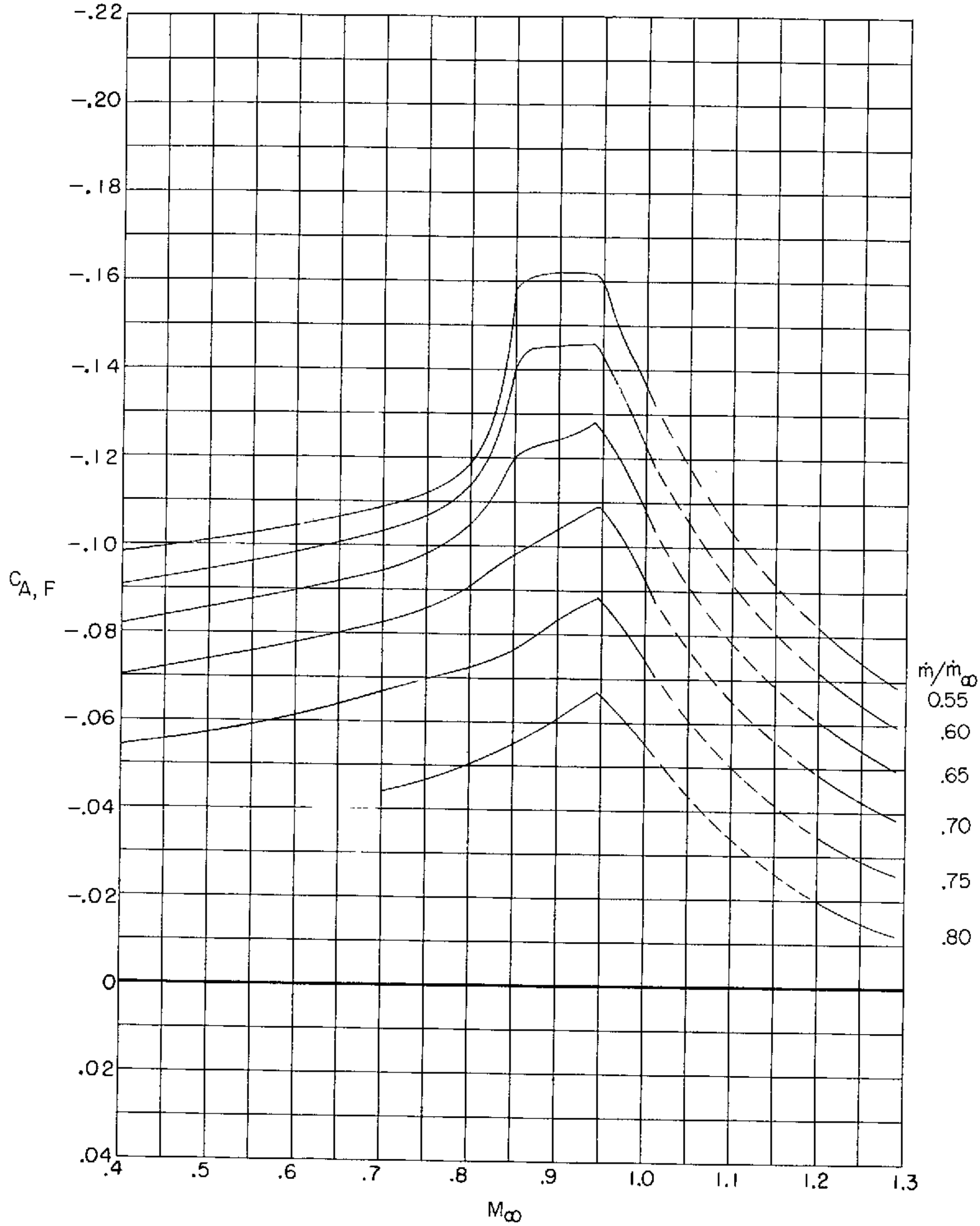

(c) NACA 1-89-100.

Figure 30.- Continued.

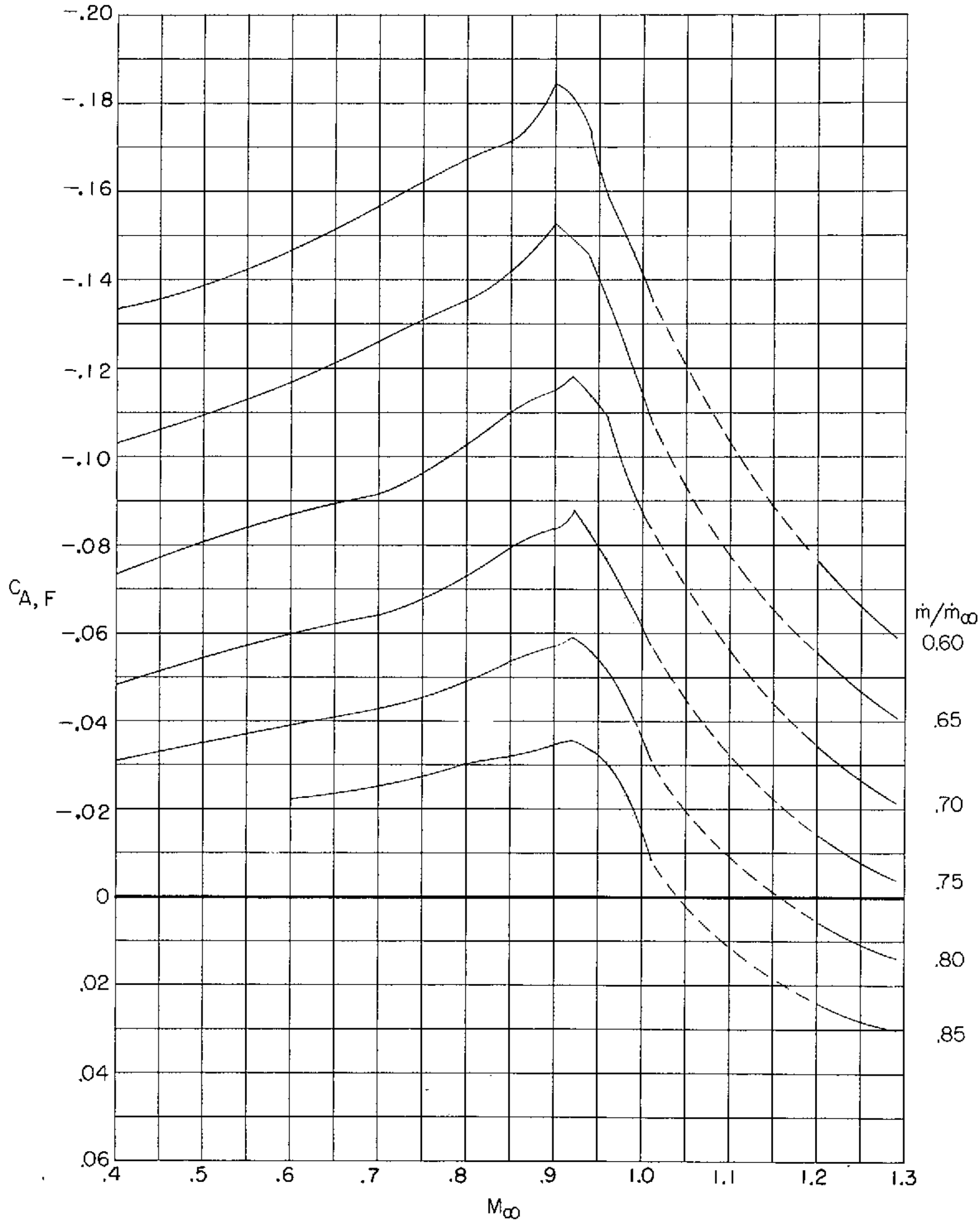

(d) NACA 1-85-75.

Figure 30.- Continued.

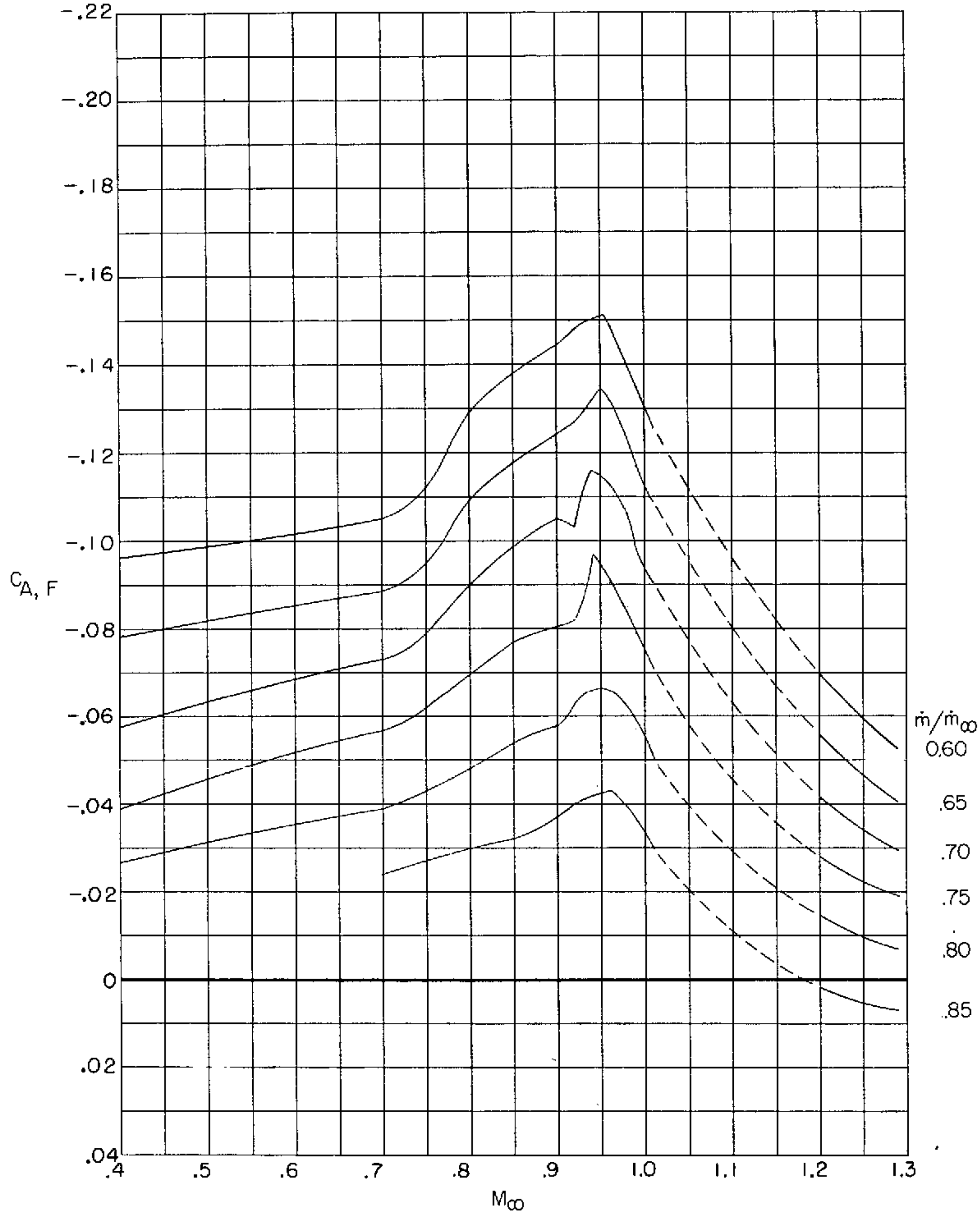

(e) NACA 1-85-125.

Figure 30.- Continued.

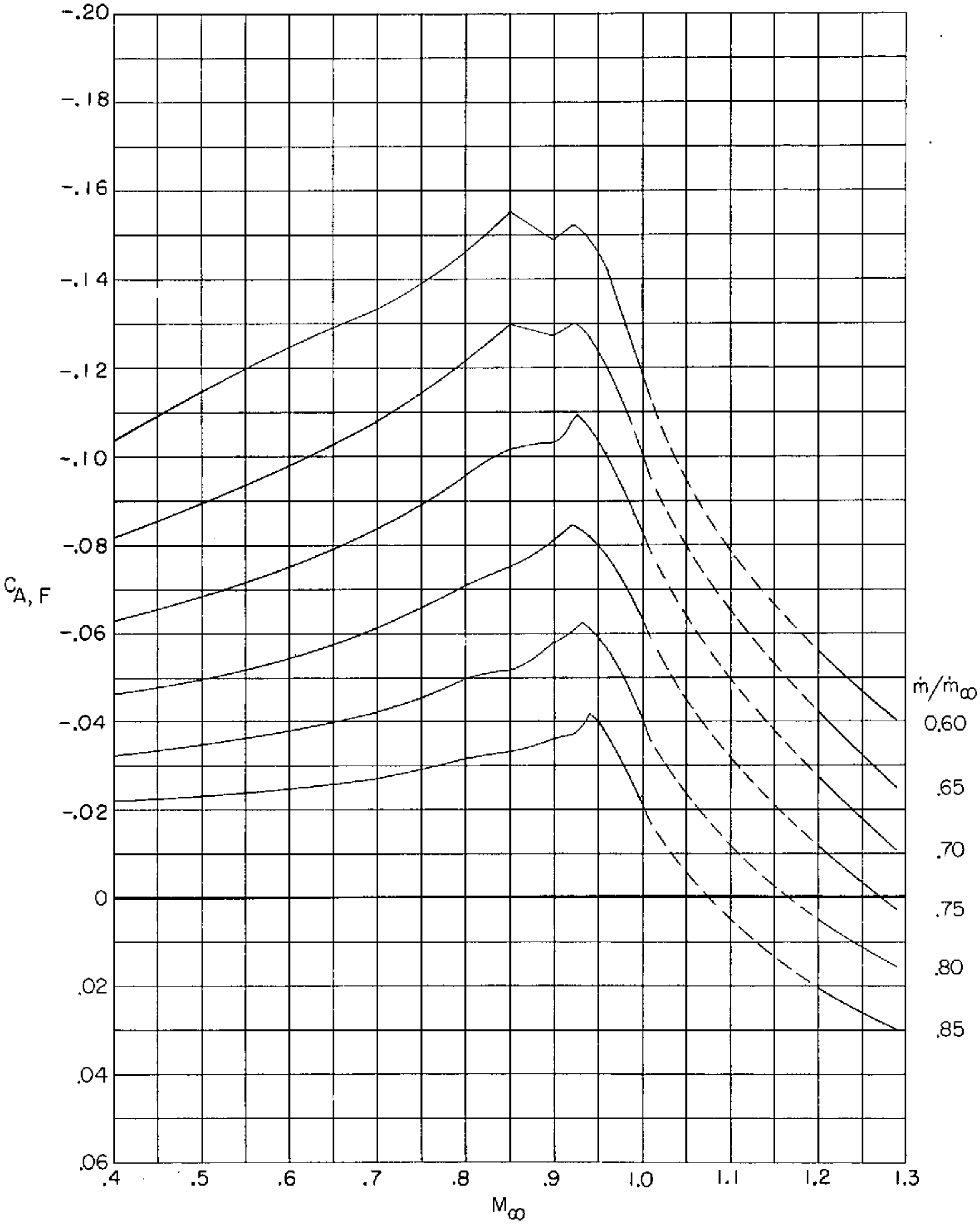

(f) Elliptical-85-100.

Figure 30.- Continued.

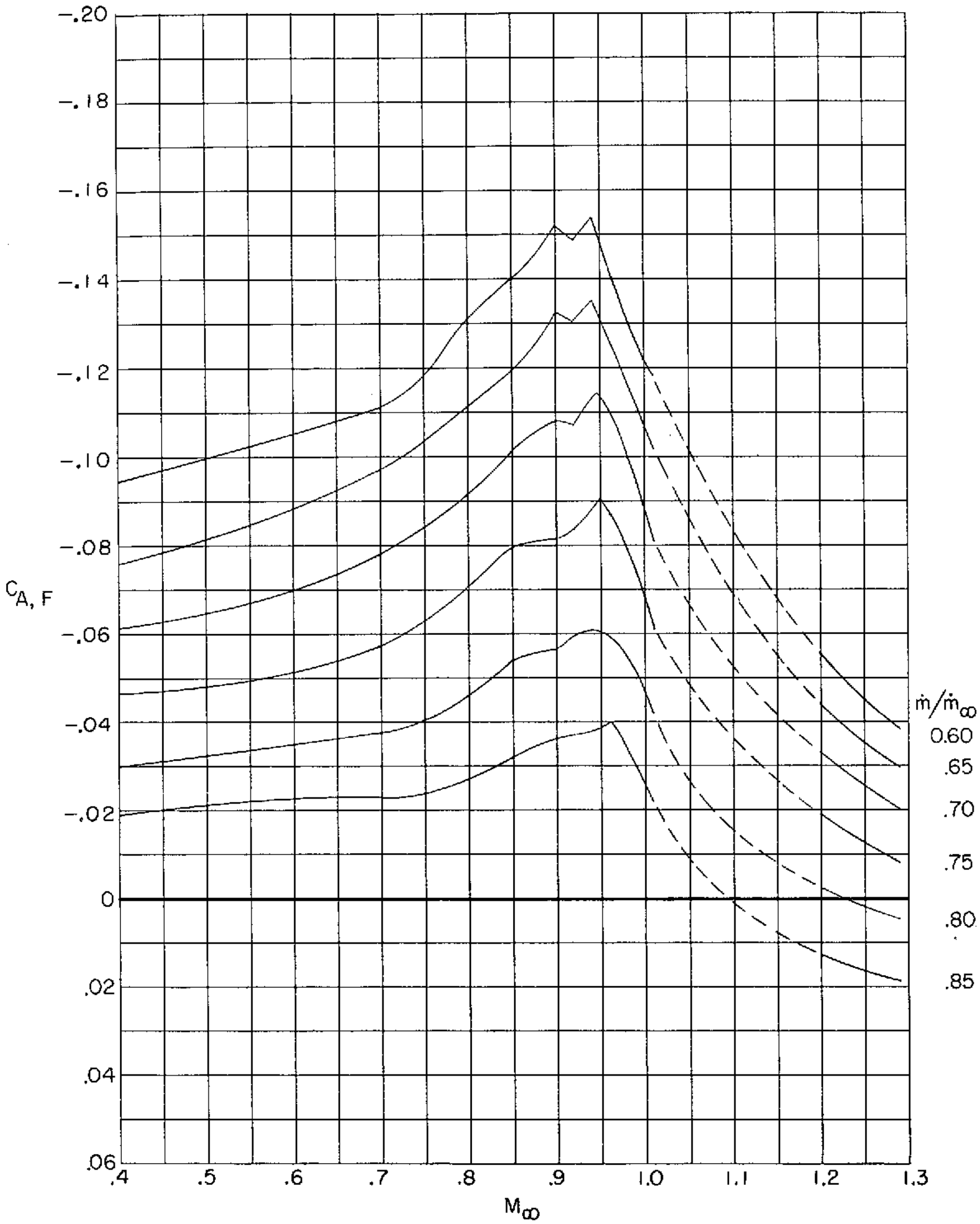

(g) NACA 1-85-100, contraction ratio 1.046.

Figure 30.- Continued.

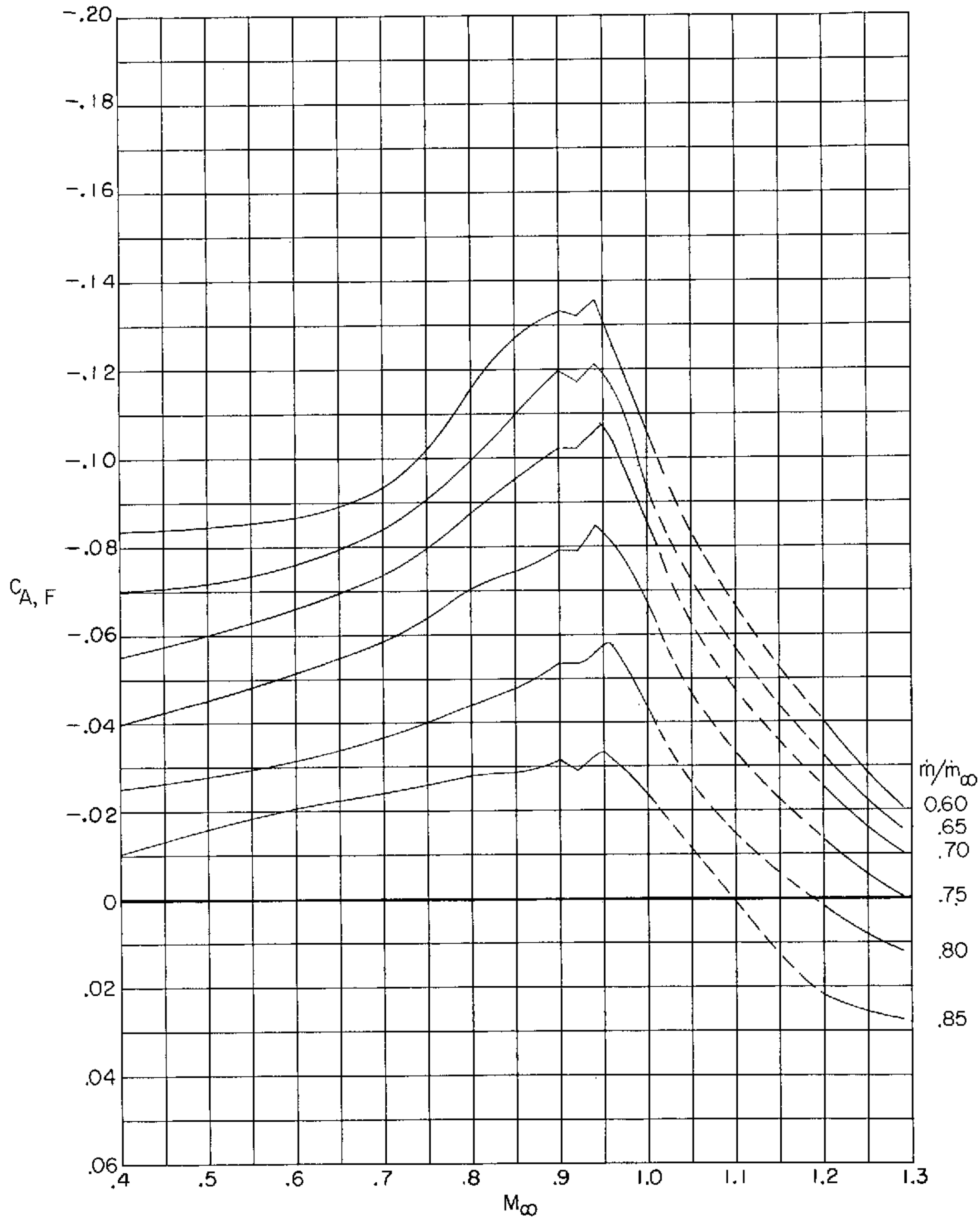

(h) NACA 1-85-100, contraction ratio 1.093.

Figure 30.- Concluded.

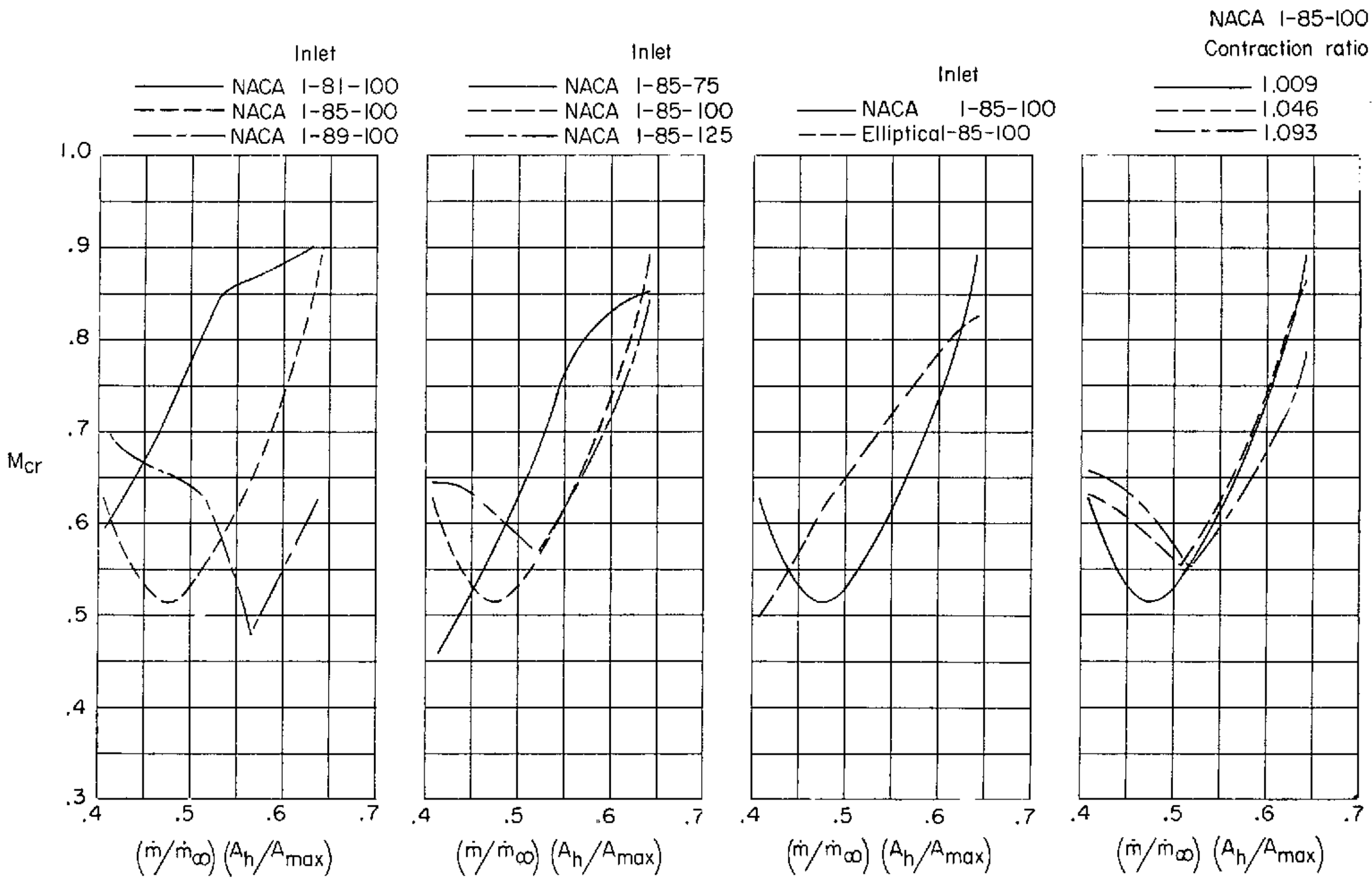

Figure 31.- Comparisons of the variation of inlet lower critical Mach number with mass-flow ratio for four geometric variables. (Lower critical Mach number obtained from experimental pressure coefficient data.)

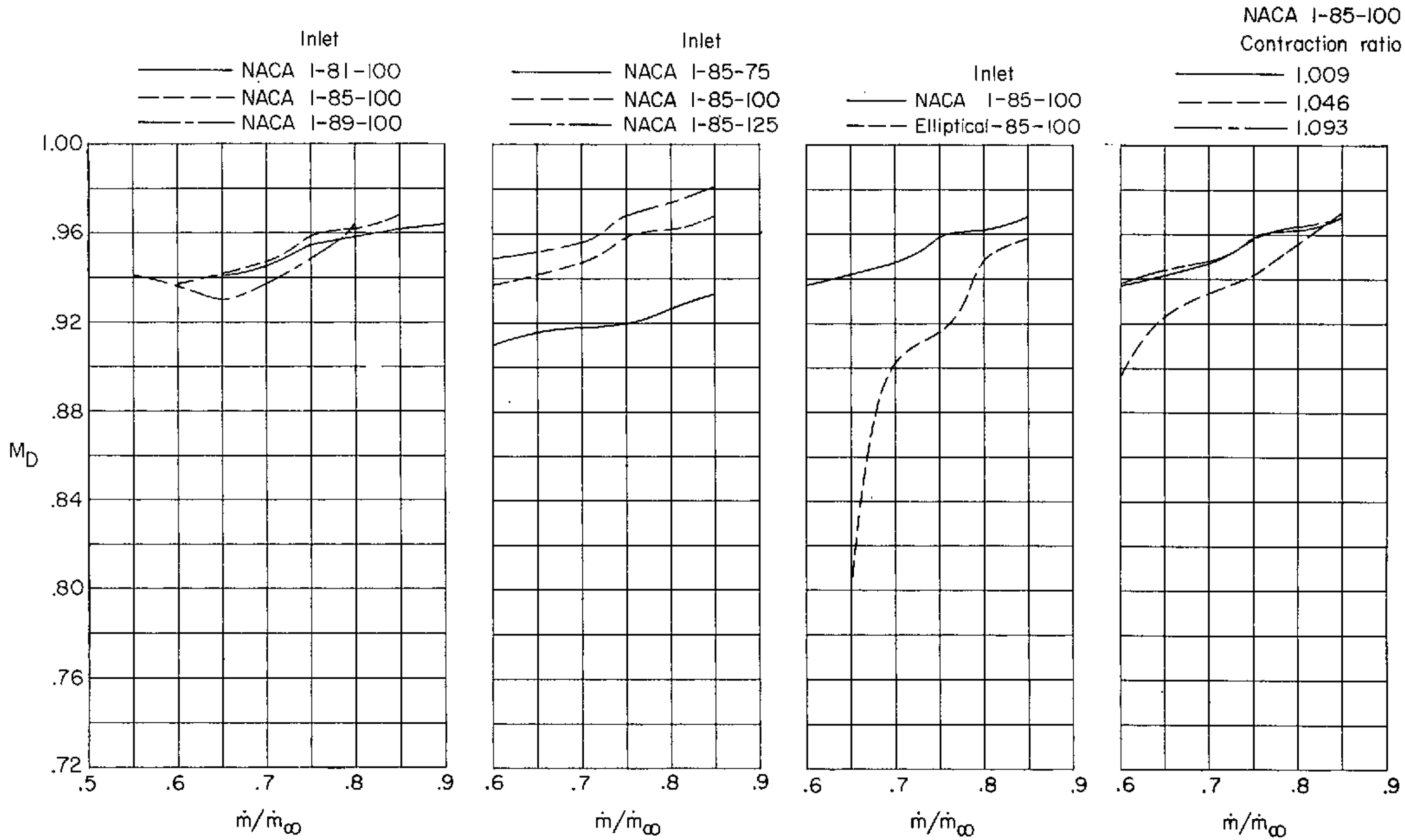

Figure 32.- Comparisons of the variation of inlet drag divergence Mach number with mass-flow ratio for four geometric variables. (Drag divergence Mach number defined as that Mach number at which C_A reaches 1.1 times the average C_A at the lower Mach numbers.)

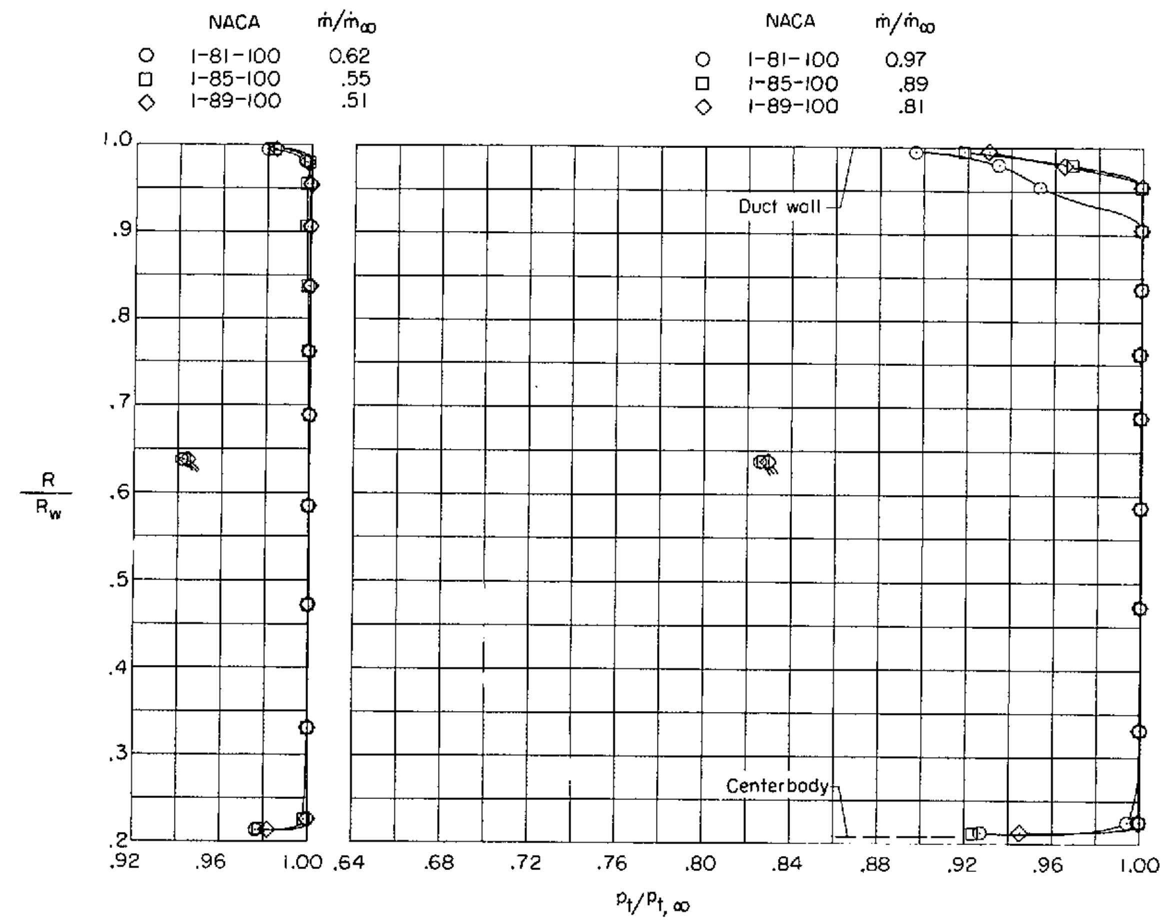

(a) M = 0.90.

Figure 33.- Total-pressure distribution across the duct at the mass-flow rake station for the three inlet diameter ratios at two mass flows. (Flagged symbols indicate static-pressure measurements.)

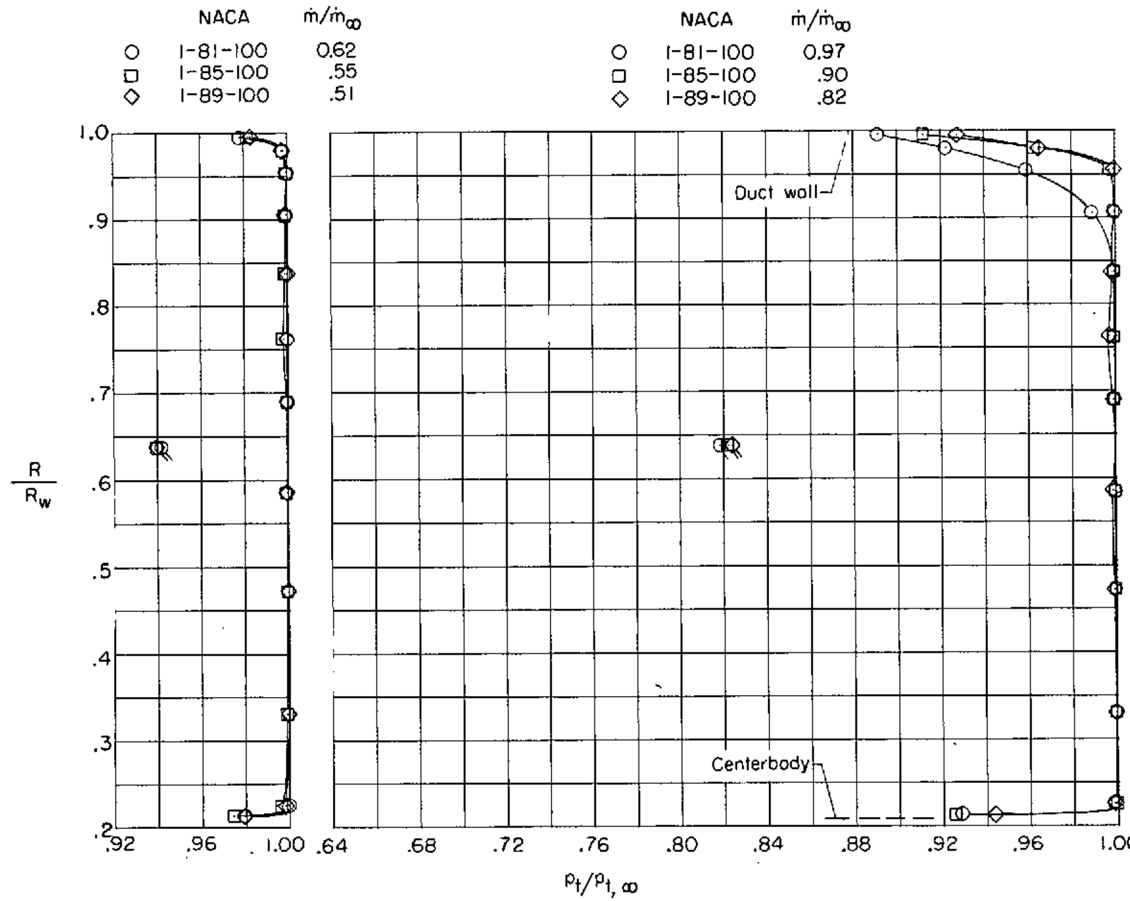

(b) M = 0.98.

Figure 33.- Continued.

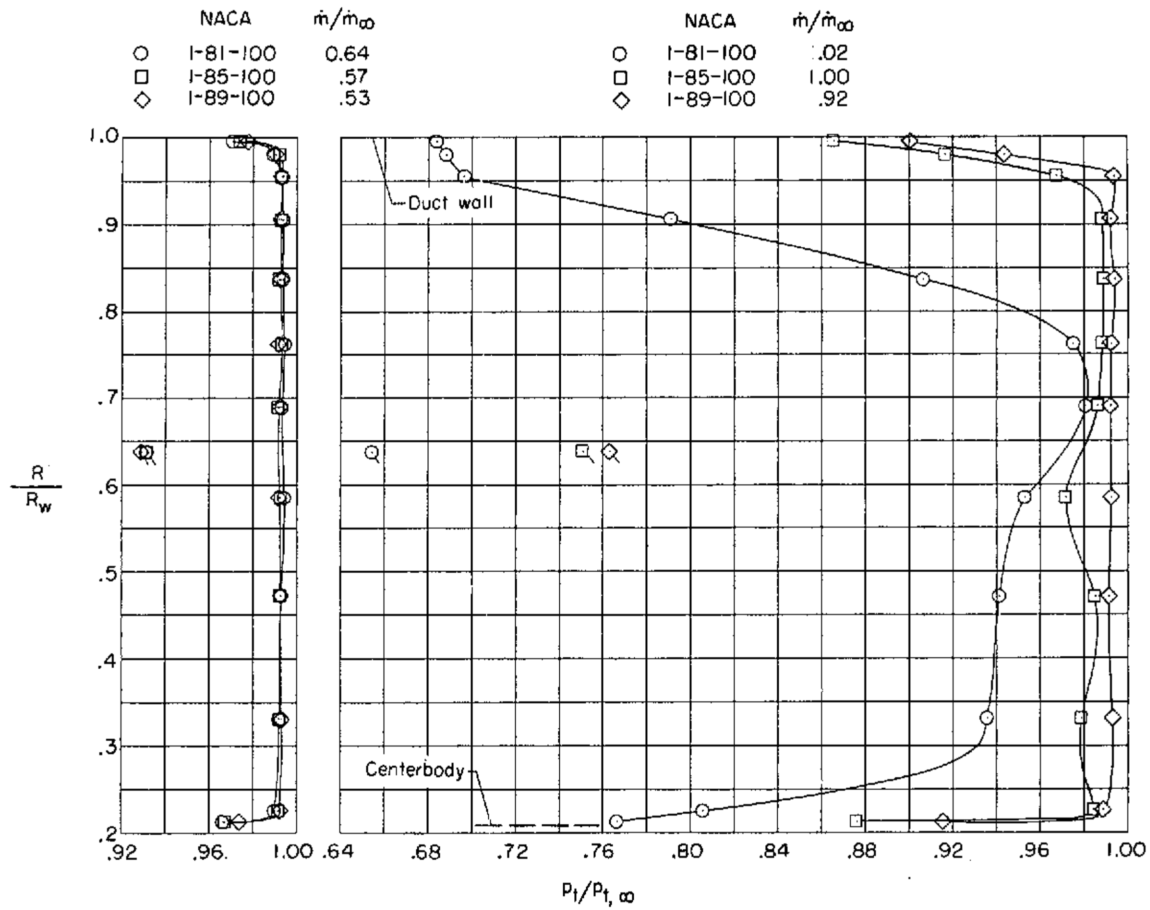

(c) M = 1.20.

Figure 33.- Concluded.

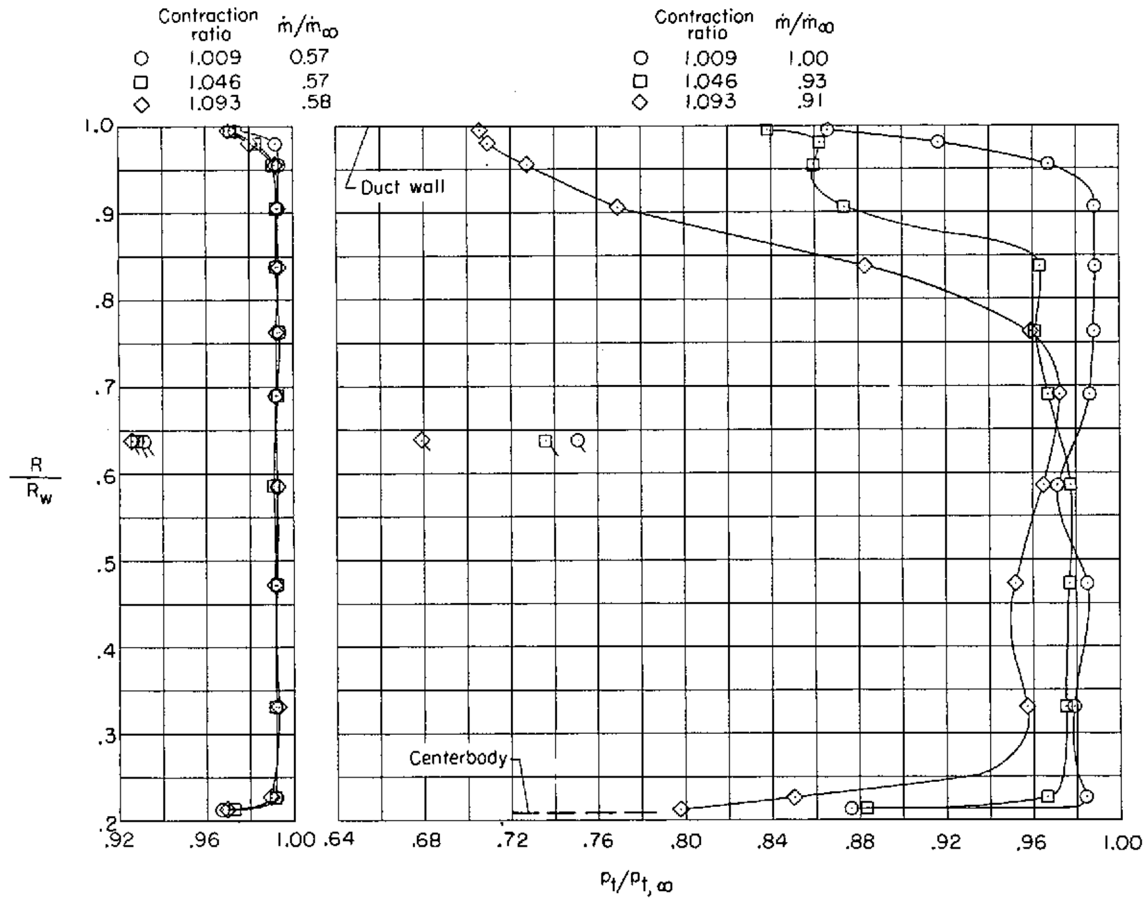

Figure 34.- Effect of internal contraction ratio on the total-pressure distribution across the duct at the mass-flow rake station for the NACA 1-85-100 at a free-stream Mach number of 1.20. (Flagged symbols indicate static-pressure measurements.)

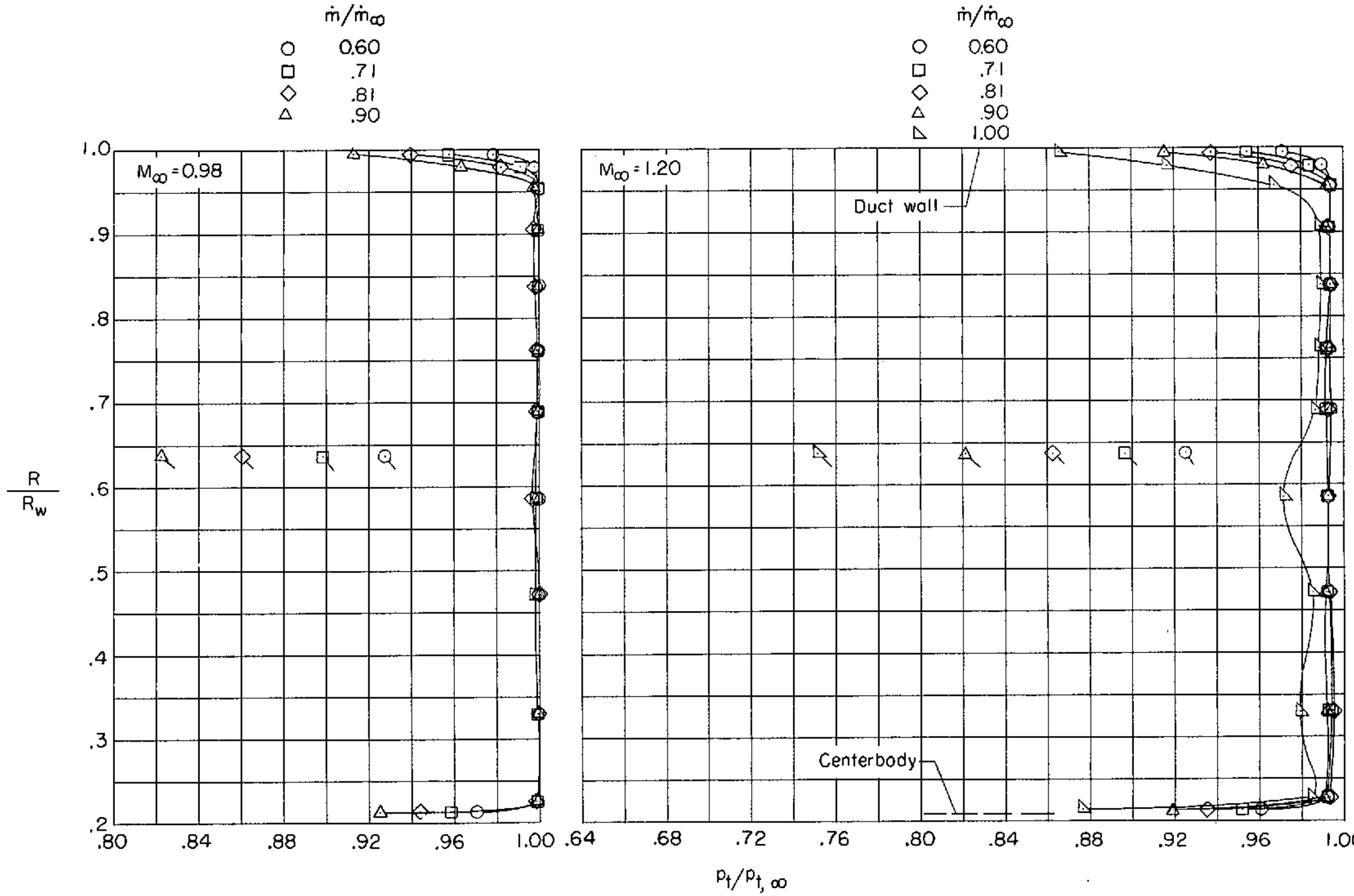

(a) Internal contraction ratio of 1.009.

Figure 35.- Effect of mass-flow ratio on the total-pressure distribution across the duct for the NACA 1-85-100 inlet with two internal contraction ratios at free-stream Mach numbers of 0.98 and 1.20. (Flagged symbols indicate static-pressure measurements.)

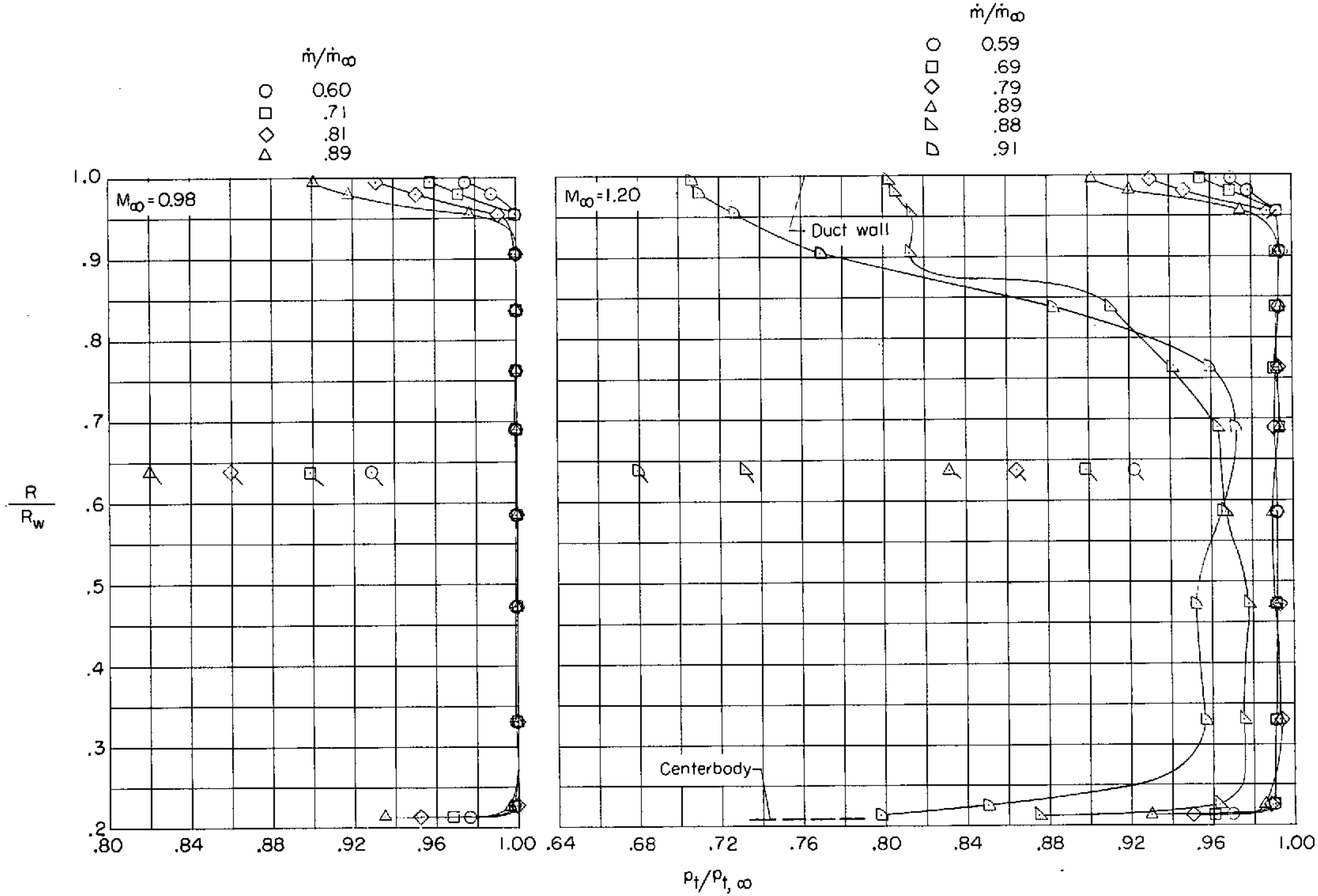

(b) Internal contraction ratio of 1.093.

Figure 35.- Concluded.

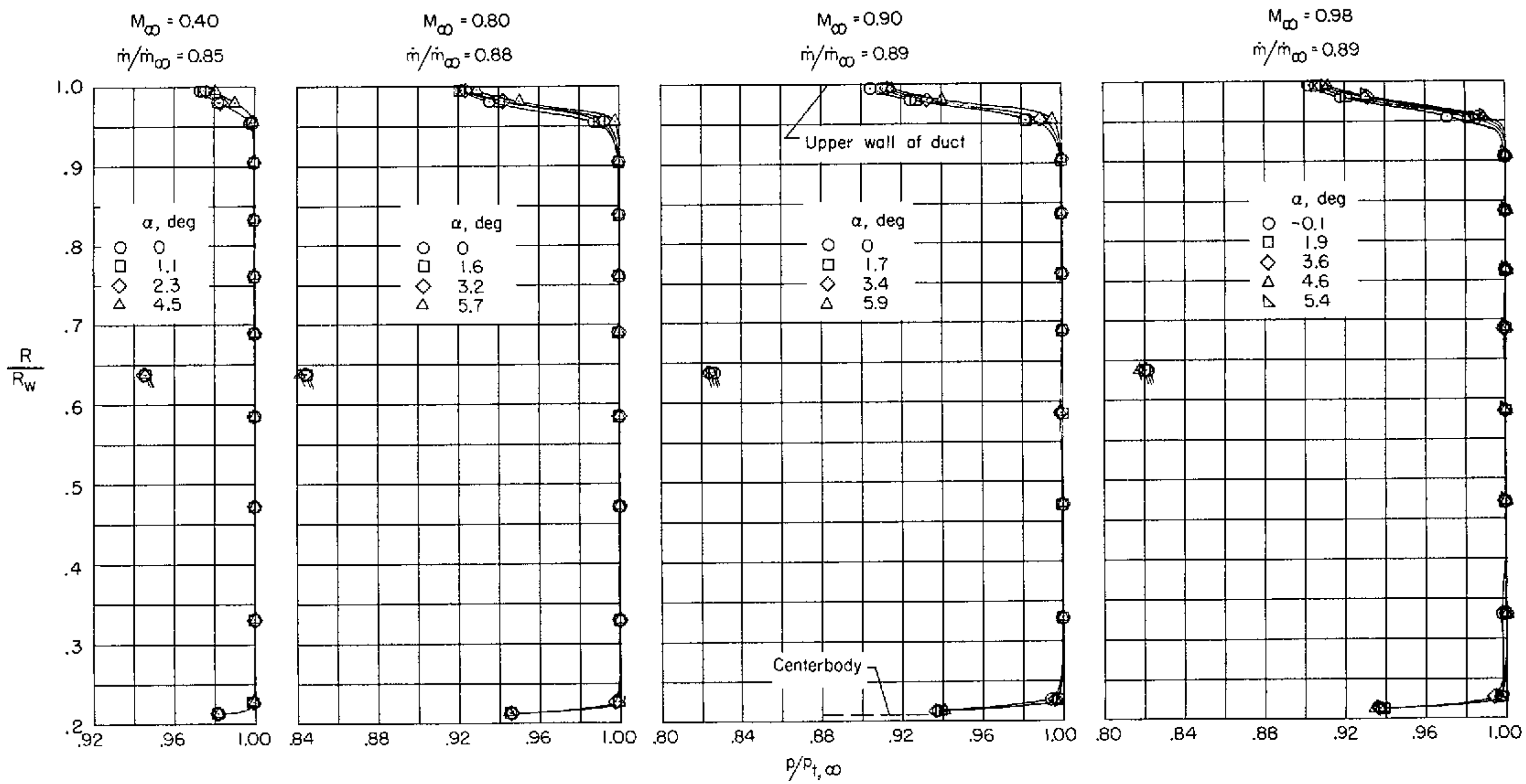

(a) Upper rake arm, $\phi = 0^{\circ}$.

Figure 36.- Effect of angle of attack on the total-pressure distribution across the duct for the upper ($\phi = 0^{\circ}$) and lower ($\phi = 180^{\circ}$) rake arms of the mass-flow rake for the NACA 1-85-100 inlet with an internal contraction ratio of 1.093. (Flagged symbols indicate static-pressure measurements.)

NASA-Langley, 1974

L-8588

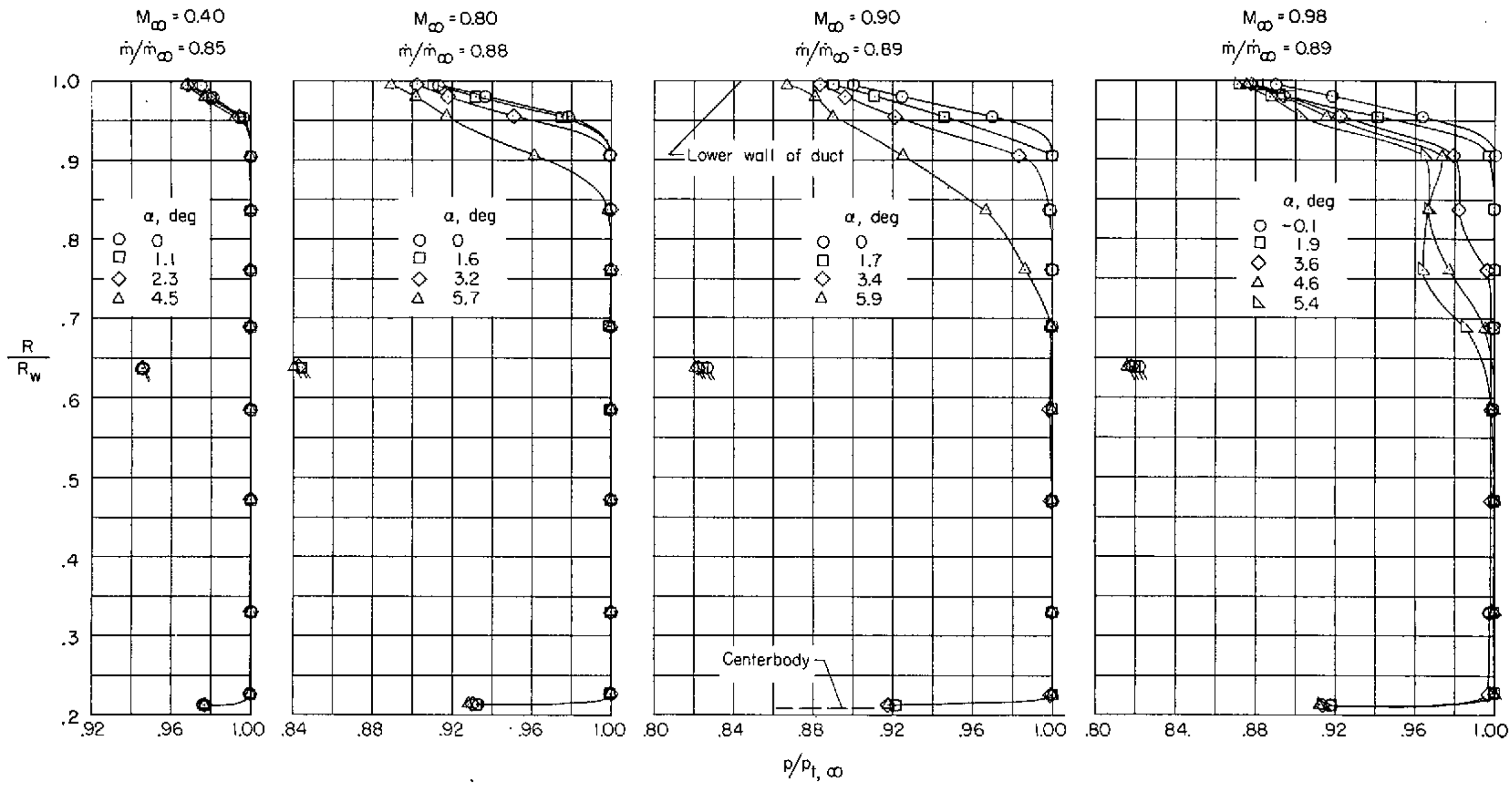

(b) Lower rake arm, $\phi = 180^{\circ}$.

Figure 36.- Concluded.